

KU LEUVEN

ARENBERG DOCTORAL SCHOOL
Faculty of Engineering Science



UNIVERSITÀ
DEGLI STUDI
FIRENZE

Efficient frequency averaging techniques for noise and vibration simulations

Roberto D'Amico

Dissertation presented in partial
fulfillment of the requirements for the
degree of Doctor in Engineering

May 2014



Efficient frequency averaging techniques for noise and vibration simulations

Roberto D'AMICO

Jury members of KU Leuven:

Prof. dr. ir. P. Wollants,
chair of the preliminary defence
Prof. dr. ir. W. Desmet, supervisor
Prof. dr. ir. D. Vandepitte
Prof. dr. ir. D. Huybrechs

Dissertation presented in
partial fulfillment of the
requirements for
the degree of Doctor
in Engineering

Jury members of Università degli Studi di Firenze:

Prof. Dr. Ing. M. Pierini, supervisor
Prof. Ing. A. Bracciali
Dr. Ing. N. Baldanzini

External examiners:

Prof. Dr. Ing. A. Carcaterra
(Università degli Studi di Roma "La Sapienza")
Prof. Dr. Ing. A. Le Bot
(CNRS - École Centrale de Lyon)

May 2014

© KU Leuven – Faculty of Engineering Science
Celestijnenlaan 300B, B-3001 Heverlee, Belgium

© Università degli Studi di Firenze – School of Engineering
Via di Santa Marta, 3, 50139 Firenze, Italy

Alle rechten voorbehouden. Niets uit deze uitgave mag worden vermenigvuldigd en/of openbaar gemaakt worden door middel van druk, fotokopie, microfilm, elektronisch of op welke andere wijze ook zonder voorafgaande schriftelijke toestemming van de uitgever.

Tutti i diritti riservati. Nessuna parte del testo può essere riprodotta o trasmessa in qualsiasi forma o con qualsiasi mezzo, elettronico o meccanico, incluso le fotocopie, la trasmissione facsimile, la registrazione, il riadattamento o l'uso di qualsiasi sistema di immagazzinamento e recupero di informazioni, senza il permesso scritto dell'editore.

All rights reserved. No part of the publication may be reproduced in any form by print, photoprint, microfilm, electronic or any other means without written permission from the publisher.

ISBN 978-94-6018-841-1
D/2014/7515/65

Acknowledgements

*Ai miei genitori,
Nunzia e Vittorio*

Looking back at my PhD from the finishing line, I can realize the beauty of the overall picture. The blurry image of four years ago, progressively went in focus, and I have to say that research is not the only color that makes of a PhD a beautiful picture. Besides uncountable colors and unpredictable shapes, the most wonderful shades are given by the people who accompanied me on this amazing journey, and I am grateful to them as they helped me to achieve such an important goal.

First of all, I would like to thank my supervisors, Prof. Marco Pierini and Prof. Wim Desmet, for their guidance during these years and for the enthusiasm they showed towards my research.

Marco, I am very grateful to you for giving me the opportunity to start this PhD and for having accompanied me as a supervisor through my entire university career.

Wim, thank you for giving me the chance to join your research group and for teaching me precious lessons that go far beyond pure technical ones.

I also thank both of you for your trust and support that allowed me to bring this PhD to completion.

Prof. Huybrechs, thanks for helping me to find my way through the complex world of complex analysis. Your invaluable suggestions and insights were always illuminating for me. Prof. Vandepitte, I really appreciated your feedback on my research and your precious inputs to improve the manuscript. Thank you Prof. Carcaterra for providing me with many useful suggestions and for the interesting discussion on my work. I would like to thank the other members of the committee, Prof. Baldanzini, Prof. Bracciali and Prof. Le Bot for reviewing my manuscript, and Prof. Wollants for chairing the preliminary defence.

Besides the guidance, fundings are always very important for research and I would like to acknowledge the European Commission for the support given through the Collaborative Project Mid-Mod (G.A. 218508) and the Marie Curie Initial Training Network Mid-Frequency (G.A. 214909), within which I held a scholarship as an Early Stage Researcher. The IWT Flanders and the Research Fund of KU Leuven are also gratefully acknowledged.

During these years I had the fortune to work in very stimulating and friendly environments, and this was certainly a boost also for my research progress. Therefore, I owe a big thanks to all colleagues from PMA and from DIEF. In particular, I would like to thank those who directly contributed to this work. Alessandro Pratellesi, you are the first one who helped me to make this picture less blurry. Thank you for having guided me during the first years of my PhD and for your patience when I had tons of questions. Bert Pluymers, you often helped me to keep things well in focus during my stay at KUL, and I am thankful for all your advices. Hendrik and Laurens, I have highly appreciated your criticism and suggestions that helped me to refine this manuscript. Thank you Karel for the interesting discussions; as you can read a bit further, the Lorentzian ***** has been tamed! I am very thankful to my beste collega's Elke, Kunmo, Onur, Stijn and Axel for providing the nice atmosphere and great time in the office and for being always willing to share with me their opinions on technical matters as well as non-technical. Giorgio Bartolozzi and Antonio Maressa, thank you for giving me your help every time I needed.

For all everyday practicalities, the support of the secretary office and IT-service of PMA and Ilaria Giorgi was very much appreciated. Thanks also to Veronique Cortens, Leen Cuypers and Chiara Cianferoni for the assistance with the PhD administration.

Vorrei anche ringraziare due insegnanti le cui lezioni mi sono state particolarmente d'aiuto in questi anni. Grazie Fausto per avermi insegnato ad affrontare le difficoltà a viso aperto e con determinazione. Grazie Marcello per avermi mostrato come la vera bellezza vada oltre il virtuosismo, un'idea che mi ha spesso ispirato nella ricerca.

Un grazie ad Andrea Cafini per la preziosa amicizia che non risente né del tempo né delle distanze.

Un ringraziamento speciale a Rossana, Federica e Riccardo per non averci mai fatto sentire lontani da casa... e per il continuo sostentamento via pacchi!

Ringrazio i miei genitori, Nunzia e Vittorio, per avermi insegnato fin da bambino quanto sia prezioso studiare e per aver lasciato che scegliessi la mia strada con libertà. Il vostro supporto, insieme a quello di Simona, è stato indispensabile per raggiungere questo traguardo. Per tutto questo vi ringrazio

di cuore.

Infine, un ringraziamento immenso a Martina per essermi stata accanto durante questi anni. Grazie per non avermi mai lasciato solo davanti ai mille ostacoli ed avermi sempre incoraggiato. Grazie per aver gioito con me delle vittorie. Grazie per aver condiviso con me tutto questo ed avermi accompagnato fin qui. Non so dove ci porterà il domani, ma sarò felice di scoprirlo insieme a te.

Grazie.

Roberto D'Amico
Leuven, May 2014

Abstract

In the latest decades, noise and vibration characteristics of products have been growing in importance, driven by market expectations and tightening regulations. Accordingly, CAE tools have become irreplaceable in assisting acousticians through the design process, and their accuracy and efficiency are essential to model the behavior of complex engineering systems.

This dissertation aims at increasing the computational efficiency of deterministic simulation techniques for steady-state noise and vibration problems. In particular, the focus is on the efficient evaluation of weighted frequency integrals. Classic approaches make use of numerical quadrature to evaluate a frequency integral. However, the response of a vibrating system is commonly a highly oscillating function of frequency, and a large number of sampling points might be required to achieve an accurate integration. As an alternative, the residue theorem is proposed to compute the weighted integrals. The refined integration over real frequencies is replaced by a few computations at complex frequencies, with a consequent increased accuracy and computational efficiency.

A weighted integral is first evaluated to compute the band-averaged input power into a vibrating system. The ideal rectangular weighting function is approximated by using the square magnitude of a Butterworth filter. Applying the residue theorem, the integral can be evaluated by computing the system response at a few points in the complex frequency plane. These points are some of the filter poles, equal in number to the order of the filter. This allows for an efficient integration, regardless of the bandwidth of analysis. Such a result is successively generalized. The band integral is computed by moving the path of integration to the complex frequency plane and applying efficient quadrature schemes. Due to the smoothness of the integrand in the complex frequency plane, the accuracy and efficiency of the technique are further increased. Moreover, it is shown that using numerical quadrature in the complex plane indirectly leads to the definition of a novel family of weighting functions over the real frequency domain.

The proposed techniques for the evaluation of the band-averaged input power are accurate, efficient, easy to implement and can be employed within any classic deterministic framework. Applications allow assessing the effectiveness of the methodology for complex geometries and frequency dependent properties, and in combination with optimization schemes.

When the order of the Butterworth filter is one, its square magnitude corresponds to the Lorentzian function, which allows computing the weighted average over a wide frequency range by evaluating the response at a single complex frequency. However, due to its bell-shape, the Lorentzian is not suitable to evaluate band values, and its use as a weighting function is investigated in three different ways. The ensemble mean input power is estimated by using the Lorentzian-weighted frequency averaging. The same procedure is used to evaluate the direct field dynamic stiffness of a component. Finally, the Lorentzian is used as a mass-frequency density function within the Fuzzy Structure Theory.

Sommario

Negli ultimi decenni, spinta da aspettative di mercato e normative sempre più stringenti, l'importanza delle prestazioni acustiche e vibrazionali dei prodotti è molto aumentata. Di conseguenza, gli strumenti CAE sono diventati insostituibili nell'assistere l'ingegnere acustico durante la fase di progettazione e la loro accuratezza ed efficienza sono essenziali per modellare il comportamento di sistemi ingegneristici complessi.

L'obiettivo di questa tesi è il miglioramento dell'efficienza computazionale delle tecniche di simulazione deterministiche per problemi stazionari nel campo dell'acustica e vibrazioni, con particolare attenzione alla valutazione efficiente di integrali pesati in frequenza. Approcci classici utilizzano tecniche di quadratura numerica per valutare suddetti integrali, ma dato che la risposta di un sistema vibrante è comunemente una funzione altamente oscillante della frequenza, un grande numero di punti di campionamento può essere necessario per ottenere un'integrazione accurata. Il teorema dei residui è proposto come alternativa per il calcolo di integrali pesati. Con tale metodo si sostituisce il raffinato campionamento sull'asse delle frequenze reali con un ridotto numero di calcoli a frequenze complesse, ottenendo un significativo miglioramento dell'accuratezza e dell'efficienza computazionale.

La soluzione di un integrale pesato è utilizzata per il calcolo della potenza mediata su bande in ingresso ad un sistema vibrante. La funzione peso rettangolare è approssimata dall'ampiezza quadrata del filtro di Butterworth. Utilizzando il teorema dei residui, l'integrale può essere valutato calcolando la risposta del sistema in pochi punti nel piano delle frequenze complesse. Tali punti corrispondono ad alcuni dei poli del filtro di Butterworth, uguali in numero all'ordine del filtro stesso. Questa procedura permette di integrare efficientemente, indipendentemente dall'ampiezza della banda.

Il risultato è successivamente generalizzato. L'integrale di banda è calcolato spostando il percorso di integrazione nel piano delle frequenze complesse e applicando schemi efficienti di quadratura numerica. Il comportamento regolare

della funzione integranda nel piano delle frequenze complesse, assicura che l'accuratezza e l'efficienza di queste tecniche siano ulteriormente migliorate rispetto all'utilizzo della media con filtro di Butterworth. Inoltre, è dimostrato che l'utilizzo di quadratura numerica nel piano complesso porti indirettamente alla definizione di famiglie di funzioni peso sull'asse reale della frequenza.

Le tecniche proposte per la valutazione della potenza in ingresso su bande sono accurate, efficienti, di facile implementazione e possono essere utilizzate con ogni metodologia deterministica classica. Una serie di applicazioni permettono di valutare l'efficacia del metodo per geometrie complesse, proprietà dipendenti dalla frequenza e in combinazione con schemi di ottimizzazione.

Quando l'ordine del filtro di Butterworth è uguale a uno, la sua ampiezza quadrata corrisponde alla funzione di Lorentz, che permette il calcolo della media pesata su ampi intervalli di frequenza valutando la risposta a una singola frequenza complessa. Tuttavia, data sua forma a campana, la Lorentziana non è adatta per la valutazione di medie su bande e il suo utilizzo come funzione peso è studiato in tre diverse situazioni. Utilizzando la media in frequenza pesata con la Lorentziana si valuta l'ingresso di potenza mediato sull'insieme di strutture nominalmente identiche. La stessa procedura è utilizzata per valutare la rigidità dinamica di campo diretto di un dato componente. Infine, la Lorentziana è usata come funzione di densità massa-frequenza all'interno della Fuzzy Structure Theory.

Beknopte samenvatting

Het belang van het vibro-akoestische gedrag van een product is in de voorbije decennia sterk toegenomen, ten gevolge van een striktere regelgeving en strengere markteisen. CAE-technieken zijn dan ook onontbeerlijk geworden voor akoestische ingenieurs tijdens het ontwerpproces. De nauwkeurigheid en efficiëntie ervan zijn cruciaal bij het modelleren van het gedrag van complexe systemen.

Deze thesis heeft als hoofddoel het verbeteren van de rekenefficiëntie van deterministische simulatietechnieken voor stationaire trillings- en geluidsproblemen. Meer specifiek ligt de focus op de efficiënte berekening van gewogen frequentie-integralen. Conventionele methodes maken gebruik van numerieke kwadratuurregels om frequentie-integralen te evalueren. De respons van een trillend systeem is echter vaak een sterk oscillerende functie van de frequentie, waardoor een groot aantal kwadratuurpunten vereist kan zijn voor een nauwkeurige integratie. Dit werk stelt de residustelling voor als alternatief voor het berekenen van gewogen integralen. De rekenintensieve integratie over reële frequenties wordt dan vervangen door een paar berekeningen op complexe frequenties. Dit leidt tot een verhoogde nauwkeurigheid en rekenefficiëntie.

Eerst wordt een gewogen integraal geëvalueerd om het bandgemiddelde ingangsvermogen in een trillend systeem te berekenen. Het ideale rechthoekige venster als wegingsfunctie wordt benaderd door de kwadratische magnitude van een Butterworth-filter. Toepassen van de residustelling laat toe om de integraal te evalueren door de systeemrespons te berekenen in een paar punten in het complexe frequentievlak. Deze punten zijn een aantal van de polen van de filter, in aantal gelijk aan de orde van de filter. Dit zorgt voor een efficiënte integratie, ongeacht de bandbreedte van de analyse. Dit resultaat wordt vervolgens veralgemeend. De bandintegraal wordt berekend door het integratiepad te verschuiven naar het complexe frequentievlak en efficiënte kwadratuurregels toe te passen. Dit verhoogt de nauwkeurigheid en efficiëntie van de techniek nog meer, dankzij de gladheid van de integrand in het complexe

frequentievlak. Voorts wordt aangetoond dat numerieke kwadratuur in het complexe vlak leidt tot de definitie van een nieuwe familie van wegingsfuncties over het reële frequentiedomein.

De voorgestelde technieken voor het berekenen van het bandgemiddelde ingangsvermogen zijn nauwkeurig, efficiënt, eenvoudig te implementeren, en kunnen toegepast worden binnen elk conventioneel deterministisch kader. Toepassingen laten toe om de doeltreffendheid van de methodologie te beoordelen voor complexe geometrieën en frequentie-afhankelijke eigenschappen, en in combinatie met optimalisatieschema's.

Als de orde van de Butterworth-filter één is, komt de kwadratische magnitude ervan overeen met de Lorentz-functie. Dit laat toe om het gewogen gemiddelde over een brede frequentieband te evalueren door de respons op een enkele complexe frequentie te berekenen. De Lorentz-functie is omwille van haar klokvorm echter niet geschikt voor het evalueren van bandwaardes, en het gebruik ervan wordt op drie verschillende manieren onderzocht. Het ensemble-gemiddelde ingangsvermogen wordt geschat door gebruik te maken van Lorentz-gewogen frequentiemiddeling. Dezelfde procedure wordt gebruikt om de dynamische stijfheid in het directe veld van een component te berekenen. Ten slotte wordt de Lorentz-functie gebruikt als een massa-frequentie-dichtheidsfunctie in het kader van de Fuzzy Structure Theory.

List of symbols

Acronyms

BEM	Boundary Element Method
CLF	Coupling Loss Factor
DOF(s)	Degree(s) of Freedom
DVA	Dynamic Vibration Absorber
FEM	Finite Element Method
FS	Fuzzy Structure
FST	Fuzzy Structure Theory
GA	Genetic Algorithm
LHP	Lower Half of the complex Plane
MC	Monte Carlo
MO	Multi-Objective
MS	Master Structure
SEA	Statistical Energy Analysis
SO	Single-Objective
UHP	Upper Half of the complex Plane
WBM	Wave Based Method

Latin symbols

a	ω_B to ω_C ratio
A	Amplification factor of the Butterworth filter
B	Square magnitude of the Butterworth filter
c_a	Speed of sound in an acoustic medium
C	Integration contour
\mathbf{C}	Damping matrix

D	Bending stiffness of a plate
\mathbf{D}	Dynamic stiffness matrix
\mathbf{D}_{dir}	Direct field dynamic stiffness matrix
e	Napier's number
E	Young's modulus
F_0	complex amplitude of harmonic force
g	Generic function
h_j	Upper bound related to the j -th mode
h	Plate thickness
$H_0^{(2)}$	Hankel function of second kind and zero order
i	Imaginary unit ($\sqrt{-1}$)
I_{\bullet}	Integral over the path \bullet
\mathbf{K}	Stiffness matrix
l_{\bullet}	Dimension along the \bullet direction
L	Lorentzian function
m_F	Mass-frequency distribution function
\mathbf{M}	Mass matrix
n	Order of Butterworth filter; order of a quadrature rule; order of a weighting function
\mathbf{n}	Normal vector
N	Number of DOFs
p	Acoustic pressure
P_{acou}	Radiated acoustic power
P_{in}	Input power
r	Euclidean distance between two points
$r(\bullet)$	Reduction coefficient related to the quantity \bullet
t	Time
T	Truncation factor
u	Complex amplitude of displacement
v	Complex amplitude of velocity
w_{\bullet}	\bullet -th weight of integration scheme
W	Generic weighting function
\mathbf{x}	Position vector
Y	Input point mobility
\mathbf{y}	Position vector
z	Complex frequency
Z	Impedance

Greek symbols

γ	Shape parameter of the Lorentzian function
----------	--

Γ	Integration path coinciding with the whole real frequency axis
$\Gamma_0(\Gamma_{0'})$	Finite integration path lying on the real frequency axis
Γ_R	Semi-circular contour path (of infinite radius) in the complex frequency plane
Γ_r	Semi-circular contour path (of finite radius) in the complex frequency plane
δ	Kronecher delta
ϵ_{abs}	Absolute error
ϵ_{rel}	Relative error
ζ_{\bullet}	\bullet -th abscissa of the integration scheme
η	Hysteretic damping loss factor
ν	Poisson's ratio
ξ_{\bullet}	Damping ratio related to the \bullet -th mode
ρ_{\bullet}	Material density of problem \bullet
ϕ_{\bullet}	\bullet -th mass-normalized mode-shape
Ψ	Wave function vector
ω	Angular frequency ($\omega \in \mathbb{R}$)
ω_0	Center frequency
ω_C	Cut-off frequency
ω_{\bullet}	\bullet -th natural frequency
ω_B	Ellipse semi-axis parallel to the imaginary frequency axis
Ω_{\bullet}	Domain of problem \bullet
$\partial\Omega_{\bullet}$	Boundary of the domain Ω_{\bullet}

Other symbols

∞	Infinity
∇	Gradient operator
∇^2	Laplacian operator
\bullet^*	Complex conjugate operator
$\langle \bullet \rangle_W$	W -weighted frequency average
$\langle \bullet \rangle_{\Delta\omega}$	Frequency average over the band $\Delta\omega$
\mathbb{C}	Set of all complex numbers
\mathbb{Z}	Set of all integer numbers
\mathbb{R}	Set of all real numbers
$\det(\bullet)$	Determinant of \bullet
$\text{res}\{\bullet\}$	Residue of the function \bullet
$\text{Re}\{\bullet\}$	Real part of \bullet
$\text{Im}\{\bullet\}$	Imaginary part of \bullet
$ \bullet $	Absolute value of \bullet
\bullet_{pc}	Quantity related to a point connection

- _a Symbol related to an acoustic domain
- _s Symbol related to a structural domain
- _p Symbol related to a plate domain
- _F Symbol related to a fuzzy structure

Contents

Acknowledgements	i
Abstract	v
Sommario	vii
Beknopte samenvatting	ix
List of symbols	xi
Contents	xv
1 Introduction	1
1.1 Current challenges in numerical steady-state vibro-acoustics . .	2
1.2 Averaging techniques and input power computation	5
1.3 Research objectives and achievements	8
1.4 Outline of the dissertation	10
2 Background on prediction and integration techniques for linear second-order dynamic systems	11
2.1 Steady-state problem formulation	12
2.1.1 Structural problem	12

2.1.2	Acoustic problem	14
2.1.3	Fluid-structure interaction	16
2.2	Response of a vibro-acoustic system	17
2.2.1	Low-frequency techniques	18
2.2.2	Pushing low-frequency techniques higher	21
2.2.3	High-frequency techniques	25
2.2.4	Pulling high-frequency techniques lower	29
2.2.5	Fuzzy Structure Theory and hybrid techniques	30
2.2.6	Non-determinism	33
2.3	Methods for oscillatory integrals	35
2.3.1	Asymptotic methods	35
2.3.2	Filon-type methods	36
2.3.3	Levin-type methods	37
2.3.4	The numerical steepest descent	37
2.3.5	Discussion	38
2.4	Position of the research with respect to the state-of-the-art	38
2.5	Conclusion	39
3	The Butterworth-weighted frequency averaging	41
3.1	Input power computation	42
3.2	Frequency integral of the input power	43
3.3	Choice of the weighting function	44
3.4	Influence of the damping model	46
3.4.1	Viscous damping	47
3.4.2	Hysteretic damping	47
3.5	Evaluation of the frequency integral	49
3.5.1	Application of the residue theorem for a general case	50

3.5.2	Integration when system poles are confined in the UHP	51
3.5.3	Integration when system poles are not confined in the UHP	53
3.6	Application cases	57
3.6.1	Simply supported plate	57
3.6.2	Stiffened plates	64
3.7	Computational considerations	68
3.7.1	Computation time	68
3.7.2	Implementation	71
3.8	Conclusion	73
4	Use of quadrature schemes in the complex frequency domain	75
4.1	Frequency-averaged input mobility	76
4.2	Evaluation of the frequency integral	77
4.2.1	Definition of the integration path C	78
4.2.2	Use of numerical quadrature schemes to evaluate I_{Γ_r}	80
4.2.3	Equivalence between Butterworth-weighted averaging and midpoint integration scheme	82
4.3	Quadrature schemes and weighting functions	84
4.3.1	Determination of weighting function parameters	84
4.3.2	Examples and discussion	88
4.4	Application cases	90
4.4.1	Use of Gaussian quadratures over Γ_r and comparison with Butterworth-weighted averaging	91
4.4.2	Adaptive integration schemes	103
4.4.3	Alternative integration schemes	108
4.5	Conclusion	108
5	Application to second-order dynamic systems of industrial complexity	113

5.1	Suspension shock-tower	114
5.1.1	Model description	114
5.1.2	Results	116
5.2	Acoustic car cavity	126
5.2.1	Input power into acoustic systems	126
5.2.2	Model description	128
5.2.3	Poles of an acoustic cavity with admittance boundary conditions	130
5.2.4	Results	132
5.3	Conclusion	140
6	Application to structural-acoustic optimization problems	141
6.1	The use of DVAs for passive vibration control	142
6.2	Theoretical aspects and numerical methodologies	144
6.2.1	Plate bending with point connections	144
6.2.2	Radiated acoustic power	146
6.3	Optimization procedures	147
6.3.1	Minimization of the power injected into the structure	147
6.3.2	Genetic algorithms	148
6.3.3	Summary and advantages of the procedure	150
6.4	Application cases	151
6.4.1	Problem description	152
6.4.2	Objective function evaluation and optimization	152
6.4.3	Single objective optimization	155
6.4.4	Multi-objective optimization	157
6.5	Conclusion	161
7	The Lorentzian-weighted frequency averaging	163

7.1	The Lorentzian function	164
7.2	Evaluation of the ensemble average input power	165
7.2.1	Lorentzian-weighted frequency-averaged input power	166
7.2.2	The choice of the γ parameter	167
7.2.3	Simply supported plate	170
7.2.4	Stiffened plates	173
7.2.5	Additional comments	178
7.3	Direct field dynamic stiffness computation	180
7.3.1	Direct field, artificial damping and Lorentzian-averaging	181
7.3.2	Point dynamic stiffness of plates	183
7.3.3	Advanced applications	185
7.4	Use of the Lorentzian function within the Fuzzy Structure Theory	186
7.4.1	The Fuzzy Structure Theory	187
7.4.2	Pierce's FST and prototype functions	188
7.4.3	Lorentzian mass-frequency density function	190
7.4.4	Additional comments	195
7.5	Conclusion	196
8	Conclusions and future research	197
8.1	Overview and main achievements	198
8.1.1	Efficient band-average input power computations	199
8.1.2	Lorentzian-weighted frequency averaging	201
8.2	Future research topics	202
A	The Wave Based Method	207
A.1	The WB modeling	208
A.1.1	Partitioning into subdomains	208
A.1.2	Field variable expansion	209

A.1.3 Construction of the system of equations	209
A.1.4 Solution and post-processing	210
A.2 Characteristics of WB modeling	210
A.3 3D bounded acoustic problem	212
A.4 Plate bending problem	214
Bibliography	217
Curriculum vitae	237
List of Publications	239

Chapter 1

Introduction

*The purpose of computing
is insight, not numbers.*

R. Hamming, [79]

The rapid increase in computational power is changing the product design process substantially, leading to an actual virtual prototyping revolution. Up to some decades ago, the overall design cycle was guided by experienced engineers, who tailored prototypes in a slow iterative building-testing-optimizing procedure. With the advent of simulation technology, prototypes turn more and more into digitalized versions, hosted by Computer Aided Engineering (CAE) platforms, embedding several modeling environments. Nowadays, engineers can quickly investigate design parameter sensitivities on virtual prototypes, leading to products with an optimized performance, available in a shorter time-to-market and with a significant reduction of development costs.

Within this evolution, also the role of acousticians and dynamicists has undergone a substantial change. In the past, noise and vibration engineers focused on the last part of the design cycle, when the product arose with some annoying noise or an unwanted vibration. Today, driven by market expectations and tightening regulations, noise and vibration characteristics of new products have received growing attention. Sound quality and vibration levels directly influence the customer experience and are key factors for marketing strategies: the sound quality inside a car cabin or the level of vibration perceived within an aircraft are everyday examples [58]. As noise exposure increases the risk of ischemia and other disturbances [3], health issues are also growing in importance, and modern urban and working environments are designed to shield people from noise pollution due to traffic and machineries.

Furthermore, the development of new high-tech products always leads to new sounds and poses novel challenges for vibro-acousticians, like for electric vehicles, where the roaring sound of the combustion engine has been replaced by the high-frequency whistling of electric motors.

In this context, CAE tools have become irreplaceable in assisting acousticians through the design process, and large research efforts have been spent on improving their capability to handle complex problems. Nowadays, many challenges are present in the world of vibro-acoustic modeling, and the aim of the presented research is to go one step further in the improvement of numerical tools for steady-state noise and vibration simulations.

1.1 Current challenges in numerical steady-state vibro-acoustics

Systems of engineering interest are usually complex [67]. Such a complexity can refer to the amount of information needed to model a system consisting of a large number of subsystems. Alternatively, the dynamic behavior of the system can be considered to be complex, in the sense that it reacts in many different manners. For example, a detailed model of a car consists of several thousands of components, and its response, up to 10 kHz, presents about one million acoustic and three million structural modes. This already gives an idea of the amount of information needed to model such a problem in a numerical environment. Additionally, the accuracy of the input data is a key factor for a reliable numerical simulation, although it is not easy to obtain in practice: properties, geometries and external influences always differ from nominal values and are inevitably affected by variability and uncertainty. As a result, the responses of nominally identical systems can significantly differ from each other, as illustrated in fig. 1.1, which shows the effect of variability on the response of 99 nominally identical cars [102]. This lack of information has drastic consequences in numerical modeling and often exacerbates vibro-acoustic problems.

Given this premise, predicting the behavior of such complex systems over the whole audio frequency range is one of the most challenging tasks for acousticians, and, for this purpose, numerical tools are required to be accurate, efficient and able to handle non-determinism.

The first challenge for the analyst is the correct modeling of the physical problem. A detailed model has to be properly reduced according to the problem to solve. This implies that not all components are modeled and that a suitable approximation for their properties is necessary. This process is not an easy task,

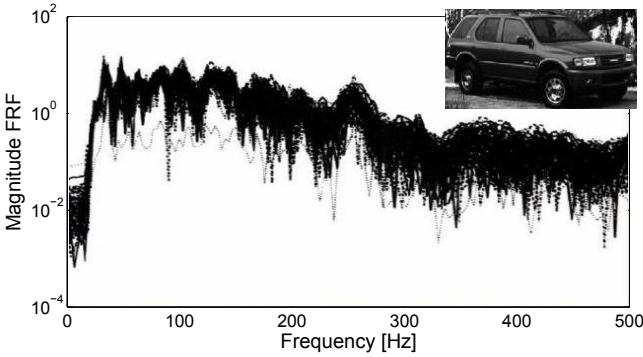


Figure 1.1: Structure-borne acoustic response at the driver’s ear measured on 99 nominally identical ISUZU RODEO’s [102].

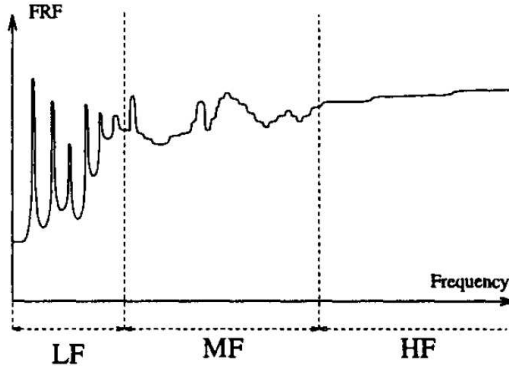


Figure 1.2: Qualitative FRF of a complex system [159].

and the model characteristics are commonly chosen as function of the frequency range of interest and the adopted numerical technique. Generally, the audio frequency range is fragmented in the low- and high-frequency regions, which are bridged by a transitional mid-frequency zone. Over these regions, the Frequency Response Function (FRF) of a complex system exhibits different behaviors, which are qualitatively illustrated in fig. 1.2 [159].

When the wavelength of analysis is larger than or similar to the characteristic dimension of the system, it belongs to the low-frequency range (LF). At these frequencies, the system response is characterized by a small number of distinguishable global modes, which correspond to resonance frequencies (see fig. 1.2). The sensitivity to variations in model properties and geometry is

small, but the influence of the boundary conditions may be large. Element-based methods, such as the Finite Element Method (FEM) [9, 223] and the Boundary Element Method (BEM) [17, 53] are well-established for low-frequency problems and provide a local approximation for the field variable. As model characteristics are considered known with high precision, these approaches are also called deterministic techniques.

When the frequency of analysis increases up to several times the fundamental frequency of the system, the vibration is qualified as high-frequency (HF) and generally implies a high modal density and high modal overlap. Consequently, the response is not dominated by individual modes, but presents a rather smooth behavior and is highly sensitive to small variations in system properties and geometry (see fig. 1.2). The fine discretization required to capture small oscillations is the first computational hurdle impeding the use of element-based techniques for high-frequency. Moreover, the impossibility of determining precise model properties leads to a conceptual limitation for deterministic approaches. For these reasons, energetic approaches are preferred for high-frequency modeling, like the Statistical Energy Analysis (SEA) [132, 133], which is the most widely used tool in this frequency range and only requires gross model parameters. Under the assumptions of a diffuse wavefield and weak coupling between system subcomponents, SEA yields the spatial- and frequency-averaged energy within each subsystem, which is also representative of the average taken on the ensemble of nominally identical structures.

Especially for built-up structures, the transition region from low- to high-frequencies is gradual and is called the mid-frequency range (MF). In this region, distinct components can carry different wavelengths and can be differently influenced by variability in system properties. Both deterministic and energetic approaches present some limitations when moving to mid-frequencies. The former require a large number of degrees of freedom (DOFs) to model the problem. Moreover, the presence of non-determinism may lead to an unsatisfactory degree of reliability and representativity of the solution. On the other hand, the wavefield diffusivity might be violated, leading to unacceptably large SEA confidence intervals.

Currently, no numerical technique exists to analyze the steady-state behavior of a structure in the whole audio frequency range. Over the last twenty years, rather than trying to formulate approaches unifying modeling procedures over the audio frequency range, narrowing the mid-frequency gap has been one of the main research challenges [50, 179]. As a result, three major families of approaches have been developed.

The first family aims at pushing low-frequency approaches higher in frequency, by increasing their computational efficiency and including non-determinism. A second family attempts to relax on the underlying assumptions of the energy methods, trying to include local or modal information to pull down the lower

frequency bound of validity. A final group of so-called hybrid approaches employs both deterministic and energetic modeling techniques in the same framework to model components which carry waves traveling at different speeds.

The techniques discussed in this dissertation aim at increasing the computational performance of classic deterministic techniques to perform averaging procedures. However, their application is not confined to the first but rather extended to all three aforementioned families. Before presenting the main research achievements, the role of averaging techniques and the computation of the input power are now introduced.

1.2 Averaging techniques and input power computation

The behavior of a vibrating system can be described by either kinematic or energetic quantities. In each case the response is a function of four variables: time, space, frequency and a vector collecting model descriptors. While time becomes redundant for steady-state phenomena, space and frequency are necessary to fully define the analysis, together with a set of descriptors grouping all the information related to geometry, material properties, boundary conditions, loadings, operating conditions, etc.

Averaging procedures can be performed over each of these variables [132]. However, while time averaging of harmonic quantities simply consists of averaging over a cycle of vibration, averaging over space, frequency and model parameters might be computationally demanding and leads to information of high practical interest.

Space-averaging can be carried out either over a part or over the whole extent of the physical domain and it gives an idea of the overall vibration level present in the component. The computational cost of this operation is relatively low and usually involves only a post-processing step.

Computing ensemble-averages involves averaging over random variations of the model parameters and allows assessing the influence of non-determinism on the system response. Estimating the ensemble behavior can be very computationally cumbersome, as stochastic techniques might be necessary. For example, a commonly used approach is the Monte Carlo (MC) method [62]. This strategy consists of running a massive amount of simulations, each time using a different set of parameters complying with the prescribed statistics. Depending on the level of variability, a MC simulation can involve hundreds or thousands of recalculations. For example, in fig. 1.3, the MC approach is employed to estimate the ensemble mean input power into a simply supported

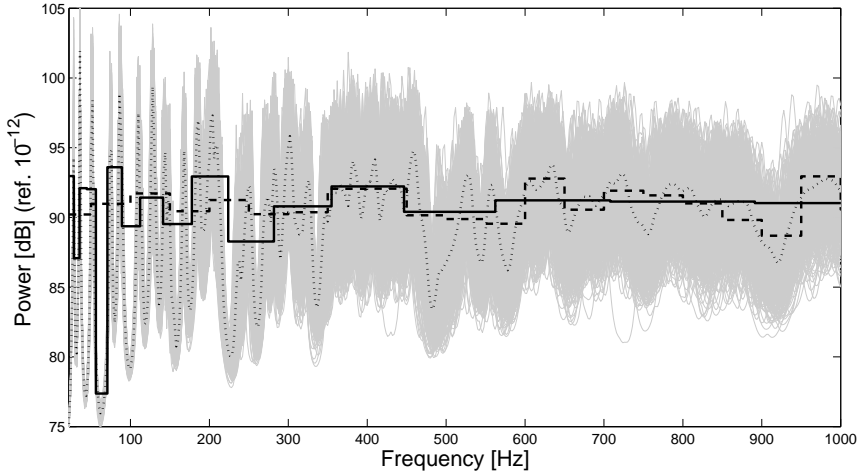


Figure 1.3: Comparison between frequency and ensemble-averaged input power for a simply supported plate perturbed with random masses. Samples (gray lines), ensemble mean (dotted line), 1/3 octave band average (solid line) and 50 Hz bandwidth average (dashed line).

plate excited by a point force and of which the material density is perturbed by means of 20 randomly distributed masses. To compute the ensemble-average, 300 samples have been used. This also highlights the large computational effort required to estimate ensemble statistics of dynamic systems.

Finally, frequency averaging procedures require the computation of weighted integrals and can have a wide range of applications. Firstly, they can provide a good approximation for the ensemble-average at a reduced computational cost. In general, this is the case when the statistical overlap is relatively large and the system response can be considered ergodic [141]. The validity of this hypothesis is strongly dependent on the choice of the frequency interval on which the average is carried out. At low-frequencies, the modal overlap is expected to be very small and a number of resonance frequencies has to be covered, say three to five [58]. With decreasing wavelength, the response shows a smoother behavior and such a frequency interval can be decreased in width. This can be seen in fig. 1.3. Nevertheless, the relation between ensemble and frequency averaging is still subject of current research [131].

In many cases, expressing the response in the format of predefined frequency bands is preferred to a high spectral resolution. For instance, for vehicle noise or building acoustics, octave or third octave bands are often used [58].

The outcomes of band-averaging are illustrated in fig. 1.3. The input power

is averaged both on one-third octave bands and on 50 Hz-bands. A good agreement between frequency and ensemble-averaging can be observed when the response statistics saturate.

The computation of weighted frequency integrals is commonly performed by means of numerical quadrature [43]. However, since the response of a dynamic system can be a highly oscillatory function, a large number of sampling frequencies might be needed to obtain accurate estimates, with a subsequent high computational cost.

In this work, the main focus is on the evaluation of the frequency-averaged input point mobility, which is straightforwardly related to the power injected by a force. As it directly connects the strength of the excitation to the vibration of the structure, an accurate evaluation of the input power is an important piece of information. Nevertheless, its estimation is a difficult task, especially for built-up systems, in which flexible and stiff components are mounted together to improve the dynamic properties of the machinery. Stiffened plates, for instance, are encountered in structures like vessels, aircraft, trains etc. In most of the cases, the machinery is designed such that heavy loads are applied on the main frame of the structure. As a consequence, stiff components control the power injected into the whole structure, and a detailed vibration analysis is required to determine its magnitude.

One way of evaluating the input power into a structure is through experimental analysis, although obtaining a direct measurement of the input power is not simple [40]. Alternatively, when the wavelength is much smaller than the characteristic dimension of the component, its geometrical features are assumed to be of infinite extent and the input mobility can be easily expressed in analytical form for common elements such as rods, beams, plates, cylindrical shells, etc. [40, 132]. This approximation is widely applied in high-frequency modeling, where energetic approaches are used. For more general structures, the most reliable way to numerically evaluate the input power is to use deterministic methods, although their accuracy comes with a higher computational cost. Approaches such as FEM and BEM are perfectly suited to investigate the effects of boundary conditions, inhomogeneities and discontinuities on the system behavior; especially in the transition region from low- to high-frequencies, where deterministic modeling is complementary to the energetic one.

Frequency-averaged input power can have many applications in vibro-acoustic design and analysis. For example, the power injected into the system constitutes the driving factor for energy approaches, which implicitly handle frequency-averaged quantities [132]. Consequently, a precise estimate of the input power can lead to a reasonable level of solution accuracy, even in the case that high-frequency assumptions are only roughly met [57]. Furthermore, the

knowledge of the input power leads to the input mobility, which can be useful to build lumped parameter systems, and allow complicated substructures to be seen as parts of a mechanical circuit [58].

Frequency averaging procedures can also be useful to perform more advanced design studies. For instance, optimizing the behavior of a structure over a band highly improves the robustness of the optimal configuration with respect to a single frequency optimization [173]. However, if not performed efficiently, the averaging operation can seriously slow down the analysis.

Finally, from a broader perspective, frequency averaging falls in the class of techniques attempting at estimating highly oscillatory integrals, which are not only confined to the noise and vibration area [33]. Those integrals are common in many other branches of computational physics, such as electromagnetism, optics, quantum chemistry, image processing etc. Although these topics are not covered in this manuscript, the following techniques can be easily extended to other domains.

1.3 Research objectives and achievements

The research presented in this dissertation aims at formulating efficient tools for performing frequency averaging operations. Classic algorithms make use of numerical quadrature techniques to estimate a weighted integral. Since the response of a vibrating system is an oscillating function of frequency, many sampling points might be required to obtain accurate estimates. On the other hand, more advanced schemes for highly oscillatory integrals require a priori knowledge of the integrand, which is often not the case for complex vibrating systems.

The residue theorem is originally employed in the following. As a result, accurate band evaluations can be obtained with a substantial reduction of computational effort.

The main achievements of the research described in this dissertation can be grouped in two categories.

Efficient evaluation of band-averaged input power This part of the research is devoted to the efficient evaluation of band integrals. Firstly, this is obtained by using the square magnitude of a Butterworth filter to approximate the rectangular weighting function. Instead of an expensive and extensive use of quadrature techniques, the average can be easily estimated by evaluating the system response at a few points in the complex frequency plane, these points being some of the filter poles, equal in number to the order of the filter. This

allows for an efficient integration, regardless of the bandwidth. Subsequently this concept is generalized. The band integral is computed by moving the path of integration to the complex frequency plane and applying efficient quadrature schemes. The smoothness of the frequency response function over the alternative path is higher and leads to more efficient and accurate integral evaluations. The application of this procedure also shows that it is possible to define a family of weighting functions corresponding to certain paths and integration schemes.

The robustness of the approach with respect to complex geometries and frequency dependent properties is proven through examples.

This strategy is also successfully exploited for optimization purposes. Thanks to its efficiency, it can quickly lead to the identification of the configuration which performs best over a frequency range.

Use of Lorentzian-weighted frequency averaging The square magnitude of the Butterworth filter of order one coincides with the Lorentzian function. Due to its bell-shape, the Lorentzian function weighs the integral over a wider frequency band, rather than providing a band value, and one single response evaluation at a complex frequency leads to the Lorentzian-weighted frequency average, without the need for refined quadrature integration. This concept is exploited in different ways.

- The possibility of representing the ensemble mean response by means of frequency averages is investigated. This requires the shape parameter, which describes the Lorentzian function, to be properly tuned. In this sense, the research attempts to connect the response statistics to the aforementioned parameter for providing an estimate of the ensemble-average.
- When performed on the dynamic stiffness of the system, the Lorentzian-weighted frequency average leads to the direct field dynamic stiffness. This information can be exploited within the context of hybrid techniques, or other strategies, where the computation of the direct field is required.
- The use of the Lorentzian function is extended to the Fuzzy Structure Theory (FST) [185] in the form proposed by Pierce [166]. In this case, the Lorentzian is employed to describe the mass-frequency density function of a fuzzy component.

As proposed in this dissertation, the use of the residue theorem to evaluate weighted integrals is novel in the field of noise and vibration. However, the presented ideas could be easily generalized and extended to other domains where the integration of highly oscillating functions is of interest.

1.4 Outline of the dissertation

This dissertation is organized in eight chapters; an appendix is added to clarify specific topics. The general outline of the manuscript is now presented.

Chapter 1 introduces the importance of fast and accurate numerical tools to improve the product design process and provides a general overview of the topics developed within this research path. Chapter 2 describes the mathematical underlying formulations for vibro-acoustic problems and illustrates the current state-of-the-art for steady-state noise and vibration modeling and highly oscillatory integral computation.

The main idea of exploiting the residue theorem to solve weighted frequency integrals is presented in ch. 3, where the square magnitude of the Butterworth filter is used to weigh a frequency integral. These concepts are further exploited in ch. 4, where the aforementioned procedure is extended towards a more general and efficient procedure for band-averaged input power evaluation. Both chapters present application cases to prove the computational benefits of the proposed strategy.

Chapter 5 and 6 are dedicated to advanced applications of the proposed strategy. In the former, a geometrically complex structural component and a frequency-dependent acoustic problem are investigated, while in the latter, the approach is used in combination with an optimization strategy, providing the best design configuration over a frequency band.

Chapter 7 focuses on the use of the Lorentzian-weighted frequency averaging procedure. In order to compute the ensemble average, the shape parameter of the Lorentzian is properly tuned based on the response statistics of the system under investigation. Moreover, in this chapter the use of the Lorentzian function is exploited to evaluate the direct field dynamic stiffness and within the context of the FST.

Conclusions and perspectives for future research are provided in ch. 8.

Appendix A describes the features of the Wave Based Method (WBM) [49], which is extensively used in some of the applications.

Chapter 2

Background on prediction and integration techniques for linear second-order dynamic systems

The response of a dynamic system in the time domain consists of a transient and a steady-state component. For asymptotically stable systems, the former dies out after the excitation is applied and the vibration is characterized by the steady-state, or time-invariant, behavior. From an analytical point of view, solving a transient problem involves the solution of a differential equation in the time domain, while for steady-state conditions, a time-harmonic solution is assumed, and the problem can be expressed in the frequency domain. Describing the mathematical formulations underlying the latter phenomena is the first objective of the following chapter. These include structural, acoustic and coupled/uncoupled vibro-acoustic problems. However, the complexity of real-life applications hampers the possibility of finding a closed-form solution for such differential equations. For this reason, numerical methods have been developed to yield an approximate solution at a reasonable expense of computational resources. The second major objective of this chapter is to provide an overview of the currently existing numerical techniques. These are divided in two main families: deterministic and energetic approaches. Such methods are not only essential to tackle low- and high-frequency problems, they also constitute the building blocks for more advanced techniques to cover

the mid-frequency range and to deal with non-determinism. In order to allow the positioning of the work into a broader perspective, the third objective of this chapter is to give a short overview of the existing techniques to estimate highly oscillatory integrals. These can be thought as a generalization of frequency averaging calculations, which are the main focus in this dissertation.

The chapter is organized as follows. Section 2.1 provides the general problem formulations. Section 2.2 describes the main features of a typical vibro-acoustic response. A survey of the numerical methods is given in sec. 2.2.1 to 2.2.6, which illustrate the state-of-the-art techniques for low-frequencies, high-frequencies, their extensions for mid-frequencies, hybrid approaches and methods to handle non-determinism. A short overview of methods for highly oscillatory integrals is given in sec. 2.3. The position of the research is discussed in sec. 2.4. Finally, sec. 2.5 is dedicated to concluding remarks.

2.1 Steady-state problem formulation

This section focuses on the description of the structural, acoustic and vibro-acoustic problem. The mathematical conventions used in the following are now introduced. The physical space \mathbb{R}^3 is a Cartesian reference system $(\mathbf{i}, \mathbf{j}, \mathbf{k})$ and a generic point is indicated as $\mathbf{x} = (x_1, x_2, x_3)$. Since linear steady-state phenomena are of interest in the following, a generic solution $w(\mathbf{x}, t) = w(\mathbf{x}, \omega)e^{i\omega t}$ to a boundary problem is harmonic with positive time dependence, where i indicates the imaginary unit, $i^2 = -1$, ω the angular frequency of analysis and t the time.

The Einstein convention for summation over repeated Latin indices is adopted.

2.1.1 Structural problem

Let Ω_s be a three-dimensional (3D) domain occupied by a structure at equilibrium, as depicted in fig. 2.1. The smooth boundary $\partial\Omega_s$, with normal \mathbf{n}_s , is divided in two non-overlapping parts, $\partial\Omega_s = \partial\Omega_{s,d} \cup \partial\Omega_{s,s}$. Over $\partial\Omega_{s,d}$ and $\partial\Omega_{s,s}$, prescribed displacements and surface forces are applied, respectively. A body force field $\mathbf{f}(\mathbf{x}, \omega)$ is also defined in Ω_s . The complex amplitude of the displacement of a particle at point \mathbf{x} is denoted by the vector $\mathbf{u}(\mathbf{x}, \omega)$.

The components of the linearized symmetric strain tensor ϵ are defined as

$$\epsilon_{kh}(\mathbf{x}, t) = \frac{1}{2} [u_{k,h}(\mathbf{x}, t) + u_{h,k}(\mathbf{x}, t)], \quad (2.1)$$

where $u_{k,h}$ identifies the rate of variation of the k -th component with respect to the h -th direction, with $k, h = 1, 2, 3$. The symmetric stress tensor $\boldsymbol{\sigma}$ can be

defined accordingly by means of the constitutive law

$$\sigma_{ij}(\mathbf{x}, t) = a_{ijkh} \epsilon_{kh}(\mathbf{x}, t), \quad (2.2)$$

where a_{ijkh} , with $i, j = 1, 2, 3$, is the tensor associated with the elastic properties of the material and is positive definite. Under steady-state conditions, the governing equation for the elastodynamics problem can be formulated as

$$\omega^2 \rho_s u_i(\mathbf{x}, \omega) + \sigma_{ij,j}(\mathbf{x}, \omega) = -f_i(\mathbf{x}, \omega) \quad \text{in } \Omega_s, \quad (2.3)$$

where ρ_s denotes the mass density of the structure. The application of boundary conditions leads to a well-posed problem. A prescribed displacement $\bar{\mathbf{u}}$ is applied on the boundary $\partial\Omega_{s,d}$,

$$\mathbf{u}(\mathbf{x}, \omega) = \bar{\mathbf{u}} \quad \text{on } \partial\Omega_{s,d}. \quad (2.4)$$

When the structure is fixed, $\bar{\mathbf{u}} = \mathbf{0}$, while if it is free $\partial\Omega_{s,d} = \emptyset$. Finally, on $\partial\Omega_{s,s}$ the surface force field, $\bar{\mathbf{s}}$, is applied,

$$\boldsymbol{\sigma}(\mathbf{x}, \omega) \cdot \mathbf{n}_s(\mathbf{x}) = \bar{\mathbf{s}} \quad \text{on } \partial\Omega_{s,s}, \quad (2.5)$$

where \mathbf{n}_s is the vector normal to $\partial\Omega_{s,s}$. If dissipation mechanisms are included in the description of the material properties, an imaginary term has to be taken into account in the stress tensor,

$$\sigma_{ij}^{(\text{diss})}(\mathbf{x}, \omega) = \sigma_{ij}(\mathbf{x}, \omega) + i\omega b_{ijkh} \epsilon_{kh}(\mathbf{x}, \omega), \quad (2.6)$$

where b_{ijkh} represents the coefficients of the damping tensor.

The general elastodynamics problem is commonly solved through the construction of a variational formulation which leads to associated mass and stiffness linear operators. For slender components like beams, plates and shells, the mass and stiffness terms result in simplified forms [76].

Time-averaged quantities are computed by averaging over a cycle of vibration and are of high interest for the steady-state analysis of vibrating systems. The potential energy density, e_{pot} , can be expressed as

$$e_{\text{pot}}(\mathbf{x}, \omega) = \frac{1}{4} a_{ijkh} \epsilon_{ij}(\mathbf{x}, \omega) \epsilon_{kh}^*(\mathbf{x}, \omega), \quad (2.7)$$

where \bullet^* indicates the complex conjugate of \bullet . The kinetic energy density, e_{kin} , reads

$$e_{\text{kin}}(\mathbf{x}, \omega) = \frac{\omega^2}{4} \rho_s u_j(\mathbf{x}, \omega) u_j^*(\mathbf{x}, \omega). \quad (2.8)$$

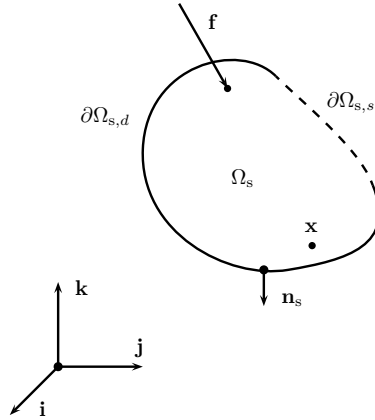


Figure 2.1: Geometrical configuration of the structural problem.

Summing kinetic and potential energy leads to the total mechanical energy density, which is widely used to describe high-frequency phenomena. The time-averaged active power injected by the source \mathbf{f} into the system is given by

$$P_{\text{in}}(\omega) = \frac{1}{2} \text{Re} \left\{ i\omega \int_{\Omega_s} u_j(\mathbf{x}, \omega) f_j^*(\mathbf{x}, \omega) d\Omega_s(\mathbf{x}) \right\}, \quad (2.9)$$

where $\text{Re} \{ \bullet \}$ is the real-part operator. Using the imaginary part operator leads to the computation of the reactive input power. Finally, the time-averaged dissipated power can be computed as

$$P_{\text{diss}}(\omega) = \frac{\omega^2}{2} \int_{\Omega_s} b_{ijkl} \epsilon_{ij}(\mathbf{x}, \omega) \epsilon_{kl}^*(\mathbf{x}, \omega) d\Omega_s(\mathbf{x}). \quad (2.10)$$

2.1.2 Acoustic problem

Let Ω_a be a 3D domain occupied by an inviscid, homogeneous and compressible fluid at rest, of smooth boundary $\partial\Omega_a$, with normal \mathbf{n}_a , as depicted in fig. 2.2. Let $p(\mathbf{x}, \omega)$ describe the low amplitude fluid oscillations at a point \mathbf{x} . Under steady-state conditions the acoustic problem is governed by the Helmholtz equation,

$$\nabla^2 p(\mathbf{x}, \omega) + k_a^2 p(\mathbf{x}, \omega) = -\frac{i}{\rho_a \omega} q(\mathbf{x}, \omega) \quad \text{in } \Omega_a, \quad (2.11)$$

where ∇^2 indicates the Laplacian operator and k_a is the acoustic wavenumber associated to the speed of sound c_a ($k_a = \omega/c_a$). The symbols ρ_a and q

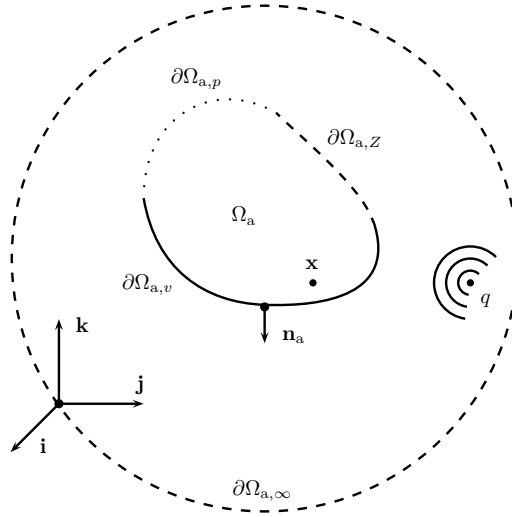


Figure 2.2: Geometrical configuration of the acoustic problem.

respectively indicate the density of the medium and the volumetric source strength located in Ω_a .

For a generic interior acoustic problem, the boundary $\partial\Omega_a$ can be split in three non-overlapping regions, such that $\partial\Omega_a = \partial\Omega_{a,v} \cup \partial\Omega_{a,Z} \cup \partial\Omega_{a,p}$. On $\partial\Omega_{a,v}$, a normal velocity \bar{v}_n is applied,

$$\nabla p(\mathbf{x}, \omega) \cdot \mathbf{n}_a = -i\omega\rho_a\bar{v}_n \quad \text{on } \partial\Omega_{a,v}. \quad (2.12)$$

where ∇ is the gradient operator. On $\partial\Omega_{a,Z}$, the pressure and its normal derivative are related through the normal impedance \bar{Z} ,

$$\nabla p(\mathbf{x}, \omega) \cdot \mathbf{n}_a = -i\frac{\omega\rho_a}{\bar{Z}}p(\mathbf{x}, \omega) \quad \text{on } \partial\Omega_{a,Z}. \quad (2.13)$$

Finally, on $\partial\Omega_{a,p}$, a prescribed pressure \bar{p} is imposed,

$$p(\mathbf{x}, \omega) = \bar{p} \quad \text{on } \partial\Omega_{a,p}. \quad (2.14)$$

When unbounded acoustic problems are considered, a fourth partition at infinity, $\partial\Omega_{a,\infty}$, has to be taken into account, over which the Sommerfeld radiation condition is imposed. This condition implies that no energy is radiated from infinity and is formalized as follows,

$$\lim_{|\mathbf{x}| \rightarrow \infty} |\mathbf{x}| \left(\frac{\partial p(\mathbf{x}, \omega)}{\partial |\mathbf{x}|} + ik_a p(\mathbf{x}, \omega) \right) = 0 \quad \text{in } \Omega_{a,\infty}. \quad (2.15)$$

Also for acoustic problems, the effects of loss mechanisms can be taken into account. Commonly, an imaginary dissipation factor is included in the description of the speed of sound propagation.

The acoustic problem can be written in an equivalent variational formulation, leading to the construction of mass and stiffness linear operators [159]. Once the pressure field is known, derived acoustic quantities can be calculated. The acoustic particle velocity $\mathbf{v}(\mathbf{x}, \omega)$ is computed as,

$$\mathbf{v}(\mathbf{x}, \omega) = \frac{i}{\rho_a \omega} \nabla p(\mathbf{x}, \omega), \quad (2.16)$$

The time-averaged total acoustic energy density is given by,

$$e_{\text{tot}} = \frac{1}{4} \left[\rho_a |\mathbf{v}(\mathbf{x}, \omega)|^2 + \frac{|p(\mathbf{x}, \omega)|^2}{\rho_a c_a^2} \right]. \quad (2.17)$$

The time-averaged active acoustic intensity $\mathbf{I}(\mathbf{x}, \omega)$ is expressed as,

$$\mathbf{I}(\mathbf{x}, \omega) = \frac{1}{2} \text{Re} \{ p(\mathbf{x}) \mathbf{v}^*(\mathbf{x}) \}. \quad (2.18)$$

If the imaginary part is computed instead of the real one, the reactive acoustic intensity is obtained. Finally, the time-averaged acoustic power P_{acou} is obtained by integrating the active acoustic intensity over a surface S ,

$$P_{\text{acou}} = \int_S \mathbf{I}(\mathbf{x}) \cdot \mathbf{n}_a(\mathbf{x}) \, ds(\mathbf{x}), \quad (2.19)$$

where \mathbf{n}_a is the normal to the infinitesimal surface ds . Integrating the reactive intensity leads to the reactive acoustic power.

2.1.3 Fluid-structure interaction

This class of problems describes the situation when an elastic structure is in contact with a fluid. In this case, there is a mutual interaction such that the fluid pressure is influenced by the structural vibrations and, vice versa, the acoustic pressure constitutes a distributed load along the interface.

If the vibro-acoustic interaction is weak, the structural and the acoustic problems can be treated separately, without taking into account the back-coupling effect of one domain on the other. This is a reasonable assumption when the elastic structure has high stiffness and the fluid is characterized by a low density. In an uncoupled model, the structural vibration provides the excitation for the acoustic volume, whose behavior does not influence the former. If the acoustic field excitation is the primary source of excitation for

the structure, their behaviors can again be analyzed separately.

On the other hand, when the fluid density is high or when the stiffness and mass of the structure is very low, interaction between the structure and the fluid is not negligible. In that case the mutual interaction has to be taken into account into a coupled vibro-acoustic model by means of coupling terms. The coupling condition for the structure is,

$$\boldsymbol{\sigma}(\mathbf{x}, \omega) \cdot \mathbf{n}_s = p(\mathbf{x}, \omega) \mathbf{n}_s \quad \text{on } \partial\Omega_{s,i}, \quad (2.20)$$

with $\partial\Omega_{s,i}$ the wetted surface, and for the fluid boundary,

$$\nabla p(\mathbf{x}, \omega) \cdot \mathbf{n}_a = \omega^2 \rho_s \mathbf{u} \cdot \mathbf{n}_a \quad \text{on } \partial\Omega_{a,i}. \quad (2.21)$$

2.2 Response of a vibro-acoustic system

Solving a vibro-acoustic problem consists of finding a solution either to eq. (2.3), to eq. (2.11) or to a coupled version of the two. Commonly, such a solution cannot be found in a closed form and numerical techniques are necessary to yield an approximation.

Generally, the response of a vibrating system is an oscillating function of space and frequency, and either a fine domain discretization or a proper number of oscillatory functions have to be employed to accurately represent its behavior. However, while the frequency response may become smoother, with decreasing wavelengths, the spatial pattern presents an increasingly oscillatory behavior. For this reason, the numerical model should be refined accordingly when moving to higher frequencies.

Based on the spatial oscillatory behavior of the solution, it is possible to divide the audio frequency range into two main regions, namely low- and high-frequency, bridged by a mid-frequency interval.

When the spatial oscillation is comparable to the characteristic size of the problem under analysis, the corresponding wavelength belongs to the low-frequency range. The response of the system is characterized by distinct resonance peaks, which involve global modes of the component, as shown in fig. 1.2. Small changes in the geometry and system properties slightly affect the response, and a relatively low number of DOFs is necessary to characterize the system behavior. The low-frequency behavior is of interest because of the global nature of the modal response, which leads to a high level of energy and large amplitude of vibration.

On the other hand, when the frequency of analysis corresponds to many times the fundamental natural frequency of the component, the vibrational regime belongs to the high-frequency region. Contrarily to the low-frequency range, high-frequency is characterized by highly oscillatory spatial patterns

and sensitivity to system parameter perturbation. The high modal overlap allows the response to be very smooth in the frequency domain, as qualitatively depicted in fig. 1.2. Due to the potential for high sound transmission and radiation and for fatigue problems, high frequencies are of high practical interest. Finding a solution to a high-frequency problem is feasible in practice but presents two main limitations. Firstly, it requires a high refinement of the numerical scheme and a consequently large computational effort. Secondly, due to the effects of uncertainties, it would lead to a result of low practical interest. For these reasons, instead of solving eq. (2.3) or (2.11), the problem is commonly reformulated in terms of averaged energetic quantities and its solution allows predicting the ensemble average, rather than the response of a single nominal structure.

Moving from low- to high-frequencies is not abrupt and consists of a gradual transition. This is particularly relevant for complex systems, whose modal density exhibits large variations over different frequency bands. In the mid-frequency region, uncertainty and variability increasingly influence the response of the system, as can be observed in fig. 1.1, and solving the governing equations as such, might be computationally very demanding. On the other hand, moving to an energetic description of the problem might yield unsatisfactory results. Currently, no approach is able to provide meaningful insight on the system behavior over the whole audio frequency range. However, rather than tackling such a unified problem, researchers have been focusing on extending the range of applicability of deterministic and energetic modeling to cover the mid-frequency gap [50]. A comprehensive review of the numerical methods for steady-state noise and vibration problems is given in the next sections, grouped as follows:

- low-frequency techniques;
- methods to push low-frequency techniques higher in frequency;
- high-frequency techniques;
- methods to pull high-frequency techniques lower in frequency;
- Fuzzy Structure Theory and hybrid techniques;
- methods to handle non-determinism.

2.2.1 Low-frequency techniques

The main assumption behind low-frequency techniques is that model properties, boundary conditions and excitations are known with absolute precision. These details allow to fully define the problem statement of eq. (2.3) and (2.11). A

variational formulation is then used to provide an approximate solution to the dynamic problem, which represents the local behavior of the field variable. The following section presents the main features of the most used tools for low-frequency analysis, namely FEM and BEM.

Finite Element Method FEM [9, 223] is the most used technique for structural applications and is also widely used for acoustic problems, especially interior ones. The generic problem domain Ω is divided into n_{el} elements of finite dimension, Ω_i (with $i = 1, 2, \dots, n_{el}$), over which the field variable $w(\mathbf{x})$ is approximated by a weighted sum of nodal values w_j with $j = 1, 2, \dots, n_{nod}$,

$$w(\mathbf{x}) \approx \hat{w}(\mathbf{x}) = \sum_{j=1}^{n_{nod}} w_j N_j^{(i)}, \quad (2.22)$$

where $N_j^{(i)}$ represents the j -th term of a low-order polynomial function describing the variable over Ω_i , also called shape function. A Galerkin weighted residual formulation is used to impose the boundary conditions and excitations, leading to the definition of a dynamic stiffness matrix, which, multiplied by the vector \mathbf{w} containing all nodal field variables, equilibrates the forcing term \mathbf{f} ,

$$(-\omega^2 \mathbf{M} + i\omega \mathbf{C} + \mathbf{K}) \mathbf{w} = \mathbf{f}. \quad (2.23)$$

The terms \mathbf{M} , \mathbf{C} and \mathbf{K} represent the mass, damping and stiffness matrices, respectively. Except for some particular cases, they are banded, symmetric, sparsely populated, positive definite and frequency independent. Moreover, due to the polynomial nature of the shape functions, the integration over the elements can be easily performed. All these advantageous characteristics allow a computationally efficient solution of the system of equations by means of both direct and modal solvers. Eventually, in the post-processing phase, the field solution can be evaluated by means of the shape functions.

Although simplicity makes FEM a very flexible tool, some limitations have to be taken into account [143]. The use of low-order polynomial functions leads to the so-called interpolation error, for which the solution may significantly differ from the exact system response. Additionally, poor accuracy is yielded when describing derivatives of primary variables, as they are computed by differentiating polynomial shape functions. Another type of error is the dispersion error, due to the difference between the real wavelength in the physical problem and the one represented in the discretized domain. This error is accumulated along the domain and highly influences the solution accuracy. These problems can be mitigated by a proper domain discretization. In the low-frequency range, the interpolation error is dominant, and six to ten linear elements per wavelength are commonly used to discretize acoustic domains [16].

For structural problems some rules are proposed in ref. [204]. When increasing the frequency, the dispersion error highly degrades the solution accuracy, and a larger number of elements might be required, with a corresponding increase of computational load.

A final disadvantage of FEM arises when dealing with unbounded domains [69]. Since the Sommerfeld condition is not inherently satisfied by the formulation, an artificial truncation boundary should be introduced to simulate energy absorption at infinity. Furthermore, the size of the problem rapidly grows when modeling the exterior domain. To tackle unbounded problems, proper strategies have been developed, i.e. Infinite Elements [15], Absorbing Boundary Conditions [70, 71] and Perfectly Matched Layer [77, 83].

Boundary Element Method BEM [17, 53] is mainly used in acoustics and is based on the discretization of the Helmholtz integral equation,

$$c(\mathbf{x})p(\mathbf{x}) = \int_{\partial\Omega_a} \left[p(\mathbf{y}) \frac{\partial G(\mathbf{x}, \mathbf{y})}{\partial n_a} - \frac{\partial p(\mathbf{y})}{\partial n_a} G(\mathbf{x}, \mathbf{y}) \right] d\partial\Omega_a(\mathbf{y}), \quad (2.24)$$

where $c(\mathbf{x})$ is a constant depending on the position of \mathbf{x} : 1/2 when \mathbf{x} is over a smooth boundary, 1 when \mathbf{x} is inside the domain and 0 when \mathbf{x} lies outside the domain. If \mathbf{x} is located over a non-smooth boundary, c is equal to $\frac{\alpha}{4\pi}$, where α is the solid angle subtended by the boundary $\partial\Omega_a$ at \mathbf{x} . The symbol G indicates the Green's kernel, which satisfies the homogeneous Helmholtz equation, and n_a is the normal to the boundary $\partial\Omega_a$ at \mathbf{y} . BE techniques do not require the discretization of the whole domain, but only of its boundaries. As a consequence, models are smaller with respect to FEM, and unbounded problems can be solved without additional conditions at infinity. However, also BEM requires mesh refinement for increasing frequencies [142], although the accuracy does not decrease when computing derived acoustic variables, i.e. velocity, as it happens with FEM. On the other hand, the computational efficiency of BEM is limited by its matrices which are complex, fully populated and frequency dependent, and their computation requires special care due to the presence of singularities in the Green's kernels.

Two different BEM formulations exist. The direct formulation is based on eq. (2.24), which is solved for the pressure and its derivative at the nodal positions. This allows solving either an interior or an exterior problem in the post-processing step. On the other hand, the indirect formulation allows handling both problems at the same time. Such a formulation is a combination of two direct problems [18] and results in a system of equations in terms of the so-called single and double layer potential densities at nodal positions. In general, the indirect BEM shows some advantages over the direct one. Its matrices are symmetric and it can handle geometries with open boundaries.

Due to its features, the BEM is widely used for exterior problems rather than interior ones [80], although the model size commonly does not exceed 10^4 elements. It is also widely used in combination with FEM to solve coupled structural-acoustic problems.

A final drawback of BEM is the non-uniqueness of the solution for exterior problems with closed geometry, which pollutes the response with fictitious resonances. The Combined Helmholtz Integral Equation Formulation [177] has been proposed as a remedy for direct BEM, while for indirect BEM the Burton and Miller approach [21] and the Internal Impedance Method [42] can be used.

2.2.2 Pushing low-frequency techniques higher

Since the solutions to eq. (2.3) and (2.11) are oscillating functions of space, a very refined domain discretization is required to capture small oscillations with reasonable precision. As a consequence, the model size and computation time drastically increase with frequency. To overcome these limitations, research has focused on the enhancement of low-frequency techniques, such that they can preserve their ability to capture the local dynamic behavior at a reduced computational cost.

This section illustrates the main enhancements to the classic FEM and BEM approaches and the so-called Trefftz approaches, as alternatives to element-based techniques.

Enhancements to FEM The first type of improvement to FEM belongs to the group of adaptive refinement techniques, which increases the model accuracy by refining the description of the field variables in the domain. The so-called h -refinement technique uses an iterative error estimator, which allows enriching the mesh wherever the solution accuracy is poor [16, 93]. The order of the polynomial can also be increased, resulting in the p -refinement [52]. The combination of the aforementioned techniques leads to the so-called hp -refinement [94, 172]. These processes allow a reduction of the number of elements, with a corresponding reduction in solving time. However, they are not very effective against dispersion errors, for which wave-based discretization methods allow enriching or even replacing the polynomial solution using plane waves or other analytical functions. The Partition of Unity Method [7] belongs to this family and allows the inclusion of a priori knowledge about the governing equation. The approximate solution to the Helmholtz equation can be expressed by using an increasing number of plane wave basis functions, leading to a reduction of dispersion and pollution errors. In the Partition of Unity FEM (PUFEM) [192], a local basis of discrete plane waves (or other

special functions) is adopted to enrich the classic FE approximation. Although the dispersion error can be reduced this way, PUFEM leads to highly oscillatory integrals and ill-conditioning problems. As an alternative approach, the Discontinuous Enrichment Method [60, 61] belongs to the family of multiscale methods. Plane wave basis functions enrich the classic polynomial field within each element, while Lagrange multipliers are used to enforce weak continuity of the solution at the interfaces. This procedure improves the conditioning of the system matrices and provides accurate results for 2D and 3D acoustic, elastodynamics and vibro-acoustic problems [195]. The method has also been extended to Partition of Unity BEM [161].

The family of stabilized formulations tackles the dispersion problem. These approaches try to reduce the phase error by adding stabilizing terms to the traditional variational formulation. In the Galerkin Least Squares (GLS) [81] approach a residual in least squares form is added to the classic Galerkin formulation and is multiplied by a stability parameter. This allows modifying the wave propagation in order to minimize the phase error [8, 198], also in the case of highly deformed meshes [82]. For 1D cases, this leads to the correct solution, while for 2D and 3D problems the direction of propagation has to be known a priori. The gradient of the residual related to the governing equation can be added to the classic formulation, leading to the so-called Galerkin Gradient Least Squares Method (GGLS) [63]. GLS and GGLS are quite similar for linear finite elements, and numerical comparisons for different configurations are reported in ref. [82]. However, they are unified under the Generalized Galerkin Least Squares Method [197], where two stabilization parameters have to be tuned.

An alternative way of reducing the dispersion error is by modifying the integration scheme used to compute the mass and stiffness matrices. By shifting the integration points with respect to the classic position suggested by the Gaussian or Gauss-Lobatto quadrature schemes, the phase error is significantly decreased [74]. Such a modified quadrature leads to a fourth-order rate dispersion error, while classic Galerkin or GLS only lead to a second order behavior. The advantage of this approach lies in the fact that the computational load of the simulation does not increase. However, so far the approach has only been applied to 2D Helmholtz problems. It is worth mentioning that for quadrilateral and hexahedral elements this scheme can be exactly retrieved by using the GGLS method. The performance of these two approaches has been compared in ref. [13, 14] through numerical examples, showing the superiority of the GGLS.

A third branch of strategies aims at enhancing the solution process, which in FEM is the most time consuming part. Solving large direct problems with classic Gaussian elimination or factorization is very demanding. Alternatively,

iterative solvers can be adopted to reduce the computational effort [55] and parallelize the process [92]. Krylov solvers can be used for steady-state simulations [176], although their robustness is highly problem dependent. Recently, much research has been conducted to develop fast frequency sweep algorithms to speed up direct computations by reducing the number of matrix inversions [85, 137]. The underlying idea is to compute the system response at one expansion frequency. Thanks to the knowledge of the derivatives of the system matrices, it is possible to determine the solution behavior at neighboring frequencies. This approach has been used to improve the performance of FEM, especially when frequency dependent components are present [188], as well as of acoustic BEM [126].

A totally different philosophy is adopted by domain decomposition strategies. These are based on the idea of splitting a large problem in parallel non-overlapping smaller ones. Component Mode Synthesis (CMS) [36] consists of dividing the original model into smaller parts, solving the subcomponents individually and then recombining the results into a global-level solution. Each subcomponent is represented in terms of uncoupled modes, and a higher computational efficiency is achieved, especially when the interface DOFs are small compared to the size of the problem. Towards the improvement of this approach, the Automated Multi-level Substructuring has been developed to allow the decomposition based on the mathematical properties of the model, rather than on the analyst's experience [10].

Enhancements to BEM In order to reduce the computational disadvantages given by fully populated BEM matrices, the Fast Multipole BEM (FMBEM) [75, 130] has been proposed for large acoustic simulations. The FM algorithm divides the domain into near and far fields. While the former is solved by using the classic BEM, in the latter, a cluster of boundary elements is formed and the solution is evaluated through multipole expansions. As a result, instead of computing the interactions between all nodes of the model, the contributions from groups of nodes are first centralized and then projected only once. The system of equations does not need a full assembly procedure to compute the matrix-vector product and the computational cost is reduced from $O(n_{\text{nod}}^3)$ for a standard BEM analysis to $O(n_{\text{nod}} \log(n_{\text{nod}}))$, with n_{nod} the number of DOFs. This also has positive effects on the memory consumption. On the other hand, for small models the large overhead of the clustering procedure is disadvantageous, making a BEM analysis more convenient. Moreover, like BEM, also FMBEM suffers from non-uniqueness, and its mitigation has been proven to be beneficial for its convergence as well [41]. FMBEM has been successfully applied for industrial problems towards the mid-frequency region [78].

The Smooth Integral Formulation (SIF) [213, 214], recently renamed Stochastic BEM (SBEM), has been proposed to extend the validity of the classic BEM to higher frequencies. The Green's kernels are perturbed by introducing geometrical variability in nodal positions and are computed in an averaged sense. This procedure leads to the computation of the First Order Moments of the field variable. Second Order Moments are then calculated by using a second set of equations, which is based on energy relationships and is complemented by auxiliary equations. The resulting quadratic average response shows a resonant low-frequency behavior, which becomes smoother as the frequency increases, offering the possibility to represent the smooth transition from low- to high-frequency. Although the computational effort increases with respect to traditional BEM, the number of elements needed to represent the solution can be highly reduced. The approach has been applied to 1D and 2D structures [211, 214], acoustic cases [170] and has been extended in a hybrid form FE/SIF [171, 212].

Trefftz approaches Instead of expressing the field variables in terms of polynomial shape functions, Trefftz methods [201] use exact information related to the governing equation and can be divided in direct and indirect ones [101, 169]. The idea underlying direct Trefftz methods is very similar to BEM. The boundary of the domain is discretized and the field variable is described in terms of polynomial shape functions. Instead of using Green's kernel to minimize the functional, a complete set of fundamental solutions is used as basis functions. Consequently, problems related to singular integrals are not present. On the other hand, indirect Trefftz approaches describe the field variable by means of a set of functions which inherently satisfy the differential equation. The weighting factors for each function are obtained by enforcing the boundary conditions. Both methods assure convergence to the exact solution and present matrix ill-conditioning [222]. While applications of the direct Trefftz strategy are very limited [28, 144, 183], the exploration of indirect approaches is quite advanced.

A whole class of Trefftz methods consists of providing the exterior/interior problem solution as a sum of contributions from sources located in the interior/exterior domain. This strategy takes different names in the literature, such as the Method of Fundamental Solutions [59], or the Equivalent Source Method [105]. The determination of the strength of the sources leads to the correct description of the field variable. However, the correct choice of their number and position is highly problem dependent and represents the main difficulty of the approach [105, 158].

For a more complete overview on Trefftz approaches for steady-state acoustic modeling the reader is referred to ref. [169].

The Wave Based Method (WBM) [49] belongs to the family of indirect Trefftz approaches. The system response is described by a weighted sum of wave functions, which inherently satisfy the governing Helmholtz homogeneous equation(s) over the smallest bounding rectangle circumscribing the actual physical domain. The weighting factors are computed by means of a Galerkin weighted residual formulation, in which the trial functions are described in terms of the same basis functions used for the field expansion. This allows to impose boundary conditions, domain interface conditions and loads for a prescribed problem. A sufficient condition for the convergence of the WBM is the convexity of the domain, which may imply the use of a large number of subdomains and a corresponding increase of computational effort. To circumvent this limitation, two extensions have been developed. The hybrid FE/WBM merges the versatility of the FEM to the efficiency of the WBM [167]. The WBM is used for large convex domains, while small details are modeled by means of the FEM. The Multi-Level WBM [202] has also been developed as a general framework to deal with multiple inclusion problems and heterogeneities, which can be modeled using the WBM as well as other deterministic techniques. So far, the WBM has been successfully applied to a large variety of problems, such as bounded [203] and unbounded [12] acoustics, structural [206, 210], vibro-acoustic [168] and poro-acoustic problems [47]. Some details of the WB formulation are described in Appendix A.

2.2.3 High-frequency techniques

In the previous section, several methodologies have been presented that break the computational limits of deterministic simulations. However, when moving to higher frequencies, uncertainty and variability inherently influence deterministic modeling, leading to predictions which in some cases are even meaningless. Consequently, rather than looking for accurate approximations of eq. (2.3) and (2.11), the problem is modified, such that the underlying equation consists of a balance between the power injected by external sources and the power exchanged and dissipated within the system. Energetic variables substitute kinematic ones and, in most of the cases they are representative of frequency averaged quantities. Additionally, for some approaches, the local information is lost.

The following section provides a brief overview of the existing techniques for the analysis of high-frequency vibration.

Statistical Energy Analysis SEA [133, 132] was introduced in the 1960s and over the years it has become one of the most used tools for high-frequency vibration analysis of large mechanical assemblies, i.e. aircraft, trains, ships,

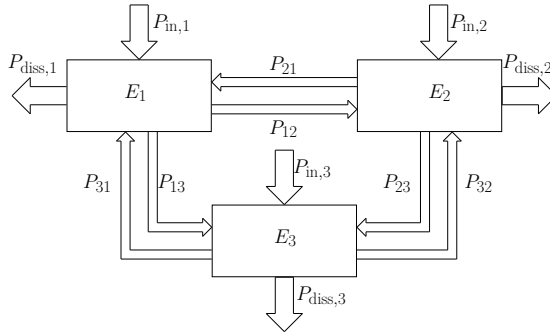


Figure 2.3: SEA subsystem network.

buildings, offshore structures, etc [37, 97]. The SEA philosophy is completely opposite to deterministic modeling. As illustrated in fig. 2.4, a complex system is represented by a network of N_{sys} subsystems. Each subsystem represents a wave-type instead of a component and is defined by gross geometrical parameters rather than precise descriptors. Primary variables are global quantities, evaluated as energy averages over the spatial extent of the j -th component, over the frequency band of interest and implicitly over the ensemble.

The fundamental assumption underpinning SEA is the wavefield diffusivity, meaning that all wave directions are equally probable, or equivalently, that all modes are equally energetic. This condition is promoted by high modal density, irregular geometrical features, broad band excitation and multiple, uncorrelated input forces. Additionally, the coupling between subsystems is supposed to be weak.

The governing SEA equations are derived from a power balance for each subsystem,

$$P_{\text{in},j} = P_{\text{diss},j} + \sum_{\substack{k=1 \\ k \neq j}}^{N_{\text{sys}}} P_{jk}. \tag{2.25}$$

The symbol $P_{\text{in},j}$ denotes the power injected into the j -th subsystem. As it represents the driving term of the energetic relation (2.25), its accuracy has considerable impact on the result of the simulation [57]. Usually, P_{in} is computed using analytical relations, evaluated through measurements, or, more expensively, by means of deterministic calculations. In the first case, it is a common procedure to use the input power into an infinite (or semi-infinite) structure [132]. This approximation leads to a reasonable accuracy when SEA

hypotheses are fully satisfied and the frequency of analysis is high. Nevertheless, when single modes have major influence on the response, the approximation of infinite systems can be inaccurate.

In eq. (2.25), the term $P_{\text{diss},j}$ represents the dissipated power and is quantified by the following relation,

$$P_{\text{diss},j} = \omega \eta_j E_j, \quad (2.26)$$

where η_j is the damping coefficient of subsystem j , which is commonly small and can be estimated through measurements. The symbol E_j represents the energy in subsystem j .

The term P_{jk} in eq. (2.25) describes the power flow between subsystems j and k , which is proportional to the difference of their uncoupled modal energies,

$$P_{jk} = \omega \eta_{jk} n_{d,j} \left(\frac{E_j}{n_{d,j}} - \frac{E_k}{n_{d,k}} \right), \quad (2.27)$$

where the symbol $n_{d,\bullet}$ indicates the modal density of component \bullet . The term η_{jk} indicates the coupling loss factor (CLF), which quantifies the ratio of the energy stored in the subsystem j to the energy transferred to subsystem k across the interface. The hypothesis of weak coupling between subsystems assures that the CLF satisfies the reciprocity relation $\eta_{jk} n_{d,j} = \eta_{kj} n_{d,k}$ [107]. As their accuracy has a high impact on the prediction, a large part of the SEA literature is devoted to their evaluation. CLFs can be computed by using either experiments or analytic models, based on wave or modal formulations. Alternatively, they can be computed by means of deterministic approaches [139, 174, 182, 196].

A key feature of SEA is that it inherently incorporates uncertainty and provides a response representative of a population of nominally identical systems. In its original formulation, SEA is only capable of predicting the mean behavior, although the variance prediction can be included [119].

Nowadays, SEA is a mature technique and has been explored in many directions. The main advantages over other high-frequency or deterministic techniques are its simplicity and computational efficiency, although accurate parameter estimators and material libraries are needed, as they have a huge impact on the reliability of the results. These advantages make SEA very versatile, especially for optimization and sensitivity studies during the preliminary design stage. On the other hand, SEA has strong limitations when moving towards lower frequencies, in particular when subcomponents do not support diffuse field or are strongly coupled. However, these conditions do not violate the validity of the power flow relationships, but the predicted response might present unacceptable deviations from the exact one. To partially overcome this difficulty, hybrid techniques have been developed.

Vibrational conductivity analysis High-frequency vibration can also be approximated by using the analogy with heat transfer. This leads to a continuum form of SEA, which has been investigated under different names: Power Flow Finite Element [152], Energy Finite Element Analysis (EFEA) [218] and Simplified Energy Method [122]. The governing equation for such a vibrational conductivity approach is

$$\omega\eta e + \nabla \cdot \mathbf{I} = P_{\text{in}} \quad (2.28)$$

where η is the damping loss factor of the component and e is the energy density. P_{in} is the power injected by a source and like in SEA, it represents the driving term. The energy flow is indicated with the vector \mathbf{I} and is imposed as a boundary condition,

$$\mathbf{I} = -\frac{c_g^2}{\omega\eta} \nabla e, \quad (2.29)$$

where c_g is the group velocity. Similarly to SEA, the vibrational conductivity analysis requires the computation of coupling coefficients and an input power term. However, despite the local nature of the approach, the smoothness of the energy field allows using a coarser discretization to solve the problem [149], which can be easily implemented and used within a commercial FE software. This might also explain the popularity of this approach.

The fact that the field is approximated by using uncorrelated plane waves can lead to accurate results for one-dimensional systems [152], but when moving to higher dimensions the approximation might lead to some problems [22, 110]. In fact, according to the vibrational conductivity, the energy density decreases with the square root of the distance from the driving point, while the exact solution decreases linearly with the distance. This can yield large errors, especially when the direct field is dominant, as it happens for heavily damped plates. Moreover, the energy density is infinite at the driving point according to the vibrational conductivity, which is true for membranes, but is not correct for plates. To overcome these issues, hybrid approaches have been developed that include direct field information [84, 184].

Other relevant techniques Transmission coefficients at a junction can be highly dependent on the direction of the incident wave. This can lead to directional wavefields which violate the diffusivity condition of classic SEA. In the Wave Intensity Analysis [108, 111] the wavefield is not assumed to be diffuse and a finite Fourier series is used to describe the directional dependency of the wave intensity in the subsystem. Relaxing on the wavefield diffusivity allows a significant improvement of the prediction with respect to SEA when its fundamental assumptions are not satisfied. The amplitudes of the Fourier expansion are determined through the solution of a power balance between

the reflected and transmitted wave intensity at the junction. Classic SEA relationships are retrieved if only the first term of the series is considered, as it represents the diffuse wave field. Also in this case the knowledge of the input power is necessary to evaluate the energy.

To provide an alternative to the vibrational conductivity, the Radiative Energy Transfer Method [123, 124] has been developed for multi-dimensional structural vibrations and enclosure acoustics. Under the assumption of uncorrelated sources and negligible wave interferences, the local energy density is computed by integrating the contribution from actual power sources and fictitious power sources distributed over the boundary. In general, the power reflected by the boundary is unknown and can be evaluated by using conventional BE schemes. The smooth response is representative of the frequency-averaged response of the system. Since the direct field is in agreement with the exact solution, this approach leads to significant improvements with respect to classic vibrational conductivity analysis [125].

Finally, instead of using a thermal analogy, the Complex Envelope Displacement Analysis (CEDA) [23] describes the problem in terms of a complex envelope. CEDA makes use of the Hilbert transform to map the fast high-frequency oscillating behavior into an envelope with low-frequency content. This allows circumventing the computational limitations connected to the prediction of high-frequency phenomena. However, extending CEDA to 2D and 3D problems requires the introduction of the Complex Envelope Vectorization (CEV) [68], which uses a vector instead of a one-dimensional variable. The possibility of using a low-frequency representation of the response allows the use of coarse meshes for modeling the physical problem. CEV yields accurate results especially when the direct field is preponderant and the modal density is relatively high.

2.2.4 Pulling high-frequency techniques lower

Energetic approaches are very reliable when the underlying hypotheses are satisfied. This is not the case for low-frequency problems. Moreover, all complex structures consist of components which carry different wavefields. This situation may violate the assumptions and lead to unreliability of classic energy techniques.

This section presents an overview of the existing techniques which allow lowering the limit of validity of high-frequency approaches, or enriching them with low- and mid-frequency information.

Energy Distribution Analysis (EDA) [64, 135] can be used to estimate parameters like CLFs at junctions for which analytical values are difficult to

compute, or where there is a strong coupling. EDA models also allow including correlated and localized excitations, contrary to pure SEA modeling, which assumes delta-correlated and broad-band excitation. Moreover, EDA provides time and frequency-averaged subsystem energies, input and dissipated powers. The approach starts from classic FE models, as only the mass and stiffness matrices are required, and its core lies in the solution of an eigenproblem and energy post-processing. In the latter process, the response is evaluated from modal interaction and by performing frequency averaging, which in most of the cases can be performed analytically. EDA can also be used to determine CLFs in a “quasi-SEA” approach, consisting of an SEA model with indirect CLFs [134]. Several aspects have to be considered when applying an ED approach. Solving a large eigenproblem might be computationally demanding, and model reduction techniques can be very advantageous. In this context, Component Modal Analysis [135] or CMS have been explored, together with the introduction of Characteristic Constraint Modes [24], to reduce the amount of problem DOFs. Furthermore, commercial packages propose automated algorithms to subdivide a complex structure in a proper set of SEA subsystems [66].

Several other approaches have been developed to enhance the CLF estimation. For example, a robust approach was proposed in ref. [196], which allows the evaluation of the mean and the variance of the energetic quantities based on uncertain parameters. Alternatively, the point-mobility theory [139] allows deriving SEA parameters based on estimates of the drive-point conductance computed at all response points and all the locations of the substructures where vibration is transmitted. These parameters can then be used in combination with classic SEA models to evaluate power transfer functions for a built-up system [138, 140]. The use of global FE can require a large computational effort. For this reason, single components can be analyzed by imposing free or clamped boundary conditions, which may lead to a rough estimate especially in the low-frequency range. A wave based substructuring technique can be applied to the bare subsystem in order to increase the accuracy of the model [174]. The point-mobility approach is quite mature in its current state and allows an efficient computation of SEA parameters starting from a FE model.

2.2.5 Fuzzy Structure Theory and hybrid techniques

At the end of the 1980s, with the necessity of analyzing complex structures at a low computational cost, Soize developed the Fuzzy Structure Theory (FST) [25, 185] (which is not related to fuzzy logic). The FST tackles all those cases of structures consisting of a stiff frame, which is called master structure, and a number of “fuzzies”, which are all the subcomponents attached

to the primary structure, of which the properties are either uncertain, unknown or not accessible to deterministic modeling. As shown in fig. 2.4, one can consider the main frame of a ship as a master structure. This part of the model can be treated with conventional modeling techniques, such as FEM. All secondary structures and equipments connected to the master structure are modeled as mass-spring-damper oscillators. According to the original Soize formulation, their properties are described in a probabilistic sense by four main parameters: the mass, damping and modal density distributions of the oscillators, and the coupling factor which allows to determine whether the component is connected through a point or a more extended junction. These parameters allow assembling a random impedance matrix $\mathbf{Z}_{\text{fuzzy}}$, which is added to the impedance of the master system,

$$i\omega (\mathbf{Z}_{\text{mast}} + \mathbf{Z}_{\text{fuzzy}}) \mathbf{w} = \mathbf{f}. \quad (2.30)$$

The random equation (2.30) is recursively solved for the displacements of the master structure, \mathbf{w} . Thanks to the knowledge of the probability distributions, it is possible to estimate the moments of the fuzzy impedance and include successive orders in the solution expansion.

The interesting aspect of the FST is the possibility of reducing a complex model to the bare DOFs of the master structure, for FE modeling. It is worth underlining that the FST is not meant to estimate the average response of an ensemble of nominally identical systems, but it allows predicting the behavior of a system of which the parameters cannot be properly modeled [159]. However, this approach also presents several difficulties. Apart from the complex mathematical formalism, it remains difficult to hypothesize fuzzy parameter distributions for complex systems. Much research has been carried out to overcome this limitation [166, 191, 215], although nowadays, the FST is not widely applied. Nevertheless, dividing the structure in a purely deterministic master structure and somewhat statistical fuzzy structures has been of inspiration for following research. In fact, all complex structures consist of components responding in different ways. While deterministic approaches can be suitable to describe the behavior of those having a few modes over the frequency band of interest, they are not convenient for modeling components with higher modal density. On the other hand, energy methods can be used for the latter, while their use might be meaningless for stiffer components. For this reason, over the last fifteen years, research has been focusing on the development of hybrid techniques, which allow the coupling between deterministic and statistical approaches. A first attempt to formulate a hybrid deterministic/statistical approach is proposed in ref. [118], where 1D structures are considered. Successively, the idea of coupling deterministic and statistical methods has been enriched with the diffuse field reciprocity relationship [116, 181], which allows to back-couple statistical systems to deterministic ones.

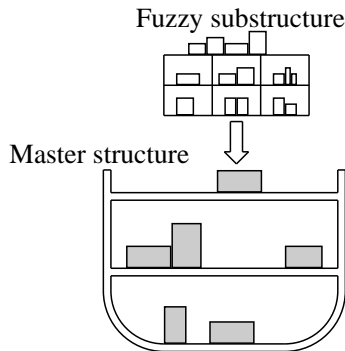


Figure 2.4: Fuzzy structure consisting of a master structure and fuzzy substructures.

As such, this relationship is the core of the hybrid deterministic/statistical approach [180] and has led to the hybrid FE/SEA and WBM/SEA [209].

In FE/SEA, stiff components are fully deterministic and are treated with FEM, although any deterministic approach can be used to model their behavior. Flexible components are treated with SEA and are assumed to be highly random, so that natural frequencies and mode shapes conform to the Gaussian Orthogonal Ensemble (GOE) [145]. Interfaces between statistical subcomponents are also modeled as deterministic DOFs.

The cross-spectrum \mathbf{S}_{ww} of the response evaluated at a point on a deterministic subsystem can be expressed as follows,

$$\mathbf{S}_{ww} = \mathbf{D}_{\text{tot}}^{-1} \left[\mathbf{S}_{ff} + \sum_k^{N_{\text{sys}}} \left(\frac{4E_k}{\omega\pi n_{d,k}} \text{Im} \left\{ \mathbf{D}_{\text{dir}}^{(k)} \right\} \right) \right] \mathbf{D}_{\text{tot}}^H. \quad (2.31)$$

The term \mathbf{D}_{tot} represents the total dynamic stiffness matrix of the whole system, and \mathbf{S}_{ff} the cross-spectral matrix of the loading applied to the master system. In absence of statistical systems, the sum disappears and eq. (2.31) provides the response of the deterministic system. If N_{sys} random subsystems are considered, the blocked contribution from the reverberant field is considered. This contribution is quantified by means of the diffuse field reciprocity relation, which connects the energy E_k in the k -th subsystem, its modal density $n_{d,k}$ and the direct field dynamic stiffness matrix, $\mathbf{D}_{\text{dir}}^{(k)}$. The latter represents the dynamic stiffness matrix of a corresponding infinitely extended component and can be computed in several different ways [34, 114, 180].

In this form, the hybrid approach allows the computation of the mean behavior of the system. However, considering GOE statistics [112, 113] it is also possible

to extend the method to the variance prediction [35, 120].

From a computational point of view, the use of SEA components results into a considerable reduction of DOFs. However, several matrix inversions are necessary within the pre-processing step, and this might not have a negligible impact on the overall solving procedure [162].

Although this hybrid approach is very recent, it has already been successfully applied to industrial problems [26, 34]. Current research is focusing on the inclusion of parametric uncertainty in the description of the deterministic system [30] and on the automatic recognition of statistical systems [115].

The possibility of hybridizing deterministic FEM and EFEA has also been investigated [88, 221] to deal with structures consisting of stiff and flexible components.

2.2.6 Non-determinism

Non-determinism plays a crucial role in numerical modeling and its influence is related to the frequency of analysis. As can be observed in fig. 1.1, with decreasing wavelength, the system behavior is increasingly sensitive to small changes.

According to the definitions provided by Oberkampf [156, 157], two main sources of non-determinism can be distinguished: variability and uncertainty. Variability describes the variation of a system property. Commonly, this is referred to as a range of values or defined by a probability density function. For example, a certain geometrical dimension can vary due to manufacturing tolerances, or the material characteristics can be affected by alterations due to external influences. On the other hand, properties that are unknown or unspecified due to a lack of knowledge, are referred to as uncertain and are commonly found when modeling boundary conditions, loadings, damping etc. The presence of uncertainty and variability is also related to the design process. In the early design stage, problems are mainly affected by uncertainties, which after a proper detection and investigation process can be characterized in a statistical sense and treated as variability. Numerical tools able to cope with non-determinism can help increasing the robustness of the design. This highlights the importance of the research in this area.

Variability can be tackled by means of probabilistic approaches. In particular, when the statistics of the random variables are well-known, parametric approaches can be used. In this case, the most direct way to obtain the response statistics is to perform an MC simulation [62]. In principle, this technique samples the design space by using a massive amount of simulations and extracts the response statistics out of these data.

Stochastic methods [178], like the Stochastic Finite Element Method [155, 189]

are also well-established in the field of probabilistic parametric modeling. Similar to classic FEM, the domain is discretized, but probabilistic models are associated to random fields. The equations of motion are then formulated by using a proper expansion or perturbation scheme. This procedure leads to the estimation of the response statistics. Nevertheless, the computational cost highly penalizes these approaches, especially for dynamic problems. Consequently, applications presented in literature are limited to simple cases [4].

A non-parametric probabilistic model has been developed by Soize [186, 187], which uses the principle of maximum entropy. The statistics of the response are generated through the randomization of the mass and stiffness matrices of the nominal system, of which the statistics are controlled by proper dispersion parameters. Since the statistics of the associated eigenproblem cannot be evaluated analytically, an MC simulation is used. The method has been applied to a wide class of problems, e.g. automotive applications [54], buildings [5] and satellites [163]. However, in [127] the physical consequences of non-parametric modeling as proposed by Soize are investigated. It is argued that the result of the approach may be conflicting with physical expectations about the analyzed systems. For instance, it is observed that, with increasing uncertainty, the average modal density diverges from the asymptotic value. However, the non-parametric approach seems to be able to deal with unknown terms of lower or higher order in the governing differential equation.

It is worth mentioning that also SEA can be classified as a non-parametric approach, while the SBEM can be treated as a probabilistic parametric approach.

In real applications, the variable statistics are often unreliable or not available, and their identification and quantification is expensive. Moreover, the computational cost of a probabilistic simulation can be very high. In this case, a non-probabilistic approach can be seen as complementary to the former and provide a range of possible responses for an input with uncertainties [146]. This allows evaluating the worst case scenarios, without necessarily taking into account a probabilistic point of view.

A class of possibilistic approaches allows taking into consideration different scenarios and different design configurations. The Interval Finite Element (IFE) [51] and the Fuzzy Finite Element (FFE) [147] analysis belong to this family. In the IFE, non-deterministic parameters are defined within a bounded interval. By taking into account all possible models, the minimum and maximum values for the response are found through by an IFE simulation. This approach is very simple, but the interdependency between the non-deterministic variables is lost during the solution procedure. This leads to an overestimation of the output interval. However, the information related to the intervals may be

affected by uncertainty. In order to describe incomplete data, the FFE has been developed. Instead of dividing a set into members and non-members of the set, a membership function is introduced to define the degree of membership of the fuzzy set. According to the α -level technique, such a membership function is divided into α levels, which identify α intervals. The fuzzy solution is computed by assembling the corresponding interval analyses at each level [44, 147]. Alternatively, an optimization approach can be used to solve the problem [45]. While the application of the IFE is mainly limited to academic cases, the FFE has already been applied to several research areas [148].

2.3 Methods for oscillatory integrals

As mentioned in the Introduction, the response of a vibrating system is often expressed in a frequency averaged format. Since the detailed response of a deterministic calculation is very sensitive to the input model parameters, narrow band responses are often of limited practical use, and, especially in the mid- and high-frequency ranges, many noise and vibration problems can be assessed by using averaged responses. These require the solution of an oscillatory integral over a band of frequencies. However, the computation of highly oscillatory integrals is a very important problem in many branches of computational analysis and not only for noise and vibration simulations. For example, in electromagnetism or telecommunications, highly oscillatory integrals are of high relevance, as well as for image processing, optics, quantum chemistry, electrodynamics, etc.

An highly oscillatory integral is formally defined as,

$$I = \int_{\omega_a}^{\omega_b} f(\omega) e^{ikg(\omega)} d\omega, \quad (2.32)$$

with $k > 0$ and with the amplitude, f , and the oscillator, g , being smooth real functions. The most direct approach to evaluate integral (2.32) is by using Gaussian quadrature. However, if the oscillation within the interval is high enough, using classic quadrature is meaningless.

In the following, four main families of methods to deal with highly oscillatory integrals are presented.

2.3.1 Asymptotic methods

Asymptotic methods [219] are based on the observation that when the oscillations of the integrand increase, they cancel out, and the integral is

mainly determined by the behavior of the integrand at the endpoints, stationary points, singularities and discontinuities. In correspondence of these regions, less cancellation occurs. According to this branch of methods, the integral is asymptotically expanded, leading to its approximation,

$$Q_s^A = - \sum_{l=1}^s \frac{1}{(-ik)^l} \left\{ \sigma_l(\omega_b) e^{ikg(\omega_b)} - \sigma_l(\omega_a) e^{ikg(\omega_a)} \right\}, \quad (2.33)$$

where the so-called moments can be computed as follows,

$$\sigma_1(\omega) = \frac{f(\omega)}{g'(\omega)}, \quad \sigma_{l+1}(\omega) = \frac{\sigma_l'(\omega)}{g'(\omega)}, \quad (2.34)$$

where s indicates the (finite) number of terms to include in the expansion. Expression (2.33) is valid only when there are no stationary points of g in the interval $[\omega_a, \omega_b]$, namely the function $g'(\omega)$ does not present any root over that interval. Moreover, the expansion can be computed only if the moments are known. The error goes to zero as fast as k^{-s-1} , meaning that the estimate becomes more accurate with increasing the oscillation of the integrand. On the other hand, when k is small, the estimate can diverge.

2.3.2 Filon-type methods

Filon quadrature was originally developed in 1928 and has been recently extended in ref. [95]. Filon-type methods suggest to integrate an approximation of f using a quadrature rule in its classical form, where the weights are computed by solving additional integrals. The approximation proposed by Iserles and Nørsett [95] is such that f and its derivatives are exactly interpolated at the endpoints and stationary points using Hermite polynomials. This leads to the approximation,

$$Q^F = \sum_{j=1}^n \sum_{l=0}^p w_{j,l} f^{(l)}(\omega_j), \quad (2.35)$$

where ω_j are n nodal points, while p is number of derivatives that are interpolated. The coefficients $w_{j,l}$ are computed by integrating the functions used as a basis for the interpolation. The error behaves as k^{-s} , where the order s depends on the number of derivatives. This holds when the quadrature points include all stationary points.

The knowledge of the integrand and its derivatives is the only requirement for the evaluation of the integral, and this constitutes the main advantage of Filon-type quadrature. On the other hand, evaluating the weights $w_{j,l}$ implies the solution of supplementary oscillatory integrals.

2.3.3 Levin-type methods

Levin-type methods [129, 160] are different from asymptotic approaches as they do not require the knowledge of the moments. The integral I is evaluated as follows,

$$\int_{\omega_a}^{\omega_b} f(\omega)e^{ikg(\omega)} d\omega = \left[F(\omega)e^{ikg(\omega)} \right]_{\omega_a}^{\omega_b}, \quad (2.36)$$

where the function $F(\omega)$ is such that,

$$\frac{d}{d\omega} \left[F(\omega)e^{ikg(\omega)} \right] = f(\omega)e^{ikg(\omega)}, \quad (2.37)$$

and is approximated by the function $v(\omega)$, built through the solution of a system of equations involving the derivatives of f . This procedure leads to the approximation,

$$Q^L = \left[v(\omega)e^{ikg(\omega)} \right]_{\omega_a}^{\omega_b}. \quad (2.38)$$

This family of integration approaches presents the same approximation accuracy of the asymptotic methods, and it provides accurate estimates for low values of k . However, the knowledge of the moments is not necessary. On the other hand, Levin-type methods only work when F is a smooth function.

2.3.4 The numerical steepest descent

The numerical steepest descent [91] presents an accuracy comparable to the asymptotic one and is dependent on the behavior of the oscillator in the complex ω -plane. In fact, the term $e^{ikg(\omega)}$ decays exponentially as g presents increasing imaginary values. Additionally, its decaying behavior is not oscillating over a path that presents a constant $\text{Re}\{g\}$. In this context, the steepest descent method makes use of the Cauchy's theorem [73], that states that a line integral of an analytic function only depends on the endpoints. The idea is then to decompose the integral, including paths on which the behavior of the integrand is exponentially decaying and non-oscillatory. These paths can always be found and only depend on the function g , regardless of f . Gaussian quadrature can be used over such alternative path.

Due to the numerical implementation in ref. [91], the method is referred to as the numerical steepest descent. In general, evaluating the path of integration requires the solution of a non-linear problem, and the presence of singularities may be an obstacle to reach accurate integration.

2.3.5 Discussion

Contrarily to classic quadrature, the error of the aforementioned techniques is inversely proportional to the power of k , meaning that the accuracy increases with increasing the oscillatory behavior. However, this holds true when the underlying hypothesis on the integrand are verified. For asymptotic and Filon-type methods, the knowledge of the moments of the integrand is necessary. Levin-type methods require the absence of stationary points. Finally, to successfully apply the numerical steepest descent, the knowledge of the oscillator is also required.

In this regard, the response of a vibro-acoustic system can be described as an oscillating function of frequency characterized by several stationary and singular points, i.e. corresponding to resonances, which are not known a priori. Additionally the phase information is not immediately available. For these reasons, the aforementioned techniques cannot be readily applied to vibro-acoustic systems, and classic quadrature remains the most reliable option to integrate over frequency.

2.4 Position of the research with respect to the state-of-the-art

A frequency averaged quantity is commonly computed by solving a weighted integral. To evaluate band-values, such a weighting function must resemble a rectangular window. Currently, the most general and widely used strategy for computing a weighted integral is to perform numerical quadrature [43] over an interval of (real) frequencies. Nevertheless, due to the oscillatory behavior of the integrand function, many integration points might be required to avoid frequency aliasing, and achieving accurate integrations can be very computationally demanding, especially for lightly damped systems. A survey of quadrature rules is not provided here, although some of them are described in sec. 4.2.2.

The alternative strategies proposed in this dissertation make use of the residue theorem [73] to evaluate frequency-averaged quantities through integration in the complex frequency plane. In particular, the focus is on input power computation, although the averaging procedure can be extended to other quantities. In the literature concerning noise and vibration modeling, the residue theorem is often employed to evaluate frequency integrals, i.e. [109, 154]. Nevertheless, its use to compute general weighted integrals as presented in this dissertation, is novel and leads to integration strategies of which the

differentiating features are the computational efficiency, accuracy, ease of implementation and wide applicability. Regarding the latter characteristic, since the proposed approaches do not rely on any fundamental approximation, they can be used in combination with any classic deterministic technique, according to the overview presented in sec. 2.2.1 and 2.2.2. Due to the increased computational efficiency with respect to classic quadrature, the present techniques can be classified as enhancements to deterministic modeling. Accordingly, they can be used to improve the performance of an optimization process over a band, for instance.

The use of such techniques is not restricted to the low-frequency domain. As highlighted in sec. 2.2.3, the accurate input power evaluation is crucial for energy-based approaches, but, in many situations, is not an easy-to-retrieve quantity. In this direction, the proposed strategies can be employed to pull high-frequency techniques lower, since an enhanced deterministic strategy can be used to provide information to energy-based approaches. This might be the case for band-averaged input power or input mobility.

Frequency averaging techniques can also be exploited in the context of non-determinism. In fact, the mean behavior of an ensemble of nominally identical structures can be approximated by the frequency averaged response of a single sample, provided that the perturbation level is high enough. In this manuscript, a Lorentzian function is used as a weighting function to perform frequency averaging. The Lorentzian function is a bell-shaped curve, of which the features are reported later in sec. 7.1 and fig. 7.1. Due to its advantageous mathematical characteristics, performing Lorentzian-weighted frequency averaging leads to significant computational benefits, especially if compared to the computation time of an MC simulations. Furthermore, the computation of the frequency-averaged dynamic stiffness, leads to the direct field dynamic stiffness matrix [116], which can be exploited in the context of hybrid deterministic/statistical approaches, as well as for CLF computation within SEA [181].

Finally, the Lorentzian function can be used as a mass-frequency distribution within the FST, according to Pierce's theory [166]. Also in this case, using the residue theorem avoids the solution of more cumbersome integrals.

2.5 Conclusion

Well-established approaches exist to model low- and high-frequency vibrations, namely deterministic and energetic approaches. However, rather than trying to unify the audio frequency range, current techniques attempt to shorten the mid-frequency region. This is done either by breaking the computational limits of low-frequency approaches or by lowering the bound of applicability of energy techniques.

Among all the deterministic techniques, much of the research is spent on improving the classic FEM formulation. This is not only due to its application flexibility. In fact, its versatility can be exploited to tackle disparate problems belonging to different scientific disciplines, allowing a quicker evolution of the basic principles towards higher computational efficiency. This is in contrast to the development of energetic approaches, which is mostly restricted to the vibro-acoustic field, apart from the application of the vibrational conductivity analysis. However, recently the use of the reciprocity relation has been extended to electromagnetism [117].

Looking at future perspectives in the world of numerical vibro-acoustics, the development of computationally efficient techniques will still be a key objective for the next years, certainly supported by a fast increase in computing power. Regarding the latter, already in 1965, Moore prophesied that the processor performance would double every 18 months [150]. So far, such a rapid growth in computational resources allowed CAE platforms to become very effective design tools, and if today's challenges are mainly restricted to simulations of complex assemblies, multi-physics and multi-scale simulation tools will certainly be tomorrow's. However, even in the most technologically advanced scenario, the impossibility of relying on precise information about the system seems evident. This problem becomes crucial at high-frequencies, where the influence of uncertainty and variability becomes irreducible.

In this context, the novel work presented in this manuscript can be positioned in different ways. The efficient computation of frequency-averaged input power can, in principle, be performed with any classic deterministic techniques. The result of the analysis can be exploited to increase the quality of an energy model or to run a faster optimization over a frequency band. On the other hand, the use of the Lorentzian-weighted frequency averaging procedure can lead to the evaluation of the mean ensemble behavior of a structure and to the direct field dynamic stiffness of a component, useful, for instance, in the context of hybrid methods or CLF computation. Finally, the Lorentzian function can be used in the context of the FST, as a prototype function for the mass of the fuzzy substructure.

The main principles underpinning the present work can be applied to other branches of computational sciences, where the integration of oscillatory functions is required. Optics, electromagnetism, image processing, quantum chemistry are some examples.

Chapter 3

The Butterworth-weighted frequency averaging

This chapter is dedicated to the introduction of an efficient technique to evaluate the input power over frequency bands. Instead of exploiting traditional numerical quadrature, the proposed approach makes use of the residue theorem to calculate a weighted integral over the frequency.

When the poles of the system are confined to the upper half of the complex frequency plane, the integral reduces to the computation of the function residues at the poles of the weighting function, which in this chapter is chosen to be the square magnitude of a Butterworth filter. The number of frequency evaluations is independent of the bandwidth, and a considerable computational saving is obtained for large frequency bands. For hysteretic damping models, system poles may be located in the lower half of the complex plane, and the application of the present technique leads to an approximate integration rather than an exact one. However, the error is strictly dependent on the rate of decay of the weighting window and can be reduced by increasing the order of the Butterworth filter.

Two application examples show that the proposed strategy provides an accurate and efficient tool for the computation of the input power over frequency bands.

The structure of the chapter is as follows. Section 3.1 introduces the existing techniques to estimate input power into vibrating systems. Sections 3.2 and 3.3 provide an introduction to the frequency-averaged input power and the use of a Butterworth filter as a weighting function. In sec. 3.4 the causality principle is recalled concerning viscous and hysteretic damping models. Successively these concepts are exploited in sec. 3.5 for the efficient computation of the frequency

integral by means of the residue theorem. Numerical examples are given in sec. 3.6. The computational performance of such a technique is illustrated in sec. 3.7, where also its implementation is discussed. Conclusions are drawn in sec. 3.8.

3.1 Input power computation

Evaluating the power injected into a structure by a source is of high interest when analyzing the vibrational behavior of a mechanical system. In the first place, it provides a direct connection between the strength of the excitation and the vibration of the structure. Secondly, it can enrich the quality of an energetic numerical model, as the input power is the driving term for approaches like SEA or EFEA.

When the wavelength is small compared to the system dimensions, the input power can be estimated by using analytical formulations, which assume that the spatial extent of the component is infinite [132]. This leads to a reasonable approximation when high-frequency hypotheses are satisfied. However, in the transition region from low- to high-frequency, single modes may dominate the response, and the previous approximation becomes less accurate. In this case, deterministic modeling is complementary to the energetic one, and approaches like FEM and BEM are perfectly suited to assess the effects of boundary conditions, inhomogeneities and discontinuities. On the other hand, such a high flexibility comes at a high computational cost of the simulation.

Deterministic modeling assumes that the position and the phase of the source are precisely defined and the existence of a coherence in the wave patterns generated into the system provides a limitation to the low-frequency range. On the contrary, according to high-frequency assumptions, it is often preferred to assume that the excitation is spatially delta-correlated and broad-band. This assures that the power is equally injected into each mode, or equivalently that the wave field is diffuse [58]. Such a rain-on-the-roof excitation is difficult to realize in a deterministic sense and, in practice, the input power is often evaluated as a frequency-averaged value.

In many cases, the response is preferred in band format. Usually, the choice of the frequency interval is such that at least a number of natural frequencies are covered, i.e. three to five [40]. Alternatively, it is common to express the response in format of frequency bands of predefined bandwidth, i.e. one or one-third octave bands. In both cases, to evaluate the average response or its band value, one could use numerical quadrature schemes [43]. However, particularly at low-frequencies, the response of a vibrating system may exhibit distinct

resonance peaks which reduce the effectiveness of the integration scheme. With increasing frequency, the solution can be rather smooth and few sampling points may be enough to evaluate the integral over the frequency band. This reduces the computational load, but at the same time the estimate may be inaccurate.

3.2 Frequency integral of the input power

The focus is on the steady-state, linear behavior of second-order dissipative systems, which can either consist of one single component, i.e. a bare plate, or of several components, i.e. mechanical assemblies. All these systems are commonly constrained and excited by an external influence, i.e. a force, which generates a proportional motion. In this context, it is useful to introduce the concept of input point mobility defined as,

$$Y(\omega) = \frac{v(\mathbf{x}_f, \omega)}{F_0}, \tag{3.1}$$

where ω is the angular frequency of analysis, F_0 represents the complex amplitude of a harmonic input force, F , such that $F = F_0 e^{i\omega t}$, with i being the imaginary unit and t the time. Finally, v represents the complex amplitude of the velocity at the excitation point, \mathbf{x}_f [139].

The knowledge of the input mobility of a dynamic system is a very important piece of information, as it leads to the power injected into the system by the external source F ,

$$P_{in}(\omega) = \frac{1}{2} |F_0|^2 \operatorname{Re} \{Y(\omega)\}, \tag{3.2}$$

that can be equivalently expressed in terms of displacements at the excitation point $u(\mathbf{x}_f, \omega)$,

$$P_{in}(\omega) = \frac{1}{2} \operatorname{Re} \{i\omega u(\mathbf{x}_f, \omega) F_0^*\}, \tag{3.3}$$

with $\operatorname{Re} \{\bullet\}$ indicating the real part of \bullet and $(\bullet)^*$ representing the complex conjugate operator. As previously mentioned, it is common practice to evaluate the input power as a frequency-averaged value,

$$\langle P_{in} \rangle_{\Delta\omega} = \frac{1}{\Delta\omega} \int_{\Delta\omega} P_{in}(\omega) d\omega, \tag{3.4}$$

where $\langle \bullet \rangle_{\Delta\omega}$ represents the frequency average operator over the band $\Delta\omega$. In order to perform the frequency integration, the eq. (3.4) can be more conveniently expressed as an integral over the whole frequency axis

$$\langle P_{in} \rangle_W = \int_{-\infty}^{+\infty} W(\omega) P_{in}(\omega) d\omega, \tag{3.5}$$

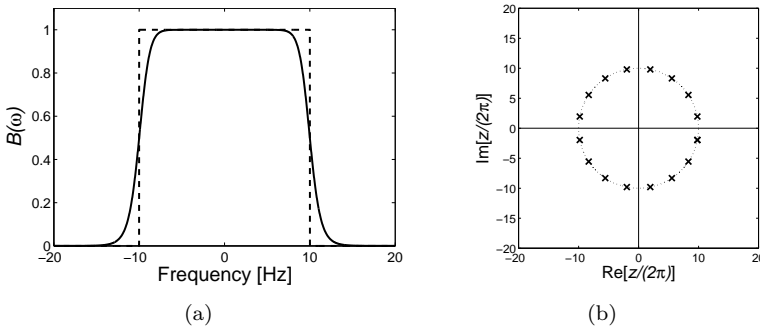


Figure 3.1: Comparison between rectangular window (dashed line) and Butterworth filter of order 8 (solid line), centered at 0 Hz and cut-off frequency equal to 10 Hz (a). Position of the poles of the aforementioned filter over the complex z plane (b).

where the frequency averaging operator $\langle P_{\text{in}} \rangle_W$ does not necessarily refer to a band and $W(\omega)$ is a generic weighting function, of which the features will be discussed in sec. 3.3. If the area below a rectangular weighting window is equal to unity, integrals (3.4) and (3.5) give the same result.

To evaluate eq. (3.5), the technique proposed in this chapter consists in evaluating the integral by means of the residue theorem [73]. As discussed in sec. 3.3 and 3.4, the position of the poles of the weighting function and the input mobility can be such that considerable benefits are achieved both in terms of computational time and accuracy.

3.3 Choice of the weighting function

In literature, several functions are available to approximate the features of a rectangular window [217]. The simplest one is the Butterworth filter, which is illustrated in fig. 3.1(a).

The square magnitude of the Butterworth filter is a real-valued function of mathematical form,

$$B(\omega) = \frac{A}{1 + \left(\frac{\omega - \omega_0}{\omega_C}\right)^{2n}}, \quad (3.6)$$

where ω_0 is defined as the center frequency and the cut-off frequency, ω_C , represents the half-width at half-maximum. Both ω_0 and ω_C are real quantities. The symbol n defines the order of the filter and the constant A represents the

amplification factor of the filter. If A is taken to be

$$A = \frac{n \sin(\frac{\pi}{2n})}{\pi \omega_C}, \quad (3.7)$$

the area under the curve is normalized and the result of integration (3.5), using $B(\omega)$, as weighting function, represents the Butterworth-weighted averaged input power. If the filter is not normalized and the amplification factor is taken to be equal to unity, the integral (3.5) provides an approximation for the input power over the ideal frequency band $[\omega_0 - \omega_C, \omega_0 + \omega_C]$. In the following, function $B(\omega)$, eq. (3.6), is applied as a weighting function, strictly speaking, and will be referred to as Butterworth filter.

To analyze the properties of the Butterworth filter, it is convenient to move to the complex frequency plane, z , such that $z \in \mathbb{C}$. In the remainder of this chapter, the notation z is used when the frequency value may be complex, while ω is used when the value is real.

For a filter of order n , $2n$ poles are located in the complex z plane at the following positions,

$$z_k = \omega_0 + \omega_C e^{-i\theta_k}, \quad (3.8)$$

where

$$\theta_k = \frac{\pi}{2n}(1 + 2k). \quad (3.9)$$

The value k is an integer ($k \in \mathbb{Z}$) which defines the position of a pole. When $0 \leq k \leq n - 1$, the k -th pole is located in the lower complex half plane (LHP); when $n \leq k \leq 2n - 1$, the k -th pole is located in the upper complex half plane (UHP). From eq. (3.8), it appears that the poles are distributed over a circle of radius ω_C and center frequency ω_0 . The position of the poles for a Butterworth filter of order 8 can be seen in fig. 3.1(b).

As n increases, the shape of the filter becomes closer to the shape of a rectangular window. This can be observed in fig. 3.2, where the area below a normalized Butterworth filter is evaluated over the range $[\omega_0 - \omega_C, \omega_0 + \omega_C]$. If the order is 1, the Butterworth filter corresponds to the Lorentzian function, which will be used later in this dissertation.

For the sake of completeness, it has to be mentioned that other types of filters exist to resemble a rectangular window, i.e. the elliptic filter and the Chebyshev filter type I and type II [217]. In this work, the Butterworth filter is chosen because of its smoothness and regularity. In fact, the aforementioned filters present ripples which degrade the regularity of the window. However, they can be used according to the present approach, once the mathematical form of the filter is known.

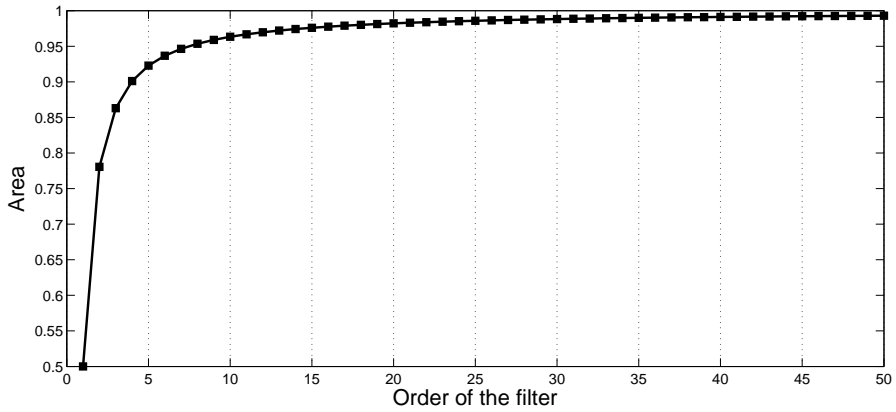


Figure 3.2: Area below a normalized Butterworth function evaluated over the interval $[\omega_0 - \omega_C, \omega_0 + \omega_C]$.

3.4 Influence of the damping model

After having introduced how the poles of a Butterworth filter are distributed over the complex plane, now the attention is focused on the poles of the input mobility and how the choice of the damping model influences their position. Any real system must respect the causality principle, which means that the past cannot depend on the future [164]. It can be shown that a causal and stable system response in the time domain leads to a transfer function which is analytic in the LHP (LHP becomes UHP if the opposite time convention $e^{-i\omega t}$ is taken), or equivalently, that the function poles are confined in the UHP [199]. The causality and the stability of the system is strictly dependent on the mathematical model used to describe the damping mechanism. In the literature several damping models are available, nevertheless some of them may violate either the causality or the stability principles and lead to ambiguities or paradoxes.

In this dissertation, only viscous and hysteretic damping are described in detail. For further clarifications the reader is referred to the specific literature concerning the topic: a survey is given in reference [164].

A final distinction has to be made between a continuous model and its numerical representation. The former consists of an ideally infinite number of DOFs, N , which is instead finite for numerical models. With increasing N , the numerical model provides a more accurate approximation to the continuous one. Since in the following the main focus is on numerical modeling, the system behavior is described by a finite set of variables.

3.4.1 Viscous damping

One of the most used and general damping models is viscous damping [40], for which the dissipation effect is proportional to the velocity of the system oscillation. The input mobility can be expressed as a modal sum,

$$Y(\omega) = i\omega \sum_{r=1}^N \frac{\phi_r^2(\mathbf{x}_f)}{\omega_r^2 - \omega^2 + 2i\omega\omega_r\xi_r}, \quad (3.10)$$

where $\phi_r(\mathbf{x}_f)$ is the mass-normalized mode shape evaluated at \mathbf{x}_f and N is the number of DOFs of the system. The symbol ω_r represents the r -th natural frequency of the system. The damping ratio ξ_r is expressed as

$$\xi_r = \frac{c_r}{2\sqrt{m_r k_r}}, \quad (3.11)$$

where m_r and k_r are respectively modal mass and stiffness of the r -th mode. It can be easily verified that for positive values of the damping coefficient, c_r , the poles of function $Y(\omega)$ lie in the UHP, as schematically illustrated in fig. 3.3. If c_r is taken to be a function of frequency, one should make sure that this does not affect the analyticity of function $Y(\omega)$ over the LHP.

Viscous damping is often used in FE modeling [223] and it may be useful to mention the conditions under which the poles of the transfer function are confined to the UHP. Firstly, a set of differential equations can be formulated in a direct fashion as,

$$\mathbf{M}\ddot{\mathbf{q}} + \mathbf{C}\dot{\mathbf{q}} + \mathbf{K}\mathbf{q} = \mathbf{f}_0, \quad (3.12)$$

where \mathbf{M} , \mathbf{C} and \mathbf{K} represent mass, damping and stiffness matrix, respectively. The generalized forcing vector is expressed as \mathbf{f}_0 and the generalized coordinates are referred to as \mathbf{q} . To assure that the poles of a system with viscous damping lie in the UHP, matrices \mathbf{M} , \mathbf{C} and \mathbf{K} have to be positive definite [106]. This condition can be verified by computing the roots of the characteristic polynomial of eq. (3.12),

$$\det(-\omega^2\mathbf{M} + i\omega\mathbf{C} + \mathbf{K}) = 0, \quad (3.13)$$

where $\det(\bullet)$ indicates the determinant operator.

When the aforementioned condition is satisfied, the mathematical model provides a causal and stable response and no system poles are present in the LHP.

3.4.2 Hysteretic damping

When the excitation is harmonic, the damping mechanism can be approximated by introducing a complex modulus. This type of damping is commonly referred

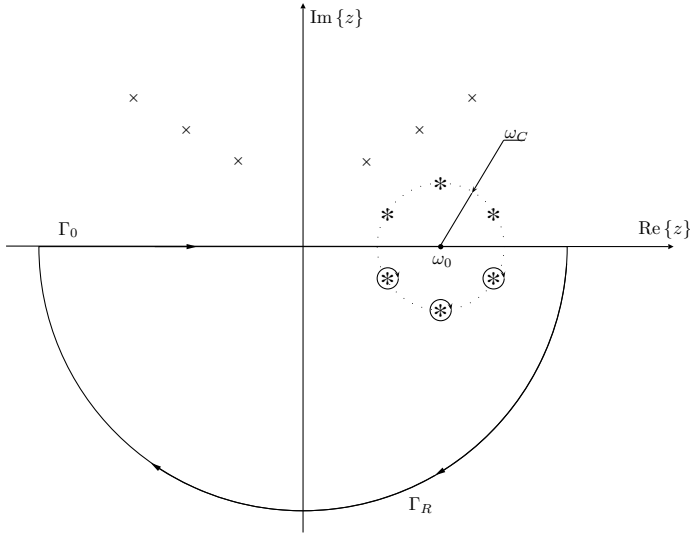


Figure 3.3: Position of system (\times) and filter ($*$) poles over the complex z plane and path of integration for the case of viscous damping.

to as hysteretic damping and is represented by a loss factor η which multiplies the Young's modulus of the material, $E(1 + i\eta)$ [40]. If, on the one hand, the use of hysteretic damping yields mathematical advantages, on the other hand, it also leads to causality problems when moving from the frequency to the time domain [38, 39].

For hysteretic damping, the input mobility can be expressed as

$$Y(\omega) = i\omega \sum_{r=1}^N \frac{\phi_r^2(\mathbf{x}_f)}{\omega_r^2(1 + i\eta) - \omega^2}. \quad (3.14)$$

By considering η as a constant and equating the denominator in eq. (3.14) to zero, one can show that the system poles lie symmetrically over the first and third quadrant of the complex z plane,

$$z_r^{(u)} = +\omega_r \sqrt{1 + i\eta} \approx +\omega_r \left(1 + i\frac{\eta}{2}\right), \quad (3.15)$$

$$z_r^{(l)} = -\omega_r \sqrt{1 + i\eta} \approx -\omega_r \left(1 + i\frac{\eta}{2}\right),$$

where the approximation holds for small values of η and the superscripts u and l refer to the upper and the lower half of the complex z plane respectively. The position of the poles is illustrated in fig. 3.4.

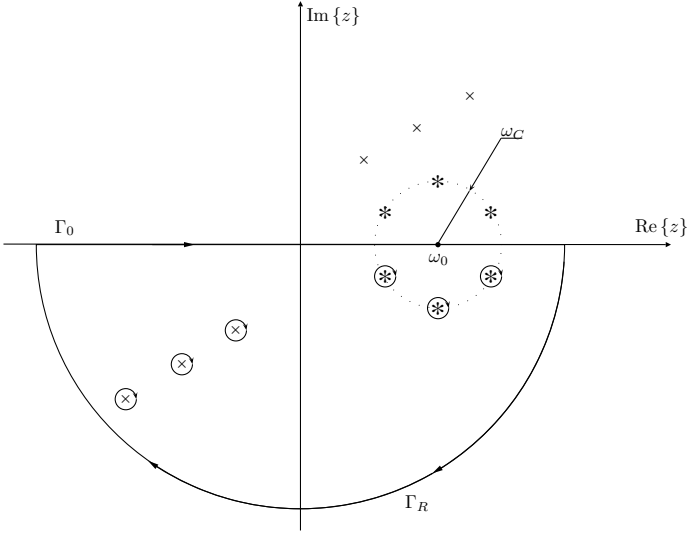


Figure 3.4: Position of system (\times) and filter ($*$) poles over the complex z plane and path of integration for the case of hysteretic damping.

3.5 Evaluation of the frequency integral

This section focuses on the efficient evaluation of integral (3.5), which is conveniently expressed in terms of displacements at the excitation point, $u(\mathbf{x}_f, \omega)$,

$$\langle P_{\text{in}} \rangle_W = \frac{1}{2} \int_{-\infty}^{+\infty} W(\omega) \text{Re} \{ i \omega u(\mathbf{x}_f, \omega) F_0^* \} d\omega. \quad (3.16)$$

By considering a real-valued weighting function, it is possible to write the frequency-averaged input power as follows,

$$\langle P_{\text{in}} \rangle_W = \frac{1}{2} \text{Re} \left\{ i \int_{-\infty}^{+\infty} W(\omega) \omega u(\mathbf{x}_f, \omega) F_0^* d\omega \right\}. \quad (3.17)$$

As previously mentioned, several numerical quadrature schemes are available to provide an estimation of integral (3.17). Nevertheless, their efficiency and accuracy are compromised by the fact that the integrand, $W(\omega) \omega u(\mathbf{x}_f, \omega) F_0^*$, is commonly an oscillating function of frequency.

An alternative way to perform the integration consists of using the complex residue theorem [73]. The theorem states that a line integral over a piecewise smooth, closed, counterclockwise oriented curve C of a function $g(z)$ analytic

inside and on C except at finitely many isolated poles, z_1, z_2, \dots, z_{N_p} , is equal to,

$$\oint_C g(z) dz = 2\pi i \sum_{s=1}^{N_p} \text{res} \{g(z_s)\}, \quad (3.18)$$

where $\text{res} \{g(z_s)\}$ is the residue of function $g(z)$ at the pole z_s . If the integration is carried out over a clockwise curve, the sign of the result changes.

3.5.1 Application of the residue theorem for a general case

The integral in eq. (3.17) is evaluated over the whole real frequency axis ω , which will be referred to as Γ . In order to apply the residue theorem to evaluate the integral

$$I_\Gamma = \int_\Gamma W(\omega) \omega u(\mathbf{x}_f, \omega) F_0^* d\omega, \quad (3.19)$$

it is necessary to move to the complex frequency z plane. The path of integration, C , is chosen to consist of a semicircle with radius R centered at the origin, Γ_R , and the part of the real frequency axis, Γ_0 , that closes the path. In principle, the curve Γ_R can be located either in the upper or in the lower half of the complex z plane. The convenience in choosing the latter will become clear later on. An example path is shown in fig. 3.4.

If the system is causal and stable, the function $u(\mathbf{x}_f, \omega)$ is analytic in the LHP and the poles are confined in the UHP. However, when the aforementioned principles are not respected, some system poles may lie in the third quadrant of the complex z plane.

Also the poles of the weighting function $W(\omega)$ are located over the complex plane. If $W(\omega)$ is a Butterworth filter, $B(\omega)$, the poles are spread both in the LHP and UHP and located over a circle, as explained in sec. 3.3.

As $R \rightarrow +\infty$, Γ_0 tends to Γ , coincident with the real frequency axis. Moreover, $I_C = I_\Gamma$, since the integral over Γ_R vanishes. To prove the latter statement, let us consider the case in which the hysteretic damping model is present (a viscous loss mechanism would lead to a similar result). Some of the system poles are located in the third quadrant and the closing path Γ_R is located in the LHP, as illustrated in fig. 3.4. Firstly, the integrand of integral I_{Γ_R} is rewritten and factorized as

$$g(z) = \frac{Az |F_0|^2 \omega_C^{2n}}{\prod_{k=0}^{2n-1} (z - z_k)} \sum_{j=1}^N \frac{-\phi_j^2(\mathbf{x}_f)}{(z - z_j^{(u)})(z - z_j^{(l)}), \quad (3.20)$$

where z_k and z_j represent the Butterworth and system poles, respectively. To evaluate the integral over Γ_R as R grows to infinity, the function $g(z)$ can be

bounded by minimizing its denominator. The smallest distance between Γ_R and a pole in the LHP is $R - |z_k^{(l)}|$ and $R - |z_j^{(l)}|$ for the Butterworth and system poles respectively. When the pole is located in the UHP, the smallest distance is equal to $|R - z_k^{(u)}|$ and $|R - z_j^{(u)}|$, respectively. Consequently, the function $g(z)$ can be bounded as,

$$|g(z)| \leq \frac{AR|F_0|^2\omega_C^{2n}}{\prod_{k=0}^{n-1}(R - |z_k^{(l)}|)\prod_{k=n}^{2n-1}|z_k^{(u)} - R|} \quad (3.21)$$

$$\times \sum_{j=1}^N \frac{|\phi_j^2(\mathbf{x}_f)|}{(R - |z_j^{(l)}|)|R - z_j^{(u)}|}.$$

Using this result to bound the integral, provides

$$\left| \int_{\Gamma_R} g(z) dz \right| \leq \frac{\pi AR^2|F_0|^2\omega_C^{2n}}{\prod_{k=0}^{n-1}(R - |z_k^{(l)}|)\prod_{k=n}^{2n-1}|R - z_k^{(u)}|} \quad (3.22)$$

$$\times \sum_{j=1}^N \frac{|\phi_j^2(\mathbf{x}_f)|}{(R - |z_j^{(l)}|)|R - z_j^{(u)}|} \sim \frac{1}{R^{2n}},$$

which tends to zero as $R \rightarrow +\infty$.

As a consequence of the previous considerations, the integral over the closed path, C , corresponds to I_Γ and by means of the residue theorem, it is possible to evaluate it as a sum of the residues of the function $g(z)$ at N system poles, $z_j^{(l)}$, and n filter poles, z_k , located in the LHP,

$$I_\Gamma = -2\pi i \left[\sum_{j=1}^N \text{res} \{g(z_j^{(l)})\} + \sum_{k=0}^{n-1} \text{res} \{g(z_k)\} \right]. \quad (3.23)$$

If the curve Γ_R is chosen to lie in the UHP, this does not hamper the use of the residue theorem. Nevertheless, as it will become clear later in this chapter, the previous choice leads to a more efficient integral evaluation.

3.5.2 Integration when system poles are confined in the UHP

When the causality and stability principles are respected, as for instance in the case of viscous damping, system poles are located over the UHP. Consequently,

the LHP is only populated by some of the filter poles and integral I_Γ can be evaluated as,

$$\int_{\Gamma} W(\omega)\omega u(\mathbf{x}_f, \omega) F_0^* d\omega = -2\pi i \sum_{k=0}^{n-1} \text{res} \{W(z_k)z_k u(\mathbf{x}_f, z_k) F_0^*\}, \quad (3.24)$$

where z_k corresponds to one of the poles of the weighting function $W(\omega)$, located in the LHP.

In general, the position of the system poles is not known *a priori*, while the position of the window poles is exactly known, provided that the window has a closed mathematical expression. The result in eq. (3.24) states that, no matter where the system poles are located, if the function $zu(\mathbf{x}_f, z)F_0^*$ is an analytic function in the LHP and vanishes sufficiently quickly as the frequency tends to infinity, the weighted frequency integral can be evaluated simply by computing the system response at some of the window poles.

In the case that the weighting function is a square magnitude of a Butterworth filter, $B(\omega)$, the residue must be evaluated at the poles z_k located over the LHP, thus considering eq. (3.8) with $0 \leq k \leq n-1$. Since the poles are simple [73], the residue can be expressed as

$$\text{res} \{B(z_k)z_k u(\mathbf{x}_f, z_k) F_0^*\} = \lim_{z \rightarrow z_k} (z - z_k) \frac{Az u(\mathbf{x}_f, z) F_0^*}{1 + (\frac{z - \omega_0}{\omega_C})^{2n}}. \quad (3.25)$$

By considering eq. (3.8) and applying the de l'Hôpital rule [73], it can be verified that this limit tends to

$$\text{res} \{B(z_k)z_k u(\mathbf{x}_f, z_k) F_0^*\} = -\frac{A\omega_C}{2n} e^{-i\theta_k} z_k u(\mathbf{x}_f, z_k) F_0^*, \quad (3.26)$$

where θ_k can be computed according to eq. (3.9).

By summing the residues at the Butterworth filter poles, it is possible to express the integral (3.24) as

$$\int_{\Gamma} B(\omega)\omega u(\mathbf{x}_f, \omega) F_0^* d\omega = \frac{i\pi A\omega_C F_0^*}{n} \sum_{k=0}^{n-1} z_k u(\mathbf{x}_f, z_k) e^{-i\theta_k}. \quad (3.27)$$

The evaluation of the integral only requires the computation of the system response at complex frequencies, which correspond to the filter poles.

As a result, the Butterworth-weighted input power, $\langle P_{\text{in}} \rangle_B$, is evaluated as

$$\langle P_{\text{in}} \rangle_B = -\frac{1}{2} \frac{\pi A\omega_C}{n} \text{Re} \left\{ F_0^* \sum_{k=0}^{n-1} z_k u(\mathbf{x}_f, z_k) e^{-i\theta_k} \right\}. \quad (3.28)$$

It is worth noting that when dealing with energetic approaches, quadratic quantities are of primary interest. The position of the poles of these quantities is symmetrically distributed over the complex z plane, as they are equal to the product of primary quantities times their complex conjugate. Consequently, the residue theorem cannot be exploited in such an efficient manner, and the frequency integral can only be analytically evaluated if the positions of the poles are known.

3.5.3 Integration when system poles are not confined in the UHP

As previously observed, when the damping mechanism is modeled using hysteretic damping, causality and stability paradoxes occur and this is confirmed by the fact that system poles are not confined in the UHP. For this reason, efficiently applying the residue theorem is not possible without the exact knowledge of the position of the system poles. At a glance, replacing the damping coefficient η with $\eta \operatorname{sgn}(\omega)$ may seem to solve the issue but it compromises the analyticity of the transfer function, which becomes discontinuous at $\omega = 0$ [38, 190]. However, as it is shown in the following, the relation obtained in eq. (3.28) can still be considered a reasonable approximation to evaluate the input power in the case of hysteretic damping.

In this context, using eq. (3.23) provides an exact result but the computational efficiency of the proposed approach is clearly reduced, and the eigenvalue problem has to be solved to evaluate I_Γ . Nevertheless, integral (3.23) can be approximated by evaluating the residues only at the filter poles located inside the path C , analogously to eq. (3.27). This can be shown by evaluating the residue of the integrand function $g(z)$, in case of hysteretic damping,

$$g(z) = \frac{Az |F_0|^2}{1 + \left(\frac{z - \omega_0}{\omega_C}\right)^{2n}} \sum_{j=1}^N \frac{\phi_j^2(\mathbf{x}_f)}{\omega_j^2 (1 + i\eta) - z^2}, \quad (3.29)$$

at the system poles.

For real-life applications, the structure is commonly constrained and it is reasonable to assume that the poles are simple, meaning that each pole has multiplicity equal to one. The residue of function $g(z)$ at a system pole, $z_j^{(l)}$, can be computed as follows,

$$\operatorname{res} \left\{ g(z_j^{(l)}) \right\} = \lim_{z \rightarrow z_j^{(l)}} \left[(z - z_j^{(l)}) \frac{Az |F_0|^2}{1 + \left(\frac{z - \omega_0}{\omega_C}\right)^{2n}} \sum_{r=1}^N \frac{\phi_r^2(\mathbf{x}_f)}{\omega_r^2 (1 + i\eta) - z^2} \right] \quad (3.30)$$

where the sum can be split,

$$\begin{aligned}
 \operatorname{res} \left\{ g(z_j^{(l)}) \right\} &= \lim_{z \rightarrow z_j^{(l)}} \left[(z - z_j^{(l)}) \frac{-Az |F_0|^2}{1 + \left(\frac{z - \omega_0}{\omega_C}\right)^{2n}} \sum_{\substack{r=1 \\ r \neq j}}^N \frac{\phi_r^2(\mathbf{x}_f)}{(z - z_r^{(u)})(z - z_r^{(l)})} \right] \\
 &+ \lim_{z \rightarrow z_j^{(l)}} \left[(z - z_j^{(l)}) \frac{-Az |F_0|^2}{1 + \left(\frac{z - \omega_0}{\omega_C}\right)^{2n}} \frac{\phi_j^2(\mathbf{x}_f)}{(z - z_j^{(u)})(z - z_j^{(l)})} \right] \\
 &= \frac{-Az_j^{(l)} |F_0|^2}{1 + \left(\frac{z_j^{(l)} - \omega_0}{\omega_C}\right)^{2n}} \frac{\phi_j^2(\mathbf{x}_f)}{(z_j^{(l)} - z_j^{(u)})}, \tag{3.31}
 \end{aligned}$$

where $z_j^{(u)}$ and $z_j^{(l)}$ are defined in eq. (3.15). The position of the poles is symmetric with respect to the origin of the coordinate system and since $z_j^{(l)} = -z_j^{(u)}$ the previous equation provides the following result,

$$\operatorname{res} \left\{ g(z_j^{(l)}) \right\} = -\frac{1}{2} \frac{A \phi_j^2(\mathbf{x}_f) |F_0|^2}{1 + \left(\frac{z_j^{(l)} - \omega_0}{\omega_C}\right)^{2n}}, \tag{3.32}$$

meaning that the residue of $g(z)$ at the system poles $z_j^{(l)}$, is dependent on the j -th mass normalized mode shape, ϕ_j , at the excitation point and on the feature of the Butterworth filter.

If I_Γ is approximated only by considering the filter poles, as in eq. (3.27), it is possible to quantify the absolute error on the input power by evaluating the residues at the system poles. In this case the absolute error ϵ_{abs} can be expressed in the following mathematical form,

$$\epsilon_{\text{abs}} = \frac{1}{2} \left| \operatorname{Re} \left\{ 2\pi \sum_{j=1}^N \operatorname{res} \left\{ g(z_j^{(l)}) \right\} \right\} \right|. \tag{3.33}$$

By introducing eq. (3.32) in the previous equation, a bounding expression can be formulated as

$$\epsilon_{\text{abs}} < \frac{1}{2} \left| \sum_{j=1}^N \frac{\pi A |F_0|^2 \phi_j^2(\mathbf{x}_f)}{1 + \left(\frac{z_j^{(l)} - \omega_0}{\omega_C}\right)^{2n}} \right|. \tag{3.34}$$

To evaluate a bounding function for the absolute error, ϵ_{abs} , one can consider the following inequality,

$$\left| \sum_{j=1}^N \frac{\pi A |F_0|^2 \phi_j^2(\mathbf{x}_f)}{1 + \left(\frac{z_j^{(l)} - \omega_0}{\omega_C} \right)^{2n}} \right| \leq \sum_{j=1}^N \frac{\pi A |F_0|^2 \phi_j^2(\mathbf{x}_f)}{\left| 1 + \left(\frac{z_j^{(l)} - \omega_0}{\omega_C} \right)^{2n} \right|}. \quad (3.35)$$

The numerator of the right-hand term in eq. (3.35) is a bounded function which is independent of frequency when system properties are frequency independent,

$$\left| \pi A |F_0|^2 \phi_j^2(\mathbf{x}_f) \right| \leq \pi A |F_0|^2 |\phi_j^2(\mathbf{x}_f)| \leq \pi A |F_0|^2 h_j, \quad (3.36)$$

where h_j is the upper bound related to the j -th mode.

Before bounding the denominator of eq. (3.35) some considerations are necessary.

Firstly, the quantity $z_j^{(l)}$ refers to the pole position over the complex plane and its real and imaginary parts are related through the damping coefficient η , which is commonly small ($\eta \ll 1$). Furthermore, since $z_j^{(l)}$ is in the third quadrant and ω_0 is real and positive, it can be verified that

$$\left| z_j^{(l)} - \omega_0 \right| \geq \left| \omega_j^{(l)} - \omega_0 \right|, \quad (3.37)$$

where $\omega_j^{(l)}$ indicates the real part of the pole $z_j^{(l)}$.

Secondly, for the denominator the following inequality holds

$$\left| 1 + \left(\frac{\omega_j^{(l)} - \omega_0}{\omega_C} \right)^{2n} \right| \geq \left| \frac{\omega_j^{(l)} - \omega_0}{\omega_C} \right|^{2n} = \frac{(\omega_j^{(l)} - \omega_0)^{2n}}{\omega_C^{2n}}. \quad (3.38)$$

Introducing eq. (3.36) and (3.38) in eq. (3.34) leads to an absolute error, ϵ_{abs} , which is bounded by a converging series,

$$\epsilon_{\text{abs}} < \frac{1}{2} \pi A |F_0|^2 \omega_C^{2n} \sum_{j=1}^N \frac{h_j}{(\omega_j^{(l)} - \omega_0)^{2n}}, \quad (3.39)$$

where h_j is an upper bound related to the eigenfunction of the j -th mode shape and $\omega_j^{(l)}$ is the real part of the correspondent eigenfrequency in the LHP.

The series in eq. (3.39) is convergent as N increases and can be considered as an upper bound for the error function. Moreover, it is clear that the bounding function has a strong dependence on the characteristics of the filter. Note that

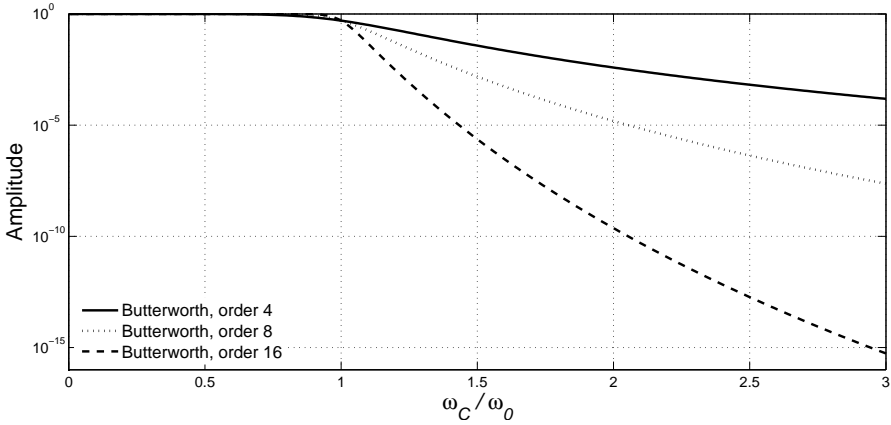


Figure 3.5: Amplitude decay for different Butterworth filters.

each term appearing in the sum in eq. (3.39) is small if ω_j is located away from ω_0 in the complex plane. In that case, the terms also quickly decrease further with increasing n . This is due to the quick decay of the amplitude of the Butterworth filter outside of a circle with radius ω_C centered around ω_0 , shown in fig. 3.4. To illustrate how fast the amplitude of the filter decreases with frequency, fig. 3.5 compares three different filters. Thus, for the bound (3.39) to be small, it is sufficient that the system pole closest to ω_0 lies at a distance bigger than ω_C . Since the system poles lie in the third quadrant, and ω_0 lies on the positive real line, this is almost always the case, except perhaps for values of ω_0 close to zero.

Finally, expression (3.39) still includes the position of the system poles and a term related to the eigenfunctions, which are not known *a priori* and make an estimate of ϵ_{abs} not possible for complex systems. For simple components, the position of the poles over the real ω axis can be hypothesized by using approximated relations to estimate the modal density $n_d(\omega) (\in \mathfrak{R}^+)$ [132, 220], which provides the number of modes over a frequency band and leads to $\omega_j^{(l)} \approx -j/n_d(\omega)$.

When the order of the filter is high enough, it is reasonable to assume that the error is negligible and the Butterworth-weighted input power can be evaluated as

$$\langle P_{\text{in}} \rangle_B \approx -\frac{1}{2} \frac{\pi A \omega_C}{n} \text{Re} \left\{ F_0^* \sum_{k=0}^{n-1} z_k u(\mathbf{x}_f, z_k) e^{-i\theta_k} \right\}. \quad (3.40)$$

The accuracy of this approximation will be assessed in the next section. However, it is important to underline that when the system poles lie in the

UHP, the residue provides an exact result just by evaluating the response at complex frequencies, which correspond to the filter poles.

3.6 Application cases

In this section, two application cases are proposed to show the level of accuracy achievable when evaluating the input power by means of the residue theorem. The first one is a simply supported rectangular plate, for which the eigenfrequencies and eigenfunctions are known analytically and allow assessing the validity of the error bounding function (3.39). The second case consists of two plates stiffened by a beam. Both examples include hysteretic damping as loss mechanism, for which the efficient evaluation of the input power results in an approximation rather than an exact result.

It is important to underline that the main concern lies with the accuracy of the integration rather than the accuracy of the model or the one of the numerical technique used to solve the physical problem. In fact, the efficiency of the frequency integration and its precision are totally independent of the ability of the model to represent the physical reality of the problem. In this regard, the main source of accuracy loss is inherent to the use of a Butterworth filter to approximate a rectangular window. As illustrated in fig. 3.2, this can be reduced by increasing the order of the filter. A second source of accuracy loss has to be considered when system poles are not confined to the UHP. This has been discussed in the previous sec. 3.5.3.

In order to quantify the accuracy of the approach, the relative error, ϵ_{rel} , is defined as

$$\epsilon_{\text{rel}} = \frac{\left| \langle P_{\text{in}} \rangle_B^{(\text{ref})} - \langle P_{\text{in}} \rangle_B^{(\text{approx})} \right|}{\langle P_{\text{in}} \rangle_B^{(\text{ref})}}, \quad (3.41)$$

where $\langle P_{\text{in}} \rangle_B^{(\text{ref})}$ and $\langle P_{\text{in}} \rangle_B^{(\text{approx})}$ indicate the reference value and its approximation, respectively.

3.6.1 Simply supported plate

This application case consists of a thin simply supported plate [128] made of steel, Young's modulus E , 210 GPa, Poisson ratio ν , 0.3 and density, 7850 kg/m³. The damping mechanism is assumed to be hysteretic and characterized by a coefficient η equal to 0.01, constant over the whole frequency range. The plate is rectangular with dimensions $l_x = 1$ m, $l_y = 0.6$ m and thickness $d = 2$ mm. A point force excitation is applied at (0.7, 0.4)m.

For simply supported plates the mass-normalized mode shapes have mathematical form,

$$\phi_{n_x, n_y}(x, y) = \frac{2}{\sqrt{M_{\text{tot}}}} \sin\left(\frac{n_x \pi x}{l_x}\right) \sin\left(\frac{n_y \pi y}{l_y}\right), \quad (3.42)$$

and eigenfrequencies are given by,

$$\omega_{n_x, n_y}^2 = \frac{D}{\rho d} \left[\left(\frac{n_x \pi}{l_x}\right)^2 + \left(\frac{n_y \pi}{l_y}\right)^2 \right]^2, \quad (3.43)$$

where M_{tot} is the total mass of the plate and D is the bending stiffness of the plate, $\frac{E d^3}{12(1-\nu^2)}$. The subscripts n_x and n_y identify the modes for each of the two directions. Thirty modes per direction are used in the framework of the Rayleigh-Ritz approach [40] to evaluate the system response.

In the remainder of this example, the Butterworth-weighted input power is computed in two different ways. On the one hand, according to the proposed technique, the band values are approximated by evaluating the residues at the filter poles, as expressed in eq. (3.40). On the other hand, having available both eigenfunctions (3.42) and eigenfrequencies (3.43) allows the computation of the exact integral (3.23) by evaluating the residues of the function $g(z)$ at all the poles located inside the integration path C in fig. 3.4. The result of the latter procedure provides a reference value for the error estimation.

The input power into the plate is shown in fig. 3.6. The frequency range of analysis sweeps 23 one-third octave bands (from 22 Hz to 4467 Hz). The narrow band input power is compared with the averages over the aforementioned bands.

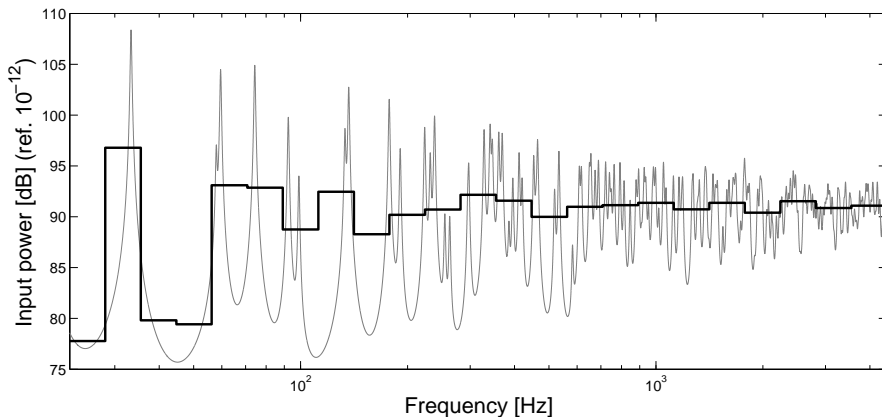


Figure 3.6: Comparison between narrow band and band-averaged input power for a simply supported plate.

Equation (3.23) is applied to evaluate the Butterworth-weighted input power, by using a filter of order 14.

In fig. 3.7, the third octave band input power is evaluated by using different weighting functions. The reference for the comparison is evaluated by using a rectangular window and is computed by means of numerical quadrature with the trapezoidal rule. A sampling step of 0.01 Hz assures that the evaluation is very accurate despite the simple integration rule used. This result is compared with the ones given by three Butterworth filters of order 8, 10 and 12, respectively. The frequency integral is evaluated by computing the integrand residues at both the system and the filter poles. This provides an exact value of integral (3.19).

As previously mentioned, the approximation of a rectangular window by means of a Butterworth filter represents the main source of accuracy loss. To further investigate this issue, the relative error with respect to the numerical quadrature is illustrated in fig. 3.8. The reference input power and its approximation are evaluated as previously explained. Filters with different number of poles are used to emphasize the effect of the order. In general, as the order increases, the approximation is closer to the one provided by a rectangular weighting function, as suggested by fig. 3.2.

Similar results are illustrated in fig. 3.9, where seven octave bands are considered (from 22.4 Hz to 2818 Hz). It is important to notice that, although the sampling scheme has a very high resolution, the numerical quadrature inevitably introduces errors which affect the comparison.

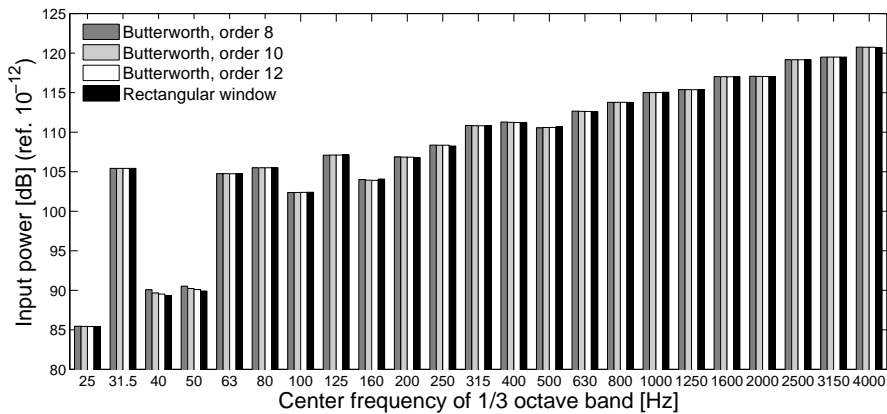


Figure 3.7: One-third octave band input power into a simply supported plate. Comparison between rectangular window and Butterworth filter as weighting functions.

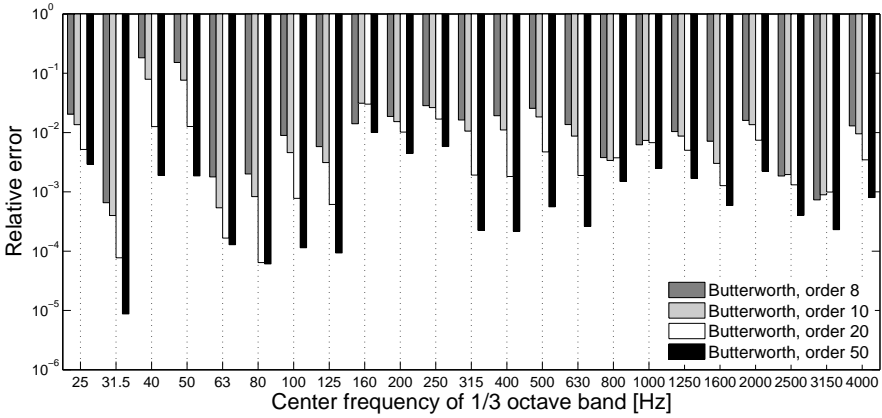


Figure 3.8: Relative error resulting from the use of a Butterworth filter to approximate a rectangular weighting function for a simply supported plate and 1/3 octave bands.

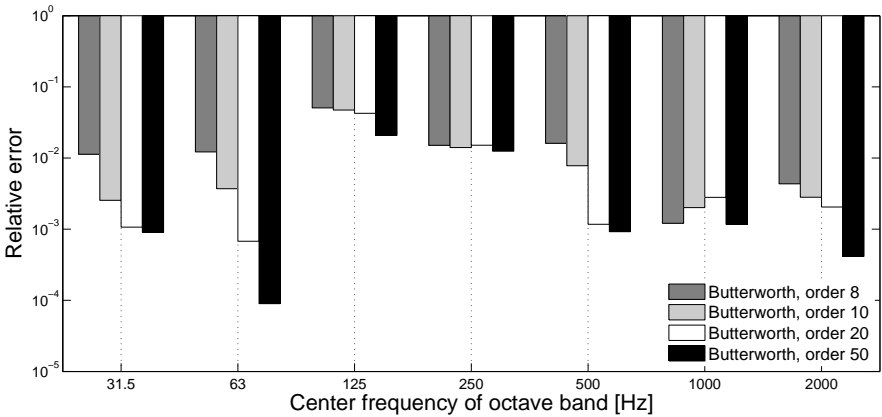


Figure 3.9: Relative error resulting from the use of a Butterworth filter to approximate a rectangular weighting function for a simply supported plate and octave bands.

If the damping model was viscous, the error resulting from the integration procedure would have been limited to the one due to the use of a Butterworth filter to resemble a rectangular window. However, the presence of hysteretic damping results in the use of an approximate relation instead of an exact one. The relative error resulting from using eq. (3.40) for one-third octave

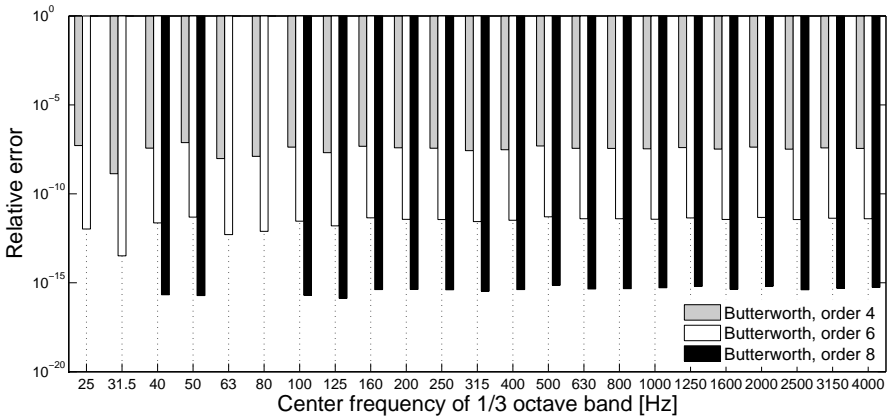


Figure 3.10: Relative error resulting from eq. (3.40) to evaluate 1/3 octave band input power into a simply supported plate.

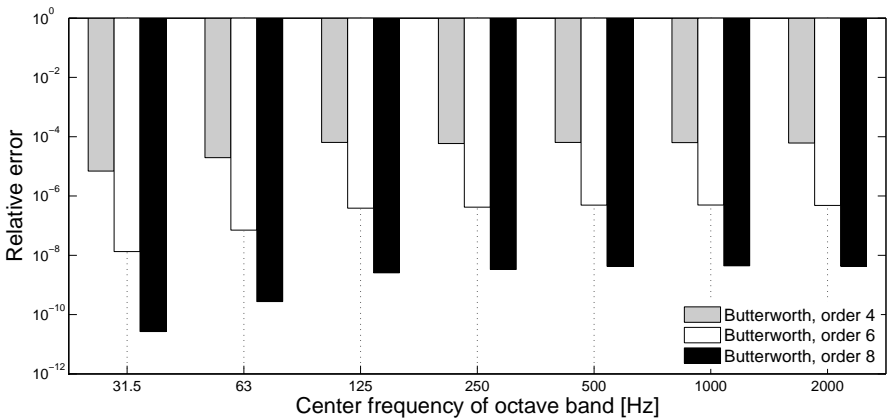


Figure 3.11: Relative error resulting from eq. (3.40) to evaluate octave band input power into a simply supported plate.

bands is quantified in fig. 3.10 and it decreases consistently with increasing order of the Butterworth filter. Double floating point format has been used in these computations. Note that for the first, second, fifth and sixth bands corresponding to order 8, the relative error is actually smaller than machine precision, due to an exact cancellation of the terms in the numerator of eq. (3.41). For higher orders of the Butterworth filter, the error from neglecting the system poles becomes very small, and machine precision accuracy is reached.

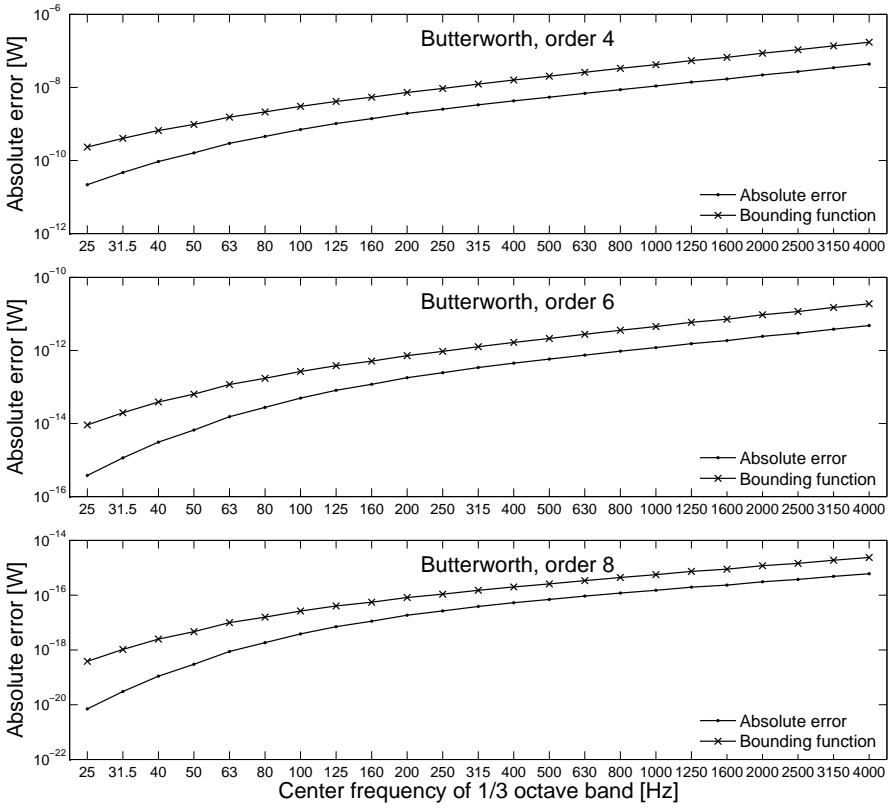


Figure 3.12: Absolute error over 1/3 octave bands resulting from eq. (3.40) to estimate the input power into a simply supported plate and comparison with the error bounding function (3.39).

Similar results are presented in fig. 3.11, where octave band computations are performed. For both examples, the reference value for the error estimation is evaluated according to eq. (3.23). Comparing fig. 3.8 with 3.10, and fig. 3.9 with 3.11, it can be observed that the error due to the use of a Butterworth filter when approximating a rectangular window, is predominant over the error due to approximation (3.40).

The absolute error on the input power and its bounding function (3.39) are shown in figs. 3.12 and 3.13 for one-third octave band and one octave band computations, respectively. As the problem eigenfunctions are known for simply supported thin plates, the parameter h_j can be estimated *a priori* from

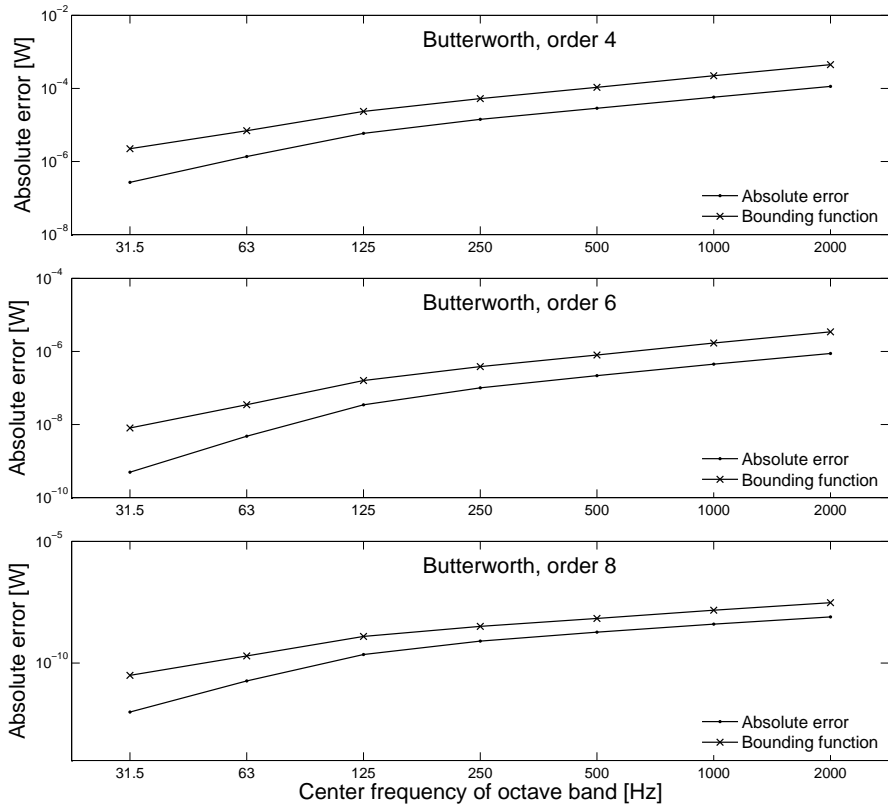


Figure 3.13: Absolute error over octave bands resulting from eq. (3.40) to estimate the input power into a simply supported plate and comparison with the error bounding function (3.39).

eq. (3.42). In fact h_j is constant for all modes and equal to $4/M_{\text{tot}}$. Moreover, to approximate the position of the poles, the modal density of a simply supported plate is used [132]. For all the analyzed cases, the function (3.39) bounds the absolute error, which is computed as the difference between the approximate Butterworth-weighted input power and its exact evaluation, as reported in eq. (3.33).

The knowledge of mode shapes and eigenfrequencies provides useful information to compare the exact evaluation of the frequency integral against its approximation. For more complex cases, their evaluation is more difficult since a complete eigenvalue problem needs to be solved. Nevertheless, this does not

introduce an obstacle to the application of the presented technique, as is done for a more realistic situation in the next example.

3.6.2 Stiffened plates

When high-frequency assumptions are not violated, treating finite structures as infinite can provide a reasonable approximation. According with the previous example, the input power into an infinite homogeneous plate is a constant function of frequency [132], and this is confirmed in fig. 3.6. In fact, when the wavelength is small enough, the band-averaged input power becomes almost constant and independent of frequency. However, there are situations in which this approximation leads to poor predictions. When dealing with low- and mid-frequencies and built-up structures, the wavenumbers of the stiff components have a strong influence on the overall response, and boundary conditions have an important impact on the behavior of the input mobility of the system. Moreover, property and material inhomogeneities may be present and influence the injected power, as well. For these cases, the use of the presented approach can be advantageous as it provides an accurate evaluation over a frequency band at a low computational cost. The structure under consideration in the next example consists of two plates connected through a stiffener. The two plates have dimensions 0.4×0.6 m each and 1 mm thickness. The material is aluminum, Young's modulus, 70 GPa, Poisson ratio, 0.3 and density, 2700 kg/m^3 . The beam is made of steel, Young's modulus, 210 GPa, Poisson ratio, 0.3, density, 7850 kg/m^3 , its length is 0.6 m and the section is 0.02×0.01 m. For all components, hysteretic damping is adopted with loss factor η equal to 0.01, constant with frequency. The system is excited by a point force located on the axis of the stiffener at 0.16 m from one of the two edges and is simply supported along the edges. The plates are discretized by 5288 quadrilateral shell elements,

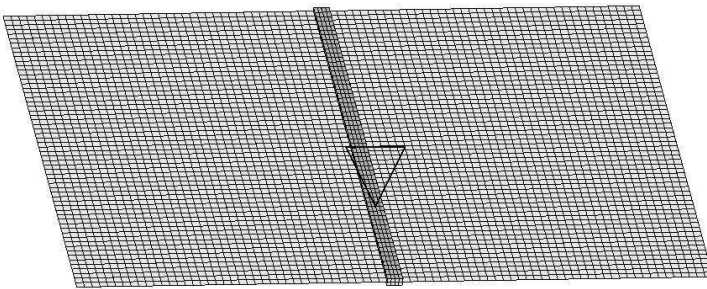


Figure 3.14: Finite element model of the stiffened plates.

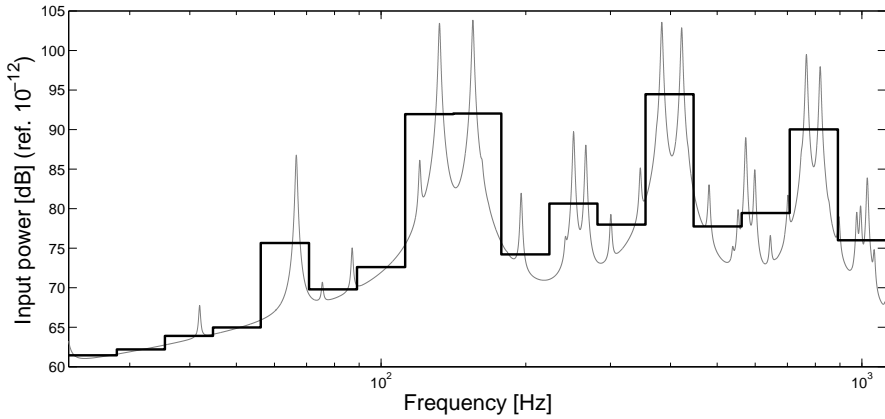


Figure 3.15: Comparison between narrow band and band-averaged input power for two stiffened plates.

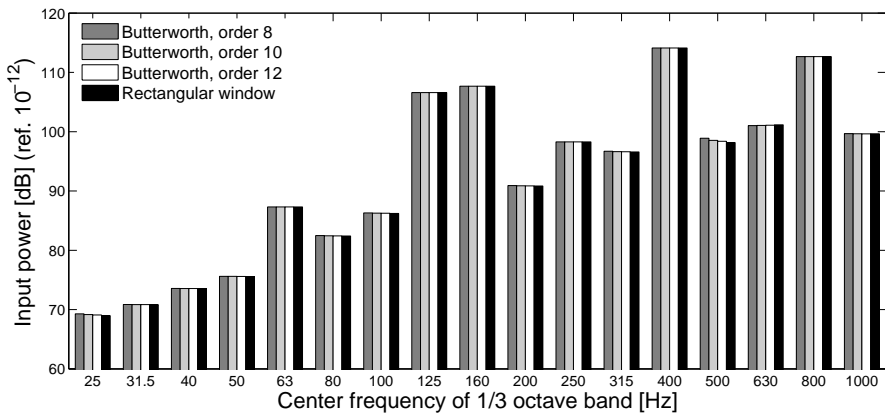


Figure 3.16: One-third octave band input power into two stiffened plates. Comparison between rectangular window and Butterworth filter as weighting functions.

while for the stiffener, 488 solid elements are used. The FE model and the geometry of the problem are illustrated in fig. 3.14. The commercial software Nastran 2010 [2] has been used to pre-process the system matrices.

As can be seen in fig. 3.15, the input mobility is characterized by peaks at the stiffener wavenumbers. Similarly to the previous case, the response has been

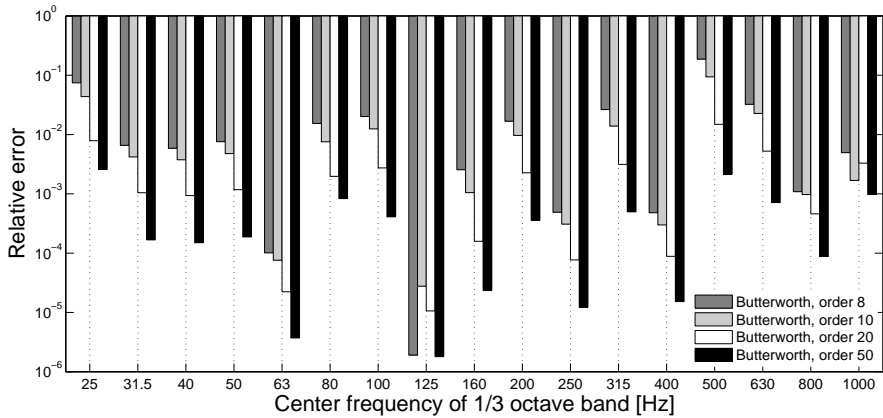


Figure 3.17: Relative error resulting from the use of a Butterworth filter to approximate a rectangular weighting function for two stiffened plates and 1/3 octave bands.

averaged over 17 bands (starting from 22.4 Hz to 1122 Hz), which in fig. 3.15 are computed by using a Butterworth filter of order 14.

For this case, evaluating the exact integral is much more difficult than in the previous example, since the eigenvalue problem should be solved entirely to compute expression (3.23). As an alternative, the frequency integral is evaluated by means of numerical quadrature, using a trapezoidal scheme with a frequency step equal to 0.01 Hz.

To investigate the use of a Butterworth filter as an approximation to a rectangular window, the one-third octave band values have been compared in fig. 3.16 for different orders. Here, the Butterworth-weighted values are computed by evaluating the residues only at the filter poles according to eq. (3.40). The relative error is illustrated in fig. 3.17, where the reference value is estimated by using a rectangular window as weighting function and numerical quadrature. Figure 3.18 shows the same comparison for five octave bands (from 22.4 Hz to 707.9 Hz) from which it is possible to draw similar conclusions. Like in the previous example, as the order of the filter increases, the Butterworth weighted integrals are closer to the ones computed by using a rectangular window.

Applying eq. (3.40) and limiting the residue evaluation to the filter poles introduces an approximation quantified in fig. 3.19, where the relative error is evaluated for different Butterworth filters covering third octave bands. Figure 3.20 illustrates the same computation over one octave bands. For each case, the reference value for the Butterworth-weighted frequency integral has been

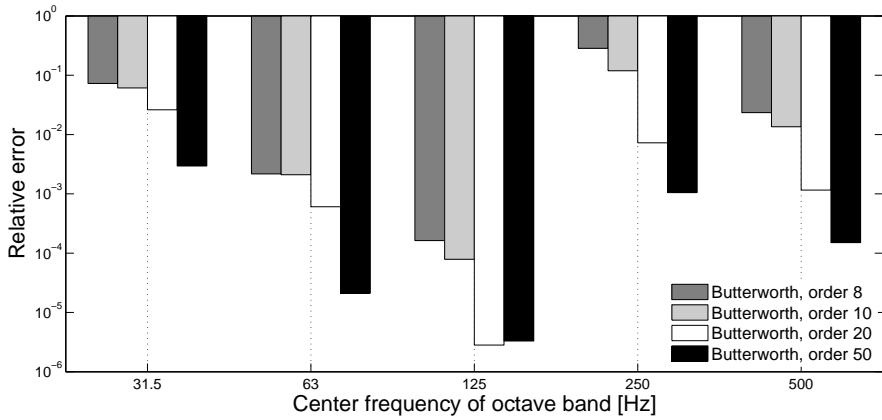


Figure 3.18: Relative error resulting from eq. (3.40) to evaluate the input power into two stiffened plates and octave bands.

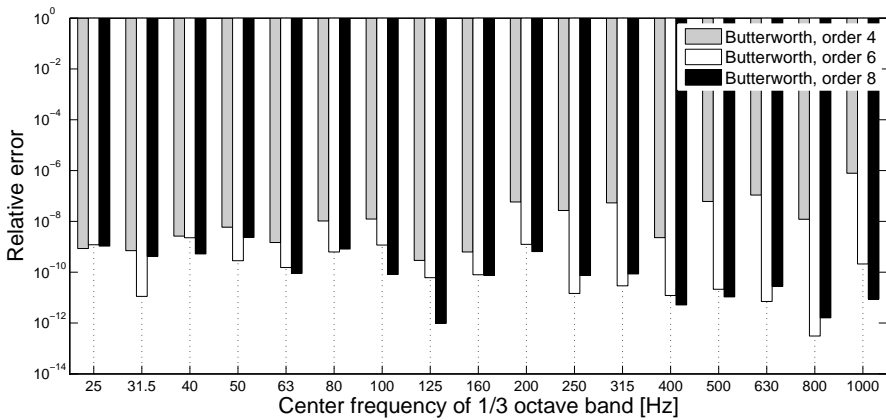


Figure 3.19: Relative error resulting from eq. (3.40) to evaluate 1/3 octave band input power into two stiffened plates.

estimated by using numerical quadrature with trapezoidal rule and 0.01 Hz step. Also in this case, as the order of the filter increases, the relative error decreases, although less regularly than in the previous case, fig. 3.10. An explanation for this can be given by considering that, in the present example, the reference values are computed using a quadrature integration, while in the previous one the integrals have been evaluated in an exact way. However, the precision is very high over the whole frequency range of analysis. Comparing figs. 3.17 and

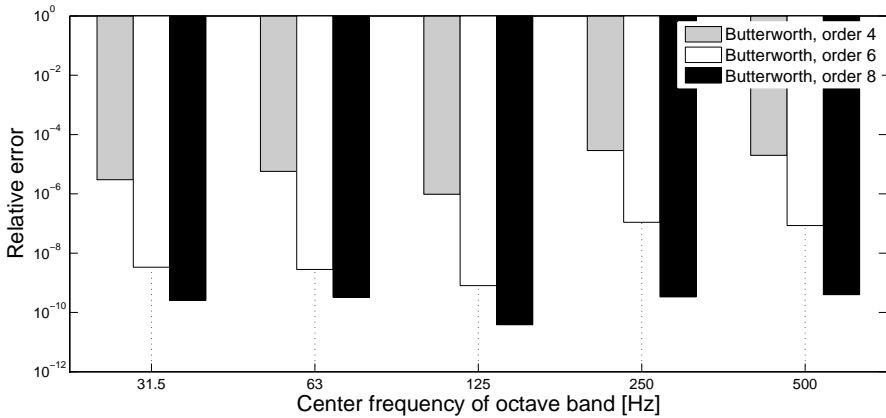


Figure 3.20: Relative error resulting from eq. (3.40) to evaluate octave band input power into two stiffened plates.

3.18 shows that the relative error for octave band input power computation is higher than in the case of third octave bands. This is due to the fact that for octave bands the ratio ω_C/ω_0 is larger than for third octave bands. As a consequence, the error in eq. (3.39) can also be larger. However, although the error is very low in general, it can be easily controlled and reduced by increasing the order of the filter.

Finally, comparing fig. 3.19 with 3.17 and fig. 3.18 with 3.20 confirms that the error due to the use of the approximate relation (3.40) is smaller than the one due to the use of a Butterworth filter to resemble a rectangular window.

3.7 Computational considerations

3.7.1 Computation time

The main advantage of the proposed procedure to evaluate the input power over frequency bands, is the considerable reduction of computation time.

When computing the frequency integral over a large bandwidth, classic numerical quadrature rules are very expensive, especially when an accurate estimation is required. This is firstly due to the oscillatory behavior of the integrand function, which may require a very refined integration step to achieve a good precision. In contrast, the residue theorem does not require a sampling procedure. To quantify the computational performance, fig. 3.21 compares

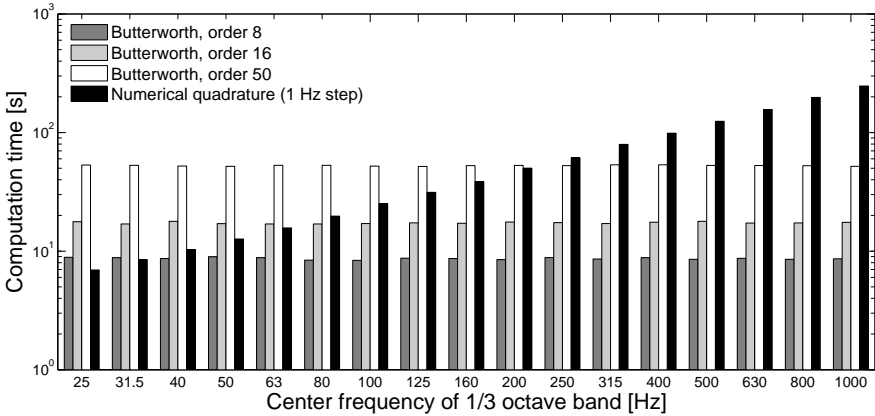


Figure 3.21: Computation time to evaluate the one-third octave band input power into two stiffened plates. Classic numerical quadrature is compared with the present technique for different orders of the Butterworth filter.

solution times to evaluate one-third octave band input power into two stiffened plates. The numerical quadrature used in this analysis has a 1 Hz step, which, although is larger than what was shown in the previous section, is a reasonable choice for a real application case. If the integration step was 0.01 Hz, like in the previous example, the elapsed time would be 100 times larger than what presented in fig. 3.21. The Butterworth-weighted frequency averaging is performed by using three different filters with increasing order, namely 8, 16 and 50. Accordingly, they require an increasing number of response evaluations at complex frequencies: 8, 16 and 50, respectively, coincident to the poles of the square magnitude of the Butterworth filter. Data are obtained using a Windows 7 64-bit desktop machine, processor Intel(R) Core 2 Quad CPU, clock rate 3 GHz and 8 GB RAM. The Matlab sparse solver [1] is used to solve the FE system of equations. As expected, the use of numerical integration leads to computation times which increase proportionally with the bandwidth. The solution time required by the proposed technique is constant over the bands and proportional to the order of the Butterworth filter. When frequency is low, the numerical quadrature is faster than the proposed approach, since the bandwidth is small. As the frequency increases, the use of the residue theorem becomes more advantageous in terms of time. The benefits can be even more evident if octave bands are taken into account, as their bandwidth is larger when compared to the one-third octave bands.

The performance in terms of solution accuracy is compared in fig. 3.22. The reference value to compute the relative error is the one obtained using a

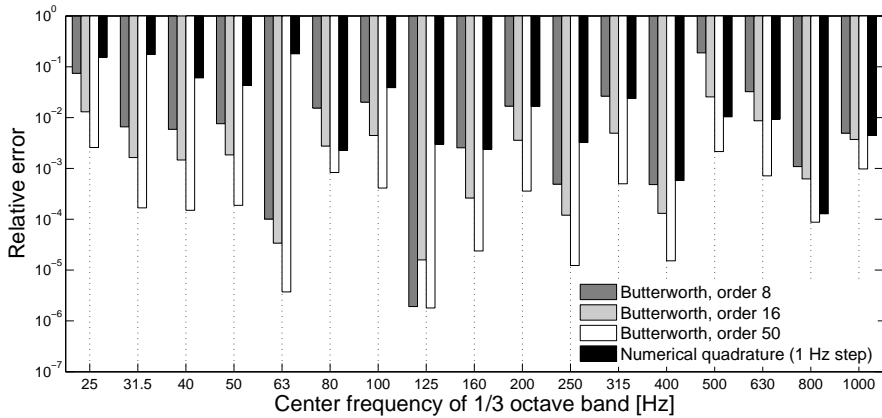


Figure 3.22: Relative error resulting from the comparison of different integration techniques and a reference value computed by means of numerical quadrature with frequency sampling equal to 0.01 Hz over 1/3 octave bands. The case analyzed consists of two plates stiffened by a beam and the hysteretic damping coefficient is equal to 0.01.

rectangular window and numerical quadrature with integration step equal to 0.01 Hz. Using a rectangular window and a quadrature integration step equal to 1 Hz allows computing relatively accurate band values. The use of a Butterworth filter in combination with the residue theorem provides accurate results as well, although the difference between the shapes of the weighting windows has to be taken into account. When the order of the filter is high, the proposed approach outperforms numerical quadrature, especially at high-frequencies where computational times are much lower. Furthermore, the use of the residue theorem allows performing band evaluations independently from any sampling refinement. This becomes particularly advantageous when the damping coefficient is very small and numerical quadrature may require a large number of sampling points to achieve an accurate evaluation of the input power. Analogously to the previous case, this issue is investigated in fig. 3.23, where the hysteretic damping coefficient is equal to 0.001. The relative error resulting from the use of a 1 Hz step quadrature rule is high, especially when compared to the values obtained by using the proposed technique. It is interesting to see that for the first band, the input power predicted by the Butterworth filter of order 8 is very poor. This is due to the fact that a sharp power peak is located at about 21 Hz, which is very close to the lower bound of that frequency band (22.4 Hz), and the system has a flat response within the band. The Butterworth function does not decay fast enough to cut the power peak out of the frequency

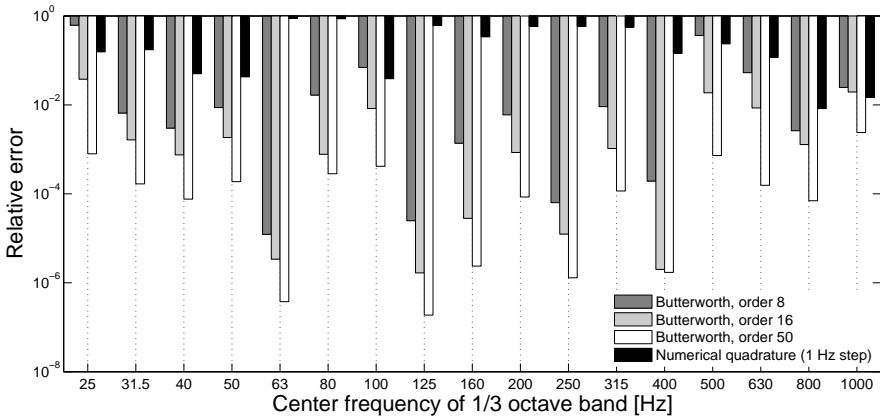


Figure 3.23: Relative error resulting from the comparison of different integration techniques and a reference value computed by means of numerical quadrature with frequency sampling equal to 0.01 Hz over 1/3 octave bands. The case analyzed consists of two plates stiffened by a beam and the hysteretic damping coefficient is equal to 0.001.

band. Nevertheless, as the order increases, the relative error becomes smaller. Finally, the computational advantage allows the present approach to be applied also in the context of mid-frequency modeling. As previously mentioned, an accurate evaluation of the input power can seriously improve the quality of an energetic model, especially where high-frequency assumptions are not completely fulfilled. Here, the residue theorem provides a valuable alternative for simulating large models and assemblies.

3.7.2 Implementation

A second major advantage of this approach is its flexibility and ease of implementation. In fact, it can be applied in combination with any deterministic approach, i.e. FEM, BEM. Moreover, the implementation does not require so much effort since the frequency integral can be evaluated as a weighted sum of the input power computed at complex frequencies instead of real ones.

It is worth noting that the use of octave and one-third octave bands is only illustrative in this chapter. The application can be extended to any type of frequency band and this choice does not affect the efficiency or the accuracy of the computation. As previously mentioned, this is valid when system poles are

confined in the UHP. On the other hand, the disadvantage of the approach is mainly related to the fact that, when some of the system poles lie in the LHP, it provides an approximate value rather than an exact one. Nevertheless, as previously shown, the error can be controlled by using a proper order of the Butterworth filter.

From a solver point of view, a direct solution is the most suitable choice for the proposed technique. In fact, the use of a modal solver would reduce the computational advantage gained by moving the integration path to the complex plane. Nevertheless, for problems in which eigenvalues and mode shapes are computed, the use of the residue theorem would provide a valuable alternative to numerical quadrature schemes for computing mean values over frequency bands in the post-processing step.

Finally, it is worth underlining the effect of a computation at a complex frequency instead of a real one on the numerical method. For approaches like BEM or the WBM handling complex frequencies instead of real ones does not require any additional computational effort. On the contrary, for FEM the introduction of complex numbers influences the computational effort to solve the problem. Nevertheless, evaluating the system matrices at a complex frequency leads to modified damping and stiffness matrices. This can be shown by considering a generic linear second-order system in which dissipation mechanisms can be described by both viscous and hysteretic damping. In this case the dynamic stiffness matrix \mathbf{D} has the mathematical form,

$$\mathbf{D}(z) = -z^2\mathbf{M} + iz\mathbf{C} + \mathbf{K}(1 + i\eta), \quad (3.44)$$

where z represents the complex frequency of analysis and may be considered one of the filter poles. Since z is a complex frequency, the previous expression can be rewritten as follows,

$$\begin{aligned} \mathbf{D}(z_r - iz_i) &= -(z_r - iz_i)^2\mathbf{M} + i(z_r - iz_i)\mathbf{C} + \mathbf{K}(1 + i\eta) \\ &= -z_r^2\mathbf{M} + iz_r(2z_i\mathbf{M} + \mathbf{C}) + i\eta\mathbf{K} + (z_i^2\mathbf{M} + z_i\mathbf{C} + \mathbf{K}), \end{aligned} \quad (3.45)$$

where z_r and z_i represent respectively the real and imaginary part of z . Note also that as the filter poles are in the LHP, both of them are positive numbers in eq. (3.45). It is evident from eq. (3.45) that the dynamic stiffness matrix evaluated at a complex frequency can be reformulated as a modified dynamic stiffness evaluated at a real one. Moreover, the second and the fourth terms of eq. (3.45) correspond respectively to a modified viscous damping and stiffness matrices. In case the FEM solver can only handle real frequencies, eq. (3.45) can be used to reformulate matrices and evaluate the problem solution.

3.8 Conclusion

In this chapter, an efficient technique to evaluate the input power over frequency bands is presented. In contrast to numerical quadrature schemes, the residue theorem can be efficiently exploited to compute a weighted integral over the frequency. In fact, when system poles are distributed only in the upper half of the complex frequency plane and the residue evaluation is limited to the poles of the weighting function, which is a Butterworth filter in this chapter.

When system poles are not confined in the upper half plane, evaluating the integral by computing the residues at the filter poles results in an approximation, rather than an exact result. However, as the order of the filter increases, the error decreases and the frequency band values are estimated very accurately.

Two application examples are shown to assess the accuracy of the proposed strategy. Firstly, the possibility of approximating a rectangular window by means of a Butterworth filter is investigated. By increasing the order, the shape of a Butterworth filter is closer to a rectangular window but on the other hand the number of frequencies at which the system has to be evaluated increases as well. As a rule of thumb, a filter of order 8-10 allows achieving accurate frequency band evaluations at a low computational cost. Secondly, as both examples include hysteretic damping, the accuracy is assessed of the proposed technique when system poles are not confined in the UHP. In fact, the error function is proven to show a decay rate which is proportional to the order of the filter. Consequently, it can be easily and efficiently controlled. Finally, the computational efficiency of the method is shown by comparing its performance with numerical quadrature. Especially when the structure is lightly damped, the proposed strategy shows major advantages, since it is independent of the refinement of the sampling procedure to approximate the integrals.

Chapter 4

Use of quadrature schemes in the complex frequency domain

The previous chapter dealt with the use of the residue theorem as an efficient alternative to classic quadrature for evaluating integrals over frequency bands. The square magnitude of a Butterworth filter was employed to approximate the features of an ideal rectangular window, which is commonly used to weigh the response over real frequencies. As a result, the band-averaged input power can be computed by evaluating the system behavior at complex frequencies instead of real ones, with these complex values being some of the poles of the Butterworth filter.

The fact that a few computations at complex frequencies allow accurate band evaluations, regardless of the bandwidth, is very advantageous from a computational point of view, and providing further improvements and insight motivates the research presented in this chapter.

The main idea lies in the generalization of the result in ch. 3. Instead of using a window to filter the response over a band, the integral is directly defined over the band itself. Thanks to the residue theorem, this problem can be equivalently solved by integrating over a path in the complex plane, which will be either a semi-circle or a semi-ellipse in the following, and on which classic quadrature can be applied. Moreover, the use of this alternative strategy indicates that the Butterworth-weighted frequency averaging presented in ch. 3, corresponds to the use of the midpoint rule over a semi-circle taken in the complex frequency plane. Consequently, more efficient techniques can be used to yield a more

accurate estimate. The use of adaptive integration schemes is also investigated to perform convergence studies.

Finally, having seen that there is an equivalence between a weighting function, i.e. the Butterworth filter, and a quadrature rule applied over a path in the complex plane, the possibility of applying the inverse procedure is investigated. In other words, for a given quadrature rule applied over a path in the complex plane, it will be shown that it is possible to formulate a weighting function located over the real frequency axis.

In order to compare the improvement with respect to results in ch. 3, the same application cases are presented. However, while in ch. 3 the investigation is limited to the evaluation of active input power, in the following both real and imaginary parts of the input mobility are used as integrand functions. Gaussian, Lobatto and Clenshaw-Curtis quadrature rules are compared, while the Gauss-Kronrod-Patterson rule is presented in the context of adaptive integration [43].

The chapter is structured as follows. In sec. 4.1 the band-averaged mobility integral is presented, while in sec. 4.2 its solution by means of the residue theorem is explained. In sec. 4.3 a possible correlation between the aforementioned integration schemes and weighting functions is proposed. Application cases are illustrated in sec. 4.4 and, finally, in sec. 4.5, conclusions are drawn.

4.1 Frequency-averaged input mobility

The band-averaged input mobility can be evaluated through the integral,

$$\langle Y \rangle_{\Delta\omega} = \frac{1}{\Delta\omega} \int_{\Delta\omega} Y(\omega) d\omega, \quad (4.1)$$

where $\langle \bullet \rangle_{\Delta\omega}$ represents the frequency average operator performed over the band $\Delta\omega$. In general, the mobility transfer function $Y(\omega)$ is frequency dependent and consists of a real part, namely the conductance $G(\omega)$, and an imaginary part, the susceptance $S(\omega)$, such that the input mobility can be expressed as,

$$Y(\omega) = G(\omega) + iS(\omega). \quad (4.2)$$

The conductance is always positive, regardless of the time convention and is related to the amount of active power injected into the system. On the other hand, the susceptance can be either positive or negative and is proportional to the reactive power. According to eq. (4.2), integral (4.1) can be rewritten as,

$$\langle Y \rangle_{\Delta\omega} = \frac{1}{\Delta\omega} \int_{\Delta\omega} G(\omega) d\omega + \frac{i}{\Delta\omega} \int_{\Delta\omega} S(\omega) d\omega, \quad (4.3)$$

which highlights the contributions of the frequency-averaged conductance and susceptance. By assuming that the amplitude of the excitation is frequency independent and constant over the band, the averaged complex input power, $P_{\text{in}}^{(c)}$, can be straightforwardly calculated from the input mobility,

$$\langle P_{\text{in}}^{(c)} \rangle_{\Delta\omega} = \frac{1}{2} |F_0|^2 \langle Y \rangle_{\Delta\omega}. \quad (4.4)$$

The approach presented in ch. 3 proposes the use of the residue theorem for the efficient evaluation of the active input power weighted by using the square magnitude of a Butterworth filter. However, without loss of generality, the approach can be extended to the evaluation of band-averaged complex quantities.

The main goal of the following sections is to generalize the strategy illustrated in ch. 3 and improve its efficiency. Moreover, results will be extended to complex quantities, rather than merely real ones.

4.2 Evaluation of the frequency integral

Integral (4.1) is rewritten as

$$I_{\Gamma_0} = \int_{\Gamma_0} Y(\omega) d\omega, \quad (4.5)$$

where Γ_0 corresponds to $\Delta\omega$. The curve Γ_0 lies over the real positive frequency axis and consists of all the frequencies inside the interval $[\omega_0 - \omega_C, \omega_0 + \omega_C]$, with ω_0 the center frequency of the interval and ω_C its half-width, which also stands for the cut-off frequency of an associated ideal rectangular window.

In order to apply the residue theorem, it is necessary to move from a real variable ω to the complex plane of variable $z \in \mathbb{C}$. Again, z is used when the frequency value may be complex, while ω is used when the value is real.

The path of integration C is chosen such that it includes Γ_0 and the closure is fulfilled by means of a smooth curve Γ_r which is located in the complex z plane. An example is illustrated in fig. 4.1, although in principle Γ_r does not need to be a circle. Hence, the residue theorem leads to the following result

$$I_{\Gamma_0} + I_{\Gamma_r} = \int_{\Gamma_0} Y(\omega) d\omega + \int_{\Gamma_r} Y(z) dz = -2\pi i \sum_{s=1}^{N_p} \text{res} \{Y(z_s)\}, \quad (4.6)$$

from which it is clear the necessity to know whether the integrand $Y(z)$ has poles located inside the path C (sec. 3.4). Furthermore, the mathematical features of the closing curve Γ_r have to be specified in order to compute I_{Γ_r} . These aspects are discussed in the following sections.

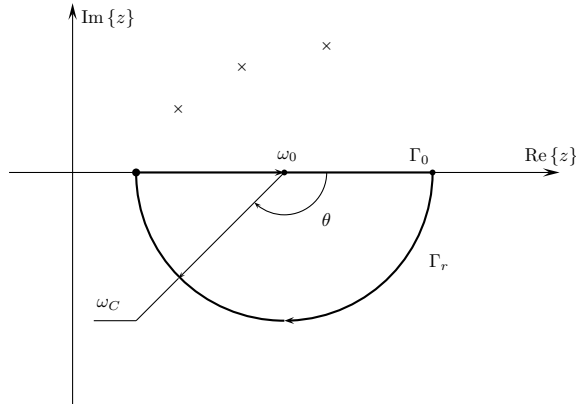


Figure 4.1: Integration path $C = \Gamma_0 \cup \Gamma_r$ in the complex z plane, with Γ_r being a semi-circle centered at ω_0 and radius ω_C . The position of the poles of the input mobility is indicated by the symbol \times .

4.2.1 Definition of the integration path C

Provided that the function $Y(z)$ is analytic in the fourth quadrant of the complex z plane, the path C can be closed in the LHP by means of a curve Γ_r . As a result of the residue theorem, since no poles lie inside the contour path C , it is possible to write,

$$I_{\Gamma_0} = - \int_{\Gamma_r} Y(z) dz = -I_{\Gamma_r}, \quad (4.7)$$

which is a very interesting result, as it substitutes an integral over the real frequency domain by using an integral over a path in the complex plane. At this stage, it is important to make a remark which will be clarified later by means of examples. As mentioned in ch. 3, moving to complex frequencies in the LHP has the effect of additional damping on the system response. Consequently, the response function becomes increasingly smoother when moving away from the real frequency axis and the integration can be performed more efficiently, with a smaller number of integration points. This should clarify, for the moment, the advantage of moving the integration path to complex frequencies instead of real ones. Nevertheless, it has to be underlined that, for non-dissipative systems, the input mobility is purely complex and system poles lie over the real frequency axis. Consequently, the knowledge of their position is necessary to evaluate I_{Γ_0} . This jeopardizes the efficiency of this approach, as the position of the singularities has to be computed through the solution of an eigenvalue problem,

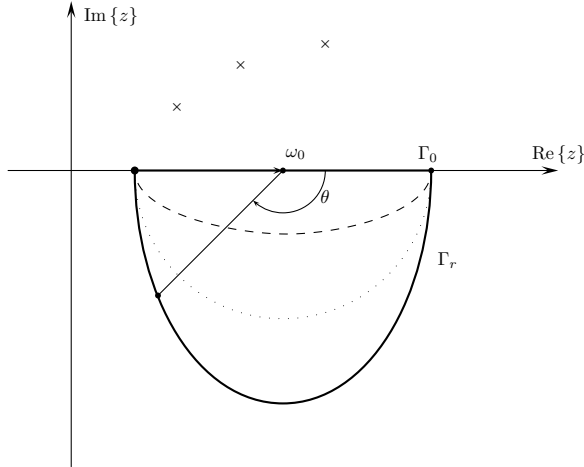


Figure 4.2: Integration path $C = \Gamma_0 \cup \Gamma_r$ over the complex z plane, with Γ_r being either a semi-ellipse or a semi-circle centered at ω_0 . The solid, dashed and dotted lines represent a semi-ellipse with $a = 2$, a semi-ellipse with $a = 0.5$ and semi-circle, respectively. The position of the poles of input mobility is indicated by the symbol \times .

and explains why only dissipative systems are considered here. However, this is not seen as a limitation, as all real systems present loss mechanisms.

In order to facilitate the mathematical description of integral I_{Γ_r} , the curve Γ_r is now taken to be either a semi-circle or a semi-ellipse. Some examples are illustrated in fig. 4.2. Both curves can be parametrized in θ , and in the following the detailed expressions for the associated integrals will be given.

Integration over a semi-circle

The semi-circle is chosen such that the radius is equal to ω_C and the center is located at ω_0 . To evaluate I_{Γ_r} , the curve Γ_r is parametrized as a function of θ , which is defined on the interval $[0, \pi]$, as illustrated in fig. 4.1. So, using cylindrical coordinates, a point taken on Γ_r can be defined as

$$z = \omega_0 + \omega_C e^{-i\theta}, \tag{4.8}$$

and

$$dz = -i\omega_C e^{-i\theta} d\theta. \tag{4.9}$$

Integral (4.7) in the complex variable z is rewritten as

$$I_{\Gamma_r} = -i\omega_C \int_0^\pi Y(z(\theta))e^{-i\theta} d\theta, \quad (4.10)$$

where θ is a real variable and the integration is performed over the interval $[0, \pi]$.

Integration over a semi-ellipse

In this case, Γ_r is a semi-ellipse. As illustrated in fig. 4.2, the curve is chosen such that the center is coincident with ω_0 , the length of the semi-axis on the real axis is equal to ω_C and the length of the semi-axis parallel to the imaginary axis is equal to ω_B .

A point over the ellipse can be defined as

$$z = \omega_0 + \omega_C \cos(\theta) - i\omega_B \sin(\theta) \quad (4.11)$$

and

$$dz = -[\omega_C \sin(\theta) + i\omega_B \cos(\theta)] d\theta. \quad (4.12)$$

Finally, the integral over Γ_r can be expressed as

$$I_{\Gamma_r} = - \int_0^\pi Y(z(\theta))[\omega_C \sin(\theta) + i\omega_B \cos(\theta)] d\theta. \quad (4.13)$$

In the following, ω_B is taken such that

$$\omega_B = a \cdot \omega_C, \quad (4.14)$$

where $a \in \mathbb{R}^+$. When $a = 1$, the ellipse is a circle and eqs. (4.10) and (4.13) provide the same result. When $a < 1$ the major axis is lying on the real axis, as indicated by the dashed line in fig. 4.2. Finally, if $a > 1$ the major axis is parallel to the imaginary axis and this configuration is represented by the solid line in fig. 4.2.

4.2.2 Use of numerical quadrature schemes to evaluate I_{Γ_r}

At this stage, the mathematical form of Γ_r has been defined and I_{Γ_r} can be evaluated by means of numerical techniques. When quadrature schemes are applied, it is common to express n integration points, ζ_j , over the interval

$[-1, 1]$, such that the integral I_{Γ_r} over a semi-circle in eq. (4.10), can be written as

$$I_{\Gamma_r} = -\frac{i\pi\omega_C}{2} \int_{-1}^{+1} Y(z(\zeta))e^{-i\theta(\zeta)} d\zeta \approx -\frac{i\pi\omega_C}{2} \sum_{j=1}^n w_j Y(z(\zeta_j))e^{-i\theta(\zeta_j)}. \quad (4.15)$$

If Γ_r is a semi-ellipse, it follows from eq. (4.13) that

$$\begin{aligned} I_{\Gamma_r} &= -\frac{\pi}{2} \int_{-1}^{+1} Y(z(\zeta))[\omega_C \sin(\theta(\zeta)) + i\omega_B \cos(\theta(\zeta))] d\zeta \quad (4.16) \\ &\approx -\frac{\pi}{2} \sum_{j=1}^n w_j Y(z(\zeta_j))[\omega_C \sin(\theta(\zeta_j)) + i\omega_B \cos(\theta(\zeta_j))]. \end{aligned}$$

Both in eq. (4.15) and (4.16), w_j represents the j -th weight associated to the integration point ζ_j . From a computational point of view the results in eqs. (4.15) and (4.16) only require the system response to be evaluated at complex frequencies instead of real ones. If the model has frequency dependent terms, i.e. damping, the strategy is still applicable as long as system poles do not lie inside the path of integration.

Weights w_j and abscissas ζ_j are chosen according to the adopted quadrature scheme. In the literature there exist several efficient schemes to evaluate integral I_{Γ_r} , and only a few of them are reported here. However, for more detailed information on the following schemes, the reader is referred to the book of Davis and Rabinowitz [43].

The most efficient scheme is the Gaussian quadrature rule, which allows exactly integrating polynomials of degree $2n - 1$. Gaussian quadrature has one main disadvantage related to the possibility of reusing abscissas and weights from previous evaluations to perform adaptive integration. In fact, if one wishes to increase the accuracy of an integral estimate based on n Gauss points by using $m > n$ Gauss points, these m points and their weights need to be recomputed. This hampers the possibility of straightforwardly exploiting the concept of adaptivity (also called nested quadrature) and reusing the initial n function evaluations. To overcome this limitation, Kronrod proposes to start with a set of n Gauss points and add $n + 1$ abscissas (and $2n + 1$ new weights) to the previous set. The extra points are the zeros of Stieltjes polynomials. This allows exactly integrating a polynomial of degree $3n + 1$, if n is even, and $3n + 2$, if n is odd, and provides information related to the convergence of the estimate. In case the estimate obtained by applying the Kronrod scheme does not show a satisfying convergence, Patterson suggests to add $2n + 2$ abscissas (and $4n + 3$ new weights), which lead to an exact integration of a polynomial of degree $6n + 5$. The Patterson sequence used in this work is: 3 Gauss points,

7 Kronrod points, 15 Patterson points (G3-K7-P15).

So far, only open quadrature schemes have been mentioned, meaning that the endpoints of the interval are not included in the set of abscissas. On the other hand, the scheme is said to be closed if the integrand function is also evaluated at the endpoints. Among all cases where closed rules can be helpful, the situation where the integrand has singular-like behavior at the boundaries of the integration interval, is of particular interest. This might be the case if a system pole lies very close to the endpoint of the band. Lobatto rule is based on Gaussian quadrature rule to which the end points are added. Consequently, also the weighting factors are modified with respect to the classic Gauss rule. Lobatto quadrature provides exact integration for polynomials of degree $2n - 3$. The Clenshaw-Curtis quadrature scheme also belongs to the family of closed techniques. Instead of locating the abscissas at zeros of Legendre polynomials, the Clenshaw-Curtis scheme requires the abscissas to be zeros of Chebyshev polynomials. Although in theory, it can only exactly integrate polynomials of degree n , in practice, it shows an accuracy which is comparable to Gaussian quadrature [200]. In fact, for a low number of integration points, the error rate decays to the power of $-2n$, which means it converges as fast as Gaussian schemes [216]. Finally, it is worth mentioning that the Clenshaw-Curtis rule also allows adaptive integration by doubling its order.

In fig. 4.3 the abscissas of the aforementioned integration schemes are compared.

4.2.3 Equivalence between Butterworth-weighted averaging and midpoint integration scheme

After having seen how classic quadrature schemes can be used to evaluate integral I_{Γ_r} , it is interesting to analyze the result provided by the use of the midpoint rule performed over a semi-circle and verify that this corresponds to Butterworth-weighted averaging proposed in ch. 3.

The midpoint rule belongs to the family of rectangular rules and exactly integrates linear functions. The integration interval is divided into n panels and the integrand is evaluated at the center point of each panel. Taking into account the semi-circle in fig. 4.1 and dividing it into n equal panels, one can locate the integration points at the following positions,

$$z_k = \omega_0 + \omega_C e^{-i\theta_k}, \quad (4.17)$$

where

$$\theta_k = \frac{\pi}{2n}(1 + 2k) \quad (4.18)$$

and k is an integer ($k \in \mathbb{Z}$), such that $0 \leq k \leq n - 1$. The corresponding weights are equal to $\frac{2}{n}$, namely the length of the k -th panel on the interval

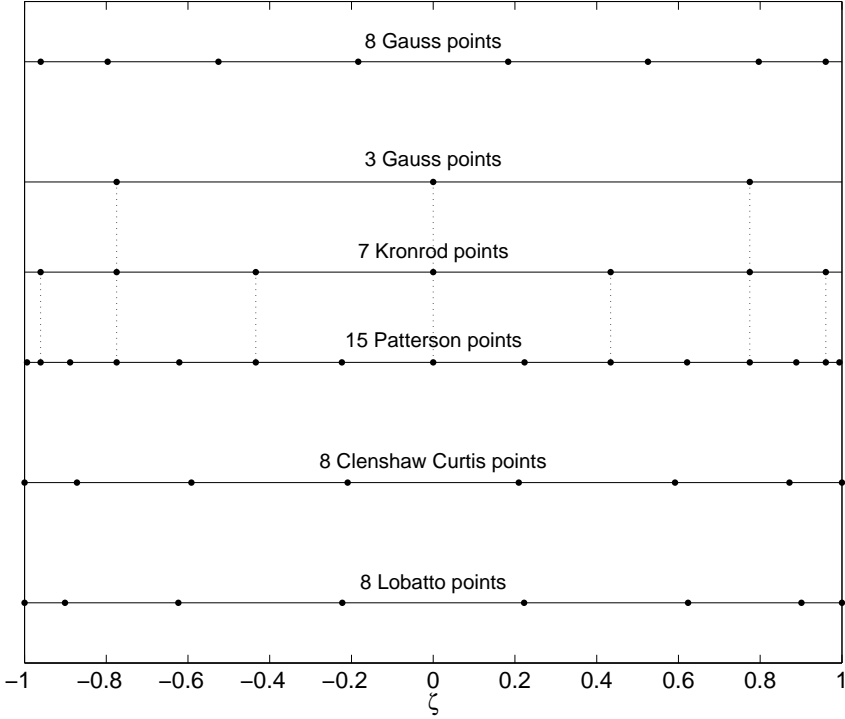


Figure 4.3: Abscissas for different quadrature rules.

$[-1, 1]$. Consequently, if I_{Γ_0} is evaluated by using the midpoint rule over a semi-circle, the integration (4.15) results in

$$I_{\Gamma_0} = \frac{i\pi\omega_C}{n} \sum_{k=0}^{n-1} Y(z_k)e^{-i\theta_k}, \tag{4.19}$$

which is equivalent to eq. (3.27). In other words, evaluating the Butterworth-weighted frequency-averaged input mobility is equivalent to using the midpoint rule over a semi-circle in the complex z plane. In fact, the poles of a Butterworth filter centered at ω_0 and with cut-off frequency ω_C are located over a circle of center ω_0 and radius ω_C . Their positions are equally spaced and exactly correspond to the positions of the integration points of the midpoint rule over the same circle. Finally, the order of the equivalent Butterworth filter is equal to the number of integration points used to integrate I_{Γ_r} .

The evident connection between the Butterworth-weighted averaging procedure

and the integration in the complex plane motivates the following investigation to see whether it is possible to apply the inverse procedure. In other words, from a generic integration scheme performed over a curve in the complex plane, we want to define an equivalent window in the real frequency domain. This will be the topic of the next section.

4.3 Quadrature schemes and weighting functions

So far, the focus has been on the evaluation of the averaged input mobility over the band Γ_0 . This has been accomplished by applying the residue theorem and by equating I_{Γ_0} to the integral carried out over a secondary curve Γ_r , which lies in the complex plane. Numerical quadrature is used to estimate I_{Γ_r} . In sec. 4.2.3, it has been proven that there is an equivalence between using the midpoint quadrature rule in combination with the aforementioned procedure and the evaluation of the Butterworth-weighted averaging. In this section, the inverse procedure is proposed.

The starting point is the average value of a generic function $g(\omega)$ over the band Γ_0 , provided the integration scheme performed over a given Γ_r . After having defined the mathematical features of a generic weighting function, W , its parameters are chosen such that the corresponding W -weighted frequency average of $g(\omega)$, over the whole real frequency axis, equals the average of $g(\omega)$ over the band Γ_0 , which is computed by means of numerical integration over Γ_r . According to the previous cases, this procedure is developed for Γ_r being either a semi-circle or a semi-ellipse.

Although this inverse procedure does not seem to be always possible, it provides further insight into why the accuracy of the band evaluation significantly increases when more accurate integration schemes are used over the path Γ_r .

4.3.1 Determination of weighting function parameters

First of all, the W -weighted integral of the function $g(\omega)$ over the real frequency axis is computed as follows,

$$I_{\Gamma_{0'}} = \int_{\Gamma_{0'}} W(\omega)g(\omega) d\omega. \quad (4.20)$$

To evaluate $I_{\Gamma_{0'}}$ by means of the residue theorem, it is necessary to move to the complex frequency z plane. The path of integration C is chosen to consist of the curve $\Gamma_{0'} = [-R, R]$, which lies on the real frequency axis, and a semi-circle Γ_R lying in the LHP, centered at the origin and of radius R which ensures C

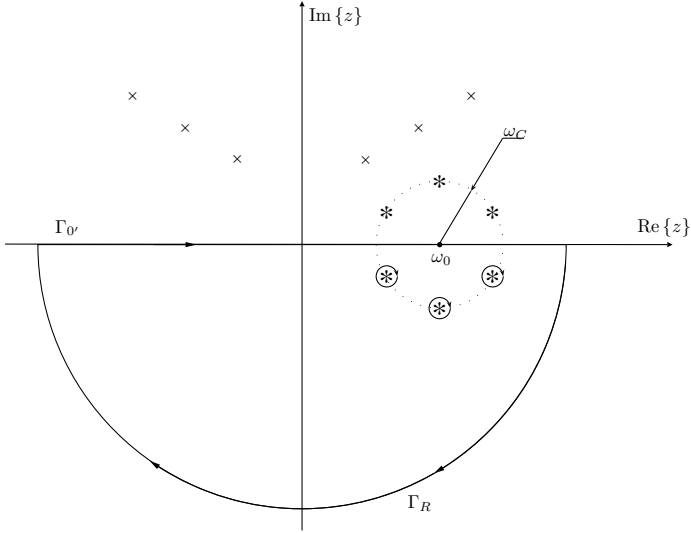


Figure 4.4: Position of system (×) and filter (*) poles over the complex z plane and path of integration.

is closed. The idea is to let $R \rightarrow +\infty$, such that $\Gamma_{0'} \rightarrow \Gamma$, where Γ coincides with the whole real frequency axis.

Regarding the weighting function, $W(z)$, is defined as a rational function of complex variable,

$$W(z) = \sum_{j=1}^{2n} \frac{A_j}{z - z_j}, \tag{4.21}$$

where n is defined as the order of the weighting function and z_j identifies the position of a pole in the complex plane. Suppose that n poles are located in the LHP, while the remaining n are located in the UHP and are defined as the complex conjugates of the former. In order to associate a weighting function on the real frequency axis with an integration scheme performed over a path Γ_r in the complex plane, it is assumed that the poles in the LHP are located at the integration points over Γ_r . Moreover, it is assumed that none of the poles lies on the real frequency axis. An example is illustrated in fig. 4.4, where Γ_r is a semi-circle centered at ω_0 and of radius ω_C . The coefficient A_j associated with a pole in the UHP is taken to be the complex conjugate of the corresponding pole in the LHP. These conditions are imposed to assure the symmetry of the weighting function.

Now the weighting function $W(z)$ can be reformulated as

$$W(z) = \sum_{j=1}^n \left(\frac{A_j}{z - z_j} + \frac{A_j^*}{z - z_j^*} \right). \tag{4.22}$$

The function $g(z)$ is supposed to be analytic in the LHP, which is a reasonable assumption, as it may resemble the transfer function of a causal and stable system. Finally, it is hypothesized that when $|z| \rightarrow \infty$

$$|W(z)g(z)| \rightarrow 0, \tag{4.23}$$

so the integrand function vanishes over the semi-circle I_{Γ_R} as $R \rightarrow \infty$. This hypothesis mainly defines the behavior of $g(z)$, as $W(z)$, by definition, vanishes at infinity. As g resembles the system vibration, it is not supposed to influence the overall vanishing behavior of $|W(z)g(z)|$. If this was the case, the response of a damped system would show an oscillating behavior with amplitude which increases to infinity faster than the vanishing of W , when $|z| \rightarrow \infty$.

The residue of function $W(z)g(z)$ can be evaluated at z_j as

$$\begin{aligned} \text{res} \{W(z_j)g(z_j)\} &= \lim_{z \rightarrow z_j} (z - z_j) \left[\sum_{i=1}^n \left(\frac{A_i}{z - z_i} + \frac{A_i^*}{z - z_i^*} \right) \right] g(z) \tag{4.24} \\ &= \lim_{z \rightarrow z_j} (z - z_j) \left[\sum_{\substack{i=1 \\ i \neq j}}^n \left(\frac{A_i}{z - z_i} + \frac{A_i^*}{z - z_i^*} \right) + \left(\frac{A_j}{z - z_j} + \frac{A_j^*}{z - z_j^*} \right) \right] g(z) \\ &= A_j g(z_j). \end{aligned}$$

As the function $g(z)$ is supposed to be analytic in the LHP, the poles inside the path C are n poles of the weighting function, z_j , and after applying the residue theorem, one obtains

$$I_{\Gamma} + I_{\Gamma_R} = \int_{-\infty}^{+\infty} W(\omega)g(\omega) d\omega = -2\pi i \sum_{j=1}^n g(z_j)A_j. \tag{4.25}$$

Finally, the coefficients A_j have to be determined, such that the integral over Γ provides the same result as $I_{\Gamma_0}(= -I_{\Gamma_r})$, which corresponds to the integral over the band centered at ω_0 and of half-width ω_C . Integral I_{Γ_r} is computed by means of numerical quadrature, as reported for example in eqs. (4.15) and (4.16). The coefficients are readily obtained by equating each of the n terms in (4.25) to the corresponding weighted term in the Riemann sum of the integral over Γ_r and assuming that the function g coincides with the mobility function

Y.

At this stage, a strategy to determine the poles and the coefficients of function (4.22) has been presented. As it will be shown by means of examples, such a procedure allows to represent the features of the weighting function corresponding to the quadrature scheme used to estimate integral I_{Γ_0} . In the following paragraphs, the explicit expressions of $W(\omega)$, for Γ_r being either a semi-circle or a semi-ellipse, are given.

It is worth mentioning that the aforementioned procedure to determine the weighting function which corresponds to an integration scheme is applicable to open integration schemes. For closed schemes, end points are included into the set of integration points and the procedure does not seem to be applicable. In fact, if a pole is located at the end point, its position is purely real over Γ_r , meaning that W would show a singular behavior on the real axis, compromising the shape of the corresponding weighting function. This does not mean that closed rules cannot be used to evaluate integral (4.7).

Poles z_j located over a circle

When Γ_r is a semi-circle, the coefficients A_j can be determined by using eq. (4.15),

$$A_j = -\frac{1}{4}\omega_C e^{-i\theta_j} w_j, \tag{4.26}$$

where w_j and θ_j correspond to the weighting coefficient of the j -th integration point and its angular position on the interval $[0, \pi]$. Finally, the weighting function $W(\omega)$ has the following form,

$$W(\omega) = -\frac{\omega_C}{4} \sum_{j=1}^n w_j \left(\frac{e^{-i\theta_j}}{\omega - z_j} + \frac{e^{i\theta_j}}{\omega - z_j^*} \right). \tag{4.27}$$

By applying the Euler formula and after some calculations, eq. (4.27) can be reformulated as

$$W(x) = \sum_{j=1}^n w'_j \frac{1 - x \cos(\theta_j)}{x^2 - 2x \cos(\theta_j) + 1}, \tag{4.28}$$

where $x = \frac{\omega - \omega_0}{\omega_C}$ and $w'_j = \frac{w_j}{2}$. Expression (4.28) allows one to normalize the position of the filter on the real frequency axis with respect to the center frequency and the width of the band. Moreover, it highlights the fact that $W(x)$ is a real-valued function.

Poles z_j located over an ellipse

In case the poles are located over an ellipse, the coefficients of the weighting function can be determined from eq. (4.16),

$$A_j = -\frac{1}{4} [\omega_B \cos(\theta_j) - i\omega_C \sin(\theta_j)] w_j \quad (4.29)$$

and the weighting function,

$$W(\omega) = -\frac{1}{4} \sum_{j=1}^n w_j \left[\frac{\omega_B \cos(\theta_j) - i\omega_C \sin(\theta_j)}{\omega - z_j} + \frac{\omega_B \cos(\theta_j) + i\omega_C \sin(\theta_j)}{\omega - z_j^*} \right]. \quad (4.30)$$

Also in this case, after some calculations, eq. (4.30) can be reformulated as

$$W(x) = \sum_{j=1}^n a w'_j \frac{1 - x \cos(\theta_j)}{x^2 - 2x \cos(\theta_j) + \cos^2(\theta_j) + a^2 \sin^2(\theta_j)}, \quad (4.31)$$

where again $x = \frac{\omega - \omega_0}{\omega_C}$ and $w'_j = \frac{w_j}{2}$.

4.3.2 Examples and discussion

Equations (4.27) and (4.30) provide general expressions that associate an integration scheme, performed over Γ_r , with a weighting function over Γ .

Now the features of the weighting functions obtained by means of the aforementioned procedure are illustrated.

Figure 4.5 compares different weighting functions obtained by means of the aforementioned strategy. Four different types of weighting functions are compared to the ideal rectangular window. In particular, the midpoint and Gaussian integration rules are used over a circle; the former resulting in the square magnitude of a Butterworth filter. Gaussian quadrature is also used over two different ellipses, with $a = 2$ and $a = 0.5$, respectively. The obtained weighting functions are shown for different numbers of integration points, namely 6, 8 and 10, and their positions over circles and ellipses are illustrated as well.

Results show that the weighting function described by using Gaussian quadrature better resembles a rectangular window with respect to the Butterworth filter. Moreover, as the number of integration points increases, the Gauss-based weighting functions tend to the rectangular window much quicker than the Butterworth one. This can be seen as a consequence of the higher precision of Gaussian quadrature with respect to the midpoint rule. On the other hand, the Gauss-based weighting functions assume negative values just

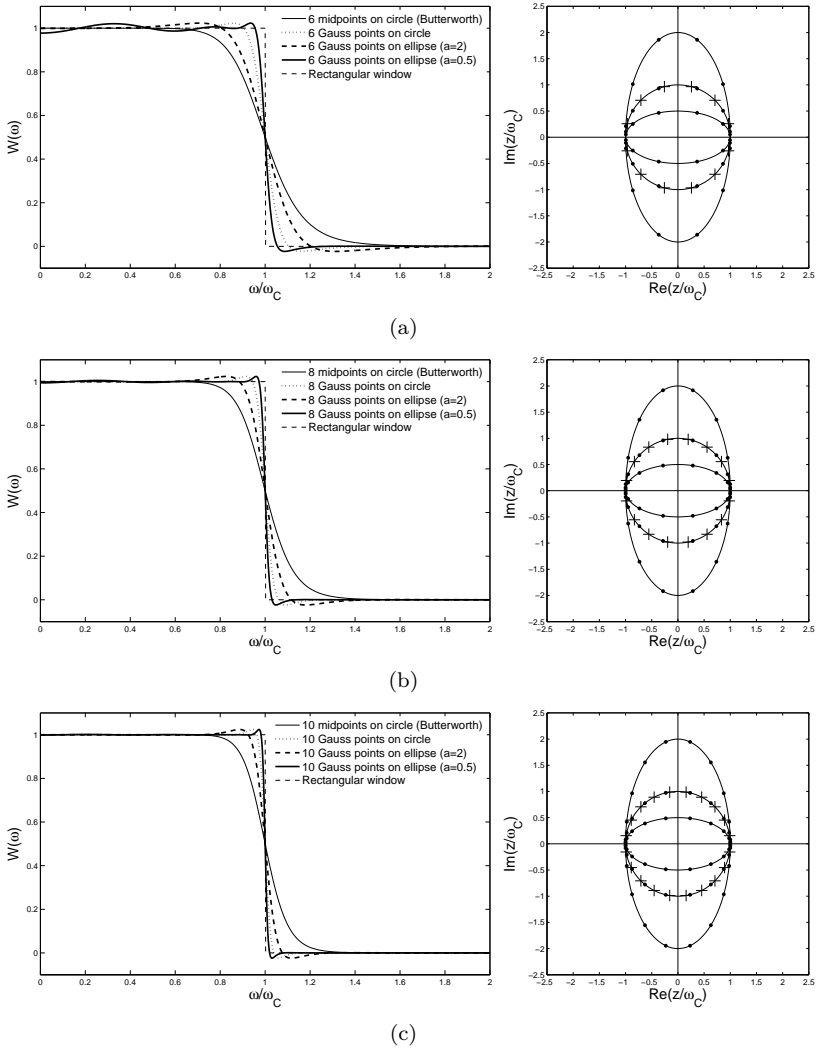


Figure 4.5: On the left, comparison between the rectangular window and weighting functions obtained by using midpoint rule over a semi-circle, Gaussian rule over a semi-circle, Gaussian rule over a semi-ellipse with $a = 2$ and with $a = 0.5$. On the right, Gaussian integration points (\bullet) over a circle, ellipse with $a = 2$ and $a = 0.5$ and midpoint rule integration points over a circle (\times). Figures (a), (b) and (c) refer to 6, 8, and 10 integration points, respectively.

above the cut-off frequency and show one or more overshoots within the band of interest. Results also show that using an ellipse with major axis located over the real frequency axis has a sharper cut-off behavior, but also more pronounced ripples, as the number of integration points decreases.

The result of the aforementioned procedure is not explored in detail here. Future research will focus on possible extensions of these concepts and on the proposed connection between weighting functions and integration schemes.

4.4 Application cases

In this section, three aspects of the proposed numerical strategy are investigated for the application cases presented in ch. 3, consisting of a simply supported plate and two plates stiffened by a beam. In sec. 4.4.1, the accuracy achieved by using the midpoint integration scheme over a circle (equivalent to Butterworth-weighted frequency averaging) is compared to Gaussian quadrature applied over both circles and ellipses. In sec. 4.4.2, the performance of Kronrod and Patterson adaptive schemes is presented. Finally, in sec. 4.4.3, the accuracy of two alternative integration rules, namely Lobatto and Clenshaw-Curtis schemes, is assessed.

It is important to underline that the ability of the proposed approach is strictly related to the oscillatory behavior of the integrand function, which is not known *a priori* and is to be considered uncorrelated from the engineering complexity of the analyzed case. The following examples represent, in this sense, a valid benchmark. In fact, the bare plate presents a number of modes which increases with wider one-third octave bands, meaning that the function becomes more and more oscillatory over the frequency bands of interests. On the other hand, when a stiffener is added, the behavior of the input mobility becomes more oscillatory at the beam resonances. This is closer to what happens when components with different modal densities are assembled together.

In order to quantify the accuracy of the approach, the relative error, ϵ_{rel} , is defined as

$$\epsilon_{\text{rel}}\{\bullet\} = \frac{\left| \langle \bullet \rangle_{\Delta\omega}^{(\text{ref})} - \langle \bullet \rangle_{\Delta\omega}^{(\text{approx})} \right|}{\left| \langle \bullet \rangle_{\Delta\omega}^{(\text{ref})} \right|}, \quad (4.32)$$

where $\langle \bullet \rangle_{\Delta\omega}^{(\text{ref})}$ and $\langle \bullet \rangle_{\Delta\omega}^{(\text{approx})}$ indicate the reference value and its approximation, respectively. The quantity \bullet can be either complex input power or complex input mobility, as in both cases it leads to the same relative error. However, the following narrow band plots refer to the input mobility, as it is the integrand function in previous integrals.

Three types of integration paths are benchmarked in the next sections: semi-circle, semi-ellipse with $a = 2$ and semi-ellipse with $a = 0.5$. Midpoint rule is used only over the circular path as it corresponds to the Butterworth-weighted integration scheme used in ch. 3. On the other hand, the Gaussian quadrature is performed over all types of paths by means of 6, 8 and 10 integration points. In order to show the advantages of performing adaptive integration, the Kronrod and Patterson rules are also applied in the sequence G3-K7-P15. The reference solution in all cases is evaluated by integrating over a semi-circle by means of a very refined Gaussian scheme consisting of 200 points. The computation times are not discussed in this chapter, as they lead to conclusions similar to what is presented in ch. 3. It is worth remarking the fact that the present approach requires the system of equations to be solved as many times as the number of the integration points. This is, in general, independent of the bandwidth. On the other hand, classic integration rules performed over the real axis require a number of sampling points which increases with the bandwidth and so does the computation time.

4.4.1 Use of Gaussian quadratures over Γ_r and comparison with Butterworth-weighted averaging

Simply supported plate

The parameters related to this application case are described in sec. 3.6.1. The complex input mobility into the plate is shown in fig. 4.6. The frequency range of analysis sweeps 23 one-third octave bands (from 22 Hz to 4467 Hz). The narrow band input power is compared with the averages over the aforementioned bands.

In figs. 4.7 and 4.8, the relative errors on the real and imaginary input mobility are shown, respectively. In general, when performed over the same circle, Gaussian quadrature performs better than the midpoint rule and, consequently, it better approximates the band-average value with respect to the Butterworth filter. It can be noted that the imaginary value over the band centered at 1600 Hz is largely overestimated for a low number of integration points. This may be explained by investigating the behavior of the integrand functions over the integration path. In fig. 4.9, the real and imaginary input mobility is plotted as a narrow band response function over different paths. The solid line in the left figures represents the mobility as function of real frequency. The other lines on the right represent the mobility evaluated over Γ_r , which is a function of the variable $\theta = [0, \pi]$. The bands under consideration are the 9th (centered at 160 Hz) and the 19th (centered at 1600 Hz). As expected, the real part is always

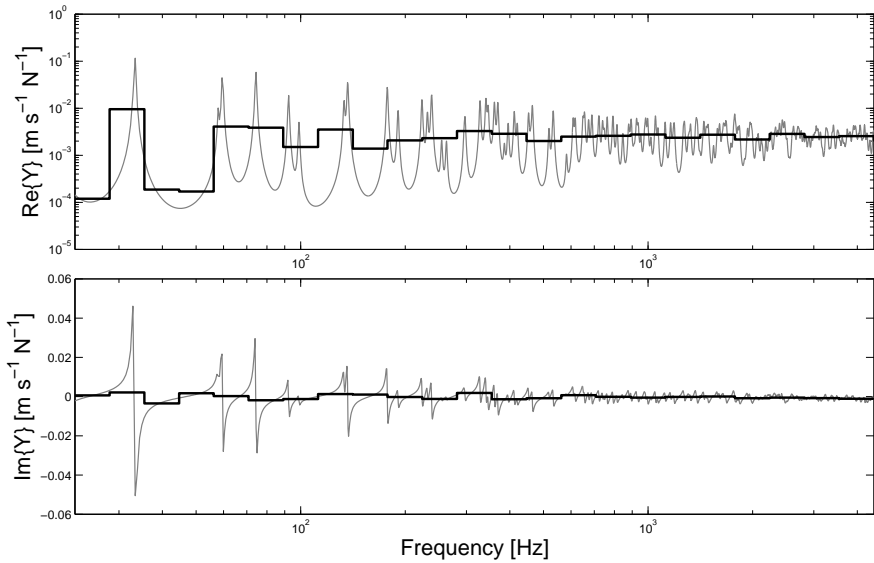


Figure 4.6: Comparison between narrow band and band-averaged input mobility for the simply supported plate of sec. 4.4.1.

positive while the imaginary part assumes both positive and negative values. Observing fig. 4.9(b), it is clear that the input mobility is a highly oscillatory function over the real frequency band of interest. On the other hand, it is possible to appreciate that the integrand function becomes much smoother when evaluated over paths located in the complex plane. In fact, when Γ_r is either a semi-circle or a semi-ellipse, it does not present any pronounced oscillation. Further insight can be gained by observing fig. 4.10, where the real and imaginary parts of input mobility are represented over the complex frequency plane. The peaks of the function correspond to the resonance frequencies of the plate, which are located in correspondence of the poles of the mobility. Since damping mechanism is present, their positions have both a real and (positive) imaginary part. However, when moving towards larger negative imaginary frequencies, the mobility shows a very smooth behavior. When integrating over paths in the complex plane, the integrand function is evaluated on contours taken over such a smooth surface, which inherently lends itself to an easier integration through classic quadrature rules. Moreover, since no poles are present in the LHP, the calculation of the residues is not necessary to estimate the frequency integral. These observation explain why a highly accuracy can be achieved by just using a few integration points. However, particular care has to be taken when sampling the regions close to the endpoints

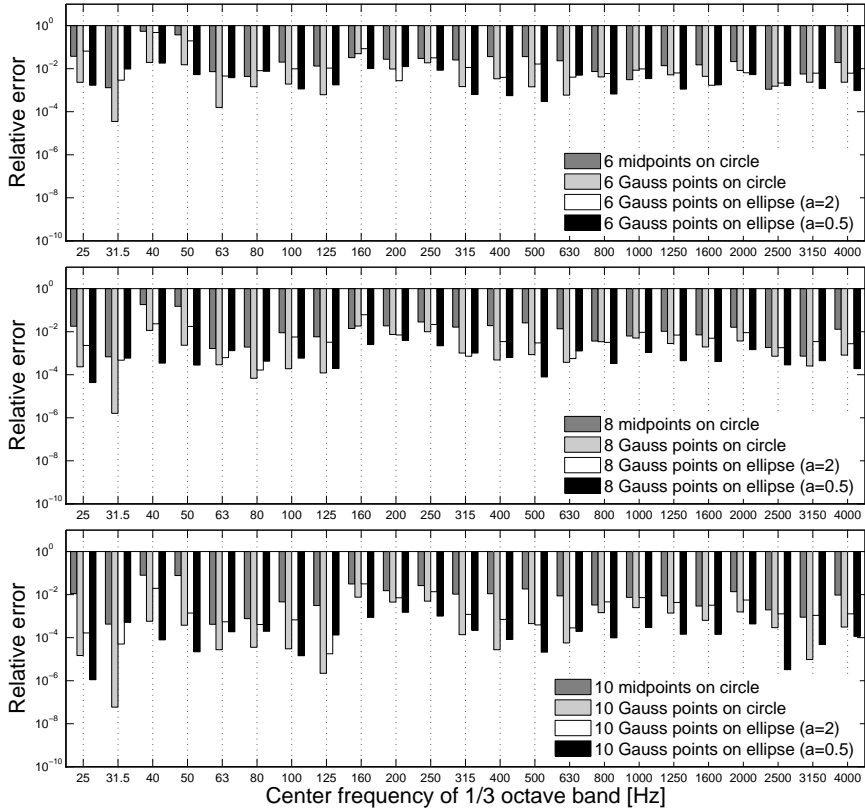


Figure 4.7: Error related to the real band-averaged input mobility of the simply supported plate for 6 (top), 8 (center) and 10 (bottom) integration points taken over either a semi-circle or a semi-ellipse.

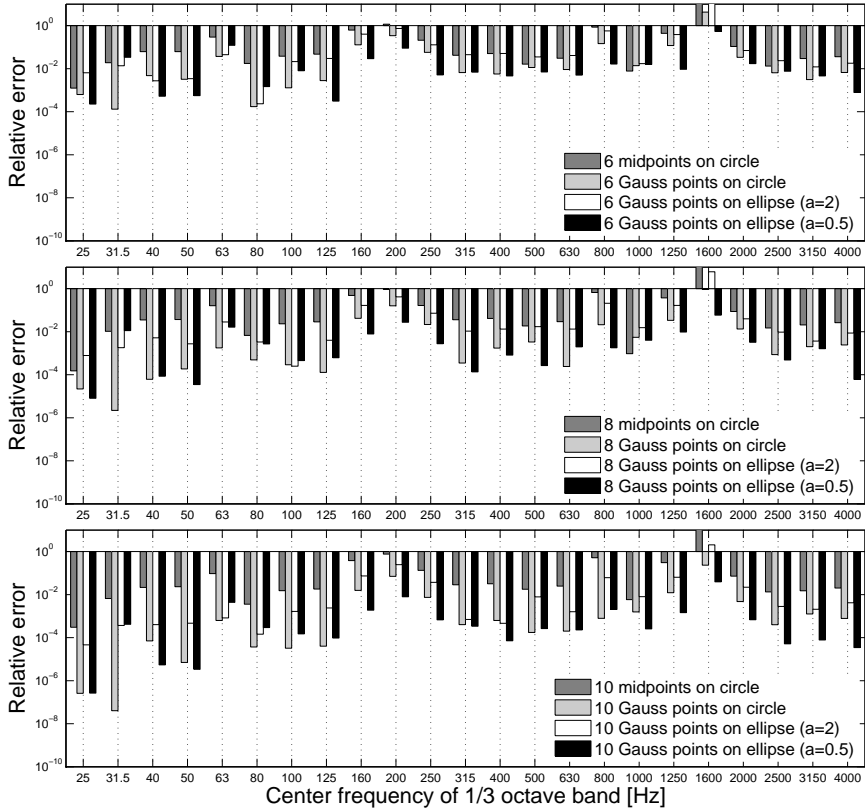
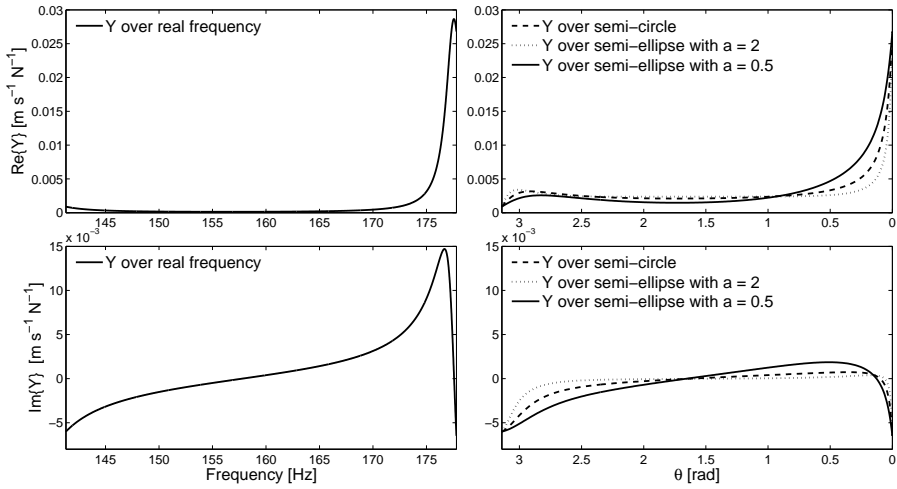
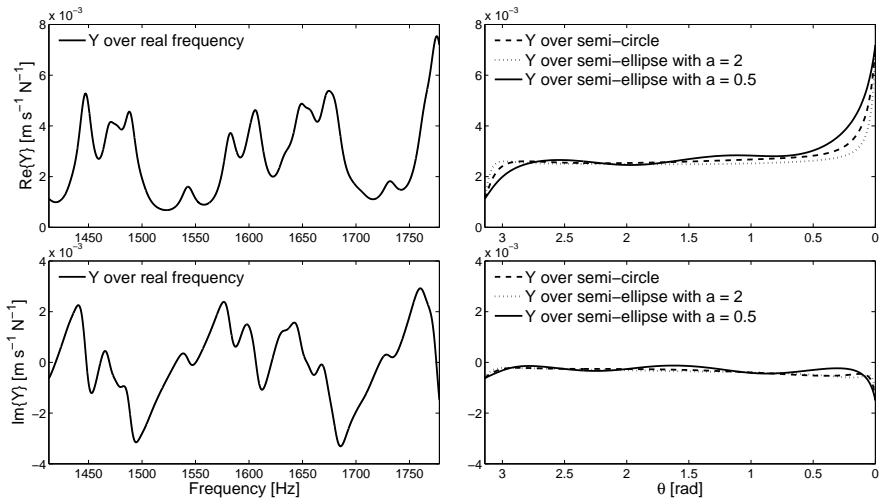


Figure 4.8: Error related to the imaginary band-averaged input mobility of the simply supported plate for 6 (top), 8 (center) and 10 (bottom) integration points taken over either a semi-circle or a semi-ellipse.

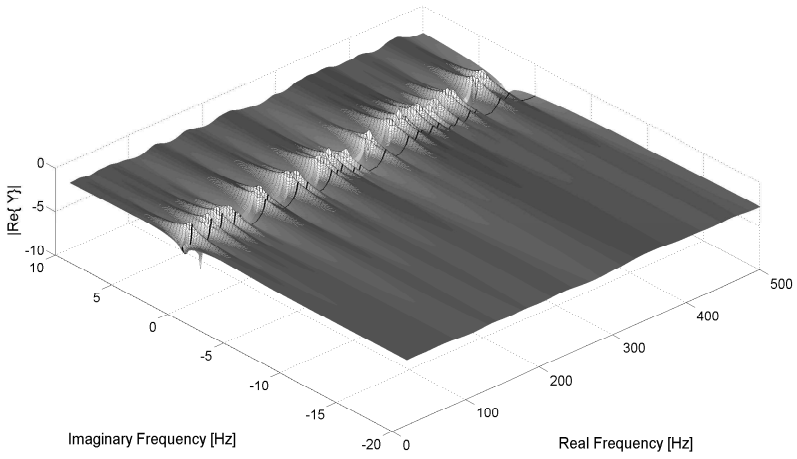


(a)

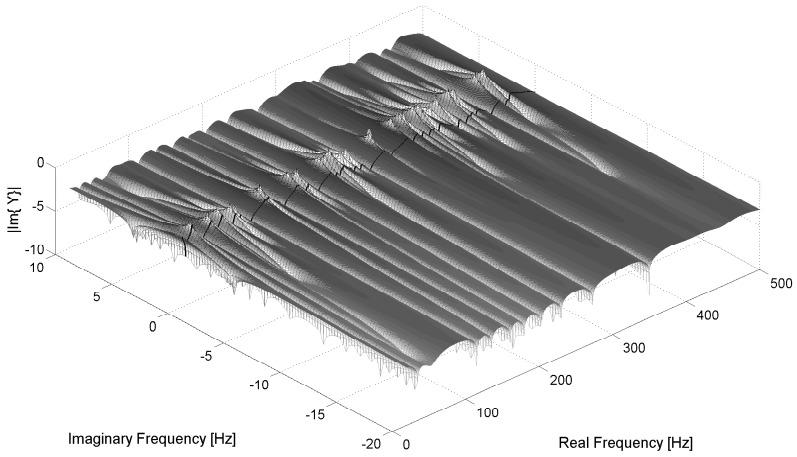


(b)

Figure 4.9: Real and imaginary part of the the mobility function evaluated over the real axis (left), semi-circle, semi-ellipse with $a = 0.5$ and with $a = 2$ (right). Figure (a) refers to the 9th and (b) to the 19th third octave band. Note the right figures are function of θ .



(a)



(b)

Figure 4.10: Real and imaginary parts of the input mobility over the complex frequency plane. The black solid line indicates the function over the real frequency axis.

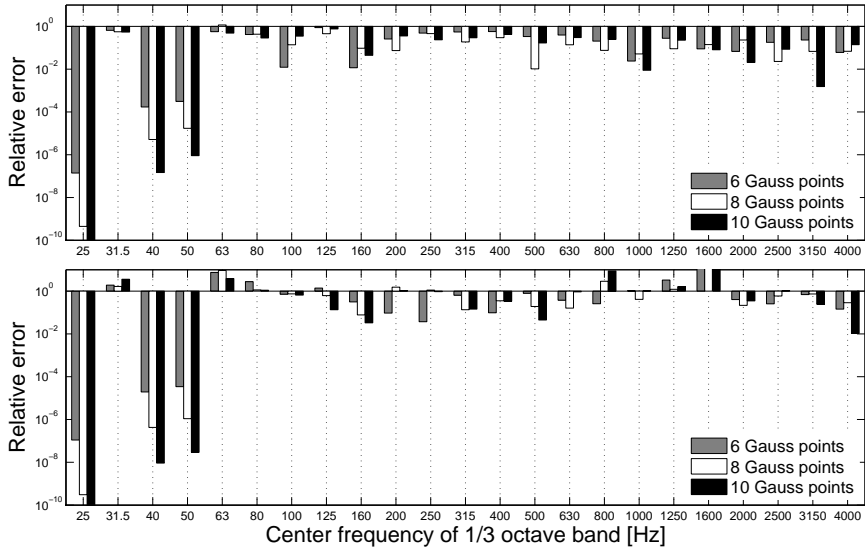


Figure 4.11: Error related to the real (top) and imaginary (bottom) band-averaged input mobility of the simply supported plate for 6, 8 and 10 Gauss integration points taken over the real frequency band.

of the integration path, where the integrand can show abrupt increases or decreases. This is probably what causes inaccurate integration when only a few integration points are used. In fact, as the number of integration points increases, over the 1600 Hz band, the accuracy improves as well. In this regard, it is important to notice that when Γ_r is an ellipse with $a = 0.5$ the integrand has less abrupt variation close to the endpoints, although the function presents some small oscillations inside the frequency band of integration, which are also expected when moving Γ_r closer to the real frequency axis. This explains why the integration over the ellipse with $a = 0.5$ provides more consistency to the results in all the benchmark cases presented in this article. Due to abrupt variations, results are less accurate if Γ_r is predominantly extended in the direction perpendicular to the real frequency axis. Data related to the integration over a semi-ellipse with $a = 2$, are an example. Furthermore, from more extensive investigations, which are not reported here, it has been observed that using larger values of a worsens the accuracy of the integration. In general, the choice of the a parameter is user-dependent and its optimization may be difficult, if not impossible. On the other hand, using a semi-circle eliminates this degree of freedom and yet provides good accuracy, although setting $a = 0.5$ seems to perform well in all analyzed cases.

The performance of Gaussian schemes over different paths is also confirmed by the shape of the weighting functions in fig. 4.5. When Γ_r is a semi-ellipse with $a = 0.5$, the shape of the weighting function is closer to an ideal rectangular window and it gives larger weight to the zones closer to the endpoints. When Γ_r is either a semi-circle or a semi-ellipse with $a = 2$, the weighting function is still closer to a rectangular window than a Butterworth filter.

Figure 4.11 allows assessing the accuracy of the proposed approach against Gaussian quadrature performed over the real axis. When the behavior of the integrand is not oscillatory, integrating over the real frequency axis provides more accurate results. This can be observed by comparing how the mobility oscillates over the first, third and fourth band in fig. 4.6 with corresponding relative error in fig. 4.11. However, when this is not the case, moving to the complex plane guarantees a significant improvement in terms of accuracy.

Stiffened plates

The structure under consideration in the next example was described in sec. 3.6.2. As it can be seen in fig. 4.12, the input mobility is characterized by peaks at the stiffener resonances. Similarly to the previous case, the response

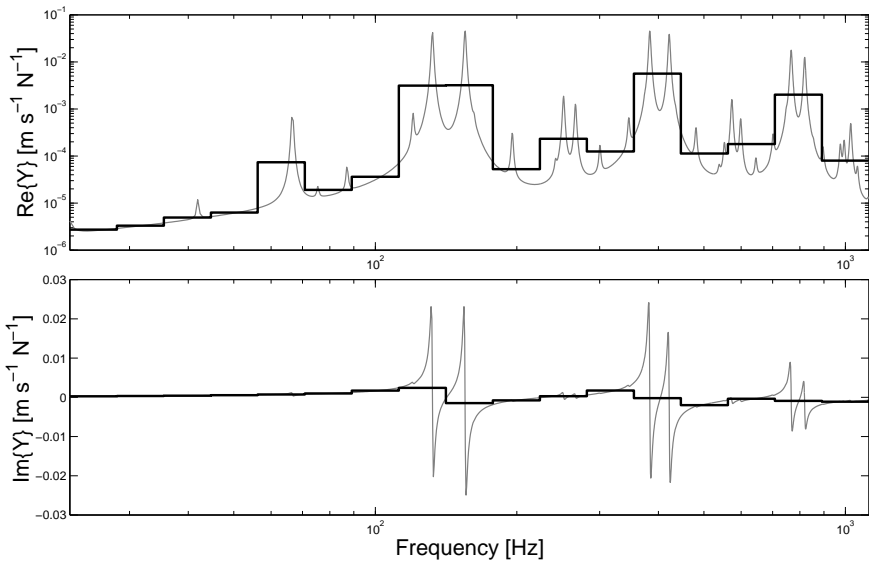


Figure 4.12: Comparison between narrow band and band-averaged input mobility for the stiffened plates of sec. 4.4.1.

has been averaged over 17 one-third octave bands (starting from 22.4 Hz to 1122 Hz). In figs. 4.13 and 4.14, the errors on the real and imaginary part of the band-averaged input mobility are shown. Results confirm what was observed in the previous case. Again, Gaussian quadrature shows a better performance with respect to the midpoint rule, and integrating over a semi-ellipse with $a = 0.5$ provides accurate results which are consistent for all cases.

In general, the accuracy of the integration is higher than what was obtained in sec. 4.4.1. This may be explained by considering the behavior of the integrand function. The simply supported plate presents a higher modal density and thus, a higher oscillatory behavior. On the other hand, the stiffened plate presented here has a less oscillatory behavior and this may facilitate the integration procedure. However, this does not reduce the relevance of this application case. In fact, the input mobility into a stiffened structure is highly influenced by the behavior of the stiffener. As it can be observed in fig. 4.12, higher peaks are located at the beam wavenumbers and this makes the integrand function more oscillatory at the corresponding bands. Nevertheless, this does not seem to affect the accuracy of the integration.

Similarly to what illustrated in the previous section, in fig. 4.15 the behavior of the mobility function is compared when the frequency of analysis is either real or complex. The response is evaluated at the corresponding 8th and 16th third octave bands. The left-hand side figures illustrate the behavior of the mobility over the interval of real frequencies. The plots on the right-hand side show the mobility as a function of θ , in which semi-circles and semi-ellipses in the complex plane are parametrized. Although in figs. 4.15(a) and 4.15(b) the integrands are less oscillatory than for the bare simply supported plate, they preserve a smooth behavior when moving to the complex frequency plane. This explains the higher accuracy achievable by using a smaller number of integration points. Additionally, while the behavior of the mobility over the real axis is strictly dependent on the interval of analysis, in the complex plane this relation seems to be less strict. This may indicate a small dependence between the frequency interval of integration and the behavior of the mobility in the complex plane. Nevertheless, as also indicated in the previous section and confirmed in the next chapter, the oscillatory behavior can be highly influenced by the path chosen in the complex plane. As the path moves closer to the real frequency axis (i.e. semi-ellipse with $a = 0.5$), some oscillations may appear in the central region of the θ interval. On the other hand, when the path of integration presents branches that move almost perpendicularly to the real frequency axis (i.e. semi-ellipse with $a = 2$), prominent oscillatory behavior can be present at the endpoints of the interval.

Finally, in fig. 4.16, the relative error corresponding to the use of Gaussian quadrature over the real frequency axis is shown. Also in this case, when the integrand is not oscillatory, the accuracy is very high. Nevertheless, even

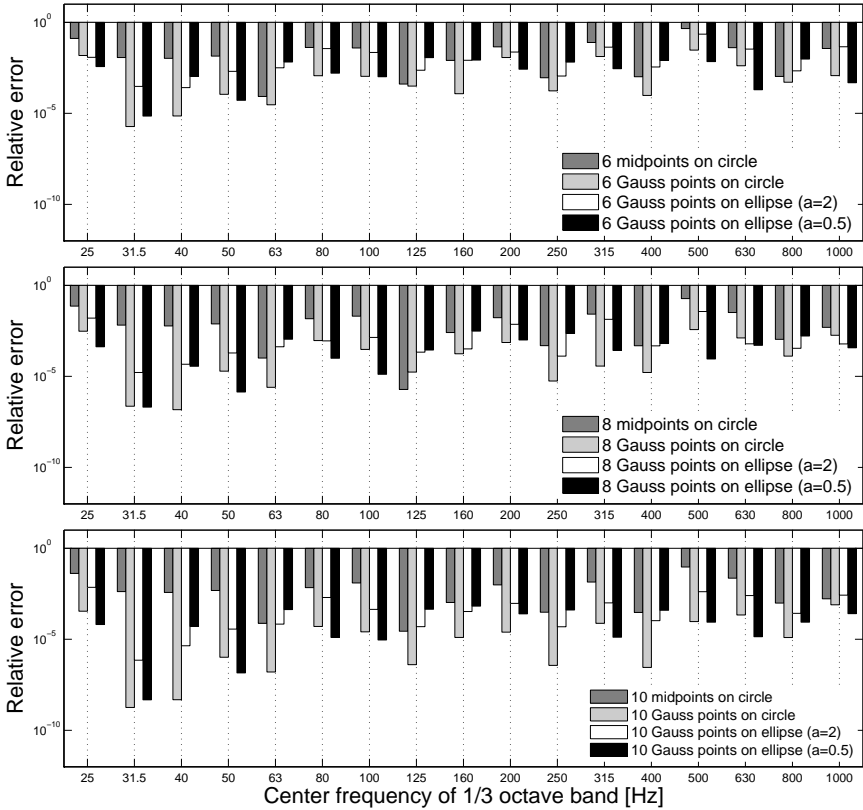


Figure 4.13: Error related to the real band-averaged input mobility of the stiffened plates for 6 (top), 8 (center) and 10 (bottom) integration points taken over either a semi-circle or a semi-ellipse.

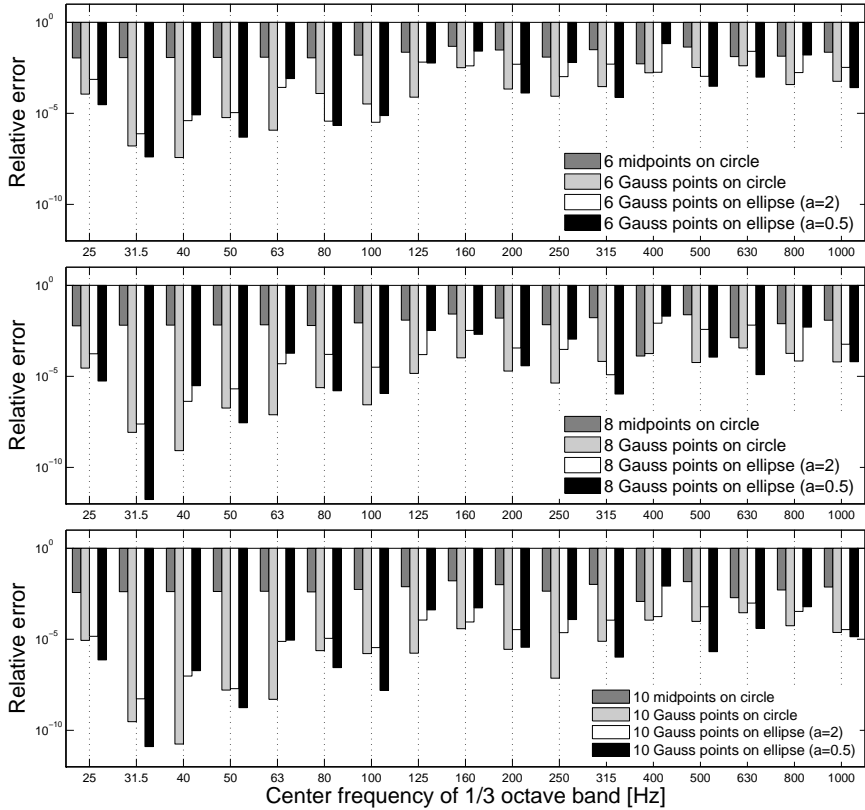
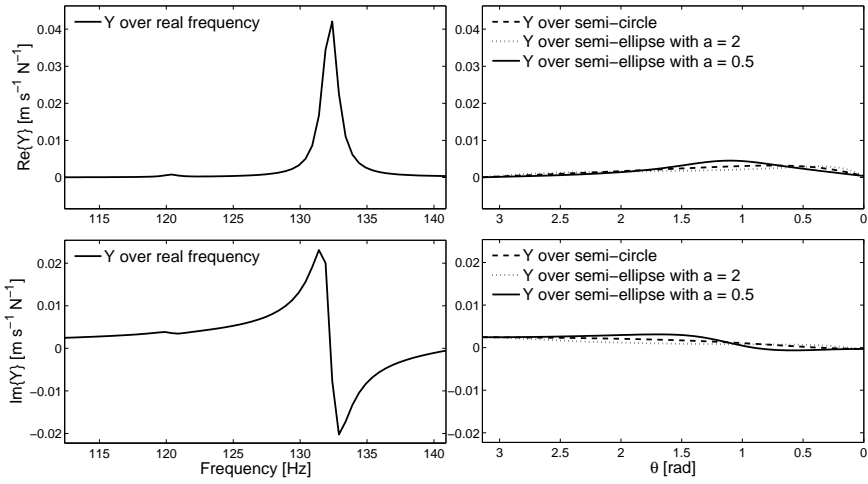
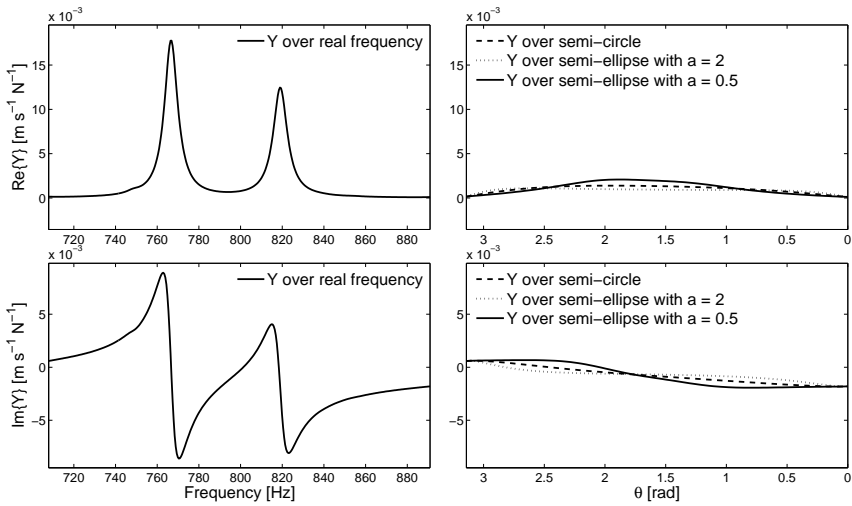


Figure 4.14: Error related to the imaginary band-averaged input mobility of the stiffened plates for 6 (top), 8 (center) and 10 (bottom) integration points taken over either a semi-circle or a semi-ellipse.



(a)



(b)

Figure 4.15: Real and imaginary part of the the mobility function evaluated over the real axis (left), semi-circle, semi-ellipse with $a = 0.5$ and with $a = 2$ (right). Figure (a) refers to the 8th and (b) to the 16th third octave bands. Note the right figures are function of θ .

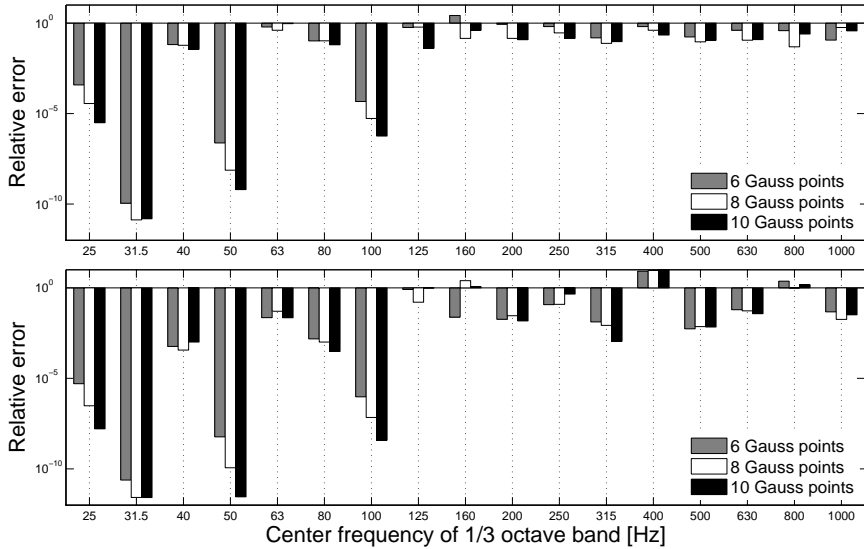


Figure 4.16: Error related to the real (top) and imaginary (bottom) band-averaged input mobility of the stiffened plates for 6, 8 and 10 Gauss integration points taken over the real frequency band.

when this condition is not satisfied, using the residue theorem provides more accurate results. This can be seen by comparing the behavior of the first seven bands in fig. 4.12 to the corresponding relative error in fig. 4.16. When the input mobility presents a peak, the accuracy of Gaussian quadrature drops if performed over the real frequency axis.

4.4.2 Adaptive integration schemes

In this section, the effectiveness of adaptive integration is investigated. In the series of figs. 4.17 to 4.20, the Patterson adaptive scheme is applied in the sequence G3-K7-P15 for the aforementioned application cases. Results show an increasing convergence towards the reference value as the order of the quadrature increases. If the convergence reached after 15 Patterson evaluations is not satisfactory, one might perform a successive refinement by using 31 Patterson points (or P63, P127, P255 if necessary). Note that when performing the G3 sequence the accuracy might not be very high, due to the low number of integration points.

When considering an adaptive scheme, one should always take into account

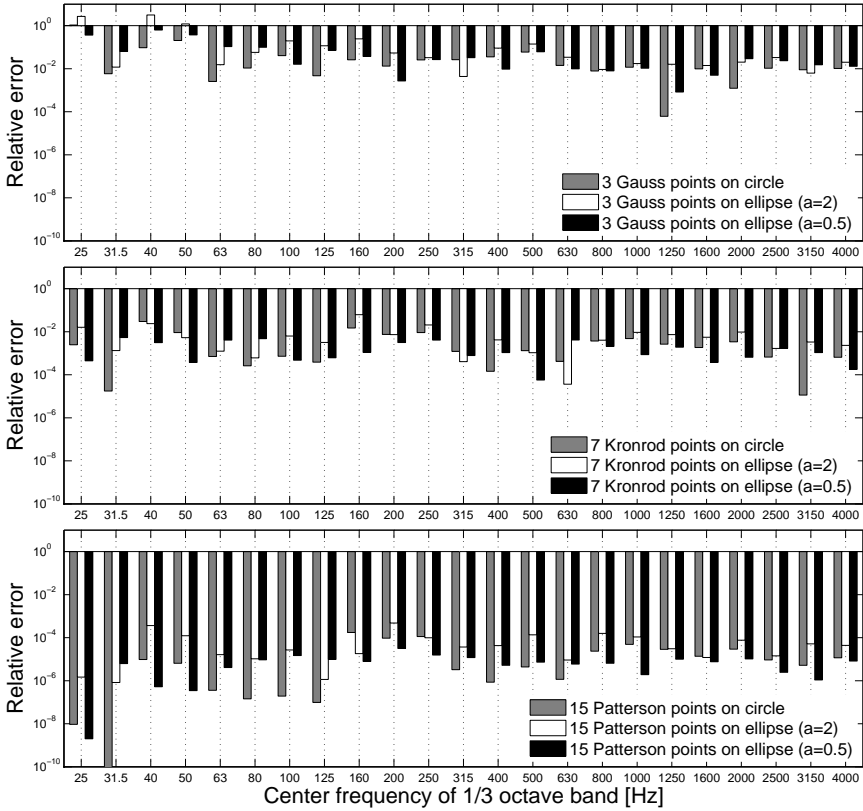


Figure 4.17: Error related to the real band-averaged input mobility of the simply supported plate evaluated by using adaptive integration schemes: 3 Gauss points (top), 7 Kronrod points (center) and 15 Patterson points (bottom).

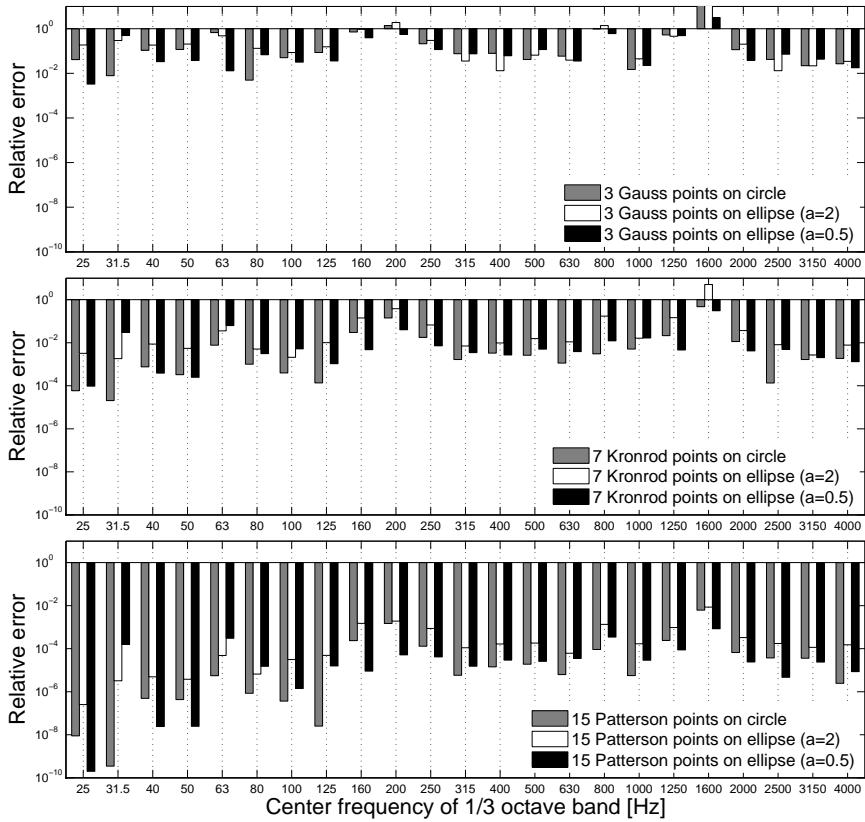


Figure 4.18: Error related to the imaginary band-averaged input mobility of the simply supported plate evaluated by using adaptive integration schemes: 3 Gauss points (top), 7 Kronrod points (center) and 15 Patterson points (bottom).

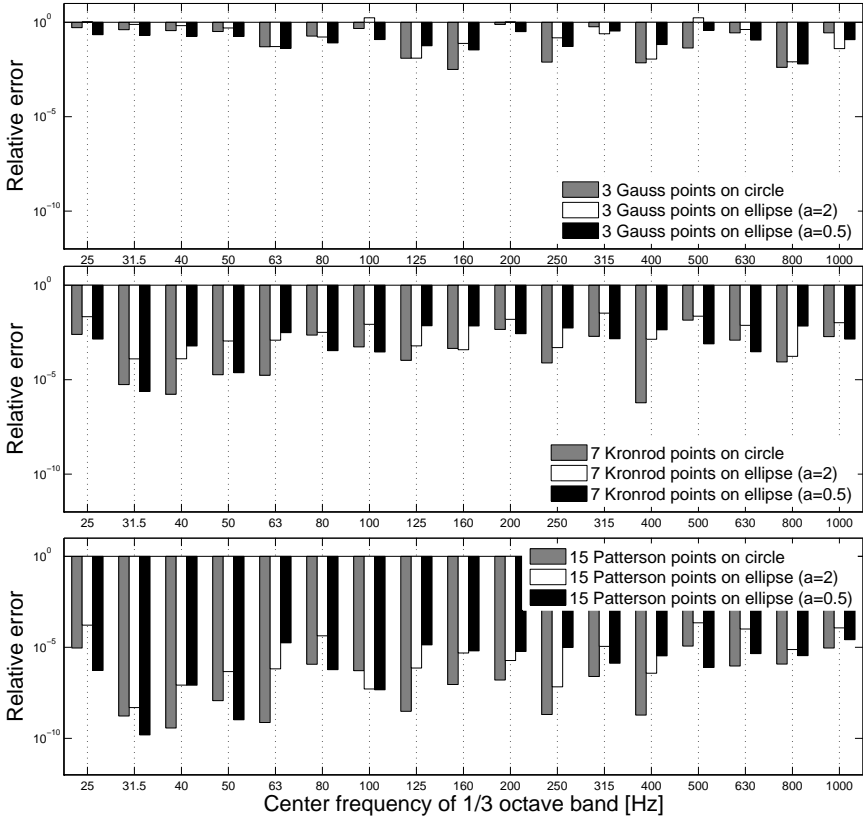


Figure 4.19: Error related to the real band-averaged input mobility of the stiffened plates evaluated by using adaptive integration schemes: 3 Gauss points (top), 7 Kronrod points (center) and 15 Patterson points (bottom).

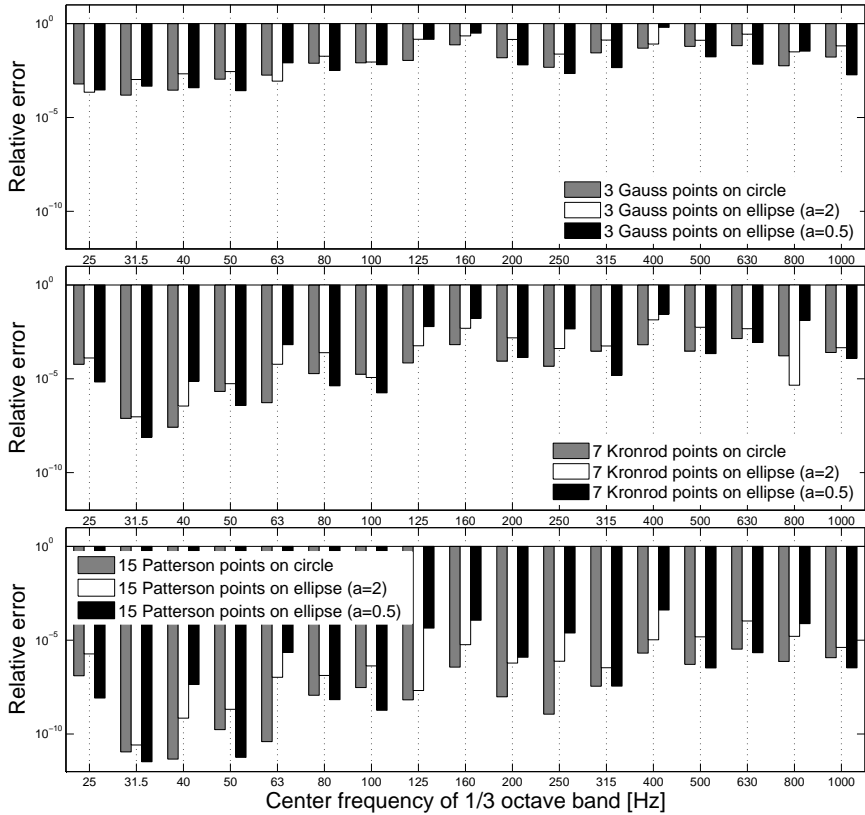


Figure 4.20: Error related to the imaginary band-averaged input mobility of the stiffened plates evaluated by using adaptive integration schemes: 3 Gauss points (top), 7 Kronrod points (center) and 15 Patterson points (bottom).

the fact that the information related to the convergence is paid at the cost of a lower accuracy, as Kronrod and Patterson rules have worse convergence rates than the Gaussian quadrature. This can be observed by comparing the accuracy provided by 10 Gauss points, which is already satisfactory, to the one obtained by using 15 Patterson points. The gain in accuracy for the P15 scheme may not justify the computational cost of 5 additional calculations for each frequency band, unless one is interested in the convergence rate.

It is worth mentioning that also the midpoint rule can be used adaptively and so does the Butterworth-weighted averaging. Nevertheless, its use is very disadvantageous for this application. In fact, besides the poor convergence rate, the number of points to refine the integration is very large. For example one sequence is M3-M9-M27-M81. Using a trapezoidal rule rather than the midpoint would lead to a sequence growing with a factor of two in each step, although its accuracy would not be very high. On the other hand, using an adaptive Clenshaw-Curtis rule might provide very precise estimates and a sequence which doubles the number of points at each step. This is considered a valid alternative to the Gauss-Kronrod-Patterson, but it is not reported in this manuscript.

4.4.3 Alternative integration schemes

As a final investigation, the Lobatto and Clenshaw-Curtis quadrature rules are shortly benchmarked in this section. Figures 4.21 to 4.24 show their performances when 8 integration points are used for the aforementioned cases. Although they both provide more accurate results than the midpoint rule over a semi-circle, they approximately have the same precision and, in general, are slightly less accurate than Gaussian quadrature.

4.5 Conclusion

In ch. 3, the residue theorem has been proposed to efficiently evaluate frequency-averaged input power. The possibility of extending that result motivated the research described in this chapter. Instead of computing the integral by using quadrature rules over the real frequency axis, the integration path is deformed and moved to the complex plane. This assures the integrand to be smoother and permits an accurate integration by using classic quadrature techniques with reduced number of sampling points.

This procedure is readily linked to the one proposed in ch. 3, where a Butterworth filter has been used as a weighting function. In fact, in this chapter it is proven that evaluating the Butterworth-weighted frequency average

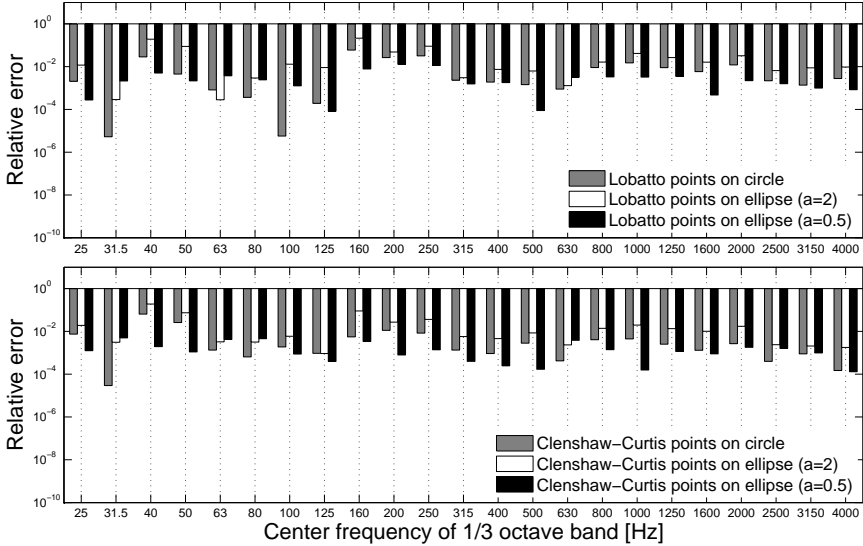


Figure 4.21: Error related to the real band-averaged input mobility of the simply supported plate evaluated by using Lobatto (top) and Clenshaw-Curtis (bottom) quadrature with 8 points.

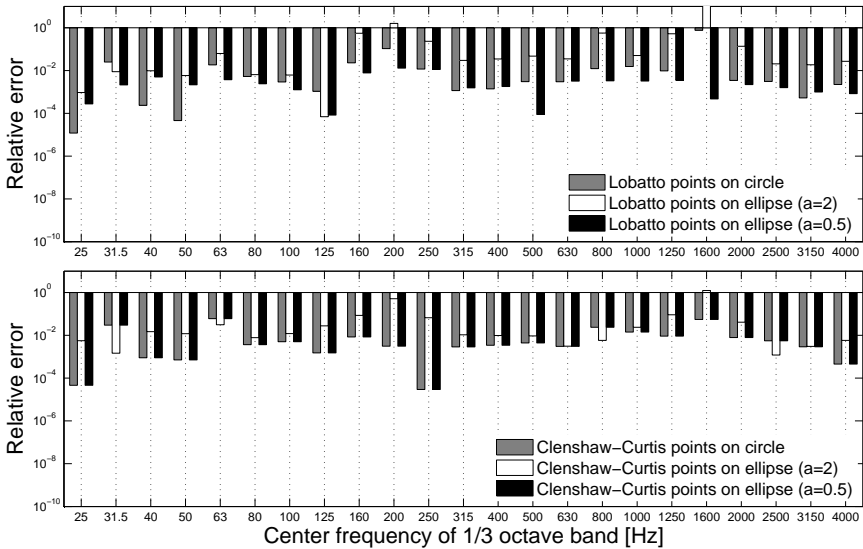


Figure 4.22: Error related to the imaginary band-averaged input mobility of the simply supported plate evaluated by using Lobatto (top) and Clenshaw-Curtis (bottom) quadrature with 8 points.

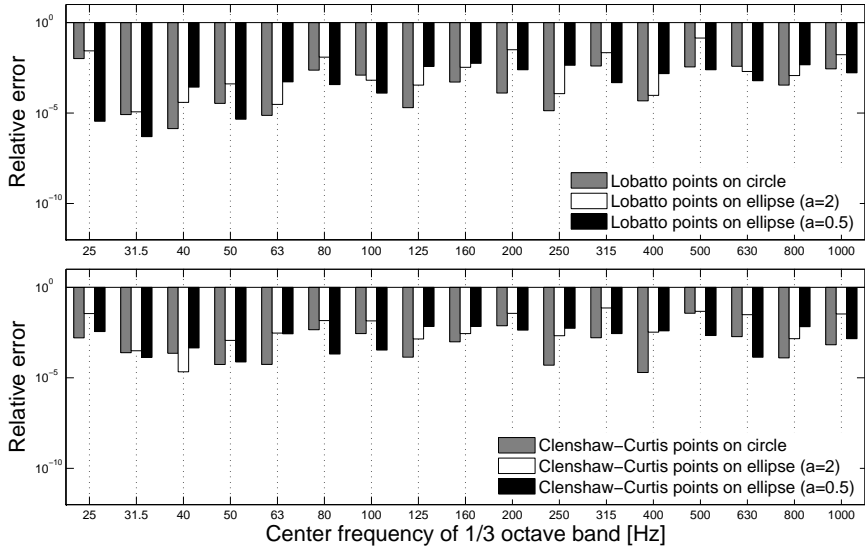


Figure 4.23: Error related to the real band-averaged input mobility of the stiffened plates evaluated by using Lobatto (top) and Clenshaw-Curtis (bottom) quadrature with 8 points.

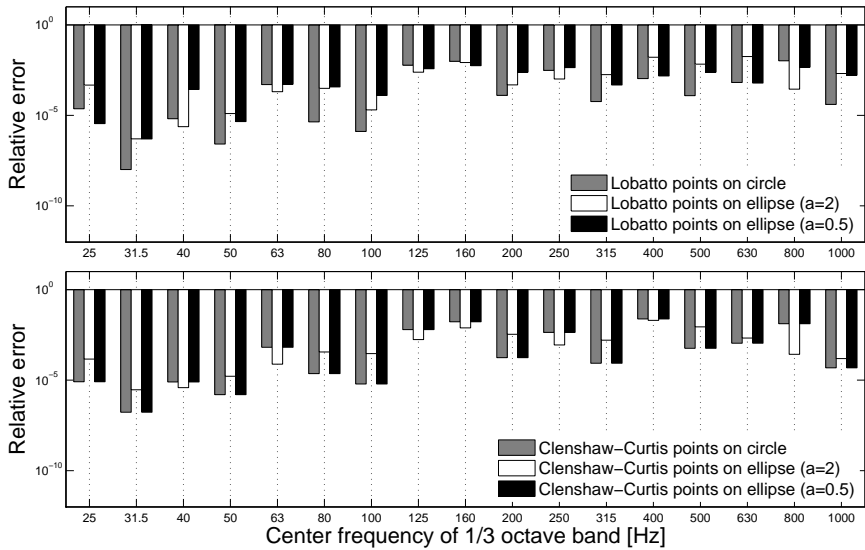


Figure 4.24: Error related to the imaginary band-averaged input mobility of the stiffened plates evaluated by using Lobatto (top) and Clenshaw-Curtis (bottom) quadrature with 8 points.

corresponds to using the midpoint rule over a semi-circle in the complex plane. Moreover, also the inverse procedure is formulated, namely, for a given open quadrature rule in the complex plane, it is possible to express a frequency weighting function over the real frequency axis.

In order to benchmark the improvements, two application cases are proposed. For both cases, Gaussian, Clenshaw-Curtis and Lobatto quadrature rules are performed over semi-circles and semi-ellipses, used as integration paths in the complex plane. Results show a very high accuracy at a computational cost which is reduced with respect to the results shown in ch. 3. In order to perform adaptive quadrature, the Gauss-Kronrod-Patterson rule is presented, which allows convergence evaluation.

With the present advances, the proposed strategy provides an even more efficient tool to evaluate frequency-averaged input mobility. Moreover, the ease of implementation allows to straightforwardly use it in combination with deterministic methodologies for fast and accurate calculations.

Chapter 5

Application to second-order dynamic systems of industrial complexity

In the previous chapters, the residue theorem has been employed to efficiently evaluate the band-averaged power injected by a force into a vibrating system. The approach has been benchmarked on both bare and stiffened plates. However, most real-life applications present complex geometrical features and frequency dependent properties. While analytical expressions may lead to rough predictions for these cases, the present approach improves the computational performance of accurate deterministic modeling.

The following chapter focuses on two application cases, which present a higher complexity than the previous ones. The first example consists of a suspension shock-tower for automotive applications and allows assessing the ability of the technique to integrate the response of a component with a complex geometry. In the second case, the model under analysis is a simplified acoustic car cavity, excited through the firewall and with frequency dependent absorbing walls. This configuration allows benchmarking the approach for acoustic problems with distributed excitations and frequency dependent properties.

The chapter is divided in three main sections. The suspension shock-tower case is presented in sec. 5.1, while sec. 5.2 is dedicated to the acoustic example. Finally, conclusions are drawn in sec. 5.3.

5.1 Suspension shock-tower

This application case is dedicated to the investigation of the effects of geometrical complexity on the accuracy of the band-averaging procedures. In sec. 5.1.1, the numerical model is presented, while results are illustrated in sec. 5.1.2.

5.1.1 Model description

This example consists of a suspension shock-tower, fig. 5.1(a), located inside a Chrysler Neon, fig. 5.1(b). The component is made of steel, Young's modulus 210 GPa, Poisson ratio 0.3, density 7850 kg/m³. Its thickness is 2 mm. The model dimensions are such that the diagonal of a parallelepiped circumscribing the shock-tower is about 450 mm. Hysteretic damping model is used with coefficient η equal to 0.01. The FE mesh consists of 5876 nodes and 5874 shell elements, as illustrated in fig. 5.1(a). The mean dimension of the elements is 5 mm. Also in this case Nastran has been used to pre-process the system matrices, which are successively solved in Matlab.

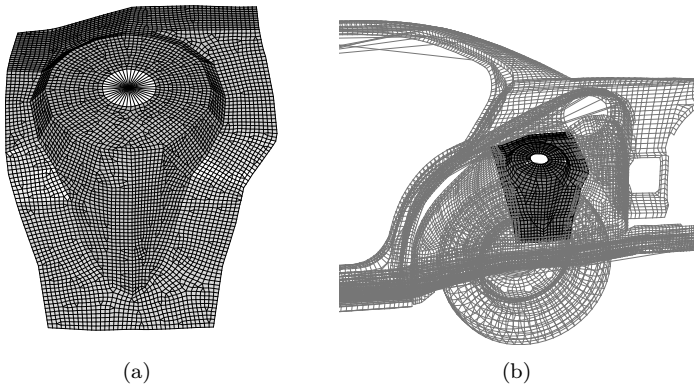


Figure 5.1: Finite element model of the shock-tower (a). Position of shock-tower within the car assembly (b).

Clamped boundary conditions are applied along the outer edges. However, since using the residue theorem allows a quick band evaluation, one might rapidly perform analyses with different types of boundary conditions. This highlights the high potential of this strategy to provide fast and accurate results, when insight at a component level is required.

A harmonic point force is applied at the center of the hole of the shock-tower

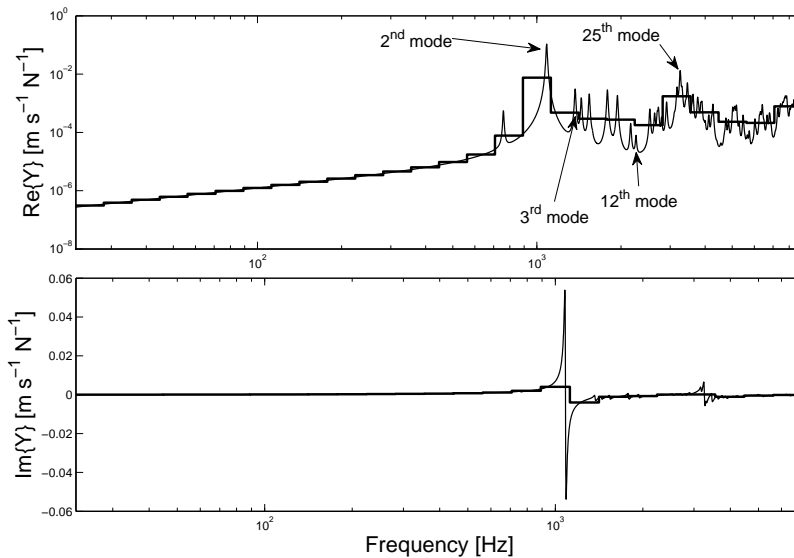


Figure 5.2: Comparison between narrow band and band-averaged input mobility for the shock-tower.

cap and represents the force transmitted from the wheel through the suspension. All degrees of freedom over the hole edge are rigidly connected, as shown in fig. 5.1(a).

The geometrical features of this component pose a serious limitation to classic models based on the assumption of an unbounded domain. According to SEA modeling, the system under analysis could be decomposed into a number of subcomponents, which carry different wavelengths. For example, the upper face could be modeled as a plate, which is connected to the rest of the structure through a stiffener. As such, the junction is difficult to model with bare analytical formulations, and estimating the input power as the one into an infinite plate would actually lead to a poor prediction, especially at low frequencies. More in general, assuming that the input power into a component of a built-up structure is independent of the coupling with other components may be incorrect in many situations. In fact, the assumption is reasonable for weakly coupled components, namely components that do not share global modes. In this situation, the power injected into the isolated subsystem can be assumed to be independent of the surrounding ones. On the other hand, when the coupling is strong, the behaviors of the coupled components tend to merge and the power injected into the coupled system has to be considered

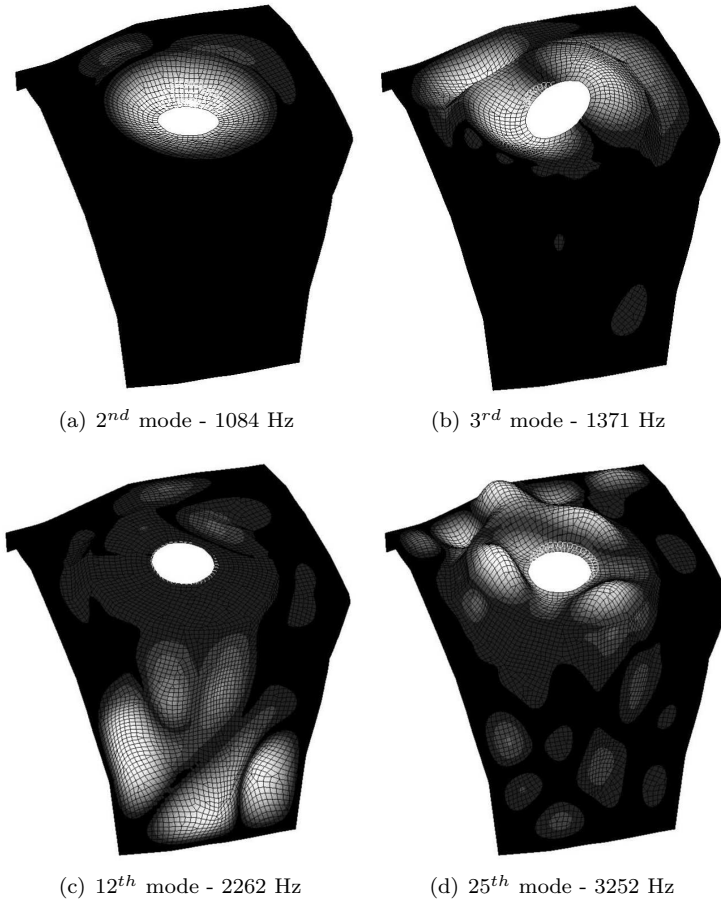


Figure 5.3: Selected mode shapes of the suspension shock-tower.

[136]. Such a situation is very common at low frequencies, where global modes are present and highlights the advantage of modeling a complex component by means of deterministic techniques, which allow investigating the effects of boundary conditions and inhomogeneities on the system response accurately.

5.1.2 Results

In a first analysis, the frequency range of interest covers 26 one-third octave bands (from 22.4 Hz to 8913 Hz). The real and imaginary parts of the input

mobility are shown in fig. 5.2, and to gain further insight in the system behavior some mode shapes are analyzed in fig. 5.3. The mobility peak at 1084 Hz corresponds to the second mode of the system (fig. 5.3(a)) and involves the vibration of the top circular plate of the shock-tower in the direction of the excitation force. At this frequency a large amount of power can be injected into the system. A large amount of power can also be injected at 3252 Hz, where the structure has its 25th mode (fig. 5.3(d)), and the top plate shows again a vibration predominant in the excitation direction. In correspondence of the 3rd mode (fig. 5.3(b)), the top plate is twisting rather than pulsating. This explains the lower mobility to which the surrounding of the plate is also contributing. Finally, the injected power is low when the modes shapes show large amplitude oscillations in other areas of the structure and do not involve the vibration of the top plate, as for the 12th mode (fig. 5.3(c)).

The hysteretic damping model is used with a constant loss factor, and system poles populate the first and third quadrant of the complex frequency plane. This condition allows replacing the integration over an interval of real frequencies with one over a path in the complex plane. To compute the band values, the same integration schemes adopted in ch. 4 are employed in this example, namely 6, 8 and 10 Gauss points over semi-circles and semi-ellipses with coefficient a equal to 0.5 and 2. The midpoint rule is also used over semi-circles to allow a comparison with the Butterworth-weighted average.

The relative error is computed as in eq. (4.32), and the reference values are evaluated by using 200 Gauss points over semi-circles. Figures 5.4 and 5.5 show the relative error on the averaged real and imaginary parts of the mobility. Since no resonance is present within the first fifteen bands, the integrals are estimated with very high precision, but also for increasing frequencies the accuracy remains high. Compared to the midpoint rule, Gaussian quadrature provides more accurate band evaluations, especially when used over semi-ellipses with $a = 0.5$.

In fig. 5.6, Gaussian quadrature integration is performed over the real axis with the same number of points as in the previous cases. When the mobility is not oscillating, the integration is very accurate. However, it becomes less accurate with increasing frequency, due to the presence of resonance peaks. Over these bands, the use of the residue theorem provides significant advantages in terms of accuracy.

Note that in fig. 5.6, for low frequencies, an increase in the number of Gauss point does not correspond to an increase in accuracy. This stagnation means that a few Gauss points taken over the real axis provide more accurate integration than a large number of Gauss points taken in the complex plane. The fact is not surprising, since the integrand is extremely smooth at real low-frequencies, while moving to the complex plane may introduce numerical errors

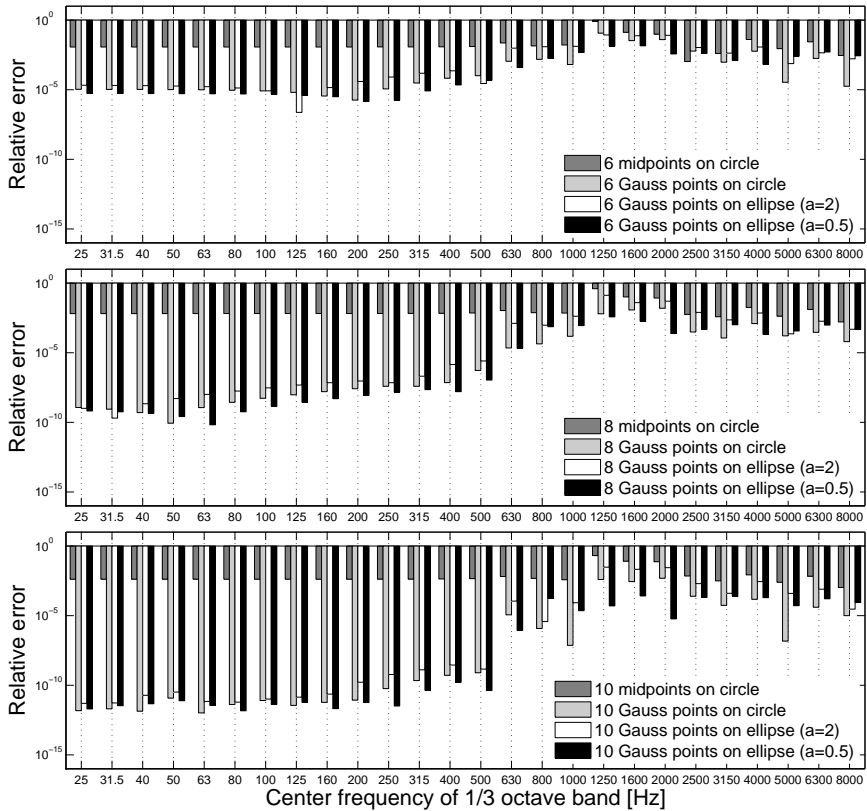


Figure 5.4: Error related to the real band-averaged input mobility of the shock-tower for 6 (top), 8 (center) and 10 (bottom) integration points taken over either a semi-circle or semi-ellipse. One-third octave band results.

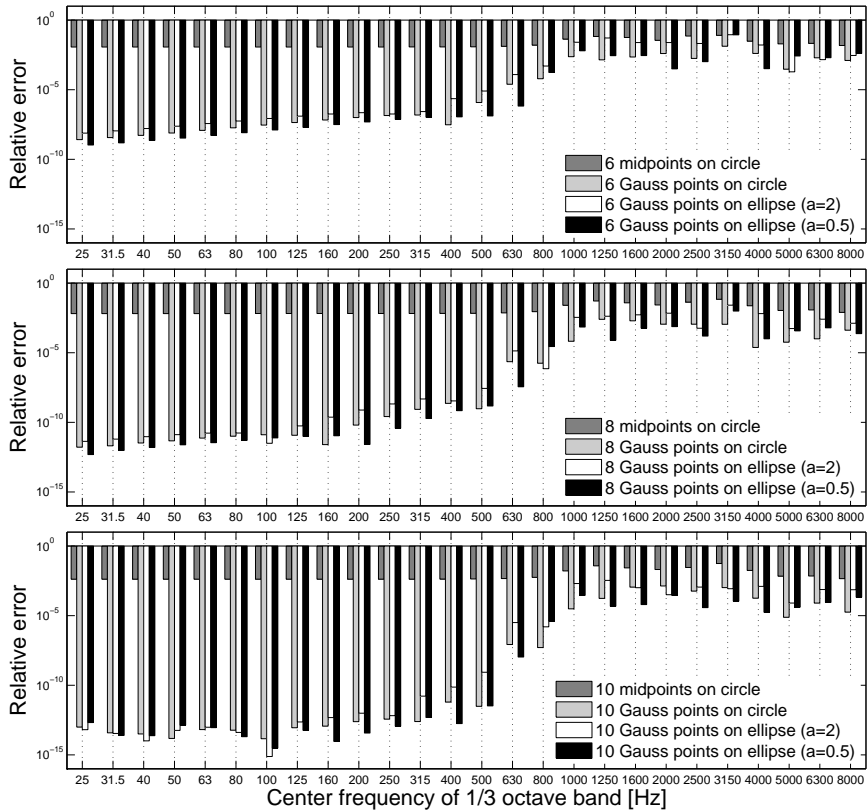


Figure 5.5: Error related to the imaginary band-averaged input mobility of the shock-tower for 6 (top), 8 (center) and 10 (bottom) integration points taken over either a semi-circle or semi-ellipse. One-third octave band results.

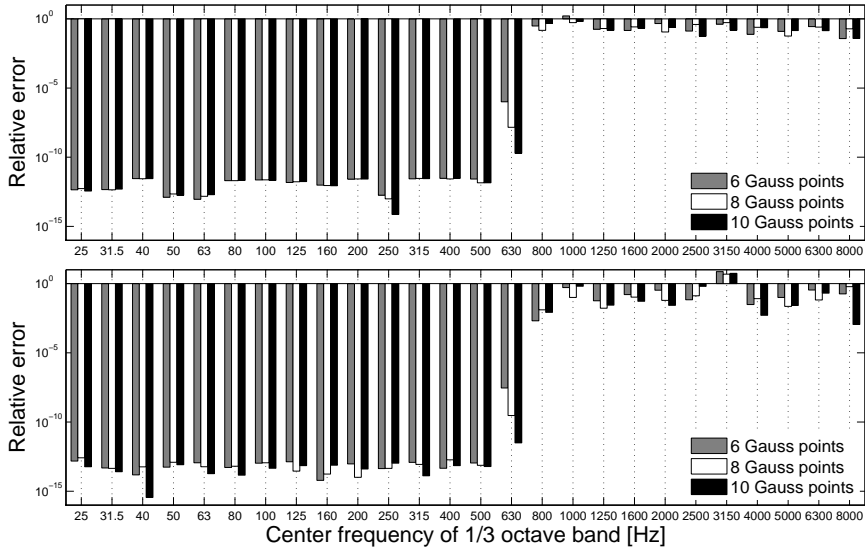
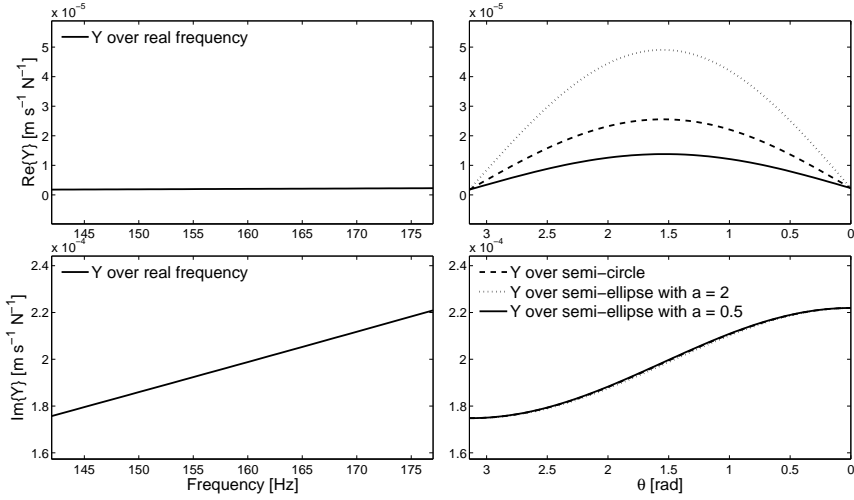


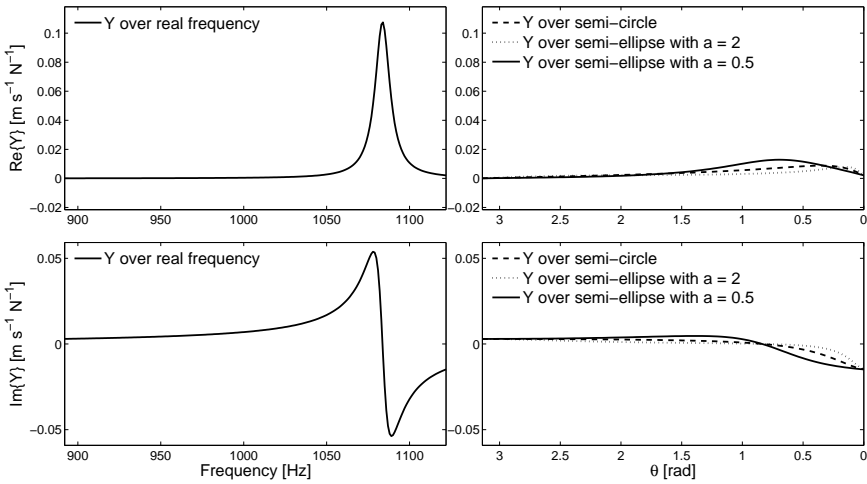
Figure 5.6: Error related to the real (top) and imaginary (bottom) band-averaged input mobility of the shock-tower for 6, 8 and 10 Gauss points taken over the real frequency band. One-third octave band results.

and small oscillations, especially close to the endpoints, see fig. 4.9. However, the accuracy level is very high, and this does not compromise the validity of the previous results. Moreover, the oscillatory behavior of the function is not known a priori and using the residue theorem seems to be more reliable for band computations. In figs. 5.7 and 5.8, the mobility is plotted as a function of either real and complex frequency. Four third octave bands are investigated, namely the 9th, 17th, 22nd and 24th band. The left-hand side figures show the real and imaginary parts of the mobility as a function of real frequencies, while on the right-hand side, the frequency of analysis is taken in the complex frequency plane over either semi-circles and semi-ellipses, and the function is parametrized in $\theta \in [0, \pi]$. Note that the θ -axis is reversed in order to show that the mobility at $\theta = 0$ and $\theta = \pi$ assumes the same values as at the lower and upper bounds of the real frequency interval.

Comparing the function over different paths in the complex plane it is possible to notice that the oscillating behavior gradually decreases with increasing the distance from the real axis. Consequently, when using a small semi-ellipse, some oscillations may be present inside the interval of integration. On the other hand, by using a large semi-ellipse, the integrand shows a non-oscillatory behavior in the middle region of the θ interval, but it presents more abrupt

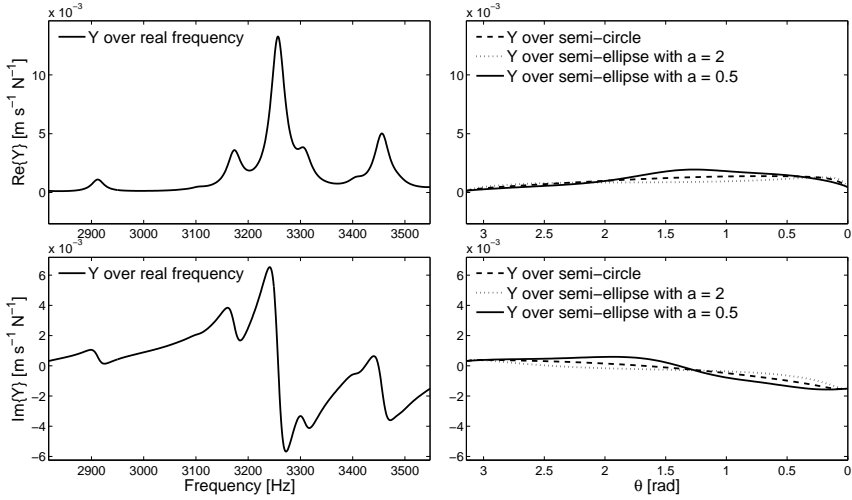


(a)

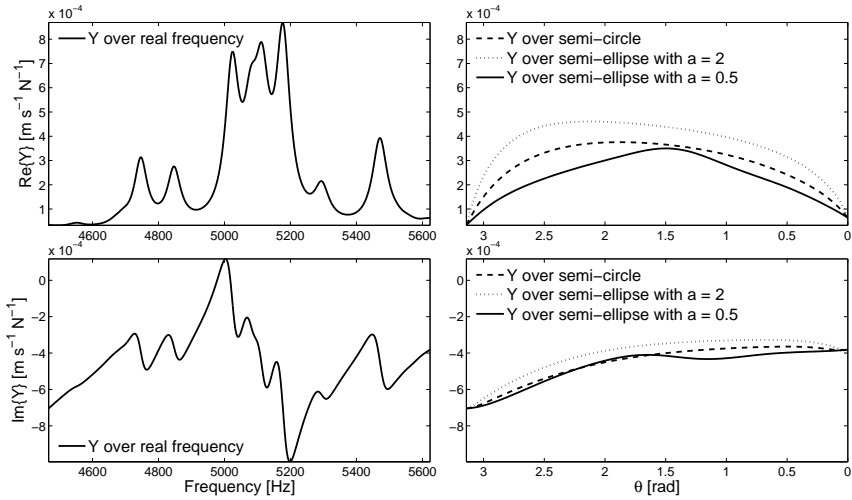


(b)

Figure 5.7: Real and imaginary part of the the mobility function evaluated over the real axis (left), semi-circle, semi-ellipse with $a = 0.5$ and with $a = 2$ (right). Figure (a) refers to the 9th and (b) to the 17th third octave bands. Note the right figures are function of θ .



(a)



(b)

Figure 5.8: Real and imaginary part of the the mobility function evaluated over the real axis (left), semi-circle, semi-ellipse with $a = 0.5$ and with $a = 2$ (right). Figure (a) refers to the 22nd and (b) to the 24th third octave bands. Note the right figures are function of θ .

variations close to the endpoints. This effect seems common when moving in the direction perpendicular to the real frequency axis. As observed also in the previous chapter, using $a = 0.5$ leads to a good balance between these two effects and a consequent good accuracy level. On the contrary, when $a = 2$, the behavior at the endpoints may be sharp leading to poor accuracy levels, in some cases. However, the best path of integration is problem dependent and difficult to determine a priori.

As previously explained, when the mobility is not oscillating over the interval, using quadrature over real frequencies is more effective with respect to the integration in the complex frequency plane. In fact, oscillations close to the endpoints are inevitably introduced, see fig. 5.7(a). However, as the frequency increases, the oscillatory behavior becomes more prominent over real frequencies, while plots over paths in the complex frequency plane preserve their non-oscillatory behavior.

Figures 5.7 and 5.8 not only provide an insightful explanation regarding the high accuracy and efficiency of the proposed strategies. They also show a low dependency between the width of the frequency interval and the oscillatory behavior of the integrand in the complex plane.

Results obtained for 9 octave bands (from 22.4 Hz to 5263 Hz) are reported in figs. 5.9 and 5.10. They confirm the aforementioned observations regarding the level of accuracy. Note the ability of the approach to estimate the ninth octave band value (width equal to 2445 Hz), with a relative error lower than 1% just by using 6 system evaluations.

Figure 5.11 shows the accuracy provided by Gaussian quadrature performed over the real axis, which also in this case proves to be precise only in absence of mobility oscillations.

It is interesting to observe that using the residue theorem to integrate over wider bands does not seem to affect the precision of the estimates, which present values comparable to the ones obtained for third octave bands. On the other hand, the accuracy decreases when integrating the oscillating mobility over the real frequency axis.

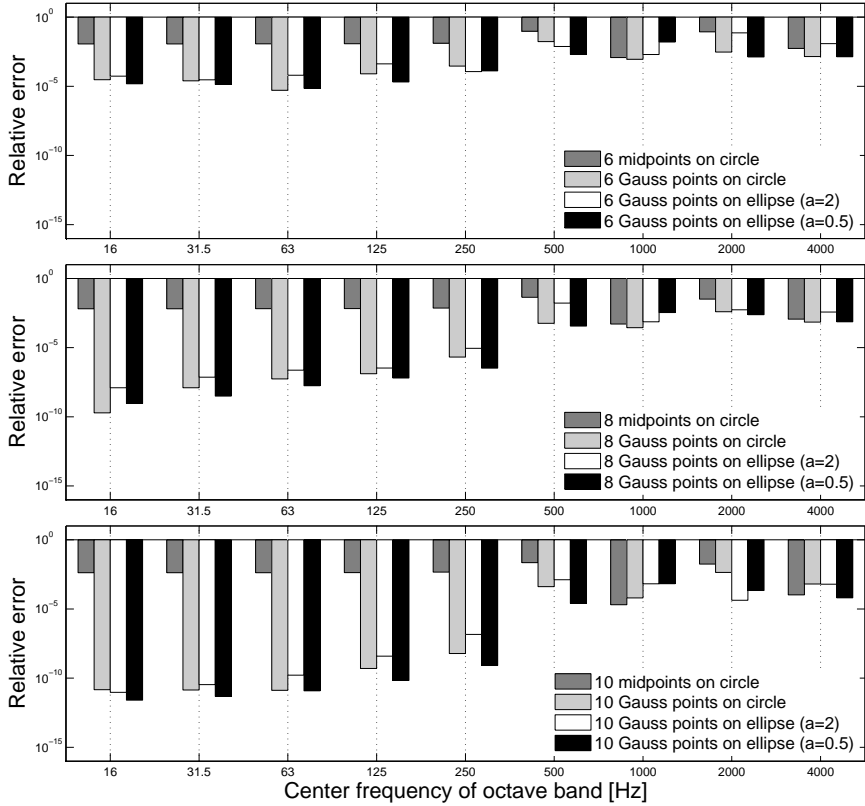


Figure 5.9: Error related to the real band-averaged input mobility of the shock-tower for 6 (top), 8 (center) and 10 (bottom) integration points taken over either a semi-circle or semi-ellipse. Octave band results.

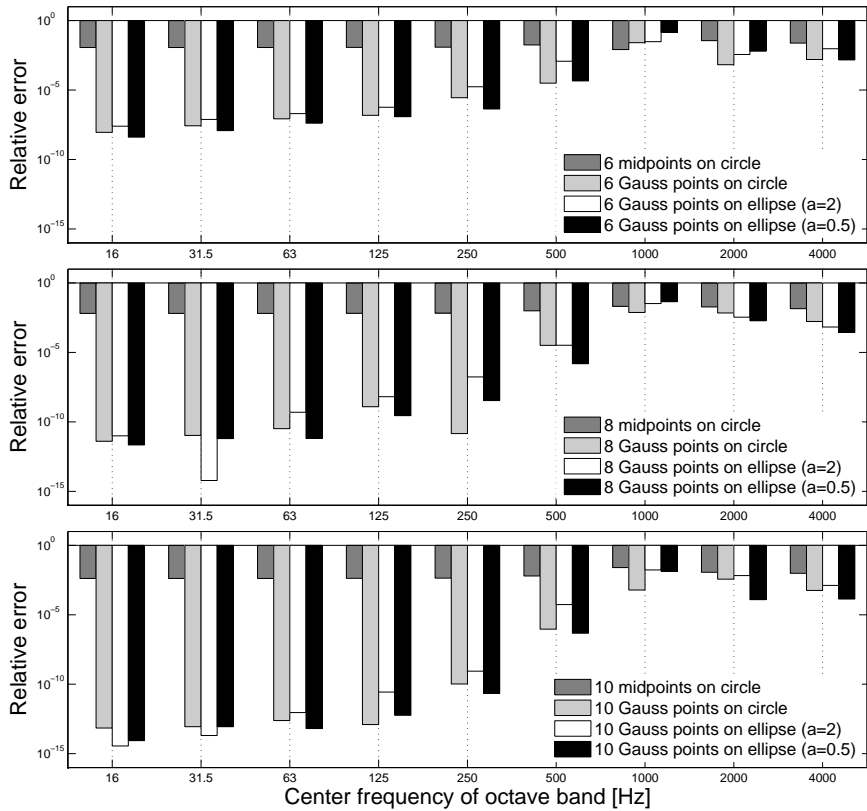


Figure 5.10: Error related to the imaginary band-averaged input mobility of the shock-tower for 6 (top), 8 (center) and 10 (bottom) integration points taken over either a semi-circle or semi-ellipse. Octave band results.

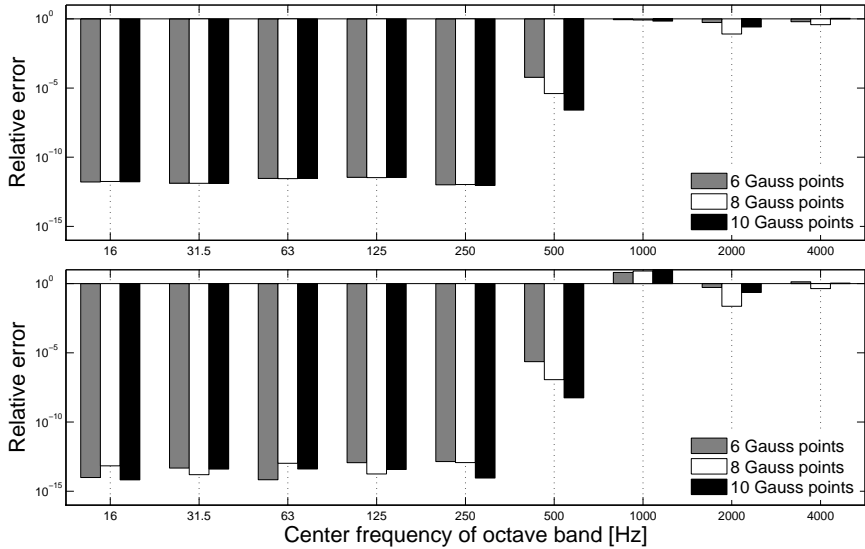


Figure 5.11: Error related to the real (top) and imaginary (bottom) band-averaged input mobility of the shock-tower for 6, 8 and 10 Gauss points taken over the real frequency band. Octave band results.

5.2 Acoustic car cavity

This application case deals with the input power into an acoustic system which resembles a car cavity. The computation of input power into acoustic systems is introduced in sec. 5.2.1. Successively, the analyzed model is described in sec. 5.2.2. In sec. 5.2.3, the approximate position of the poles for an acoustic system with admittance boundary conditions is discussed. Finally, in sec. 5.2.4 the accuracy and computational performance for this application case are assessed.

5.2.1 Input power into acoustic systems

Prescribed (non-zero) boundary conditions are a source of injected power for acoustic systems. Either pressure or its spatial derivatives can be defined over a portion of the boundary and excite the system. Estimating the active input power in this case requires the integration of the active acoustic intensity over the corresponding portion of the boundary. At a point \mathbf{x} on the boundary $\partial\Omega_a$,

the active intensity can be estimated as

$$\mathbf{I}(\mathbf{x}) = \frac{1}{2} \text{Re} \{ p(\mathbf{x}) \mathbf{v}^*(\mathbf{x}) \}, \quad (5.1)$$

and the power injected into the system reads,

$$P_{\text{in}} = \int_{\partial\bar{\Omega}_a} \mathbf{I}(\mathbf{x}) \cdot \mathbf{n}_a(\mathbf{x}) \, d\partial\bar{\Omega}_a, \quad (5.2)$$

where $\mathbf{n}_a(\mathbf{x})$ is the normal to the boundary $\partial\bar{\Omega}_a$ at point \mathbf{x} . Analogously, to evaluate the reactive input power, it is necessary to integrate the imaginary part of the complex intensity vector over the surface $\partial\bar{\Omega}_a$.

For the BEM, the computation of the input power does not necessarily require the post-processing step. In fact, the solution of a BEM problem leads to the pressure and its derivative at the nodal locations, which can then be integrated according to eq. (5.2). A similar situation is encountered in WB modeling, as the wave functions computed at the Gauss points over $\partial\bar{\Omega}_a$ can be stored during the pre-processing step and reused for the integration (5.2).

For distributed loadings, the residue theorem can be straightforwardly used to evaluate the band average input power, whether the prescribed conditions are uniform or non-uniform. On the other hand, if the power is injected by a vibrating structure, the use of the residue theorem may be more problematic. This is mainly due to the fact that on the interface both velocity and pressure are initially unknown. Furthermore, the poles of the intensity function (5.1) may be located both in the UHP and in the LHP, and this reduces the efficiency of the proposed strategy. Alternatively, if the systems are uncoupled, one can first compute the velocity at a given point on the interface and successively use it as a boundary condition for the acoustic problem. This procedure is possible only if the prescribed velocity function does not present any unknown singularity in the LHP.

Active power can also be injected by point sources. Acoustic monopoles are an example often encountered in practice and their field can be expressed as

$$p(r_q) = i\omega\rho_a q \frac{e^{-ik_a r_q}}{4\pi r_q}, \quad (5.3)$$

where q represents the volume velocity, given by the product of the normal velocity and the surface area of the radiator and r_q is the distance between the source and the target point.

The issue with the evaluation of the complex power injected by a monopole source is the singularity it presents for $r_q \rightarrow 0$. In fact, this makes it impossible to retrieve the pressure value and evaluate the power. One can easily remedy

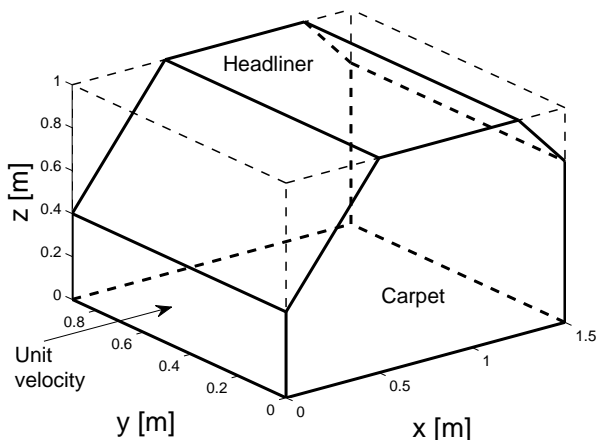


Figure 5.12: Car-like cavity and bounding box for WB modeling.

this by modeling the monopole as a sphere, or a more complex object and impose a velocity boundary condition over its surface. The input power can be estimated by using eq. (5.2), allowing also the inclusion of source directivity information. Traditional approaches like FEM and BEM can be used to model such a problem. Alternatively, in the framework of the WBM, the Multi-level strategy [202] can be successfully exploited.

5.2.2 Model description

The car-like acoustic cavity under analysis is represented in fig. 5.12 and is filled with air of density 1.225 kg/m^3 , speed of sound 340 m/s and acoustic loss factor equal to 0.001 . The main dimensions of the cavity are $l_x = 1.5 \text{ m}$, $l_y = 0.9 \text{ m}$ and $l_z = 1.0 \text{ m}$. The volume is excited through the firewall (corresponding to the face on the yz -plane passing through the origin) by a unit velocity boundary condition (1 m/s). A frequency dependent admittance boundary condition is applied over the top and the bottom face of the cavity. The normalized admittance, $\bar{A}_n = \rho_a c_{a,0} A_n$, applied over the headliner surface, is expressed as a cubic function of frequency,

$$\bar{A}_n^{(\text{headl.})}(\bar{f}) = i0.025 + i0.034\bar{f} + (0.25 + i0.67)\bar{f}^2 - (0.15 + i0.60)\bar{f}^3, \quad (5.4)$$

while on the carpet, the following normalized admittance condition is applied,

$$\bar{A}_n^{(\text{carpet})}(\bar{f}) = i0.08 + i0.2\bar{f} + (1.72 + i1.77)\bar{f}^2 - (1.13 + i1.92)\bar{f}^3, \quad (5.5)$$

where $\bar{f} = 2\pi\omega/2000$. Impedance values are taken from ref. [188]. The normalized admittance is shown as a function of frequency in fig. 5.13. A purely reflecting boundary condition is applied over the remaining surfaces of the model.

The WBM is used to simulate the behavior of the cavity, and the adopted formulation for 3D acoustic problems is detailed in Appendix A. The advantage in using the WBM for this application is not only related to its higher convergence with respect to classic element-based techniques. Unlike the FEM, the introduction of complex frequencies of analysis does not influence the computational effort of the WBM, as its matrices inherently handle complex quantities.

From a modeling point of view, while element-based techniques use mesh enrichment, the WBM allows refining the solution accuracy simply by increasing the number of wave functions employed to represent the field variable expansion. According to the current WB modeling procedure, the number of wave functions is a function of the (real) frequency of analysis and of a truncation parameter T , which is set equal to 2 in the following cases. However, moving the frequency of analysis to the complex plane may lead to a number of wave functions which differs from the one necessary when the problem is computed at a real frequency. The difference in the number of wave functions may affect the solution accuracy and, indirectly, influence the precision of the band evaluation. In order to restrict the assessment only to the accuracy of the band calculation, the number of wave functions is kept constant over each interval of analysis. This number is chosen according to the upper bound of the frequency interval, as it assures the highest accuracy over the band of interest.

There are several aspects of interest in the following application. First of all, an acoustic enclosure has an asymptotic modal density which increases with the square of the frequency. Thus, also the oscillatory behavior of the mobility

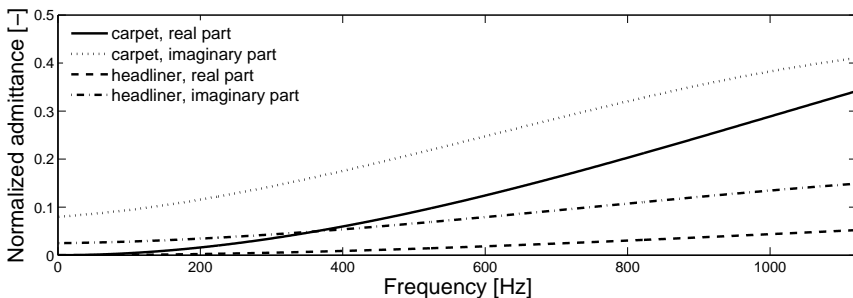


Figure 5.13: Normalized admittance as function of frequency.

increases with frequency. The type of excitation does not take place at a single point, but is distributed over a surface, and the boundary conditions are frequency dependent. Moreover, the presence of the admittance boundary condition leads to a modification of the acoustic behavior compared to the case of purely reflecting boundaries. Consequently, system resonances are influenced both in amplitude and location. However, system poles are not expected to invade the LHP and the proposed approach can still be applied. Before presenting the results, this is proven in a simplified analysis reported in the next section.

5.2.3 Poles of an acoustic cavity with admittance boundary conditions

The goal of the following section is to provide an approximation for the position of system poles when the acoustic cavity presents absorbing walls.

Consider an acoustic volume, for example a rectangular room of domain Ω_a , and suppose that an admittance boundary condition is applied over the walls, $\partial\Omega_a$. Under steady-state conditions, this problem can be formulated as follows,

$$\begin{cases} \nabla^2 p(\mathbf{x}, \omega) + k_a^2 p(\mathbf{x}, \omega) = 0 & \text{in } \Omega_a \\ \nabla p(\mathbf{x}, \omega) \cdot \mathbf{n}_a(\mathbf{x}) = -i\rho_a \omega A_n p(\mathbf{x}, \omega) & \text{on } \partial\Omega_a \end{cases}, \quad (5.6)$$

where the symbol A_n indicates the normal admittance. Loss mechanisms are included in the description of the speed of sound by introducing a loss factor, η , such that

$$c_a = c_{a,0} (1 + i\eta). \quad (5.7)$$

Consequently, also the wavenumber $k_a = \frac{\omega}{c_a}$ is complex.

A general solution to problem (5.6) is not easy, as the presence of absorbing walls leads to frequency dependent eigenvalues and to eigenfunctions which do not necessarily satisfy orthogonality [20]. To simplify the analysis, assume that the walls are almost rigid and that the admittance value is very low, $\rho_a c_{a,0} |A_n| < 1$. Under this assumption, the eigenfunctions of the Neumann problem can be considered a reasonable approximation for the ones related to the current auto-adjoint problem and they can be used to find the approximated eigenvalues of the Helmholtz problem (5.6) [20].

Multiplying the Helmholtz equation by the n -th eigenfunction ϕ_n and integrating over the acoustic volume Ω_a , leads to

$$\int_{\Omega_a} (\nabla^2 p + k_a^2 p) \phi_n \, d\Omega_a = 0. \quad (5.8)$$

The term $\phi_n \nabla^2 p$ can be expressed as the sum of $p \nabla^2 \phi_n$ and the divergence of $\phi_n \nabla p - p \nabla \phi_n$, and by using Gauss's theorem [73], expression (5.8) can then

be reformulated as

$$\int_{\Omega_a} p (\nabla^2 \phi_n + k_a^2 \phi_n) d\Omega_a + \int_{\partial\Omega_a} \phi_n \nabla p \cdot \mathbf{n}_a d\partial\Omega_a = 0, \quad (5.9)$$

where it has been considered that ϕ_n satisfies the reflecting boundary conditions. Applying the homogeneous Helmholtz equation, the equality $\nabla^2 \phi_n = -k_n^2 \phi_n$ can be used in the first integrand, where k_n^1 is the wavenumber corresponding to the Neumann problem eigenvalue, which must be real and positive. Moreover, the gradient of the pressure in the second integral can be written according to the admittance boundary condition. These considerations lead to

$$\int_{\Omega_a} p (k_a^2 \phi_n - k_n^2 \phi_n) d\Omega_a - i\rho_a \omega A_n \int_{\partial\Omega_a} \phi_n p d\partial\Omega_a = 0. \quad (5.10)$$

The pressure p can be written as an expansion of orthogonal eigenfunctions ϕ_n with coefficients a_n . Due to the mode orthogonality, expression (5.10) can be reformulated as follows,

$$(k_a^2 - k_n^2) a_n - ik_{a,0} \sum_m B_{nm} a_m = 0, \quad (5.11)$$

where

$$B_{nm} = \frac{1}{V_a} \int_{\partial\Omega_a} \phi_n \rho_a c_{a,0} A_n \phi_m d\partial\Omega_a, \quad (5.12)$$

and V_a is the volume of the enclosure. Since the walls are almost rigid, one can assume that the terms B_{nm} , with $m \neq n$ are of minor importance, and the poles can be found by evaluating the roots of the function,

$$k_a^2 - k_n^2 - ik_{a,0} B_{nn} = 0. \quad (5.13)$$

If the walls are perfectly rigid, $B_{nn} = 0$, and the angular frequency of the system poles is identified by

$$\omega_{1,2} = \pm \omega_n (1 + i\eta), \quad (5.14)$$

where ω_n is the real part of the n -th eigenvalue. This result confirms that in absence of damping, system poles are purely real. When a loss mechanism is introduced in the fluid description, they populate the first and third quadrant of the complex frequency plane.

The analysis of the position of the poles may be difficult when both the real and imaginary parts of the admittance are non-zero. To simplify the investigation, an undamped system is considered. In this case, the n -th eigenvalue is located at

$$\omega_{1,2} = \frac{c_{a,0}}{2} \left(iB_{nn} \pm \sqrt{4k_n^2 - B_{nn}^2} \right). \quad (5.15)$$

¹The subscript a is omitted for the problem eigenvalues.

For real B_{nn} with increasingly positive values, poles present a larger imaginary part and a smaller real one. Consequently, with increasing real admittance, the resonance peaks become smoother and move towards lower frequencies. On the other hand, for a purely imaginary admittance, eigenvalues move towards higher frequencies for increasingly negative values and lower frequencies for increasingly positive ones.

To see the effect of damping and admittance on the position of the poles for the analyzed system, the active input power into the complex frequency plane is shown in fig. 5.14. Four different configurations of the car cavity are analyzed as combinations of the system with and without damping or admittance boundary condition. Since the integration is carried out over the real frequency axis, the contour plots are limited to the first and fourth quadrant of the complex frequency plane. For the case without damping nor absorption, the active power is zero over the real frequency axis. However, the position of the poles can still be identified. A slight movement towards higher imaginary frequencies of the eigenvalues can be observed when damping is added to the system, as predicted by eq. (5.14). Moreover, since a loss mechanism is present, the input power is non-zero over the real frequency axis. A significant change in the position of the poles can be seen when an admittance boundary condition is included in the model. Since both real and imaginary parts in (5.4) and (5.5) are positive, the poles move towards lower real and larger imaginary frequencies, as predicted by the previous simplified mathematical model. If the real part of the admittance is negative, system eigenvalues move towards negative imaginary frequencies. In this case, the model represents the situation where the wall reacts anticipating the pressure wave, meaning that the condition is anti-causal.

The previous analysis confirms that no poles lie in the fourth quadrant of the complex plane for the case under investigation. This condition allows the efficient application of the residue theorem for band integration.

5.2.4 Results

The following analysis is carried out over 17 one-third octave bands (from 22.4 Hz to 4467 Hz). Figure 5.15 shows the active and reactive components of the input power. Also in this case the error is quantified through eq. (4.32), and the reference solution is estimated by means of 200 Gauss points distributed over semi-circles.

The relative error over the bands is shown in figs. 5.16 and 5.17, for the active and reactive input power, respectively. The level of precision is good, and already 6 points provide satisfactory accuracy for several bands. Using 6 points to integrate the reactive power over the 500 Hz and 630 Hz bands leads to poor

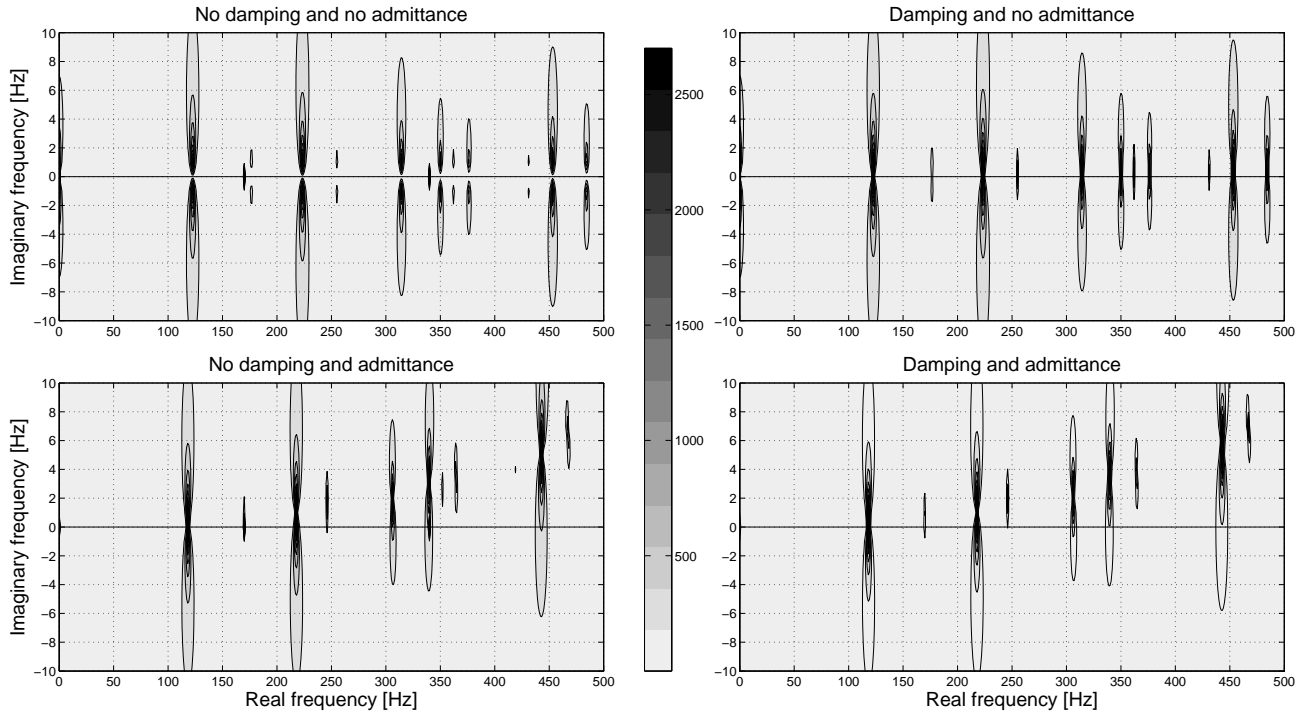


Figure 5.14: Contour plot of the active input power over the complex frequency plane. The unit in the color map is [W].

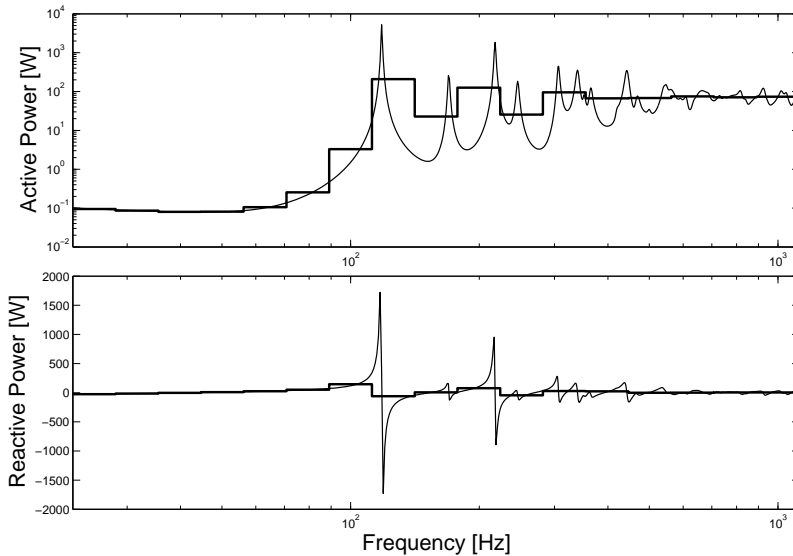


Figure 5.15: Comparison between narrow band and band-averaged input power into the car cavity.

results. However, the estimate becomes more accurate with increasing the number of integration points.

Figure 5.18 reports the accuracy of Gaussian quadrature with 6, 8 and 10 points, and the trapezoidal rule with a 1 Hz resolution step. The accuracy of Gaussian integration is high when the function does not oscillate, namely for very low frequencies and for high frequencies, in the case of active power. When the integrand contains more peaks, 6 to 10 Gauss points provide rough estimates of the band value. On the other hand, the accuracy of the trapezoidal rule is strictly dependent on the width of the band. For narrow bands, the small number of sampling points is not sufficient to achieve high precision, and Gaussian quadrature is clearly better. When the width of the band increases, the trapezoidal scheme provides more accurate estimates than Gaussian. However, the increased accuracy comes at a higher computational cost.

Comparing fig. 5.18 with figs. 5.16 and 5.17 confirms that the residue theorem can be used as an accurate alternative to classic quadrature on real frequencies. In figs. 5.19 and 5.20, the input power is plotted as function of real frequencies and θ , which is used to parametrize semi-circles and semi-ellipses in the complex frequency plane. The conclusions are very similar to the ones in the previous

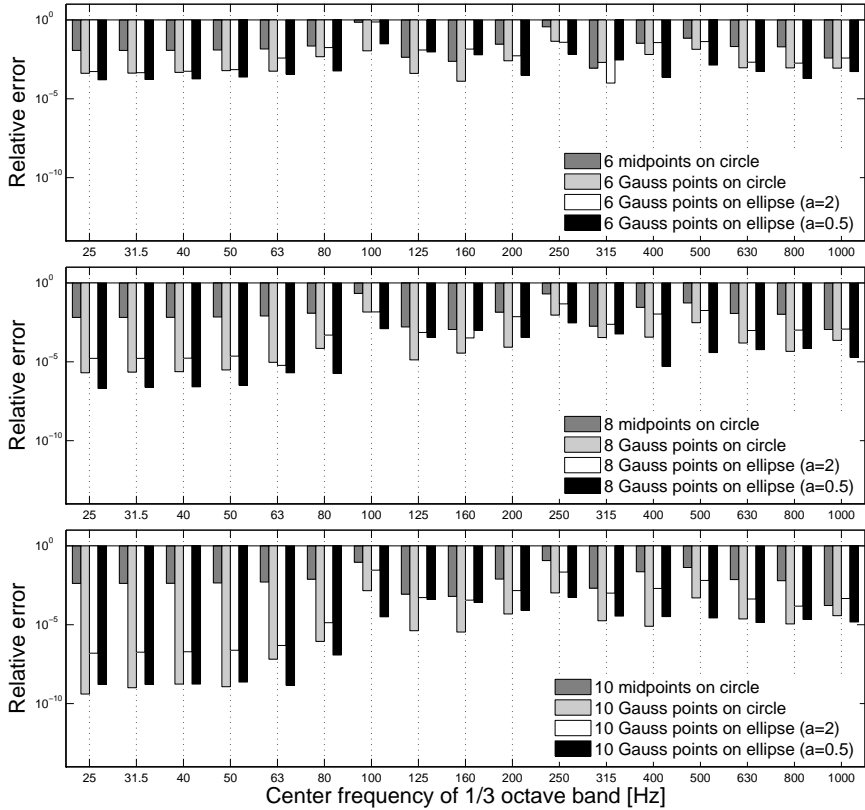


Figure 5.16: Error related to the real band-averaged input power into the car cavity for 6 (top), 8 (center) and 10 (bottom) integration points taken over either a semi-circle or semi-ellipse. One-third octave band results.

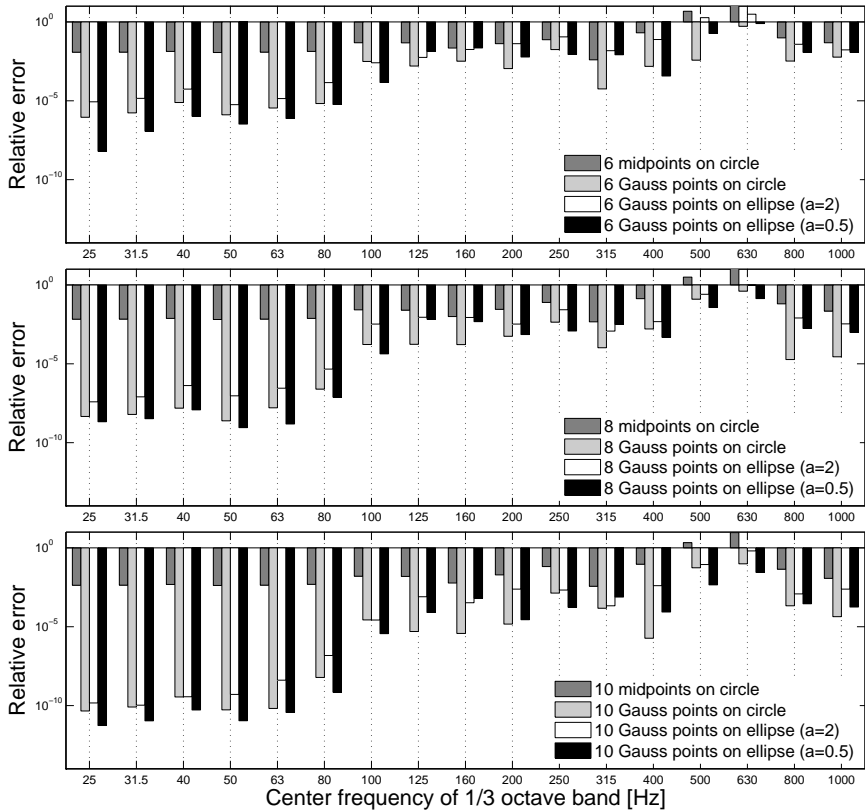


Figure 5.17: Error related to the imaginary band-averaged input power into the car cavity for 6 (top), 8 (center) and 10 (bottom) integration points taken over either a semi-circle or semi-ellipse. One-third octave band results.

case. When the power is not oscillating over real frequencies, numerical quadrature is more effective, as slight oscillations are inevitably introduced when moving to the complex frequency plane. On the other hand, with increasing frequencies, the input power oscillates much less over semi-circles and semi-ellipses in the complex plane, if compared to its behavior over real frequencies. Also in this case, the dependency between the oscillating behavior over the θ interval and the frequency interval of analysis, seems not to be strict. Additionally, in figs. 5.19 and 5.20 can be observed a global behavior similar to figs. 5.7 and 5.8, meaning that the accuracy of the present techniques is not strictly related to the nature of the dynamic problem under analysis, nor on its geometrical complexity.

Finally, fig. 5.21 shows the advantage in terms of computation time, with respect to trapezoidal integration. The reason why the overall computation time increases with frequency is due to the truncation rule used in the WB model. As previously mentioned, the number of wave functions is kept constant over each band and increases with frequency. The significant reduction of solving time provided by the use of the residue theorem is evident, especially over the largest intervals, which require several function evaluations to compute the band value.

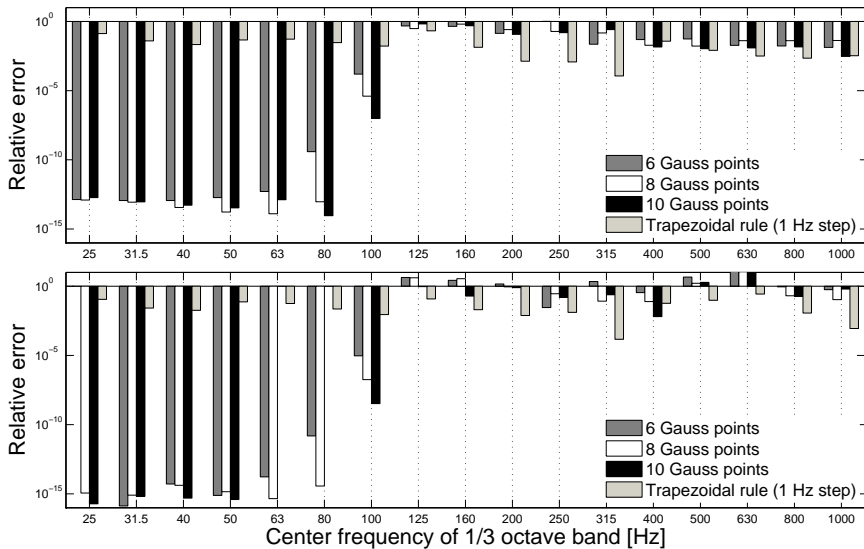
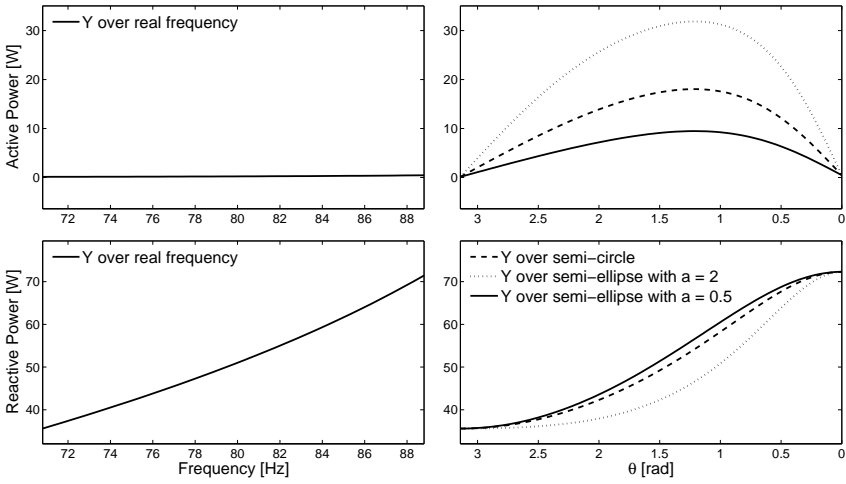
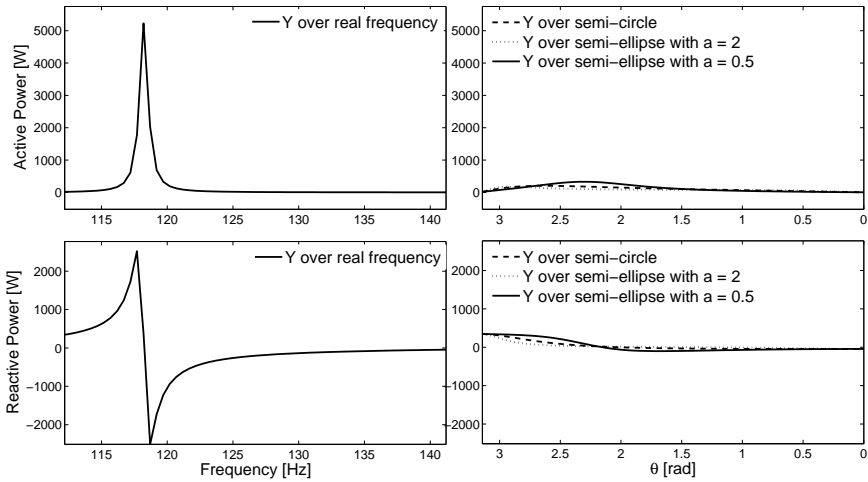


Figure 5.18: Error related to the real (top) and imaginary (bottom) band-averaged input power into the car cavity for 6, 8 and 10 Gauss points taken over the real frequency band. Octave band results.

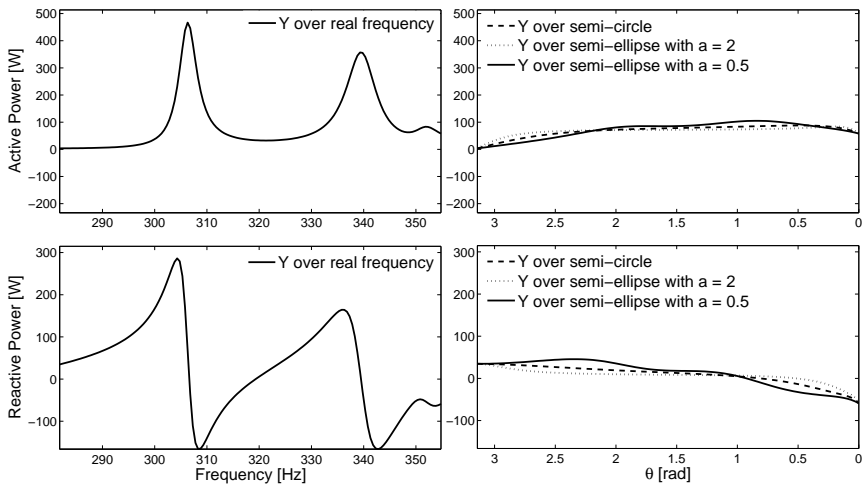


(a)

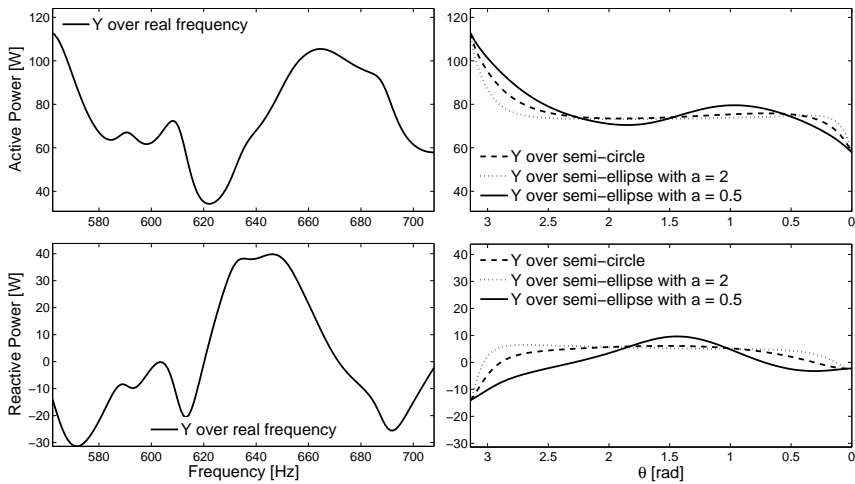


(b)

Figure 5.19: Real and imaginary part of the the input power evaluated over the real axis (left), semi-circle, semi-ellipse with $a = 0.5$ and with $a = 2$ (right). Figure (a) refers to the 6th and (b) to the 8th third octave bands. Note the right figures are function of θ .



(a)



(b)

Figure 5.20: Real and imaginary part of the the input power evaluated over the real axis (left), semi-circle, semi-ellipse with $a = 0.5$ and with $a = 2$ (right). Figure (a) refers to the 12th and (b) to the 15th third octave bands. Note the right figures are function of θ .

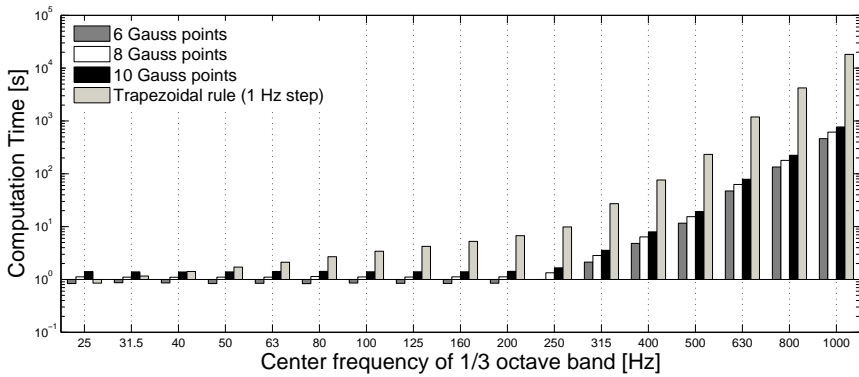


Figure 5.21: Computation time for the car example.

5.3 Conclusion

In this chapter, the approach presented in chs. 3 and 4 is applied to two examples.

The first application consists of a suspension shock-tower excited by a point force. The component has a shape which is less regular than the ones examined in the previous chapters, thus providing a benchmark of higher geometrical complexity.

An acoustic enclosure resembling a car cavity is investigated in the second example. The cavity is excited through a prescribed velocity applied to the firewall and presents frequency dependent absorption boundary conditions over the walls. In this case, the approach is tested for an acoustic problem with a distributed excitation and frequency dependent properties.

In both examples, the residue theorem has proven to be a very efficient and accurate alternative to classic quadrature for the evaluation of band-averaged input power.

Chapter 6

Application to structural-acoustic optimization problems

Reducing the vibration of a mechanical structure and its radiated noise is a challenging goal for acousticians. In this regard, optimization techniques are very helpful to identify the best performing configuration. However, when the target is a band rather than a single frequency, classic quadrature techniques may require a large number of samples to achieve accurate estimates of the band-averaged values, and this dramatically slows down the computation.

The main achievement of the research presented in this chapter, is the formulation of an efficient numerical strategy to optimize the properties of Dynamic Vibration Absorbers (DVAs) in order to improve the dynamic behavior of the structure over a frequency band. Instead of using global displacements or acoustic-related quantities, the input power into the structure is used as an objective function. In fact, minimizing the power injected by a force into a vibrating system leads to a minimization of its input point mobility and allows an indirect reduction of the global vibration and radiated acoustic power. This strategy has been proposed and successfully applied in ref. [96] for topology optimization. However, when the target is a band rather than a single frequency, the computation can be prohibitively demanding. In order to increase the computational performance, the residue theorem is adopted to evaluate the frequency-averaged input power.

In the following chapter, Genetic Algorithms (GAs) [87] are used for the

optimization process and the WBM is employed to simulate the dynamic behavior of the plate. Compared to traditional FEM, the WBM shows a higher convergence rate and does not restrict the DVA position to nodal locations. Moreover, when dealing with point connections, only a few rows and columns have to be added to the system of equations of the bare structure. These advantageous features perfectly fit the framework of an optimization scheme. The vibration reduction of a rectangular plate excited by a point force is investigated in two different scenarios. In the first case, one DVA is optimized such that it can minimize the input power over one band. In the second case, two DVAs are used to minimize the input power over two frequency bands. In all cases, minimizing the band-averaged input power leads to a reduction of the global vibration and radiated acoustic power. Additionally, the obtained designs are proven to be robust against variations in the DVA parameters. The computational performance is assessed, in order to show the significant advantages of the use of the residue theorem against classic quadrature techniques.

The chapter is organized as follows. A short literature survey on the use of passive devices for vibration control is given in sec. 6.1. Theoretical and numerical aspects related to the problem formulation are presented in sec. 6.2. In sec. 6.3, the optimization procedure is illustrated and validated by numerical examples in sec. 6.4. Finally, conclusions are drawn in sec. 6.5.

6.1 The use of DVAs for passive vibration control

The vibration of a structure and its radiated noise are key aspects to consider when designing a mechanical system. This can be achieved by changing the properties of the system, i.e. by varying its stiffness, mass or damping, or by actively acting on the oscillation by introducing external influences. The former strategy is called passive vibration control, and among the numerous passive devices, DVAs are widely used [48, 90, 193].

A DVA is generally modeled as a mass-spring-damper resonator, and, due to the light-weight properties, it can be easily installed on engineering structures, such as vehicles and industrial machineries [194]. Its ability to absorb energy from the host structure is maximal at its resonance frequency and is also related to the damping coefficient. Conventional approaches suggest to design the DVA such that it can abate the vibration level of one mode. This is commonly done by considering the behavior of the bare structure, rather than a coupled fluid-structure model. However, this procedure is not always very effective. In fact, when the noise at one tone is reduced, the noise at other frequencies may increase, resulting into a global worsening

of the perceived sound. Furthermore, DVAs can lose their efficiency when small changes occur with respect to the nominal host system or to the original resonator design. In real-life applications, operating conditions or manufacturing processes inevitably introduce uncertainty and variability in the model description, causing possible changes in the forcing frequency or in the system response. These reasons motivate the strong need for DVA design procedures to improve the vibrational behavior over a band rather than at a single target frequency. In this regard, optimization techniques are very helpful to identify the best performing configuration. A procedure is proposed in ref. [173], where the properties of the DVA are optimized by solving a non-linear constraint optimization problem. The behavior of the structure improves significantly over the band of interest, and the final design is proven to be robust against variations of the DVA properties. A very recent approach [46] is based on the minimization of the worst-case gain in the frequency band of interest; GAs are used to perform the optimization. Also in ref. [89], GAs are used to optimize the parameters of DVAs and Helmholtz resonators, where the objective function is the acoustic potential energy within a payload fairing. Due to the large number of passive systems, the energy is smeared out over a broad frequency range, similarly to what is observed in Soize's fuzzy structure theory [185].

In ref. [27], the use of DVAs for vibration reduction in both narrow and wide frequency bands is investigated. It is observed that the choice of the DVA parameters are strongly dependent on the bandwidth and its location. In fact, for larger bandwidths, the optimal DVA should not be located at the point with maximum vibration, and multi-modal coupling has to be taken into account during the design phase. Moreover, the optimal damping is strongly dependent on the target band.

An alternative way of creating a stop-band behavior is proposed in ref. [31], where a grid of resonators properly distributed over a panel, allows the global vibration level to be significantly attenuated over a band of frequencies. Instead of determining the properties by means of an optimization procedure, the ratio between the frequency of the resonator and the propagating wave frequency of the unit cell is proven to be key for the efficiency of the grid. These ideas are brought to practical applications in ref. [32], where honeycomb core panels combine high stiffness to mass ratio with an excellent capability of attenuating global vibration over a band.

The choice of the band-averaged input power as an objective function for optimal DVA design, together with the application of the residue theorem to significantly speed up the computation, constitute the core of the proposed optimization process and the main novelty of the following chapter.

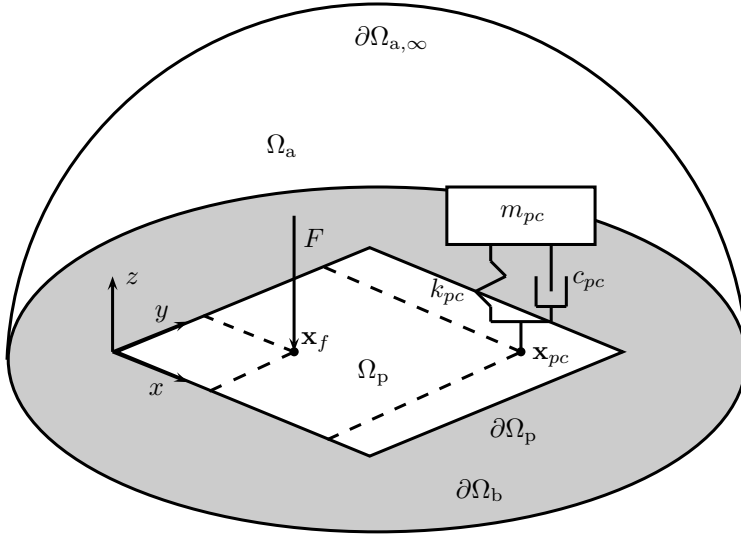


Figure 6.1: Problem geometry.

6.2 Theoretical aspects and numerical methodologies

The focus in this application is on the acoustic radiation from a baffled thin plate with resonators attached, as illustrated in fig. 6.1. In the following sections, the numerical approaches to predict the response of the uncoupled vibro-acoustic system are presented. In particular, to solve the structural problem, the WBM is used with its extension to point connections [208]. On the other hand, the Rayleigh integral is used to compute the acoustic power radiated from the plate [40].

6.2.1 Plate bending with point connections

For thin plates and low frequencies, the effects of rotary inertia and shear deformation can be neglected. This leads to the Kirchhoff theory [128]. When n_{pc} point connections are taken into account, the out-of-plane displacements w of a plate in bending are governed by the following partial differential equation,

$$\nabla^4 w(\mathbf{x}) - k_b^4 w(\mathbf{x}) = \frac{1}{D} F_0 \delta(\mathbf{x}, \mathbf{x}_f) + \frac{1}{D} \sum_{i=1}^{n_{pc}} F_{0,pc,i} \delta(\mathbf{x}, \mathbf{x}_{pc,i}), \quad \text{in } \Omega_p, \quad (6.1)$$

where k_b is the bending wavenumber, and D is the bending stiffness. The symbol F_0 represents the complex amplitude of the harmonic point force applied at \mathbf{x}_f , while $F_{0,pc,i}$ is the force exerted by the i -th point-connected DVA. δ indicates the Dirac delta function. The plate surface coincides with the two-dimensional domain Ω_p of boundary $\partial\Omega_p$. Simply supported boundary conditions are imposed over $\partial\Omega_p$, meaning the prescribed displacements and bending moments are zero.

The bending of a bare, simply supported plate can be modeled by using the WBM, as described in Appendix A. According to the formulation presented in ref. [208], the effect of n_{pc} DVAs is now included into the WB formulation. The variable expansion (A.20) results in the following,

$$w(\mathbf{x}) \approx \hat{w}(\mathbf{x}) = \mathbf{\Psi}(\mathbf{x}) \cdot \mathbf{c} + \hat{w}_f(\mathbf{x}) + \sum_{i=1}^{n_{pc}} \hat{w}_{pc,i}(\mathbf{x}), \quad (6.2)$$

with $\mathbf{\Psi}$ and \mathbf{c} vectors containing n_b wave functions Ψ_b , and the corresponding contribution factors c_b . The function \hat{w}_f is the particular solution of eq. (6.1) subject to the point force of amplitude F_0 , eq. (A.10). The symbol $\hat{w}_{pc,i}$ denotes the particular solution for the force exerted on the plate by the i -th point connection,

$$\hat{w}_{pc,i}(\mathbf{x}) = -\frac{if_{pc,i}(\omega)w_{pc,i}}{8k_b^2D} \left[H_0^{(2)}(k_b r_{pc,i}) - H_0^{(2)}(-ik_b r_{pc,i}) \right], \quad (6.3)$$

where $r_{pc,i}$ is the Euclidean distance between \mathbf{x} and the location of the i -th DVA, $\mathbf{x}_{pc,i}$, $H_0^{(2)}$ is the Hankel function of second kind and zero order, and $f_{pc,i}(\omega)$ represents the force-displacement relation with mathematical expression,

$$f_{pc,i}(\omega) = \frac{F_{0,pc,i}}{w_{pc,i}} = \frac{m_{pc,i} \omega^2 (k_{pc,i} + i\omega c_{pc,i})}{k_{pc,i} + i\omega c_{pc,i} - m_{pc,i} \omega^2}, \quad (6.4)$$

where $m_{pc,i}$ is the mass of the i -th DVA, $k_{pc,i}$ is its stiffness and $c_{pc,i}$ the damping coefficient. The introduction of the particular solution (6.3) into the residual formulation (A.29) leads to a system of $(n_b) \times (n_b + n_{pc})$ equations, to which n_{pc} auxiliary equations are added as follows,

$$w_{pc,i}(\mathbf{x}_{pc,i}) = \mathbf{\Psi}(\mathbf{x}_{pc,i}) \cdot \mathbf{c} + \hat{w}_f(\mathbf{x}_{pc,i}) + \sum_{i=1}^{n_{pc}} \hat{w}_{pc,i}(\mathbf{x}_{pc,i}). \quad (6.5)$$

The system of equations now has the form

$$\begin{bmatrix} \mathbf{A} & \mathbf{B}_{pc} \\ \mathbf{C}_{pc} & \mathbf{D}_{pc} \end{bmatrix} \begin{Bmatrix} \mathbf{c} \\ \mathbf{w}_{pc} \end{Bmatrix} = \begin{Bmatrix} \mathbf{f} \\ \mathbf{f}_{pc} \end{Bmatrix}, \quad (6.6)$$

where \mathbf{A} and \mathbf{f} are the matrix and the right-hand side of the system related to the bare plate, without point connections. The vector \mathbf{w}_{pc} is composed of the displacements at each point connection location. For the sake of brevity, matrices \mathbf{B}_{pc} , \mathbf{C}_{pc} , \mathbf{D}_{pc} and vector \mathbf{f}_{pc} are not reported in detail here. The reader is referred to ref. [208] for their complete expressions. However, it is worth noting that the inclusion of point connections does not influence the main matrix, \mathbf{A} , and only requires the addition of n_{pc} columns and n_{pc} rows to the system. As a consequence, to analyze different configurations, the main system \mathbf{A} is not recomputed. Moreover, since the WBM matrices are generally very small, preprocessing the WBM matrices is more expensive than solving the system. Hence, this constitutes an advantageous property of the WBM for procedures which require iterations, such as optimization strategies and MC simulations [208].

6.2.2 Radiated acoustic power

In the following applications, the thin baffled plate is immersed into a fluid. Under steady-state conditions, the acoustic problem is governed by the Helmholtz equation,

$$\nabla^2 p(\mathbf{x}) + k_a^2 p(\mathbf{x}) = 0, \quad \text{in } \Omega_a \quad (6.7)$$

where p is the acoustic pressure, k_a is the acoustic wavenumber $\frac{\omega}{c_a}$, with c_a the speed of sound in the medium of density ρ_a . The three-dimensional semi-unbounded fluid is represented by the domain Ω_a . The boundary can be split in three non-overlapping regions, $\Omega_p \cup \partial\Omega_b \cup \partial\Omega_{a,\infty}$, where Ω_p is the fluid-plate interface boundary, $\partial\Omega_b$ is the infinite baffle and $\partial\Omega_{a,\infty}$ is the boundary at infinity, on which the Sommerfeld condition is applied.

The interaction between fluid and structure can be modeled in two ways. When the structure has high stiffness and is in contact with a low-density fluid, the interaction between the two is weak and can be neglected. The two domains can be considered separately and each one serves as an exterior excitation for the other. If the elastic structure is immersed in a high-density fluid, the two are strongly coupled and mutually interacting with each other. In this case, they have to be modeled as a coupled vibro-acoustic system. Although this approximation is valid in any case, it is more computationally demanding, due to coupling terms taken into account.

In the following case, the plate presents a high stiffness and the fluid has low density, thus it is reasonable to assume that the mutual interaction is weak and negligible. Under this assumption, the problem can be treated as uncoupled, and the normal plate velocity distributions are independent of the surface pressures.

A reflecting boundary condition is applied over the baffle $\partial\Omega_b$, while on the boundary Ω_p , a velocity boundary condition is applied from the structural vibration. This is formalized as follows,

$$\mathcal{L}_v [p(\mathbf{x})] = i\omega w(\mathbf{x}), \quad (6.8)$$

where \mathcal{L}_v is the normal velocity operator $\mathcal{L}_v(\bullet) = \frac{i}{\rho_a \omega} \frac{\partial \bullet}{\partial n_a}$.

The acoustic radiated power can be used as a measure of the noise emitted from a structure. Supposing that the surface of the plate is part of an infinite plane, the pressure at a point $\mathbf{x} \in \Omega_a$ can be computed by means of the Rayleigh integral,

$$p(\mathbf{x}) = \frac{i\omega\rho_a}{2\pi} \int_{\Omega_p} v_n(\mathbf{y}) \frac{e^{-ik_a R}}{R} d\Omega_p(\mathbf{y}), \quad (6.9)$$

where $R = |\mathbf{x} - \mathbf{y}|$, and v_n is the normal velocity. The acoustic power radiated from the vibrating plate can be computed by integrating the acoustic intensity over the surface Ω_p , obtaining the following expression,

$$P_{\text{acou}} = \frac{\omega\rho_a}{4\pi} \int_{\Omega_p} \int_{\Omega_p} v_n(\mathbf{y}) \frac{\sin(k_a R)}{R} v_n^*(\mathbf{x}) d\Omega_p(\mathbf{y}) d\Omega_p(\mathbf{x}), \quad (6.10)$$

which can be computed as suggested in [86]. A singularity occurs when $R = 0$. However, as $R \rightarrow 0$, $\sin(k_a R)/R \rightarrow k_a$. In the following application cases, integral (6.10) has been integrated by using 400 Gauss points over the surface Ω_p .

6.3 Optimization procedures

This section presents the key points of the optimization procedure proposed in the following chapter. In sec. 6.3.1, the choice of the band-averaged input power as a cost function, is discussed. Section 6.3.2 is dedicated to the description of the main features of GAs. Finally, sec. 6.3.3 summarizes the main aspects of the optimization procedure.

It is worth noting that the use of Butterworth-weighted frequency averaging is only illustrative in the following examples. The approach can be easily extended to the use of classic quadrature in the complex plane, as presented in ch. 4.

6.3.1 Minimization of the power injected into the structure

When dealing with the optimization of the dynamic behavior of a structure, it is of major interest to minimize the vibration. Depending on the problem, one

may be interested in minimizing either the global or the local response. On the other hand, if the main concern is with the improvement of the noise emission, it may be of importance to minimize the acoustic power radiated from the structure.

The choice of the objective function plays a crucial role in the optimization process, and some computational aspects have to be taken into account. For example, using the acoustic radiated power, or any other acoustic-related quantity, as an objective function can lead to computationally demanding simulations. In fact, both structural and acoustic problems have to be solved for each iteration of the optimization process. This can significantly slow down the calculation time.

As an alternative to reduce the acoustic radiated power, Jog [96] suggests to minimize the power injected into the uncoupled structure. This strategy leads to a minimization of the input mobility of the structure. As a consequence, structural resonances are drifted away from the target frequency and the overall level of vibration is decreased. Moreover, when the vibro-acoustic model is uncoupled, the optimization is performed on the bare structure, reducing the computational cost. The potential of this approach has been shown by means of several examples in ref. [151].

A delicate additional aspect to consider when designing a mechanical component is the frequency range over which the performance of the structure should be optimal. Usually this choice can be related to the knowledge of the external excitations. Single-tone sources are rare in real-life applications. Moreover, the presence of uncertainty and variability may influence the nominal position of a resonance frequency, reducing the effectiveness of vibration control treatments. In these situations, optimizing the behavior over a band of frequencies is often preferred rather than targeting a single frequency. Nevertheless, the increased robustness of the configuration comes at a high computational price. In fact, the use of quadrature schemes to capture highly oscillating mobility functions can dramatically slow down the efficiency of the optimization scheme.

In this context, using the residue theorem to estimate band-averaged input power provides a powerful tool to perform accurate band evaluations at a reduced computational cost. This can efficiently be embedded in an optimization process and increase the overall performance of the procedure.

6.3.2 Genetic algorithms

For this type of problems, GAs can be used [72, 87]. Unlike gradient-based optimization schemes, GAs are inspired by natural selection processes, where the best individuals dominate the population [207]. As a first step of the optimization scheme, a random population is created and ranked based on

the fitness (objective) function. Individuals with a higher ranking position have higher probability of being selected for reproduction. The successive generation consists of children created by crossover, namely randomly mixing the selected parents. In this process, the so-called mutation is also performed, by which the genetic sequence of an individual is mutated according to a random variable. The process is repeated until one of the convergence criteria is reached. The main advantage of evolutionary algorithms is their robustness, having an increased chance of finding a global optimum or near global optimum. On the other hand, they have a high computational cost.

The minimization of the input power, averaged over the interval I , can be formulated as a single objective (SO) optimization,

$$\min \langle P_{\text{in}} \rangle_I, \quad (6.11)$$

subject to the side constraints,

$$\underline{b}_j \leq b_j \leq \bar{b}_j, \quad j = 1, \dots, n_{\text{var}}, \quad (6.12)$$

where each of the n_{var} elements of the design variable vector, \mathbf{b} , is defined by the upper and lower bounds, $\bar{\mathbf{b}}$ and $\underline{\mathbf{b}}$, respectively. However, many optimization problems in engineering require the minimization of n_{obj} (conflicting) objectives. In this case, the problem is referred to as a multi-objective (MO) optimization and analogously to (6.11), it can be formulated as,

$$\min \left[\langle P_{\text{in}} \rangle_{I_1}, \langle P_{\text{in}} \rangle_{I_2}, \dots, \langle P_{\text{in}} \rangle_{I_{n_{\text{obj}}}} \right], \quad (6.13)$$

subject to the side constraints (6.12). Two main strategies exist to deal with MO problems [153, 224]. According to the first category, the MO functions can be aggregated into a single function by means of a weighted sum, and the problem can be solved with SO optimization strategies. Here the choice of the weights plays a crucial role. Alternatively, it is often preferred to know the so-called Pareto front, which is the locus on which all the non-dominated solutions lie.

In the following application case, the first strategy is applied to solve an MO problem. The power injected into different bands will be aggregated, weighted with equal weights and minimized by using GAs. However, the choice of the weights is in general not straightforward. In fact, if the power injected into one band is predominant with respect to other bands of interest, one could end up with a solution which attempts to minimize such a band and leave the others unaltered. Although this might be the best configuration, a different choice of the weighting factors may lead to a solution that is more effective for other bands.

6.3.3 Summary and advantages of the procedure

The aim of this section is to summarize the procedure adopted for the optimization and highlight the advantages in using the WBM in this context. Among all the properties of the WB modeling for vibration problems, two are of particular interest for this specific application. First of all, the WBM is a meshless approach. Consequently, it allows locating the resonator at any point over the plate and it does not require any re-meshing procedure. Using classic FEM would be much more disadvantageous, as the position of the DVA is confined to nodal points. Secondly, the WBM shows a higher convergence rate than element-based approaches, and a lower number of degrees of freedom is needed to model the problem. This becomes even more important when point connections are present, as they introduce a local perturbation, which requires a high mesh resolution to be properly captured. For point connections, another advantage is that the system of equations consists of a main part representing the bare system, \mathbf{A} and \mathbf{f} , and a number of rows and columns, \mathbf{B}_{pc} , \mathbf{C}_{pc} , \mathbf{D}_{pc} and \mathbf{f}_{pc} , of which the size is proportional to the number of point connections. Consequently, moving the position of a DVA or changing its properties does not require a change in the main system of equations.

To evaluate the input power over a band, only a few computations at complex frequencies are required, according to the procedure presented in ch. 3. So, the small matrices of the bare system can be computed at the aforementioned complex frequencies and stored in memory. At each iteration they are recalled and complemented with the point connection contributions. The problem is solved for the wave contribution factors, and the input power is computed.

GAs are used to solve the following optimization problem, that is performed in four steps:

1. Problem definition. Data related to the problem geometry, material, boundary conditions, excitation etc. are defined. Parameters of the GA are specified, i.e. tolerance, population size, crossover fraction, etc.
2. Determination of the n complex frequencies of analysis. According to the order of the Butterworth filter to use, the complex frequencies, at which the solution has to be computed, are determined,

$$\mathbf{z} = [z_1, z_2, \dots, z_k, \dots, z_n]. \quad (6.14)$$

3. Evaluation and storage of system matrices. The WB matrices and right-hand side vectors for the bare system are computed at each complex frequency,

$$\mathbf{A}_1, \mathbf{A}_2, \dots, \mathbf{A}_k, \dots, \mathbf{A}_n, \mathbf{f}_1, \mathbf{f}_2, \dots, \mathbf{f}_k, \dots, \mathbf{f}_n. \quad (6.15)$$

Since n is normally small and the WB matrices have a reduced number of DOFs, storing the matrices does not require large memory consumption.

4. Optimization process. At each iteration, l , system matrices are recalled and complemented with a number of columns and rows equal to the number of point connections considered in the problem. Also the right-hand side dimensions are increased,

$$\begin{bmatrix} \mathbf{A}_k & \mathbf{B}_{pc,k,l} \\ \mathbf{C}_{pc,k,l} & \mathbf{D}_{pc,k,l} \end{bmatrix} \begin{Bmatrix} \mathbf{c}_{k,l} \\ \mathbf{w}_{pc,l} \end{Bmatrix} = \begin{Bmatrix} \mathbf{f}_k \\ \mathbf{f}_{pc,k,l} \end{Bmatrix}, \quad (6.16)$$

the letter k denotes the k -th complex frequency. Successively, the system of equations is solved, and the input power is evaluated. This process is repeated until convergence is reached and the band-averaged input power is minimized.

The applicability of this strategy can easily be extended to an FE model. In fact, introducing a DVA at a certain point location involves the modification of the mass, stiffness and damping matrices of the corresponding node. Matrices can be computed only once and stored in memory. Within the iterative optimization procedure, the best configuration can be found. Although the WBM is more advantageous for this specific application, the proposed strategy can be used for cases where the potentialities of FEM are exploited at best, i.e. for complex geometries.

The algorithms applied here for the optimization process belong to the category of non-gradient based. Nevertheless, the procedure can be extended to gradient based algorithms, as shown by Koo [103]. In ref. [103], FEM is used to simulate the behavior of a vibrating cube, in which the thickness of a group of shell elements represents a set of design variables. The Adjoint Variable Method [29, 104] is used for the optimization process, while the residue theorem is used to evaluate the band-averaged power injected by harmonic point force excitations. This combination leads to a drastic abatement of the acoustic power radiated from the structure, with a significant improvement of the computational performance.

6.4 Application cases

The following section is dedicated to the application examples. Model properties and problem details are reported in sec. 6.4.1. In sec. 6.4.2, the numerical procedures employed to compute the objective function are introduced and used in sec. 6.4.3, for SO optimization, and in sec. 6.4.4 for multiple band minimization.

6.4.1 Problem description

The plate under consideration is simply supported and rectangular of dimensions 1×0.6 m, 1 mm thick. The material is steel of Young's modulus 210 GPa, density 7800 kg/m^3 and Poisson ratio 0.3. The damping mechanism is hysteretic with constant loss factor equal to 0.01. The plate is baffled and radiates in air characterized by a density of 1.225 kg/m^3 , and a speed of sound of 340 m/s. The source is a harmonic point force arbitrarily chosen at (0.85, 0.15)m.

The WBM is used to predict the behavior of the plate, and a truncation factor $T = 2$ is chosen. To evaluate the acoustic radiated power, the Rayleigh approach is used, as described in eq. (6.10).

Two frequency ranges are of interest in the following examples. The first band covers the region from 26 Hz to 32 Hz. Over that band, two modes are strongly contributing to the system response and they are located at 29.1 Hz (3,1) and 29.9 Hz (1,2). The second frequency range of interest sweeps frequencies from 58 Hz to 79 Hz. In this band, four modes are contributing, and two of them strongly radiate. They are located at 64.1 Hz (1,3), 66.9 Hz (4,2), 68.5 Hz (5,1) and 71.6 Hz (2,3). All the mode shapes are indicated in fig. 6.2.

According to classic applications, the vibration level of the plate can be reduced by tuning the DVAs on structural resonances. This procedure leads to a reduction of the vibration at the target frequency, but it may result in a worse performance for the neighboring frequencies. To reduce this effect, a de-tuned configuration is often preferred, resulting into a mass-like or stiffness-like impedance of the resonator. This allows improving the vibrational behavior also for other frequencies. To further decrease the vibration level, several DVAs can be added to the host structure, especially when more than one mode is tackled. In the following applications, a reduced number of DVAs is used to tackle a band on which several modes are contributing. This serves as a pure example to show the potential of the present strategy for vibration control problems. However, also in this case, the number of DVAs can be increased to obtain superior noise and vibration reduction.

6.4.2 Objective function evaluation and optimization

Two types of optimization problems are carried out. The first one focuses on the minimization of the input power over the band (58,79) Hz as an SO optimization. The second one attempts to find the optimal design on the bands (26,32) Hz and (58,79) Hz, using an MO optimization process. In all optimization processes, the design variables are the coordinates of the DVAs

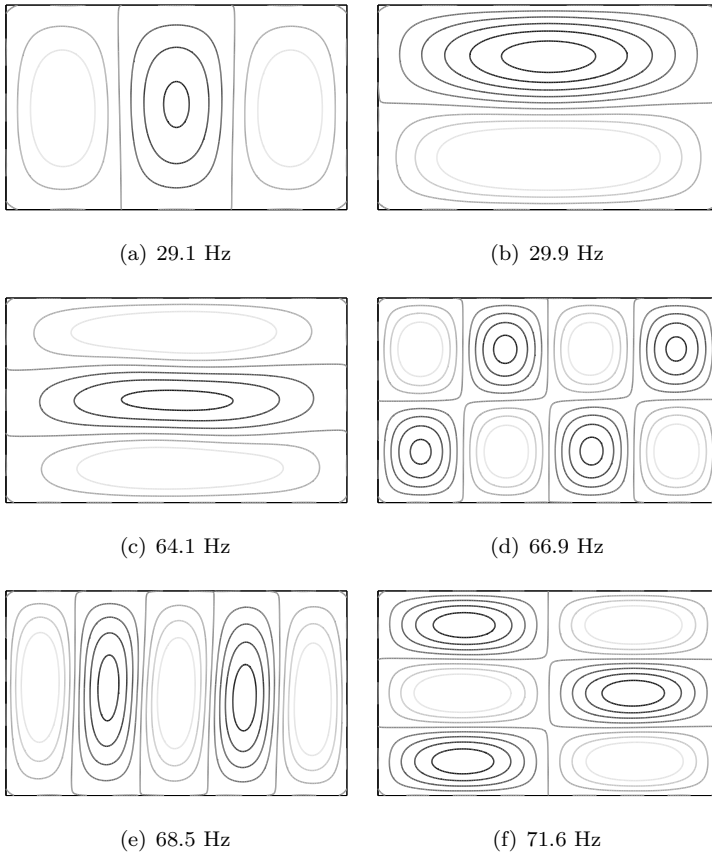


Figure 6.2: Mode shapes inside the first band, (a) and (b), and the second band, (c) to (f).

on the plate and their resonance frequencies.

Different techniques are used to compute the objective function. Butterworth filters of order 4 (B4), 8 (B8) and 20 (B20) are used to evaluate the band-averaged power injected into the structure. Besides the number of computations, these schemes also differ in the weighting function. For a filter of order 4, a small weight is still assigned to frequencies outside the band. This is shown in fig. 6.3, where the square magnitude of a Butterworth filter is illustrated for the aforementioned cases. With increasing order, the shape of the filter becomes closer to that of a rectangular window. Alternatively, the trapezoidal scheme is used as a quadrature rule to estimate the band power.

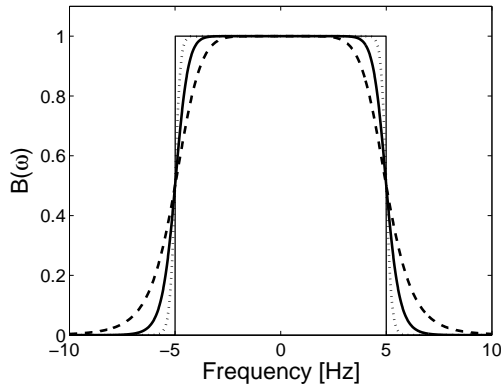


Figure 6.3: Comparison between a rectangular window (thin solid line) and function $B(\omega)$ of order 4 (dashed line), 8 (thick solid line) and 20 (dotted line). The window is centered at 0 Hz and has a cut-off frequency equal to 5 Hz.

Three different integration steps are tested, namely 1 Hz (T1.0), 0.5 Hz (T0.5) and 0.2 Hz (T0.2). Finally, to compare the results provided by the input power minimization with a more classic approach, the space- and frequency-averaged displacement is used as an objective function. In this case, the trapezoidal rule with 0.5 Hz step is used to average over the frequency (D-T0.5), while 1600 integration points are taken over the plate surface. In general, using classic quadrature schemes is more demanding, and the inaccuracy due to the rough integration step also influences the convergence of the optimization algorithm, as it will be shown in the following. Note that T1.0, T0.5 and T0.2 require 7, 13 and 31 function evaluations over the first band, and 22, 43 and 106 for the second band, respectively. By using the Butterworth-weighted frequency averaging, the function has to be evaluated only 4, 8 or 20 times according to the number of complex frequencies.

Regarding the optimization schemes, the objective is normalized with respect to the power injected into the bare plate, and the convergence is always reached when the average change in the fitness value is less than the tolerance (10^{-7}) for 10 successive generations.

To quantify the reduction with respect to the initial design, a reduction coefficient, $r_{(\bullet)}$, is used and is computed by means of the following relation

$$r_{(\bullet)} = 100 \cdot \frac{\bullet_{\text{ini}} - \bullet_{\text{opt}}}{\bullet_{\text{ini}}}, \quad (6.17)$$

where \bullet_{ini} stands for the initial value and \bullet_{opt} stands for the optimized value. Reduction coefficients will refer to the band-averaged input power, acoustic

Simul. ID	B4	B8	B20	T1.0	T0.5	T0.2	D-T0.5
x_{pc} [m]	0.879	0.879	0.878	0.878	0.878	0.878	0.870
y_{pc} [m]	0.124	0.124	0.125	0.123	0.125	0.125	0.137
f_{res} [Hz]	85.9	85.9	86.1	86.7	86.0	86.1	72.4
t_{opt} [s]	198.0	406.0	1256.6	1590.7	2412.3	6059.9	4266.3
Gen. [-]	41	44	55	62	46	48	51
r_{pow} [-]	74.0	74.0	74.0	74.0	74.0	74.0	70.3
r_{disp} [-]	92.5	92.5	92.2	92.0	92.3	92.2	95.6
r_{rad} [-]	88.4	84.4	87.9	87.2	88.0	87.9	95.0

Table 6.1: Optimal configurations for the case of SO optimization.

radiated power and square averaged displacements. The averages are computed using numerical quadrature with trapezoidal rule and 0.1 Hz sampling step. All simulations are run on a Windows 7 64-bit desktop machine, processor Intel(R) Core 2 Quad CPU, clock rate 3 GHz and 8 GB RAM. GAs in Matlab are used to perform the optimization procedures.

6.4.3 Single objective optimization

In this case, one DVA is used to reduce the vibration over the second band. The three design variables are the x and y position of the DVA on the plate and its resonance frequency. The mass of the resonator is 2% of the mass of the bare plate, and the damping ratio is 0.1. Regarding the GA settings, the population consists of 30 individuals and the crossover fraction is 0.5.

The optimal configurations and optimization parameters are reported in tab. 6.1. When the input power is minimized, all the optimization processes lead to similar designs. The resonator is located close to the excitation point, as it might be expected, and its resonance frequency falls above the interval of interest (86.1 Hz). It can be verified that this configuration minimizes the band-averaged input power.

All optimal designs present a noticeable improvement over the band. Data related to solving times show the computational advantages of the proposed approach, which are evident when comparing the design B4 with the ones obtained with more refined schemes.

Minimizing the space- and frequency-averaged displacement leads to configuration D-T0.5, reported in tab. 6.1. The location of the resonator is not far from the one provided by the input power minimization. However, the resonance frequency for the D-T0.5 case falls inside the frequency band under

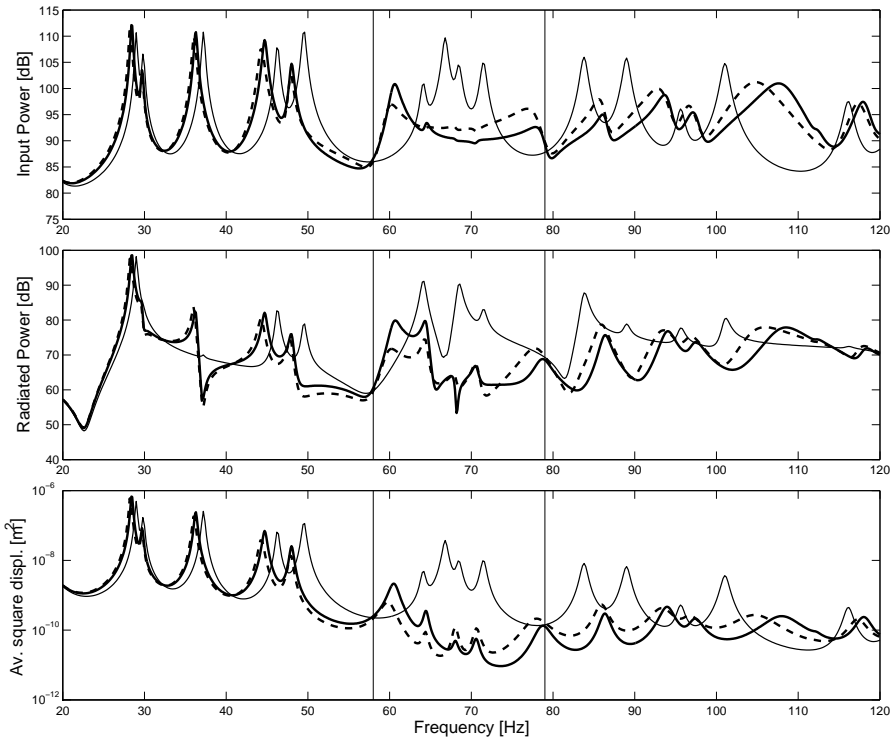


Figure 6.4: SO optimization. Initial configuration (thin solid line); B20 (thick solid line); D-T0.5 (dashed line).

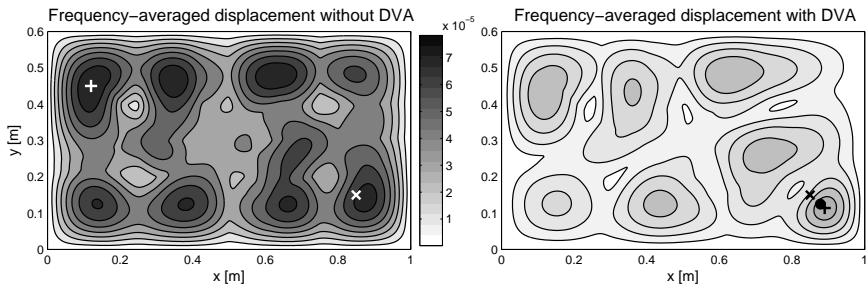


Figure 6.5: Contour plot of frequency-averaged displacement, $\langle |w| \rangle$, over the band (58, 79) Hz. The symbol \times indicates the point force, \bullet the location of the DVA, and $+$ the maximum displacement point ($7.83e-5$ m without DVA and $2.88e-5$ m with DVA). The unit of the contour map is [m].

Parameter	Deviation
x_{pc} [m]	± 0.005
y_{pc} [m]	± 0.005
f_{res} [Hz]	± 1
m_{pc} [%]	± 25
c_{pc} [%]	± 25

Table 6.2: Deviation from the nominal values for the DVA parameters.

analysis. The reduction of radiated power and averaged displacement of the D-T0.5 configuration are higher than the ones of the B-series. However, this comes at a much higher computational cost, which becomes significant when comparing the performance of design B4 with D-T0.5. The improvements on the narrow band response can be observed in fig. 6.4, which compares designs B20 and D-T0.5 in terms of input power, radiated acoustic power and averaged square displacement. The four peaks present on the narrow band input power are reduced over the frequency interval. This leads to strong improvements of the vibrational behavior of the panel. The configuration B20 presents a higher input power peak compared to the D-T0.5, which also leads to a higher radiated power and displacement level. However, as reported in tab. 6.1, the power injected over the band is smaller for the B20 configuration.

Figure 6.5 shows the local behavior of the frequency-averaged displacement over the plate for the initial configuration and the B20 design. The presence of the resonator allows reducing the overall vibration of the plate in an average sense.

To verify the robustness of the optimal configuration B20, all five DVA parameters are perturbed from their nominal values according to uniform distributions with boundaries reported in tab. 6.2. All five parameters are uniformly distributed variables. Accordingly, a set of 300 random samples has been considered to compute the mean response and the upper and lower bounds of the input power, as shown in fig. 6.6. The deviation of the samples from the mean response is larger inside the band than for other frequencies. However, the perturbed design preserves improved characteristics compared to the initial one.

6.4.4 Multi-objective optimization

MO optimization is investigated in this example. As previously mentioned, there are two bands of interest, namely from 26 to 32 Hz and from 58 to 79 Hz. Two DVAs are used to reduce the vibration. The mass of each device is equal

to 0.1% of the mass of the bare plate, and their damping ratio is equal to 0.1. Six design variables are considered, corresponding to x and y positions and the resonance frequencies of the two resonators. The GA population consists of 40 individuals and the crossover fraction is 0.5.

The optimal configurations are shown in tab. 6.3, where the subscripts refer to the DVA when describing the location and resonance, and to the band

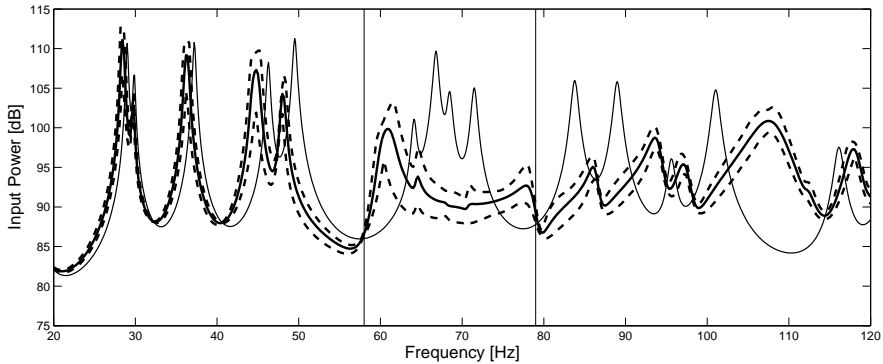


Figure 6.6: Effect of perturbation on DVA properties for the case of SO optimization. Initial configuration (thin solid line); ensemble average (thick solid line); upper and lower bounds of the ensemble (dashed lines).

Simul. ID	B4	B8	B20	T1.0	T0.5	T0.2	D-T0.5
$x_{pc,1}$ [m]	0.502	0.503	0.505	0.722	0.701	0.505	0.504
$y_{pc,1}$ [m]	0.408	0.410	0.413	0.249	0.258	0.412	0.367
$f_{res,1}$ [Hz]	29.9	29.5	29.5	59.5	62.1	29.2	28.8
$x_{pc,2}$ [m]	0.882	0.883	0.882	0.871	0.894	0.882	0.874
$y_{pc,2}$ [m]	0.121	0.123	0.124	0.131	0.118	0.122	0.135
$f_{res,2}$ [Hz]	79.9	80.2	80.2	81.4	84.6	80.2	70.9
t_{opt} [s]	747.6	1839.1	4420.2	1933.4	6808.6	13167.2	9388.5
Gen. [-]	66	82	79	43	80	63	62
$r_{pow,1}$ [-]	30.2	30.6	30.5	-2.9	-1.9	30.7	22.4
$r_{disp,1}$ [-]	90.1	90.0	89.5	-1.1	-1.9	89.6	93.3
$r_{rad,1}$ [-]	87.5	88.1	87.9	8.7	-3.9	88.4	89.7
$r_{pow,2}$ [-]	51.5	51.5	51.6	63.8	61.7	51.5	49.8
$r_{disp,2}$ [-]	86.7	86.4	86.3	92.7	91.7	86.4	92.3
$r_{rad,2}$ [-]	66.6	66.3	66.2	79.4	74.6	65.9	87.0

Table 6.3: Optimal configurations for the case of MO optimization.

for the reduction coefficients. Negative values in the reduction coefficients indicate that the optimal design is worse with respect to the initial one. This happens when rough trapezoidal quadrature schemes are not able to accurately represent the band value, and the optimization algorithm leads to a result which is not satisfactory. On the contrary, the residue theorem allows an accurate band evaluation, and results provided by the B-series do not differ much from each other. This explains why configurations T1.0 and T0.5 yield reduction coefficients r_{pow} , which are higher than the others on the second band, but much lower on the first one. In those configurations both DVAs tackle the same band.

In general, using the Butterworth-weighted frequency averaging procedure allows a significant speed up of the computation. This is clear when comparing configurations B4 and T0.2. In fact, although the optimal designs are not very different from each other, a speed up factor of about 17 can be observed. Also in this case, the minimization of the input power leads to a reduction of the radiated sound power and the averaged displacement over the plate.

Although the lowest displacement level is not achieved in the B-series designs, reduction coefficients are not much lower than the D-T0.5 ones, especially on the first band. This can also be observed in fig. 6.7, where the narrow band responses of configurations B20 and D-T0.5 are illustrated. Conclusions similar to the ones for the previous example can be drawn for results on the band (58, 79) Hz, although the improvement is lower due to the reduced weight of the device in the current application. On the other hand, configurations B20 and D-T0.5 provide similar responses over the first band. From a computational point of view, the proposed approach highly outperforms the strategy adopted to design the D-T0.5 configuration, proving that it can be a very efficient tool for optimizing the DVA parameters in an early stage design.

In fig. 6.8 and 6.9, the frequency-averaged displacements are illustrated for the configuration B20. The first resonator tackles the modes present in the first band and is located close to the center of the plate. Its resonance falls inside the band of interest (29.5 Hz) and allows achieving a significant reduction of the overall displacement level. The second resonator is located close to the excitation point, like in the previous case, and its resonance frequency is above the band (80.2 Hz).

The robustness of configuration B20 against variability is assessed in fig. 6.10. The DVA parameters are perturbed according to tab. 6.2, and 300 random samples have been used to predict the ensemble behavior. Similarly to the previous example, over the bands of interest, the scatter on the response is larger than for other frequencies. However, the perturbation does not worsen the overall performance of the optimal design, compared to the initial behavior of the system.

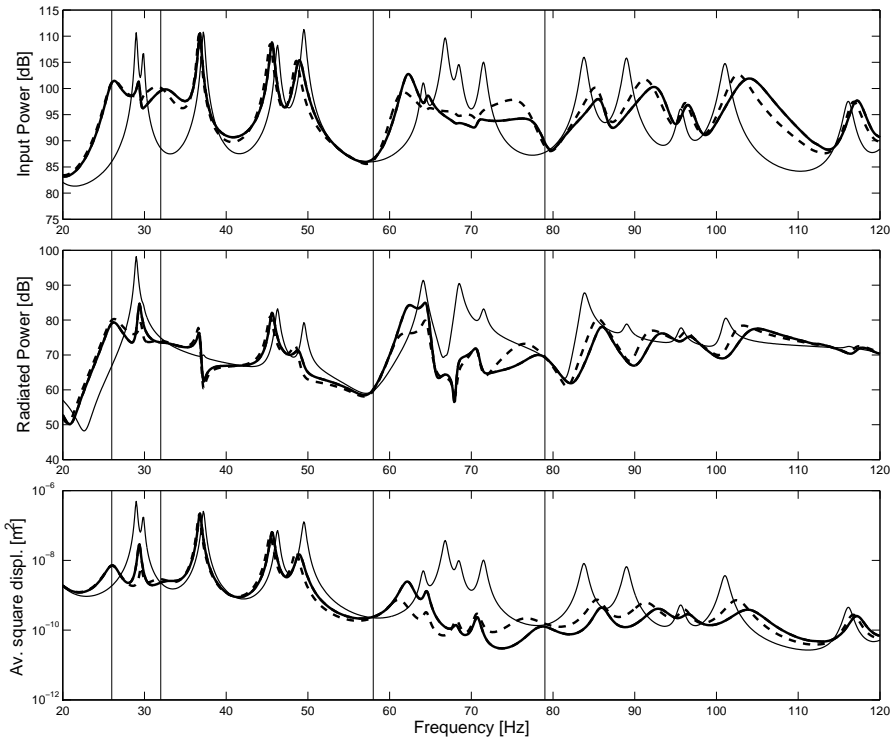


Figure 6.7: MO optimization. Initial configuration (thin solid line); B20 (thick solid line); D-T0.5 (dashed line).

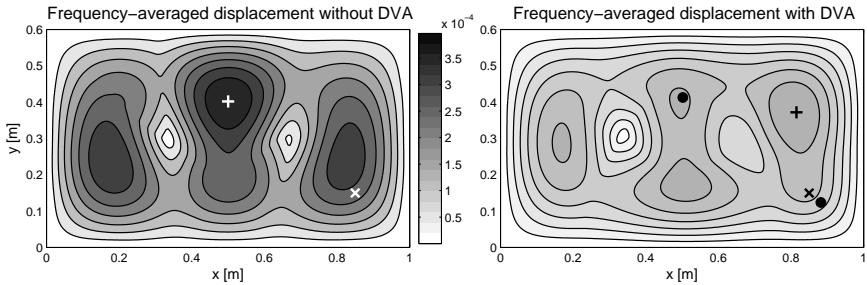


Figure 6.8: Contour plot of frequency-averaged displacement, $\langle |w| \rangle$, over the band (26, 32) Hz. The symbol \times indicates the point force, \bullet the location of the DVA, and $+$ the maximum displacement point ($3.97e-4$ m without DVA and $1.40e-4$ m with DVA). The unit of the contour map is [m].

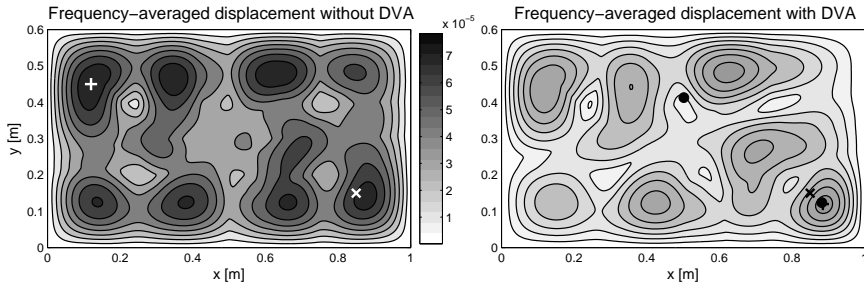


Figure 6.9: Contour plot of frequency-averaged displacement, $\langle |w| \rangle$, over the band (58, 79) Hz. The symbol \times indicates the point force, \bullet the location of the DVA, and $+$ the maximum displacement point ($7.83\text{e-}5$ m without DVA and $3.76\text{e-}5$ m with DVA). The unit of the contour map is [m].

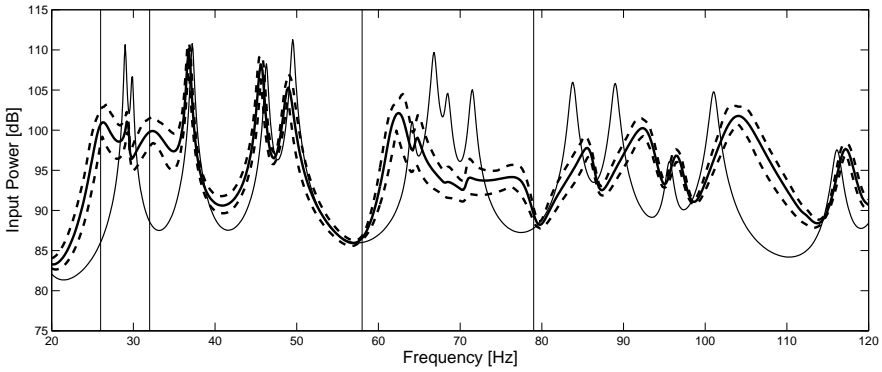


Figure 6.10: Effect of perturbation on DVA properties for the case of MO optimization. Initial configuration (thin solid line); ensemble average (thick solid line); upper and lower bounds of the ensemble (dashed lines).

6.5 Conclusion

This chapter presents a strategy to reduce the global vibration and radiated acoustic power, by minimizing the input power over a frequency band. The main feature of the present approach is the efficiency achieved by exploiting the residue theorem. Instead of requiring a refined quadrature integration, few calculations at complex frequencies allow accurate band computations, regardless of the bandwidth. This allows to significantly speed up the optimization process over frequency bands.

The strategy has been applied to optimize the properties of DVAs in order to improve the dynamic behavior of a baffled plate. In the first example, the properties of one DVA are optimized to minimize the power injected by a point force over a single frequency band. In the second one, the characteristics of two DVAs are optimized to tackle two frequency bands. GAs have been used as an optimization tool in combination with the WBM, which shows high potential and efficiency for this application. For both examples, the optimization strategy has been proven to be very effective in reducing the radiated acoustic power and the overall displacement level over the band. A significant gain in computation time is achieved compared to classic schemes. Finally, the optimal configurations have been proven to be robust against DVA parameter variability.

Although in this application the optimization strategy has been tested only on baffled plates, the underlying idea can be easily extended to more complex cases. A possible application could be related to the automotive field, where one may be interested in minimizing the power injected by a broad-band vibration of the engine into the car frame. The present techniques can be used to quickly determine a design configuration to reduce the global vibration level.

Chapter 7

The Lorentzian-weighted frequency averaging

So far, the focus was on the computation of averages taken over bands of frequencies. In ch. 3, such a procedure is performed by approximating the features of a rectangular window by means of the square magnitude of a Butterworth filter. With increasing order, the shape of the filter comes closer to the one of an ideal square window. On the other hand, when the order of the filter is one, the square magnitude of a Butterworth filter coincides with the Lorentzian function.

The Lorentzian is a bell-shaped curve and is defined by a center frequency and a shape parameter. Since it presents only one pole in the LHP, the Lorentzian-weighted frequency average can be computed by adding to the real frequency of analysis an imaginary part, which depends on the shape parameter. This characteristic makes it particularly attractive, as it can lead to an average over a broad frequency range by means of a single computation. However, due to its bell-shape, the Lorentzian only roughly approximates a rectangular window, and its use is not as straightforward and intuitive as for band averaging.

The purpose of this chapter is indicating possible ways of employing the Lorentzian-weighted frequency averaging in the context of vibro-acoustic modeling. Rather than drawing definitive conclusions regarding its use, the objective is to initiate the exploration of this novel area, proposing possible applications and directions for future research.

After the introduction of the Lorentzian in sec. 7.1, three applications are explored in the context of noise and vibration simulations.

- **Evaluation of the ensemble-averaged input power.** Under ergodic assumption, frequency averaging can be employed to estimate the ensemble mean behavior of perturbed systems, with significant reduction of computations. In this context, the Lorentzian function can be used as a weighting function to perform frequency averaging and estimate the ensemble mean input power. However, to compare frequency- and ensemble-averaged quantities, the choice of the width of the Lorentzian is not straightforward. This is the main research issue addressed in sec. 7.2, where two strategies are proposed to tune the shape parameter on the amount of variability present in the system.
- **Computation of the direct field dynamic stiffness.** The direct field dynamic stiffness allows the calculation of the power exchanged by a system and is widely used in the context of hybrid approaches as well as for CLF computations in SEA [181] (sec. 2.2.5). One way of evaluating the direct field dynamic stiffness is through the ensemble averaging of the dynamic stiffness, and the use of the Lorentzian-weighted frequency averaged dynamic stiffness in this context is investigated in sec. 7.3.
- **Lorentzian as mass-frequency density function in the FST.** A key parameter for the application of the FST, as proposed by Pierce [166], is the mass-frequency distribution function. This allows the definition of the fuzzy impedance, which is a key ingredient for the application of the FST (sec. 2.2.5). In sec. 7.4, the Lorentzian function is used as a mass-frequency density function. Its advantageous mathematical features allow simplifying the integration procedure and the calculation of the impedance.

The chapter is concluded with sec. 7.5, where some remarks and observations are reported.

7.1 The Lorentzian function

The Lorentzian function, also known as Cauchy distribution, is a single-peak function of mathematical form,

$$L(\omega) = \frac{1}{\pi\gamma} \frac{1}{1 + \left(\frac{\omega - \omega_0}{\gamma}\right)^2}, \quad (7.1)$$

where ω_0 is the location of the peak of the distribution and γ is a shape parameter, which specifies the half-width at half-maximum. The Lorentzian

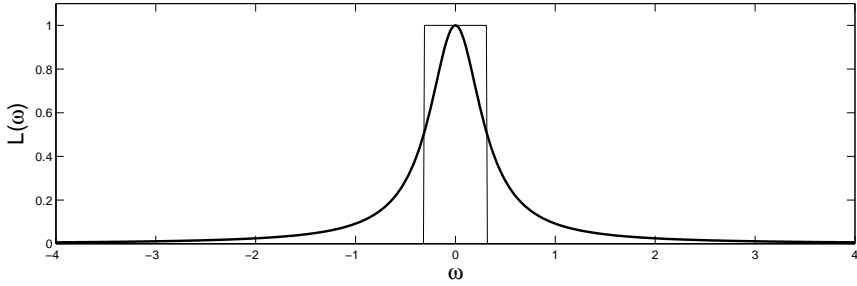


Figure 7.1: Lorentzian function centered at $\omega_0 = 0$ and with $\gamma = 1/\pi$.

is symmetric around ω_0 and its features are illustrated in fig. 7.1.

The maximum amplitude of the Lorentzian is equal to $1/(\pi\gamma)$ and the corresponding cumulative distribution function is,

$$l(\omega) = \frac{1}{2} + \frac{1}{\pi} \arctan\left(\frac{\omega - \omega_0}{\gamma}\right). \quad (7.2)$$

Unlike the Normal distribution, the Lorentzian belongs to the family of heavy-tailed distributions, as its tails are not exponentially bounded. Consequently, its mean is undefined and its variance is infinite. More in general, the Lorentzian function has no finite moments of any order. These characteristics make it suitable to model extreme risk analysis and financial problems. The Lorentzian can also be considered as a ratio distribution between two centered Normal distributed variables. For this reason, it is also called Normal ratio distribution.

As it can be observed from eq. (7.1), the Lorentzian function corresponds to the square magnitude of a Butterworth filter of order one. The shape parameter γ corresponds to the cut-off frequency ω_C of a Butterworth filter. Two poles are located in the complex frequency plane, at $\omega_0 \pm i\gamma$.

7.2 Evaluation of the ensemble average input power

Most manufactured systems with nominally identical properties show a significant deviation from their nominal characteristics [102]. This is mainly due to the production and assembly processes, as well as the operational and environmental conditions, which influence the system properties. From

a computational point of view, the presence of such a variability creates several difficulties for the prediction of the dynamic behavior of the ensemble of structures. For this reason, when the statistical overlap is sufficiently high [141], the response is considered ergodic and the ensemble mean can be approximated with frequency average values [131]. In this regard, the Lorentzian allows a straightforward evaluation of the frequency-averaged input power, but in order to represent the ensemble mean the parameter γ has to be properly tuned.

The main goal of this section is to investigate the possible correlation between γ and the amount of variability present in the system, in order to predict the average input power for the ensemble of structures. Two strategies to tune the parameter γ , are proposed in sec. 7.2.2 and applied to single- and multi-component systems in sec. 7.2.3 and 7.2.4, respectively. Additional comments are reported in sec. 7.2.5.

7.2.1 Lorentzian-weighted frequency-averaged input power

As discussed in ch. 3, the frequency-averaged input power can be expressed as an integral over the whole frequency axis,

$$\langle P_{\text{in}} \rangle_W = \int_{-\infty}^{+\infty} W(\omega) P_{\text{in}}(\omega) d\omega, \quad (7.3)$$

where $W(\omega)$ represents a generic weighting function. So far, the interest has been mainly focused on approximating the band value, which requires $W(\omega)$ to be as close as possible to a rectangular window. Under the hypothesis of system poles lying in the UHP, the Butterworth-weighted frequency average reads,

$$\langle P_{\text{in}} \rangle_B = -\frac{1}{2} \frac{\pi A \omega_C}{n} \text{Re} \left\{ F_0^* \sum_{k=0}^{n-1} z_k u(\mathbf{x}_f, z_k) e^{-i\theta_k} \right\}, \quad (7.4)$$

where the notation is the same as adopted in ch. 3. When $n > 1$, the band-average is computed as a weighted sum of system responses computed at certain complex frequencies. If $n = 1$, the square magnitude of the Butterworth filter is equal to the Lorentzian, and the Lorentzian-weighted frequency average can be evaluated by computing the system response at one complex frequency corresponding to the pole of the weighting function, lying in the LHP,

$$\langle P_{\text{in}}(\omega_0) \rangle_L = \frac{1}{2} \text{Re} \{ v(\omega_0 - i\gamma) \cdot F_0^* \}, \quad (7.5)$$

where according to definition (7.1) and (3.7), $A = 1/(\pi\gamma)$. When the loss mechanism is modeled as hysteretic, system poles are not confined in the

UHP and (7.5) is an approximation rather than an equation. As a result the Lorentzian-weighted frequency averaging can be evaluated by shifting the frequency of analysis to a complex frequency, and a full frequency sweep can be run, providing the mean as a narrow-band response. However, the possibility of predicting the ensemble mean through the Lorentzian-weighted frequency average requires the γ parameter to be tuned, and contrarily to band averaging its choice is far from obvious and will be discussed in the next section.

7.2.2 The choice of the γ parameter

Variability in the system properties produces scatter on the natural frequencies and perturbs the nominal mode shapes. Based on this consideration, two strategies are proposed to tune the γ parameter.

First strategy

The first strategy takes into account the eigenfrequency statistics and the concept of Statistical Overlap Factor (SOF). The SOF was introduced by Manohar and Keane, to estimate the frequency beyond which individual modes cease influencing the response [141]. Its mathematical expression is defined as follows,

$$S_k = \frac{2\sigma_k}{\mu_k}, \quad (7.6)$$

where σ_k is the standard deviation of the k -th natural frequency from its mean value, and the mean frequency spacing, μ_k , is equal to the inverse of the modal density.

According to definition (7.6), statistical overlap occurs when the random change in the position of a natural frequency exceeds the mean frequency spacing. Consequently, the SOF provides a measure of the number of crossing and veering modes that can occur in a perturbed system. When the frequency is low, the perturbation has often negligible effects on the eigenvalue statistics and statistical overlap barely occurs. When the wavelength becomes smaller, the perturbation has a major influence on the position of the natural frequencies, which can cross or veer from each other. As a result, the SOF increases with frequency until it saturates, meaning that further perturbation has negligible influence on the eigenvalue statistics [98, 99, 112, 113].

To evaluate the statistics, an ensemble of perturbed systems is taken and, based on the eigenvalues of each realization, it is possible to extrapolate the mean and the variance of each perturbed natural frequency. To facilitate the prediction of the SOF for simple systems, it is possible to approximate it analytically using

a first-order perturbation analysis [100].

For rectangular plates perturbed by N_m randomly distributed masses of mass m_a , the variance of a natural frequency is approximated, as suggested in ref. [100]. The mathematical relation, based on a first-order perturbation analysis, assumes that the k -th natural frequency is modified according to the following relation,

$$\omega_k^2 \rightarrow \omega_k^2 \left[1 - \sum_{j=1}^{N_m} m_a \phi_k^2(\mathbf{x}_{m_j}) \right], \quad (7.7)$$

where ϕ_k is a mass normalized mode shape function associated to the k -th mode. As a result, the variance of the position of the k -th eigenvalue can be written as,

$$\sigma_k^2 = 0.3125 \frac{N_m m_a^2}{M_{\text{tot}}^2} \omega_k^2, \quad (7.8)$$

where M_{tot} is the total mass of the bare plate.

Expression (7.8) provides a useful guideline for the degree of statistical overlap, but is considered invalid as the SOF approaches unity, that is when the standard deviation σ_k is equal to half the mean frequency spacing, μ_k , and after which frequency further perturbation does not significantly influence the average response.

In principle, σ_k is a discrete function and quantifies the spread around a certain eigenfrequency, ω_k . However, it can be calculated as a continuous function of frequency,

$$\sigma^2 = 0.3125 \frac{N_m m_a^2}{M_{\text{tot}}^2} \omega^2. \quad (7.9)$$

This provides a general trend for the influence of the uncertainty on the system response over the frequency range of interest. In order to cover the scatter in the response and compare the Lorentzian averaging with ensemble averaging, the γ parameter is chosen equal to σ in eq. (7.9). As the position of the nominal natural frequencies is modified due to the perturbation, the width of the Lorentzian is taken to be large enough to encompass the spread in the response and provide a frequency-averaged value. After σ reaches unity, it is kept constant for higher frequencies. Accordingly, also γ is considered as a constant value.

Note that natural frequencies are not supposed to be Lorentzian distributed. The Lorentzian is only used as a weighting function to perform frequency averaging.

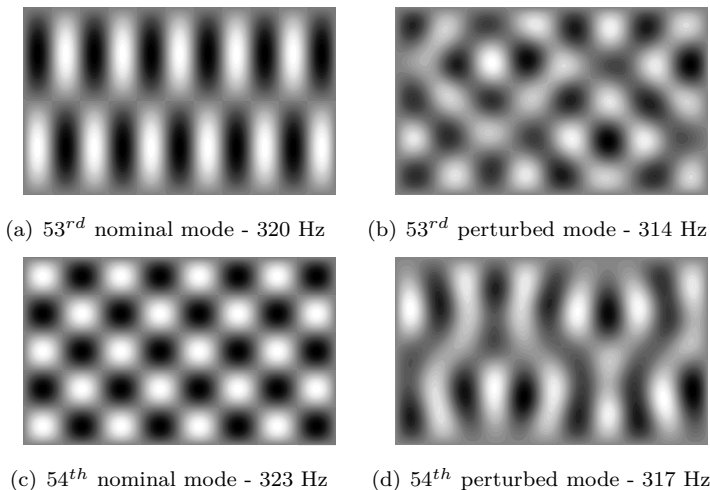


Figure 7.2: Comparison between nominal (left) and perturbed modes (right).

Second strategy

By applying the first approach, the information related to the behavior of the nominal system tends to get lost with increasing the statistical overlap, and the statistics are characterized by the mean distance between two successive eigenfrequencies. As an example consider fig. 7.2. Figures 7.2(a) and 7.2(c) show the 53^{rd} and 54^{th} nominal mode shapes and eigenfrequencies of a simply supported plate. When the plate is perturbed with 20 randomly distributed masses, the corresponding eigenfrequencies move from their nominal positions. Over the ensemble, the location of the perturbed eigenfrequencies leads to the determination of the statistics related to the corresponding nominal eigenfrequencies and successively to an estimate for σ_{53} and σ_{54} . According to the first strategy, the obtained σ can be used to tune γ .

The procedure described so far does not take into account the mode shapes of the corresponding eigenfrequencies and where they move with respect to their nominal position. Since the frequency averaging is performed on the nominal response, knowing how much each eigenfrequency moves when the corresponding mode shape is perturbed may provide indication on how to weigh its contribution. From fig. 7.2, one may conclude that when the 53^{rd} mode is perturbed, it can move to the 54^{th} eigenfrequency position, and similarly, the nominal 54^{th} can become the 53^{rd} in the perturbed configuration. Accordingly, the statistics differ from the ones only based on the eigenfrequencies.

Based on these consideration, the second proposed strategy attempts to

associate the perturbed mode shapes to the corresponding nominal ones, and to evaluate the eigenfrequency statistics accordingly.

Following this idea, after having computed the nominal natural frequencies and mode shapes, the eigenvalues and eigenvectors of the perturbed systems are evaluated through MC simulations. For each realization, perturbed mode shapes are associated to the nominal ones according to the highest Modal Assurance Criterion (MAC) value [56]. Perturbed eigenvalues are reorganized as function of the nominal mode shapes, and the statistics of the nominal natural frequencies are evaluated. Since the standard deviation obtained by applying this procedure, is highly oscillating, a linear approximation is used to regularize it and tune γ as explained in the previous strategy.

It is important to underline the conceptual limits of this procedure. At low frequencies, individual modes dominate the average response of the structure, and investigating the statistics of perturbed mode shapes can be relatively easy. As frequency increases, the behavior of the perturbed system becomes sufficiently random that the knowledge of the nominal mode shapes is no longer required to determine the average response. Consequently, due to the complexity of mode shapes, tracking modes becomes difficult and less reliable.

7.2.3 Simply supported plate

In this section, the Lorentzian-weighted frequency averaging is applied to evaluate the input power into a Kirchhoff plate perturbed by randomly distributed masses.

Model and numerical methods

The plate under investigation is simply supported of dimensions of 1×0.6 m and 1 mm thickness. The material is aluminum, Young's modulus 70 GPa, density 2700 kg/m^3 , Poisson ratio 0.3 and hysteretic damping coefficient 0.01. A harmonic unit force excitation is applied at point (0.7, 0.4)m. The system is perturbed by adding randomly distributed masses over its surface, for a total of four different cases consisting of 10, 20, 30 and 50 masses. Each mass is 0.2% of the total mass of the bare plate. The analyses are performed up to 1 kHz, in which frequency range the plate under consideration has approximately 185 modes.

Eigenfrequency statistics are estimated through MC simulations consisting of 200 realizations each. Natural frequencies and mode shapes are evaluated by means of an FE model consisting of 6165 nodes and 6000 quadrilateral shell

elements of mean size 10 mm. The software Nastran is used to solve the eigenproblems. On the other hand, to evaluate the narrow band input power, the WBM is employed with a truncation factor $T = 2$. The effect of point masses is included into the WB model by using the same strategy illustrated in sec. 6.2.1. In fact, if the resonator presents infinite rigidity, it behaves like a pure point mass, and the force-displacement relation (6.4) becomes $m_j\omega^2$. The formulation is fully detailed in ref. [208].

Results

The results provided by the two aforementioned strategies for the eigenfrequency statistics evaluation are illustrated in fig. 7.3. The thick irregular line represents the standard deviation evaluated without using mode-tracking. For all cases, σ increases with decreasing wavelength, until after a certain frequency further perturbation has negligible influence on the average response. Such a saturation point shifts towards lower frequencies with increasing perturbation. The thick regular line represents the analytical approximation, which is based on eq. (7.8), up to the point when the SOF reaches unity; for increasing frequencies, the standard deviation is kept constant. In all cases, the σ value computed by the MC simulation is approximated with reasonable accuracy by the analytical model.

Thin lines are representative for the statistics evaluated by retrieving nominal modes in the perturbed configurations. The irregular line indicates the result obtained from an MC simulation. When frequency is low, the thick and the thin lines are almost overlapping and perturbed mode shapes present eigenvalues not far from their nominal position. Contrarily to the previous strategy, the standard deviation does not level off with increasing frequencies, and the more the system is perturbed, the steeper the trend is. To approximate the behavior of the standard deviation a regular fitting over the whole set of data is performed, and it is represented by the thin regular lines. This allows regularizing the curves and expressing the γ parameter as a linear function. For high perturbation levels, the two strategies behave differently from each other. On the contrary, for a low number of masses, σ evaluated by mode tracking can be well approximated by the relation (7.8), considered over the whole frequency range.

Once the standard deviations are approximated, the γ parameter is tuned accordingly. To evaluate the ensembles, each of the following MC simulation consists of 50 realizations. Figure 7.4 shows the results when γ is tuned according to the first approach (thick regular line in fig. 7.3). After the SOF reaches unity, the approximation of the standard deviation is taken to be constant. Consequently, the width of the Lorentzian function does not increase

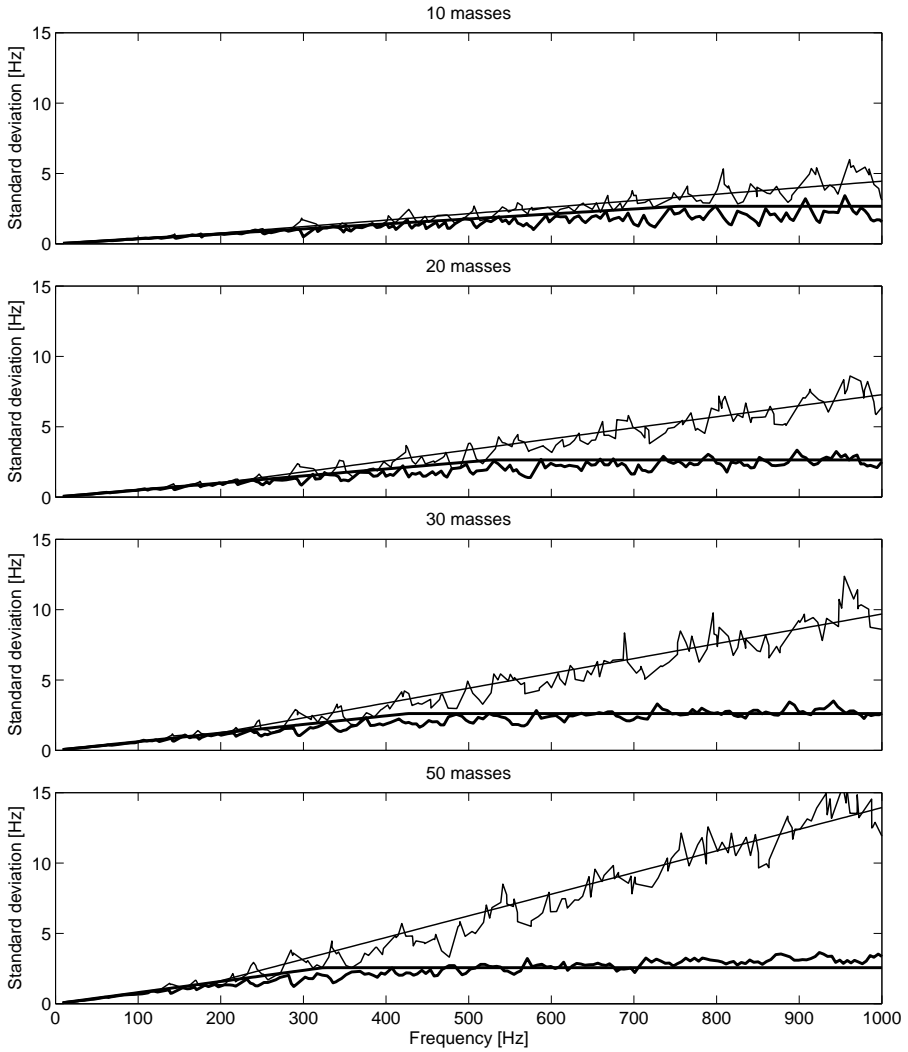


Figure 7.3: Standard deviation of the eigenvalue distributions evaluated without tracking nominal modes (thick irregular lines), by tracking nominal modes (thin irregular lines) and respective approximations (thick and thin regular lines).

with frequency and leads to an overestimation of the average response.

In fig. 7.5, the Lorentzian is tuned on the linear approximation of the standard deviation evaluated by using mode tracking. For all cases there is a good agreement between MC mean values and Lorentzian-weighted frequency averages, especially in the higher frequency range, where the previous approach overpredicts the mean response. Moreover, as frequency increases the frequency-averaged power tends to the input power into an infinite plate (dashed line).

7.2.4 Stiffened plates

The aim of the following section is to investigate the applicability of the Lorentzian-weighted frequency averaging to predict the ensemble behavior of a structure consisting of multiple components.

Model and numerical methods

The system under investigation is shown in fig. 7.6. The structure is made of two plates connected through a beam; all the edges of the structure are simply supported and the excitation is a unit point force located 0.1 m away from one end of the beam.

The Bernoulli theory is used to model the beam of length 0.6 m and cross-section 0.01×0.01 m. The material is steel, Young's modulus 210 GPa, Poisson ratio 0.3, density 7850 kg/m^3 and hysteretic damping loss factor equal to 0.01. The Kirchhoff theory is applied to model the plate of dimensions 1.2×0.6 m and 0.75 mm thickness. They are made of aluminum, Young's modulus 70 GPa, Poisson ratio 0.3, density 2800 kg/m^3 and hysteretic damping loss factor equal to 0.01.

To evaluate the average response, the structure is perturbed by adding randomly distributed masses on both plates. A coupled WBM-Rayleigh-Ritz approach is used to predict the behavior of the system. The former was used to model the plates with $T = 2$, while the latter to model the beam, including 15 modes. Two MC simulations are performed with respectively 30 and 50 additional masses for each plate and consisting of 50 realizations. Each additional mass is 0.3% of the total mass of the bare plate and each MC simulation consists of 50 realizations. No perturbation is introduced on the beam.

Natural frequencies and mode shapes of the bare plates are evaluated by means of an FE model consisting of 7200 quadrilateral shell elements of mean size 10 mm. The software Nastran is used to solve the eigenproblems and each MC simulation consists of 200 realizations.

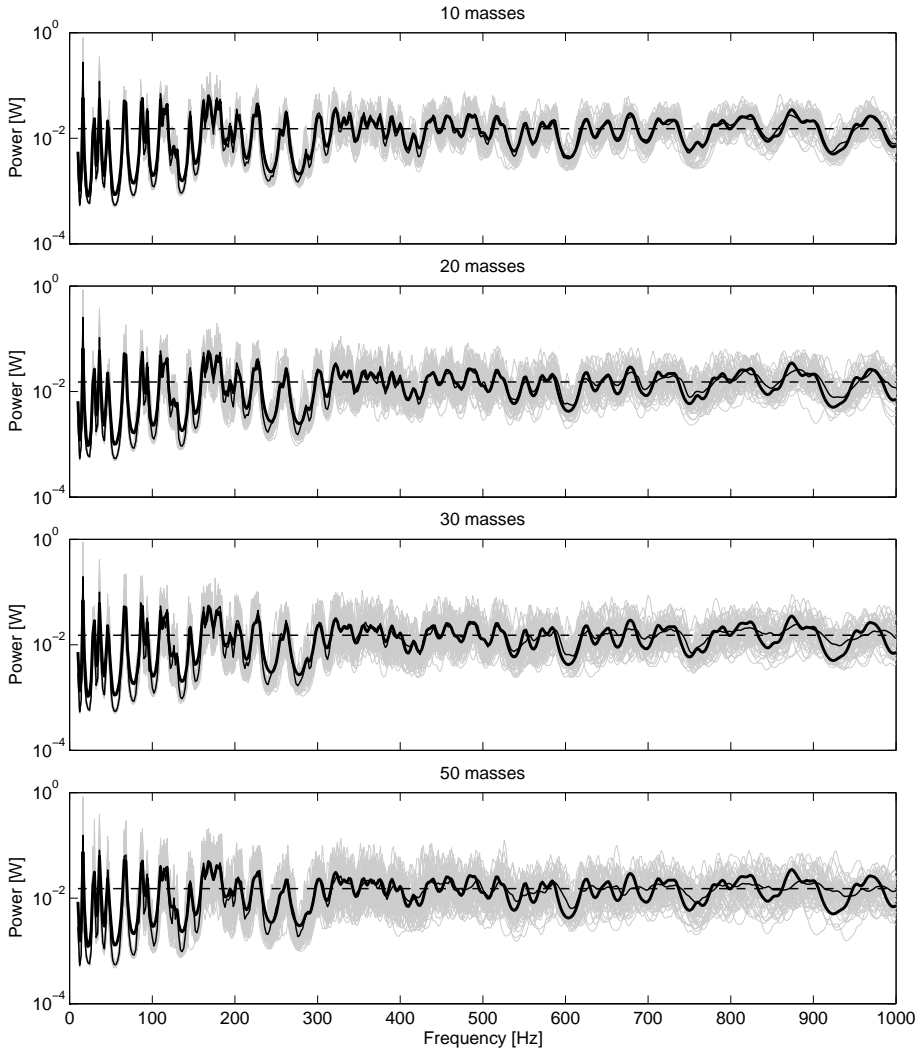


Figure 7.4: Input power evaluation. Comparison between MC samples (gray lines), MC average (thin solid lines), Lorentzian frequency average with γ tuned with the first approach (thick solid lines) and input power to an infinite plate (thin, dashed lines).

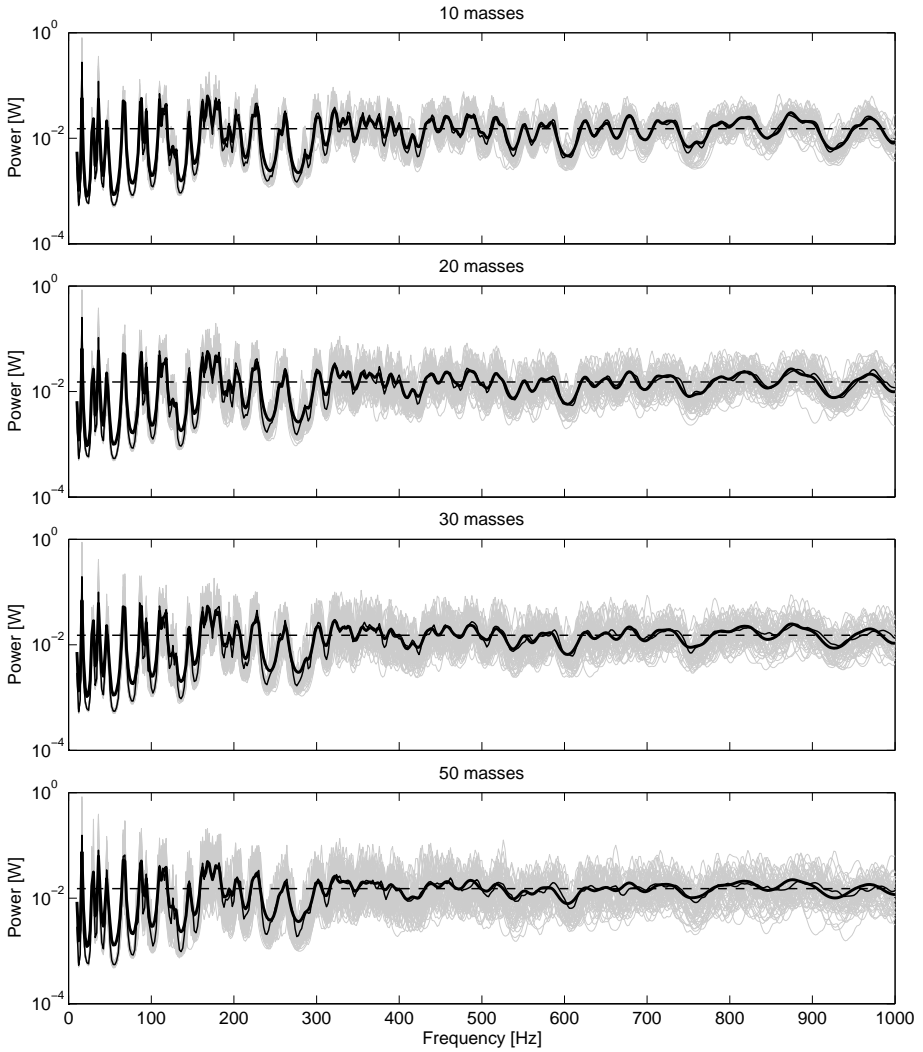


Figure 7.5: Input power evaluation. Comparison between MC samples (gray lines), MC average (thin solid lines), Lorentzian frequency average with γ tuned with the second approach (thick solid lines) and input power to an infinite plate (thin, dashed lines)

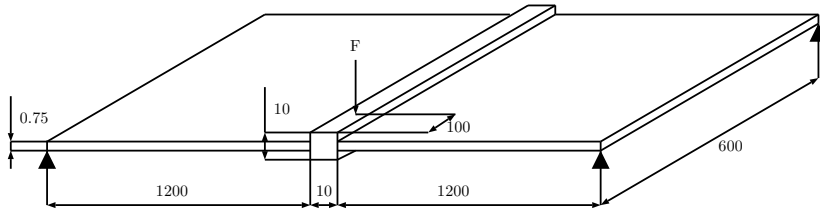


Figure 7.6: Geometry of the stiffened plates. Dimensions are in [mm] and not to scale.

Results

Using the strategies described in the previous section and tuning γ by using eigenfrequency statistics may be very problematic for multi-component structures. On the one hand, no analytical relation exists to deal with the approximation of the eigenvalue statistics for coupled systems. On the other hand, tracking modes for multi-component structures may lead to unreliable results, especially when the subsystems show different dynamic behaviors. Alternatively, the width of the Lorentzian can be chosen to encompass a number of natural frequencies of the most flexible parts. In fig. 7.7, the frequency-averaged input power is computed by using two different γ parameters, which are kept constant over the whole frequency range. The first one covers 10 modes of the bare plate, while the second one encompasses 30 modes. The averaged response is sensitive to the choice of the shape parameter. For large values of γ , the peaks of the plates are filtered out and the ones of the beam are flattened. As a result, the frequency-averaged response is far from the ensemble average. In this case, the use of band averaging might provide more insightful results, rather than a narrow band frequency-averaged response.

A second proposal to predict the ensemble average of multi-component systems, can be made by selectively applying the averaging procedure on subsystems which present a higher sensitivity to the perturbation.

In the current application, the beam has a modal density lower than the plates, and it is reasonable to assume that its behavior is less sensitive to variability over the frequency range under analysis. On the contrary, the behavior of the plates can be highly altered by the introduction of random masses. Accordingly, the Lorentzian is used to filter only the response of the plates, while the beam is treated deterministically.

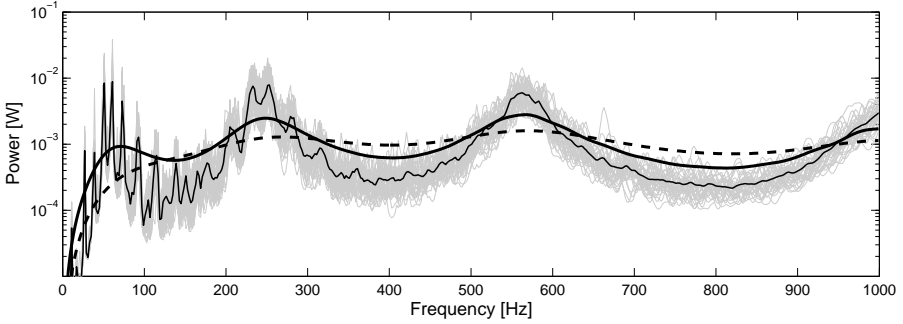


Figure 7.7: Mean input power for the case with 50 masses (thin solid line) and frequency-averaged input power with γ covering 10 (thick solid line) and 30 (thick dashed line) modes of the bare plate.

The procedure to assemble the system of equations is the following,

$$\begin{bmatrix} \mathbf{A}_b & \langle \mathbf{C}_{b,p_1} \rangle_{\gamma_b=0, \gamma_1} & \langle \mathbf{C}_{b,p_2} \rangle_{\gamma_b=0, \gamma_2} \\ \langle \mathbf{C}_{p_1,b} \rangle_{\gamma_1, \gamma_b=0} & \langle \mathbf{A}_{p_1} \rangle_{\gamma_1} & \mathbf{0} \\ \langle \mathbf{C}_{p_2,b} \rangle_{\gamma_2, \gamma_b=0} & \mathbf{0} & \langle \mathbf{A}_{p_2} \rangle_{\gamma_2} \end{bmatrix} \begin{bmatrix} \mathbf{w}_b \\ \langle \mathbf{w}_{p_1} \rangle \\ \langle \mathbf{w}_{p_2} \rangle \end{bmatrix} = \begin{bmatrix} \mathbf{f} \\ 0 \\ 0 \end{bmatrix} \quad (7.10)$$

where matrices \mathbf{A}_i refer to the i -th system matrix, matrices \mathbf{C}_{ij} refer to the coupling matrices between subsystems i and j , \mathbf{w}_i refers to the degrees of freedom of system i and \mathbf{f} to the excitation term. b , p_1 and p_2 refer to the beam and to the plates, respectively.

When the operator $\langle \bullet \rangle_{\gamma_i}$ refers to a system matrix, the parameter γ_i indicates the width of the Lorentzian. When $\langle \bullet \rangle_{\gamma_i, \gamma_j}$ refers to a coupling matrix, the parameters γ_i and γ_j are used to average out the coupling terms belonging to the component i and j , respectively. These matrices are evaluated at a complex frequency corresponding to the pole of Lorentzian in the LHP.

The eigenvalue statistics of the bare, simply supported plates are shown in fig. 7.8. They are estimated by using both the aforementioned approaches, confirming the observations of sec. 7.2.3. However, since the strategy based on mode-tracking led to more accurate predictions, its outcome is linearized and used to tune γ also for this example. According to this choice, fig. 7.9 shows the power injected into the beam when the plates are perturbed with 30 and 50 masses, respectively. For both cases, the solution is quite accurate especially in the mid- and high-frequency ranges, and the peaks of the beam are not filtered out as was the case in fig. 7.7.

As a final case, the γ parameters of the plates are chosen such that they cover 10 modes of a bare plate. According to the previous approach, this corresponds

to the situation in which the plates are highly perturbed. As can be seen in fig. 7.10, the power is characterized only by the presence of the beam resonances and it is in good agreement with the MC average when the randomness highly influences the response. Since the perturbation does not strongly affect the low-frequency behavior, there is a larger discrepancy between the MC mean and the frequency-averaged value.

7.2.5 Additional comments

The objectives of this section are two. The first one is to explore the possibility of using the Lorentzian-weighted frequency averaging to predict the mean behavior of an ensemble of systems. The second objective is to gain insight in how the shape parameter can be correlated to the amount of perturbation in the system. To this end, two approaches based on the eigenvalue statistics, have been investigated and applied to simply supported, rectangular plates. The frequency-averaged power shows a good agreement with the MC mean for all analyzed cases. However, an extension to more complex cases may present several difficulties. First of all, evaluating the eigenvalue statistics is not straightforward and using the mode-tracking strategy may be unreliable in certain situations. Moreover, their estimation still requires an MC simulation,

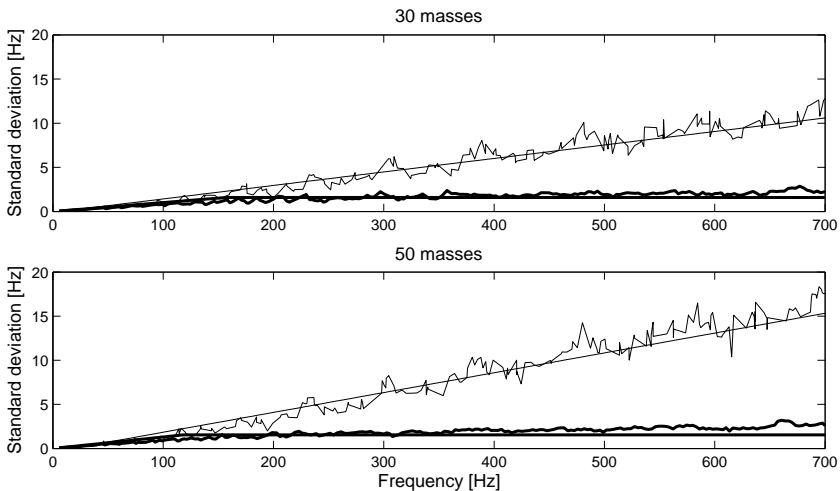


Figure 7.8: Eigenvalue statistics for bare plates perturbed with 30 (top) and 50 (bottom) masses. Standard deviation evaluated with mode tracking (thin solid lines) and without mode tracking (thick solid lines).

which is very computationally expensive. A possible way of simplifying the analysis may be a further development of eq. (7.7), as it may lead to an approximation of what is obtained by using mode-tracking.

When investigating multi-component structures, accurate results are obtained by selectively applying the Lorentzian-averaging on the subsystems which are more sensitive to perturbation. Especially when a wide Lorentzian is used, there is a very good agreement with the ensemble mean. Such a result may be explained by anticipating the concepts presented in the next section. When performing frequency averaging, scattering effects of the reverberant field are averaged out. Accordingly, only the coherent contribution of the direct field is evaluated, and the component acts like an energy sink. In the previously analyzed case, while the beam is vibrating deterministically, part of the energy is absorbed by the plates. Nevertheless, on the ensemble, the presence of a random reverberant field in the plates should act like a blocked force on the beam, as indicated in (2.31) [181]. Such a contribution is proportional to the modal energy of the plate and is not included in the system of equations (7.10). However, the average response of the primary variable seems to provide

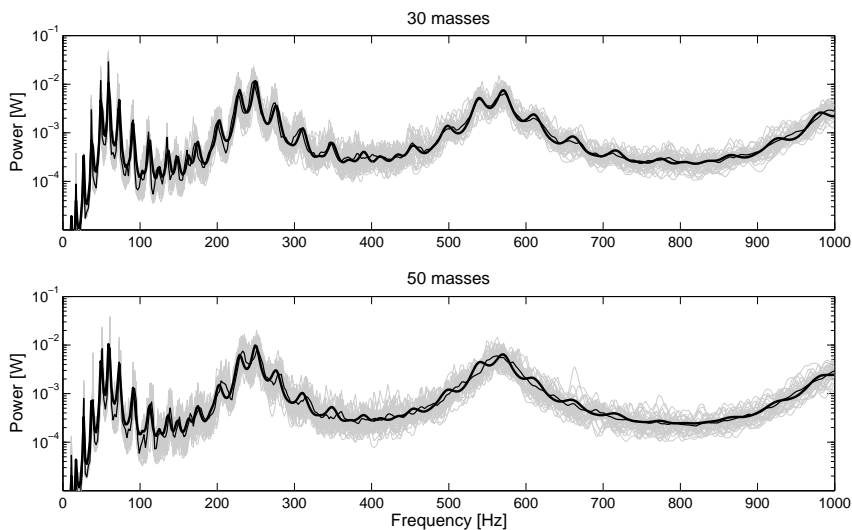


Figure 7.9: Comparison between ensemble mean (thin solid line) and frequency-averaged input power (thick solid line), for plates perturbed with 30 (top) and 50 (bottom) random masses. The γ parameters are tuned according to the approximation in fig. 7.8.

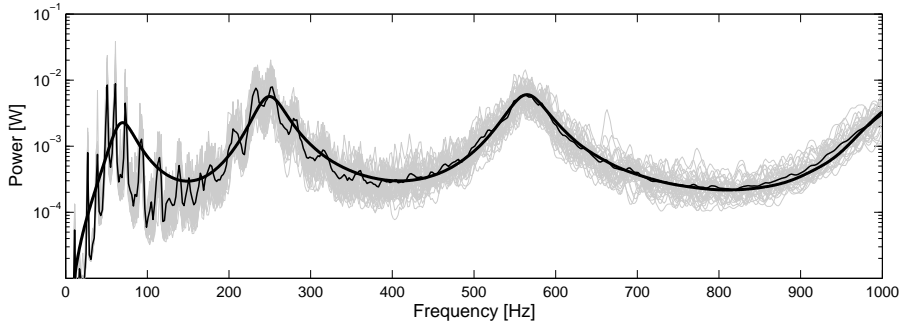


Figure 7.10: Comparison between ensemble mean (thin solid line) and frequency-averaged input power (thick solid line), for plates perturbed with 50 random masses and γ chosen to encompass 10 modes of the bare plate.

a reasonable approximation for the ensemble mean. This conclusion would suggest to further investigate to which extent the blocked force exerted by the random reverberant field can be neglected.

For the cases where the approximation holds, the average response could be predicted just by using a deterministic model, instead of hybrid deterministic/statistical ones. Moreover, as it will be shown in the following, for element-based models, the mesh can be coarsened, allowing a speed up of the computation. Finally, the smooth features of the response might facilitate the application of model order reduction techniques, like the use of Padé approximation [188], which would require a smaller number of matrix inversions to evaluate the frequency sweep.

As a final conclusion, this section attempts to explore a novel area and to answer some fundamental questions regarding the use of the Lorentzian-weighting frequency averaging. However, further research is required to exploit the underlying ideas at their maximal potential.

7.3 Direct field dynamic stiffness computation

In line with the techniques proposed in the previous chapters, the Lorentzian function has been used to evaluate frequency-averaged input power. In the following section, an alternative use of the Lorentzian-weighted frequency averaging is proposed to compute the direct field dynamic stiffness of a component at a junction. Such a quantity is very useful in the context of noise and vibration simulations, as it allows to estimate the power exchanged

by a system and is widely employed for hybrid approaches and SEA CLF calculations [181]. The following section also aims at interpreting how the physics of the problem is artificially altered when moving the frequency of analysis to the complex plane.

The use of Lorentzian frequency averaging for direct field computation is introduced in sec. 7.3.1, and applied to a plate in sec. 7.3.2. Advanced applications are discussed in sec. 7.3.3.

7.3.1 Direct field, artificial damping and Lorentzian-averaging

From a wave perspective, the response of a vibrating system can be represented as a superposition of a direct and a reverberant field [180],

$$u = u_{\text{dir}} + u_{\text{rev}}. \quad (7.11)$$

The direct field, u_{dir} , is described as the outgoing wavefield associated to a prescribed boundary condition or excitation, in the case the domain is unbounded. On the other hand, the reverberant field, u_{rev} , consists of all the waves excluded from the direct field and due to the reflection from the boundaries.

When an ensemble of nominally identical systems is taken into account, the direct field is not influenced by the properties of random boundaries, while the reverberant field is highly sensitive to randomness and may vary a lot. Moreover, in an ensemble sense, the reverberant field can be reasonably approximated by a diffuse field created by an infinite number of waves propagating in all directions with equal probability. Accordingly, the direct field is the only coherent wavefield in the component. These considerations lead to the following relation for the direct field,

$$E(u) = u_{\text{dir}}, \quad (7.12)$$

and for the reverberant field

$$E(u_{\text{rev}}) = 0, \quad (7.13)$$

where $E(\bullet)$ denotes the average taken over the ensemble.

Note that u is a primary quantity. When computing quadratic quantities, the effect of the reverberant field does not vanish, but it has to be taken into account as follows,

$$E(|u|^2) = E(|u_{\text{dir}}|^2) + E(|u_{\text{rev}}|^2). \quad (7.14)$$

After having introduced the notion of direct field, consider a generic dynamic problem expressed in terms of nodal DOFs, \mathbf{u} , which are divided in two sets.

All DOFs which allow the coupling with other components are collected into the boundary subset, \mathbf{u}_b . The remaining DOFs are collected into the \mathbf{u}_i subset, representing the internal DOFs

$$\mathbf{u} = \begin{bmatrix} \mathbf{u}_b \\ \mathbf{u}_i \end{bmatrix}. \quad (7.15)$$

The equations of motion of the system can be expressed in the form,

$$\begin{bmatrix} \mathbf{D}_{bb} & \mathbf{D}_{bi} \\ \mathbf{D}_{ib} & \mathbf{D}_{ii} \end{bmatrix} \begin{bmatrix} \mathbf{u}_b \\ \mathbf{u}_i \end{bmatrix} = \begin{bmatrix} \mathbf{f}_b \\ \mathbf{f}_i \end{bmatrix}, \quad (7.16)$$

where \mathbf{D} represents the global (frequency dependent) dynamic stiffness matrix. If the dynamic stiffness is referred to \mathbf{u}_b , the dynamic stiffness \mathbf{D}_B is the Schur complement of \mathbf{D}_{ii} , corresponding to the internal nodes, is

$$\mathbf{D}_B = \mathbf{D}_{bb} - \mathbf{D}_{bi}\mathbf{D}_{ii}^{-1}\mathbf{D}_{ib}. \quad (7.17)$$

Taking into account the previous considerations, the direct field dynamic stiffness can be obtained by averaging the dynamic stiffness matrix over the ensemble, $\mathbf{D}_{\text{dir}} = \mathbf{E}(\mathbf{D}_B)$ [116]. By assuming the equivalence between ensemble- and frequency-average, the direct field dynamic stiffness can be computed through a Lorentzian-weighted frequency averaging procedure. Accordingly, the direct field dynamic stiffness can be computed by evaluating the dynamic stiffness at a complex frequency, $\omega_0 - i\gamma$.

Alternatively, the direct field dynamic stiffness can be computed by assuming that the component is heavily damped. In fact, over an ensemble, the variance of the dynamic stiffness decreases and its value becomes deterministic by highly increasing the damping in the system [116]. On the contrary, when the damping is relatively low, waves travel from the excitation points towards the boundaries, where they are reflected. This contributes to the creation of a reverberant field within the structure. When the damping is high, waves are damped out before they can interact with each other to create a reverberant field. Consequently, the system behaves as if it was infinitely extended, and no reflection comes from the boundaries. Similarly, when computing the response at a complex frequency, an artificial damping is introduced in the dynamic stiffness matrix, supporting the equivalence between the direct field and the Lorentzian-weighted dynamic stiffness. By recalling the result in ch. 3, evaluating the system at $\omega_0 - i\gamma$ leads to the following dynamic stiffness,

$$\mathbf{D}(\omega_0 - i\gamma) = -\omega_0^2\mathbf{M} - \gamma^2\mathbf{M} + \mathbf{K} + i(\eta\mathbf{K} + 2\gamma\omega_0\mathbf{M}), \quad (7.18)$$

where only hysteretic damping is taken into account. The term $2\gamma\omega_0\mathbf{M}$ indicates the presence of an artificial damping in the system proportional to

γ . This conclusion confirms the equivalence between computing the direct field stiffness by means of ensemble averaging and assuming a high level of damping. Moreover, it confirms why the Lorentzian-weighted frequency-averaged input power of a finite system, asymptotically converges to the input power of an infinite structure, when the frequency and γ are high, see fig. 7.5. Nevertheless, it has to be underlined that the introduction of the parameter γ does not directly perturb the properties of the system, since the original damping value of the system is unaltered. Additionally, it allows a better control on the value of such a fictitious damping, as a function of frequency.

7.3.2 Point dynamic stiffness of plates

For point connections, analytical expressions exist to evaluate the direct field dynamic stiffness [121]. These assume that the domain is unbounded, neglecting the possible coherences in the wavefield, due to the presence of multiple connections. For connections of higher dimensionality, numerical methods are necessary to evaluate the direct field dynamic stiffness. A very general way of computing \mathbf{D}_{dir} is with the BEM, allowing also to take into account possible wavefield coherence between different junctions in the same component.

In the following example, the direct field dynamic stiffness of a thin plate is evaluated. The analytical formulation is compared to the Lorentzian-weighted frequency average dynamic stiffness at a point connection.

The analyzed plate has an area of 1.02 m^2 , is 3 mm thick and its geometry is shown in fig. 7.11. The material is aluminum, Young's modulus 70 GPa, Poisson ratio 0.3, 2700 kg/m^3 and hysteretic damping loss factor equal to 0.01. The

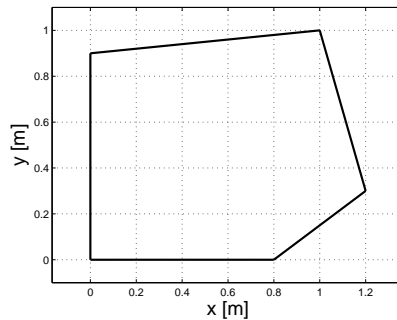


Figure 7.11: Geometry of the plate.

results provided by two FEM models are compared in the following. The mesh in fig. 7.12(a) consists of 408 nodes and 368 quadrilateral shell elements, with a mesh size of about 56 mm. On the other hand, the mesh in fig. 7.12(b) consists of 1552 nodes and 1472 quadrilateral shell elements, with a mesh size of about 28 mm. Nastran is used to pre-process the matrices, which are successively manipulated in Matlab. The plate is simply supported, and the direct field is computed with respect to the node highlighted in fig. 7.12(a). Such a node can represent either an excitation point or a deterministic connection to another system.

By assuming an infinite domain, the direct field dynamic stiffness can be computed as follows,

$$D_{\text{dir}}(\omega_0) = i8\omega\sqrt{D\rho_p d}, \quad (7.19)$$

where D is the flexural rigidity of the plate, ρ_p its density and d the thickness. On the other hand, the direct field dynamic stiffness can be computed by evaluating the Lorentzian-weighted frequency-averaged dynamic stiffness of the plate at the node of interest. This can be obtained by computing the Schur complement of the dynamic stiffness corresponding to the internal DOFs, and can be expressed as follows,

$$D_{\text{dir}}(\omega_0) = D_B(\omega_0 - i\gamma). \quad (7.20)$$

Figure 7.13 compares the direct field dynamic stiffness obtained by using the analytical formulation and the proposed approach. For the numerical models, the γ parameter is chosen such that it encompasses 10 and 30 modes in the first and the second case, respectively. The number of modes is estimated by using asymptotic modal density formulations [132].

The refined mesh provides results that in both cases are close to the analytic curve. When 10 modes are covered, the response presents some fluctuations, which are reduced by increasing γ . The model based on the coarse mesh

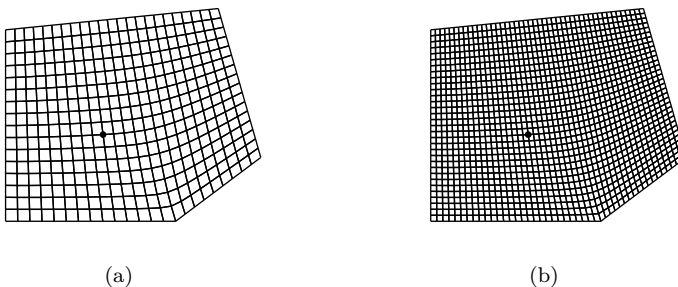


Figure 7.12: Coarse (a) and refined (b) plate mesh.

provides a result which improves with increasing the γ parameter. In fact, when γ is chosen to encompass 10 modes of the system, some prominent fluctuations are present on the response. This effect might be explained with the additional artificial damping introduced into the system. When γ is large enough to encompass 30 modes, the artificial damping is such that waves are damped out immediately and a refined mesh is not necessary to capture the behavior of the system. Accordingly, the prediction provided by such a model, is close to the analytical result.

The possibility of mesh coarsening certainly requires further investigation, as it may lead to a drastic reduction of the number of elements over the whole component, or possibly to restricting the refinement only in correspondence of the connection point.

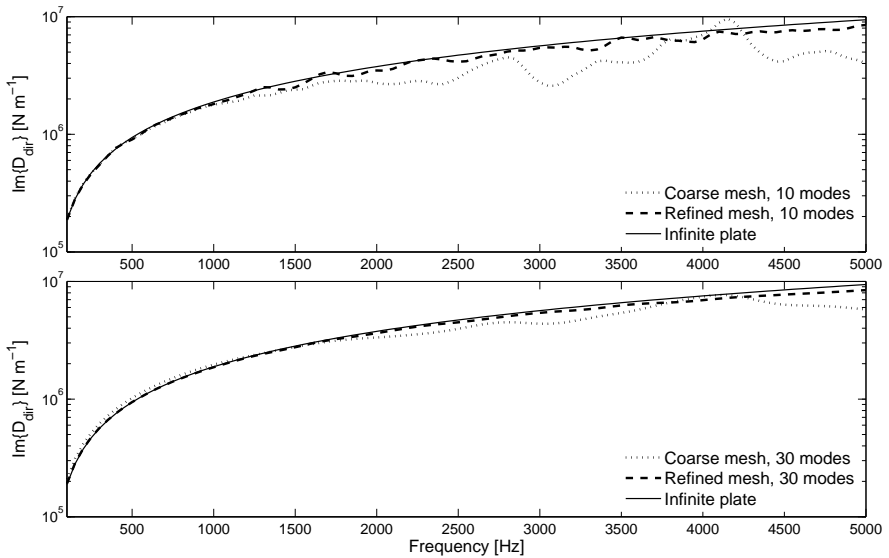


Figure 7.13: Point direct field dynamic stiffness for a plate.

7.3.3 Advanced applications

In the previous section, the Lorentzian-weighted frequency averaging is employed to extract the direct field information from the dynamic stiffness matrix. This is a very useful piece of information, as it leads to the amount of energy the system can exchange and can be exploited in the context of hybrid deterministic/statistical techniques as well as for CLF computation in standard

SEA. For example, by using the diffuse field reciprocity relation [181], the CLF, η_{ij} , can be expressed in terms of direct field dynamic stiffness matrices,

$$\eta_{ij} = \frac{2}{\pi\omega n_{d,i}} \sum_r \sum_s \text{Im} \left\{ \mathbf{D}_{\text{dir}}^{(j)} \right\}_{rs} \left(\mathbf{D}_{\text{tot}}^{-1} \text{Im} \left\{ \mathbf{D}_{\text{dir}}^{(i)} \right\} \mathbf{D}_{\text{tot}}^{-H} \right)_{rs}, \quad (7.21)$$

where i and j are two components, and $\mathbf{D}_{\text{dir}}^{(\bullet)}$ is the direct field dynamic stiffness of the corresponding component. \mathbf{D}_{tot} is the total dynamic stiffness of the junction, computed as the sum of the direct field dynamic stiffnesses. The symbol \bullet^{-H} is the Hermitian transpose operator.

In principle, eq. (7.21) can be used for any type of junction, and the direct field dynamic stiffness matrix can be calculated by applying the aforementioned strategy.

The proposed approach allows a great flexibility, as \mathbf{D}_{dir} can be evaluated by manipulating the matrices of a FEM model. No alteration to the numerical method is required, apart from the introduction of an artificial damping, due to the computation at a complex frequency. On the other hand, computing the Schur complement of the matrix corresponding to the internal DOFs requires several operations, leading to an increased computational effort. In this regard, the possibility of mesh coarsening could become very advantageous to speed up the calculation.

Future research could focus on the application of these concepts in the context of hybrid techniques and pure SEA modeling.

7.4 Use of the Lorentzian function within the Fuzzy Structure Theory

So far, the Lorentzian has been used as a weighting function for a frequency integral. The following section proposes its use as a mass-frequency density function to construct a fuzzy impedance within the FST. Similarly to what was observed in the previous sections, the unique features of the Lorentzian allow a straightforward computation of the impedance by using a complex nominal natural frequency for the fuzzy oscillator.

Soize's theory is briefly recalled in sec. 7.4.1, and in sec. 7.4.2 the extension by Pierce is introduced. In sec. 7.4.3, the fuzzy impedance based on the Lorentzian is illustrated and compared with Pierce's prototype function. Finally, sec. 7.4.4 presents a short discussion.

7.4.1 The Fuzzy Structure Theory

The FST was proposed by Soize [25, 185] to tackle large dynamic problems. The theory is based on the definition of a fuzzy structure as consisting of a master, primary structure (MS), coupled with several fuzzy substructures (FSs). The MS is a well-characterized part of the system, usually a stiff part, i.e. the frame. The FSs represent all the equipment and secondary systems, of which details are either unknown or not accessible to conventional modeling. Contrarily to classic deterministic modeling, the FSs are described in terms of random impedance operators, with the final objective of predicting the effect of the fuzzy attachments on the modulus and the phase of the response at any point of the MS.

A probabilistic approach is used to define the impedance operator, which allows modeling the effects of the FSs on the MS. This leads to the construction of the FST system of equations,

$$i\omega (\mathbf{Z}_{\text{master}} + \mathbf{Z}_{\text{fuzzy}}) \mathbf{w} = \mathbf{f}, \quad (7.22)$$

where $\mathbf{Z}_{\text{master}}$ is the impedance operator of the MS, and $\mathbf{Z}_{\text{fuzzy}}$ is the random boundary impedance of the FS. The symbol \mathbf{w} represents the random displacement field of the MS, while \mathbf{f} are the external forces applied to the MS.

The FSs behave like weakly damped resonators, and their impedance depends on four parameters: mass per unit area, rate of internal damping, modal density and the equivalent coupling factor. The latter allows a distinction between discrete (type I fuzzy impedance law) and continuous attachments (type II fuzzy impedance law). Moreover, in the original formulation, Soize also includes the cut-off frequency, which determines the frequency below which the FSs present a purely mass-like behavior.

To construct the random boundary operator $\mathbf{Z}_{\text{fuzzy}}$, each coefficient has to be defined in terms of its mean and deviation coefficient. Soize assumes that each parameter is uniformly distributed over a certain interval, and the operator is then built through a stochastic linearization process.

Once $\mathbf{Z}_{\text{fuzzy}}$ is formulated, it can be decomposed into its deterministic mean and random components, leading to a reformulation of eq. (7.22),

$$i\omega (\mathbf{Z}_{\text{det}} + \mathbf{Z}_{\text{rand}}) \mathbf{w} = \mathbf{f}, \quad (7.23)$$

where $\mathbf{Z}_{\text{det}} = \mathbf{Z}_{\text{master}} + \mathbf{E}(\mathbf{Z}_{\text{fuzzy}})$, with $\mathbf{E}(\bullet)$ the expected value operator. Equation (7.23) is a random equation and is solved recursively for \mathbf{w} in terms of its mean and higher order moments. For the sake of brevity, the details are not reported here, but the reader is referred to [159].

The main attractiveness of the FST is that modeling complex secondary systems does not introduce any additional unknown with respect to the MS model, when describing the field in terms of nodal values. This results in a significant reduction of DOFs for very large structures. However, the fuzzy impedance coefficients must be known, and, although identification methods have been developed [159], their determination remains the main hurdle limiting the applicability of the FST.

7.4.2 Pierce's FST and prototype functions

Based on Soize's theory, Pierce proposed an alternative formulation, which allows reducing the number of unknown parameters and makes the underlying mathematical formalism simpler [166].

In Pierce's formulation, the parameters characterizing the oscillators are governed by the *principle of maximum ignorance*, for which the number of attachments, their location, mass, damping and resonance frequency are unknown. The only known information is the distribution of the FS mass, m_F , with respect to its natural frequency ω_n . Such a function is called prototype mass-frequency distribution and represents the amount of mass resonating below a certain frequency ω_n . The derivative of m_F leads to the prototype mass-frequency density function, $dm_F/d\omega_n$, which plays a key role in Pierce's theory. In fact, the impedance of a FS is constructed by averaging over the natural frequency the impedance of the corresponding resonator, weighted by using the mass-frequency density function.

Such a procedure shows that the presence of a FS results in an apparent mass and damping acting on the master system. This is justified by considering that the FS consists of several resonating oscillators, of which the resonances are spread over frequency. Accordingly, they absorb energy from the MS, inducing an additional apparent damping, and, due to their motion, an additional apparent mass.

The apparent mass of a fuzzy resonator is computed from the reactance of the resonator impedance,

$$m_{F,\text{app}}(\omega) = \int_0^\infty \frac{dm_F}{d\omega_n} \left[\frac{\omega_n^2 (\omega_n^2 - \omega^2 + 4\omega^2 \xi^2)}{(\omega_n^2 - \omega^2)^2 + (2\xi\omega\omega_n)^2} \right] d\omega_n, \quad (7.24)$$

while its apparent damping is computed from the resistance,

$$R_{F,\text{app}}(\omega) = \int_0^\infty \frac{dm_F}{d\omega_n} \left[\frac{2\xi\omega^4\omega_n}{(\omega_n^2 - \omega^2)^2 + (2\xi\omega\omega_n)^2} \right] d\omega_n, \quad (7.25)$$

where ξ is the damping ratio of the resonator and ω the angular frequency of analysis. For the asymptotic limit of small damping, $\xi \rightarrow 0$, the apparent mass can be evaluated as

$$m_{F,\text{app}}(\omega) = \text{Pr} \int_0^\infty \frac{dm_F}{d\omega_n} \frac{\omega_n^2}{\omega_n^2 - \omega^2} d\omega_n, \tag{7.26}$$

and the apparent damping as

$$R_{F,\text{app}}(\omega) = \frac{\pi\omega^2}{2} \frac{dm_F}{d\omega_n}, \tag{7.27}$$

where Pr indicates the principal value of the integral [166]. With respect to Soize’s original theory, this formulation allows to account for the effects of attached structures simply by defining the mass-frequency distribution function. Furthermore, the fuzzy impedance is deterministically determined, simplifying the recursive solution of eq. (7.23).

In general, the form of the function $m_F(\omega_n)$ is not known, and it is advantageous to formulate it as dependent on a small number of parameters. A prototype function was proposed by Pierce [166], with the following mathematical form,

$$m_F(\omega_n) = m_F(\infty) \left[1 - e^{-\omega_n^2/2\omega_{F,n}^2} \right], \tag{7.28}$$

where the symbol $\omega_{F,n}$ represents the most probable natural frequency of the FS and corresponds to the frequency at which the mass per frequency reaches a maximum. The total mass of the FS is indicated by $m_F(\infty)$. The mass-frequency density function has the following form,

$$\frac{dm_F}{d\omega_n} = m_F(\infty) \frac{\omega_n}{\omega_{F,n}^2} e^{-\omega_n^2/2\omega_{F,n}^2}. \tag{7.29}$$

The behavior of these functions is shown in figs. 7.14 and 7.15 (thin solid line).

Independently from Pierce, Strasberg and Feit [191] also investigated the effects of several resonators attached on the MS. They studied the resistance and reactance of a FS, when the mass-frequency distribution function is either given by a geometric progression or a uniform variable. They also provide a relation between the resistance induced by the FS and the apparent dissipation in the MS.

More recently, Friis and Ohlrich [65] used a Gaussian function as a mass-frequency distribution to model FSs attached to a beam.

In general, in Pierce’s FST a smoothed version of the mass-frequency distribution is required. Such a smoothing effect can be seen as a sum of modes

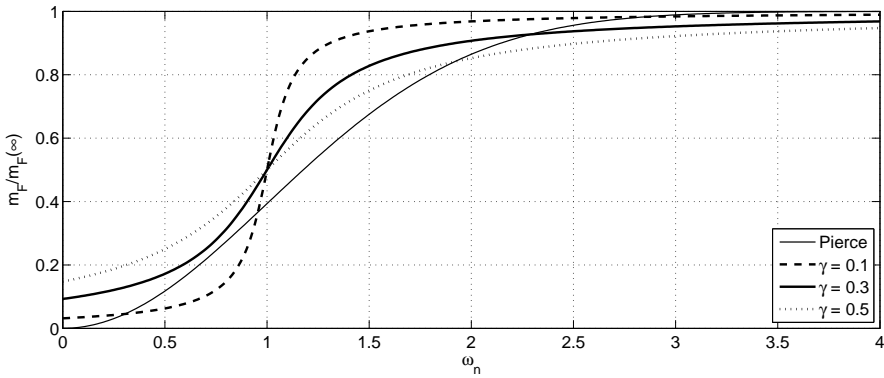


Figure 7.14: Prototype mass-frequency distribution function for $\omega_{F,n} = 1$ rad/s.

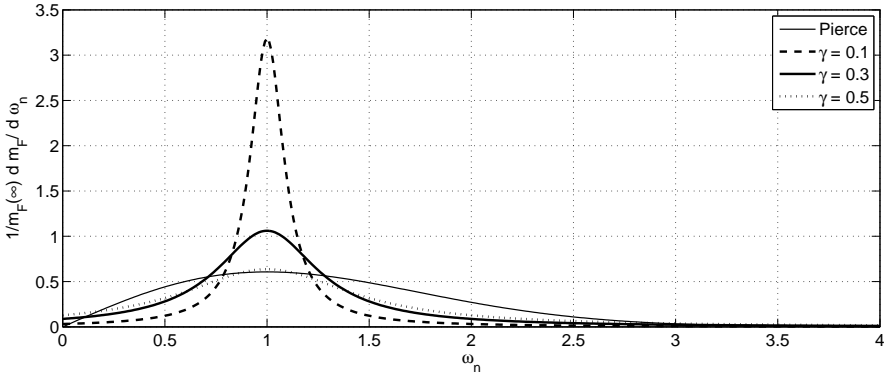


Figure 7.15: Prototype mass-frequency density function for $\omega_{F,n} = 1$ rad/s.

which are closely spaced and which create sufficient overlap. In the following section, the Lorentzian is proposed as a mass-frequency density function

7.4.3 Lorentzian mass-frequency density function

Suppose the mass-frequency distribution function has the following form,

$$m_F^{(l)}(\omega_n) = m_F(\infty) \left[\frac{1}{2} + \frac{1}{\pi} \arctan \left(\frac{\omega_n - \omega_{F,n}}{\gamma} \right) \right], \quad (7.30)$$

where the parameter γ determines the amount of mass distributed around the natural frequency $\omega_{F,n}$. The superscript l indicates the similarity with the

cumulative distribution of the Lorentzian, eq. (7.2). The features of function (7.30) are illustrated in fig. 7.14 for different values of γ . With respect to Pierce’s distribution, function $m_F^{(l)}$ is non-zero for zero frequency, but when $\gamma \ll \omega_{F,n}$, the mass distributed over negative natural frequencies is very small. However, by tuning γ parameter, it is possible to reduce this effect. Note also that the mass is distributed differently compared to Pierce’s function.

A prototype function similar to $m_F^{(l)}$ was proposed by Pierce in ref. [165], although it was never developed in detail. In ref. [165], γ is replaced by $\xi\omega_n$, meaning that the mass is mainly distributed in the half-power bandwidth of the nominal resonator. However, the use of eq. (7.30) allows generalizing such a formulation and gives the possibility of tuning the γ according to the fuzzy distribution.

By deriving expression (7.30) with respect to the natural frequency, it is possible to compute the mass-frequency density function, which in this case coincides with a Lorentzian,

$$\frac{dm_F}{d\omega_n} = \frac{m_F^{(l)}(\infty)}{\pi\gamma} \frac{1}{1 + \left(\frac{\omega_n - \omega_{F,n}}{\gamma}\right)^2}. \tag{7.31}$$

Figure 7.15 allows comparing the Lorentzian with Pierce’s prototype density. The latter covers a wide range of frequencies, while the effect is more localized for the Lorentzian. When γ is small, the mass density is more concentrated around the natural frequency and vice versa. In all cases, the Lorentzian presents a decay which is steeper than Pierce’s prototype.

In order to estimate the apparent mass and damping of a FS described by a Lorentzian prototype function, the impedance of a resonator is computed as follows,

$$Z_F^{(l)}(\omega) = \int_{-\infty}^{+\infty} \frac{m_F(\infty)}{\pi\gamma} \frac{1}{1 + \left(\frac{\omega_n - \omega_{F,n}}{\gamma}\right)^2} \left[\frac{i\omega (\omega_n^2 + 2i\omega_n\omega\xi)}{\omega_n^2 - \omega^2 + 2i\omega_n\omega\xi} \right] d\omega_n. \tag{7.32}$$

To simplify the calculation, the interval of integration is unbounded in both directions, unlike in eq. (7.24) and (7.25). However, the weighting (or density) function is commonly very small for negative frequencies, and their contribution is assumed to be negligible.

Lorentzian-based fuzzy impedance

Integral (7.32) can be computed using the residue theorem, by applying a procedure analogous to the one presented in ch. 3. In this case, the variable of

integration is the natural frequency ω_n , and over the natural frequency complex plane, the poles of the impedance are located at,

$$z_{n,1,2} = -i\omega\xi \pm \omega\sqrt{1 - \xi^2}. \quad (7.33)$$

Note that ω is the frequency of analysis, and the poles are located in the LHP. On the other hand, the Lorentzian has two poles located at

$$z_{1,2} = \omega_{F,n} \pm i\gamma, \quad (7.34)$$

one in the lower and one in the upper half of the complex plane. According to the procedure in ch. 3, the contour integration can be closed in the UHP, over which the integrand vanishes. As a result,

$$Z_F^{(l)}(\omega) = Z(\omega; \omega_{F,n} + i\gamma), \quad (7.35)$$

where Z is the impedance of the resonator, and the term inside the brackets of the right-hand side indicates that the impedance is evaluated at frequency ω , and its resonance frequency is complex, with imaginary part equal to the shape parameter.

The apparent mass resulting on the MS can be evaluated by considering the reactance of the impedance (7.35), while the additional damping is provided by its resistance. With respect to expressions (7.26) and (7.27), result (7.35) allows a direct use of the fuzzy impedance, without having to compute an additional principal value, and without introducing asymptotic approximations. Moreover, expression (7.35) gives the possibility to tune the γ parameter.

According to eq. (7.35), the fuzzy impedance is equal to the impedance of the nominal resonator with a complex natural frequency $\omega'_{F,n}$ in the form,

$$\omega'_{F,n} = \omega_{F,n} + i\gamma. \quad (7.36)$$

The introduction of an imaginary part does not lend itself to a straightforward interpretation. To gain further insight, the stiffness and the mass of the resonator can be altered such that they lead to a complex resonance frequency, $\omega'_{F,n}$.

Assume that the variation of natural frequency is generated by a variation of the stiffness, which has a real and imaginary part, k_r and k_i , respectively. Accordingly, the shift of the natural frequency can be written as

$$\sqrt{\frac{k_r + ik_i}{m_F(\infty)}} = \sqrt{\frac{k_{F,n}}{m_F(\infty)}} + i\gamma, \quad (7.37)$$

where $k_{F,n}$ represents the stiffness of the nominal resonator. Supposing that $m_F(\infty)$ is positive and real, the real part of the complex stiffness can be

expressed as

$$k_r = k_{F,n} - \gamma^2 m_F(\infty), \tag{7.38}$$

which highlights a softening effect proportional to the mass, and that γ should not exceed the natural frequency $\omega_{F,n}$, to respect the positiveness of the stiffness k_r . On the other hand, the imaginary part of the stiffness is expressed as

$$k_i = 2\gamma\sqrt{m_F(\infty)k_n}, \tag{7.39}$$

which acts like additional damping to the resonator.

As a result of the aforementioned procedure, the averaged impedance is equal to the nominal impedance, with lower stiffness and higher damping. Equivalently, the nature of the complex natural frequency can be considered as a combined effect of an altered mass and additional imaginary stiffness. The new mass is supposed to be real, to comply with its physical interpretation, while the stiffness is complex, with its real part equal to the nominal stiffness of the resonator. These considerations lead to the following relation,

$$\sqrt{\frac{k_{F,n} + ik_i}{m_r}} = \sqrt{\frac{k_{F,n}}{m_F(\infty)}} + i\gamma. \tag{7.40}$$

This allows determining the mass,

$$m_r = \frac{m_F(\infty)k_{F,n}}{k_{F,n} - \gamma^2 m_F(\infty)} \tag{7.41}$$

and imaginary part of the stiffness

$$k_i = \frac{2\gamma k_{F,n}}{k_{F,n} - \gamma^2 m_F(\infty)} \sqrt{k_{F,n} m_F(\infty)}. \tag{7.42}$$

Note that when the γ parameter is taken equal to 0, the modified mass becomes equal to the original mass, while the imaginary stiffness is equal to zero.

Comparison with Pierce’s prototype

Now the focus is on the comparison between the apparent mass and damping induced on the MS generated by Pierce’s and the Lorentzian prototypes. Figure 7.16 presents the normalized apparent mass as a function of frequency, for the two prototypes. In the limit of zero frequency, the apparent added mass is equal to the total mass of the attachment, as if the fuzzy and the MS were rigidly connected. With increasing frequency, the attachments move in-phase with the MS, and since their displacements are larger than their attachment points, the kinetic energy is higher than in the case they were rigidly connected.

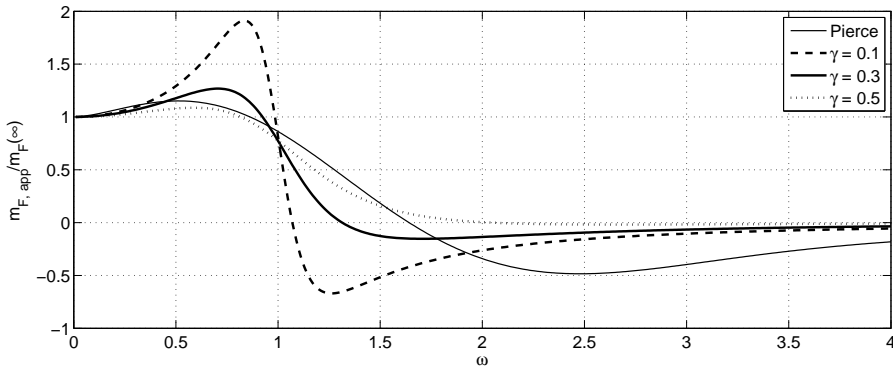


Figure 7.16: Apparent normalized mass as function of frequency for $\omega_{F,n} = 1$ rad/s.

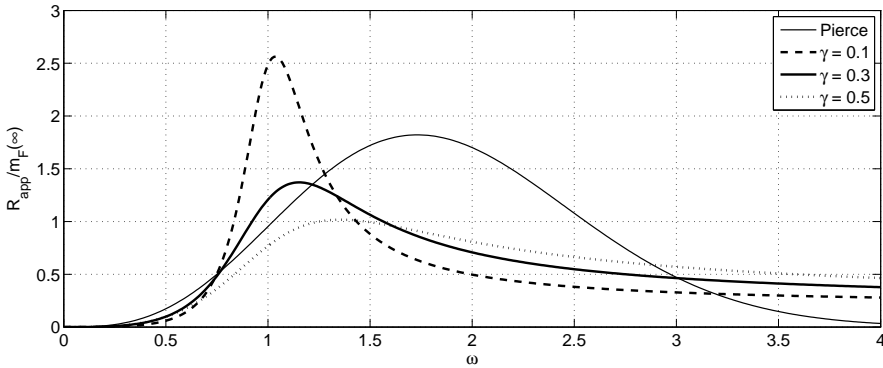


Figure 7.17: Apparent normalized damping as function of frequency for $\omega_{F,n} = 1$ rad/s.

This justifies why the apparent mass is actually larger than the physical mass. For Pierce's prototype, the apparent mass drops below one when the driving frequency is 86.5% the natural frequency and assumes negative values for frequencies larger than 164% the natural frequency. Such an apparent mass subtraction is due to the driving frequency being higher than the natural one. This causes out-of-phase motion between the MS and the attachments, which exert forces directed like the MS acceleration.

The behavior of the Lorentzian-based system fuzzy leads to similar conclusions. When the width of the Lorentzian is small, the apparent mass addition is more pronounced, and it quickly drops below zero for frequencies higher than the

natural one. The transition from mass addition to mass subtraction happens very close to the natural frequency, in agreement with the behavior of the reactance of a damped resonator. On the other hand, when γ is larger, the effect is spread over a broader frequency range, and both mass addition and subtraction effects are reduced.

Regarding the apparent damping, the model suggested by Pierce presents pronounced damping effects above the natural frequency, as shown in fig. 7.17. This might be due to the fact that a large part of the mass is distributed in that region, with a consequent large energy flow from the MS to the FS. On the other hand, the Lorentzian function produces a localized apparent damping around the natural frequency and allows more control on the distribution of the absorption. When γ is small, the apparent damping is very high around the natural frequency, with an inversely proportional decay rate. Note that the decay rate is less steep than for Pierce's prototype function.

7.4.4 Additional comments

Complex vibro-acoustic problems often present substructures which are difficult to treat using conventional modeling and induce an apparent increased damping on the MS, as proven by experimental results. To tackle this class of problems, Soize developed the FST, which was successively extended and simplified by Pierce with the introduction of the concept of prototype function.

The aim of this section is to propose the Lorentzian as a prototype function within the FST. Compared to the functions proposed in the past, the Lorentzian allows a straightforward computation of the FS impedance, without involving numerical integration. Moreover, it gives the freedom of choosing the width according to the problem.

A possible application can be in line with the one proposed in ref. [175], where the apparent mass and damping are spread over a plate. This might be the case when panels with electronic equipments are investigated. The equipment is composed by several subcomponents which behave like fuzzy substructures. Alternatively, one could concentrate the effect of a fuzzy attachment at a nodal position of a FEM model, simulating the effects of a connection to a component with a higher modal density.

Although the idea of reducing the structure to its primary components still preserves its potential and inspired successive works, key questions remain open almost 20 years after Pierce's FST appeared. The main point which is still open is how to estimate and calibrate the distribution on the secondary structures, such that it can be used during the design process.

7.5 Conclusion

The Lorentzian function corresponds to the square magnitude of a Butterworth filter of order one. Accordingly, performing only one calculation in the complex frequency domain allows computing an averaged value over a broad frequency range. However, due to its bell-shape, the Lorentzian is not suitable to approximate band-values, and its use in the context of noise and vibration simulations is far from obvious. For this reason, the nature of this chapter is purely exploratory, and attempts to answer fundamental questions regarding the use of the Lorentzian function for weighted average computations. Each of the proposed applications provides interesting perspectives and challenges for future research. .

In sec. 7.2, the Lorentzian is used to predict the ensemble average input power into systems with uncertain properties. To this end, the shape of the Lorentzian, determined by the γ parameter, is chosen according to the natural frequency statistics of the perturbed system, and two tuning strategies are investigated. The first one relies on the eigenvalue statistics approximated by a first order perturbation analysis. The second one attempts at evaluating the statistics by tracking nominal modes in the perturbed configurations of an ensemble. A good agreement between frequency and ensemble average input power is verified for plates perturbed by randomly distributed masses, when γ is tuned according to the second strategy.

The possibility of extending the ensemble mean prediction to multi-component systems is also investigated. A good level of accuracy is obtained by applying the Lorentzian averaging only on the components which present higher sensitivity to perturbation.

In sec. 7.3, the Lorentzian-weighted frequency averaging is used to compute the direct field dynamic stiffness of a component. Such a quantity can be calculated by averaging the dynamic stiffness over an ensemble, or assuming that the component is heavily damped. In both cases, this can be addressed by evaluating the Lorentzian-weighted frequency averaging: assuming the equivalence between ensemble mean, in the former, and observing that a computation at a complex frequency introduces artificial damping in the system.

Finally, in sec. 7.4.1, the Lorentzian is proposed as a mass-frequency distribution function within the FST. With respect to other prototype functions, the Lorentzian allows a straightforward evaluation of the fuzzy impedance and gives the possibility to vary the mass distribution, by tuning of the γ parameter.

Chapter 8

Conclusions and future research

The research presented in this dissertation aims at improving the computational efficiency of numerical strategies in the field of noise and vibration. In particular, the key innovative contribution is the development of efficient schemes to perform frequency averaging procedures. These require the solution of highly oscillatory integrals, which are widely applied in computational analysis.

According to classic strategies, weighted frequency integrals are evaluated by using quadrature techniques. However, due to the oscillatory nature of dynamic system descriptors, a large amount of sampling points might be needed to achieve accurate integrations, with a subsequent increase of computational effort.

In this dissertation, the residue theorem is employed to evaluate weighted frequency integrals. As a result, refined quadrature schemes are replaced by a few computations at complex frequencies, leading to more accurate integral estimates at a reduced computational cost.

This final chapter consists of two main sections. An overview of the thesis is given in sec. 8.1, which summarizes the main achievements. Section 8.2 suggests a number of interesting topics for future research.

8.1 Overview and main achievements

With respect to the state-of-the-art in the field of numerical vibro-acoustics, the present research enhances the computational performance of classic deterministic modeling. The major novel contribution lies in the introduction of the use of the residue theorem to compute weighted frequency integrals, with the integrand being a generic descriptor of the dynamic system. Such weighted integrals are used to estimate frequency-averaged quantities, although they can be easily employed to evaluate oscillatory integrals more in general.

The proposed techniques present four distinguishing characteristics:

- **Computational efficiency.** With respect to classic quadrature integration, the proposed techniques allow a significant reduction of computational resources. In fact, a refined quadrature integration is replaced by a few computations at complex frequencies, leading to a significant increase in computational efficiency.
- **Accuracy.** The accuracy of quadrature schemes is strictly dependent on the oscillatory behavior of the integrand function. Especially when resonance peaks are sharp, a refinement of the integration might be necessary. The residue theorem allows evaluating weighted integrals with an accuracy which does not strictly depend on the oscillatory behavior of the integrand function and is independent of the width of the frequency band.
- **Wide range of applicability.** The proposed integration strategies can be used in combination with any deterministic technique, as long as the requirements for applying the residue theorem are respected. No geometrical restrictions are imposed, and the strategy can be potentially extended to all fields where oscillatory integrals are of interest.
- **Ease of implementation.** The proposed strategies can be easily implemented by replacing the real frequency of analysis with a complex one. No further modification to the numerical approach is required.

The potential of these novel strategies can be exploited for different applications and serve several purposes. In this dissertation, the focus is on the computation of two types of frequency averages. The first one is the band-averaged power injected into a vibrating system by a source, for which a rectangular window is used as a weighting function. In the second one, the frequency averaging procedure is performed by using a Lorentzian as a weighting function. Due to its advantageous mathematical features, the Lorentzian allows straightforward average computations. Its use is explored in different ways in this dissertation.

8.1.1 Efficient band-average input power computations

The strategies developed in ch. 3 and 4 allow an efficient and accurate estimate of the band input power. These are further benchmarked in ch. 5 and employed to enhance optimization procedures in ch. 6.

The following sections report a global overview of the chapters, underlying the main findings.

Butterworth-weighted frequency averaging

The Butterworth-weighted frequency averaging procedure is presented in ch. 3 and constitutes the main building block of this research track.

To compute the band-averaged power injected by a force into a vibrating system, the rectangular window is approximated by using the square magnitude of a Butterworth filter. Applying the residue theorem, the integral over the whole real frequency axis is replaced by a weighted sum of system responses computed at complex frequencies. These complex frequencies correspond to the poles of the Butterworth filter lying in the lower half of the complex frequency plane.

This procedure leads to an exact evaluation when the poles of the system are confined to the upper half of the complex frequency plane. Such a condition is not satisfied when the damping mechanism is modeled as hysteretic, and system poles are located in the third quadrant of the complex plane. However, the error made by neglecting these poles is proven to be negligible, and the Butterworth-weighted frequency average can still be accurately evaluated by computing the response at only the filter poles, lying in the LHP. An analytical expression is developed to prove that the aforementioned error can be written as a bounded series and is negligible.

The proposed approach is benchmarked on a simply supported and on a stiffened plate, both modeled with hysteretic damping. Although system poles are present in the LHP, their influence is shown to be negligible. The major source of error is the approximation of a rectangular window by using the square magnitude of a Butterworth filter and can be easily controlled by increasing the order of the filter. The examples prove the effectiveness of the approach, both in terms of accuracy and solving time.

Use of classic quadrature in the complex plane

In ch. 4, the Butterworth-weighted frequency averaging technique is generalized, and further insight and improvements are presented for input power computation.

An ideal rectangular window is used to weigh the integral and instead of evaluating the band-average over an interval of real frequencies, the integration path is moved to the complex plane, where the input mobility shows a smoother behavior. Over the new contour, classic quadrature schemes can be used with a reduced number of integration points, leading to a significant reduction of the computation time and to a higher level of accuracy compared to quadrature performed over the real axis. Such a procedure is a generalization of the Butterworth-weighted frequency averaging, and it is shown that the latter corresponds to the use of the midpoint rule over a semi-circle in the complex plane.

Numerical examples allow comparing different contours (semi-circle and semi-ellipse) and quadratures (midpoint, Gaussian, Lobatto and Clenshaw-Curtis), including adaptive integration schemes (Gauss-Kronrod-Patterson) to provide convergence information. In addition, the connection between the use of quadrature rules in the complex plane and weighting functions on real frequencies is considered. It is shown that integration schemes in the complex plane lead to the definition of weighting functions resembling the features of a rectangular window.

Additional application examples are presented in ch. 5. The first case consists of a suspension shock-tower excited by a point force. Its geometry has a higher complexity compared to cases presented in the previous chapters. As a final example, the band-averaged input power is computed for an acoustic car cavity, excited through the firewall and with frequency dependent admittance boundary conditions. For both cases, the use of the residue theorem for band-integration is confirmed to be a very efficient alternative to classic quadrature.

Optimization over frequency bands

When it comes to the improvement of the vibrational behavior of a structure, a robust design which maximizes the performance over a frequency band, is often preferred. Nevertheless, using classic quadrature techniques may seriously slow down the optimization process, and applying the residue theorem can significantly enhance the computation. In this perspective, ch. 6 shows the potential of the proposed techniques within the context of structural optimization.

In the analyzed application cases, the properties and location of DVAs are chosen as design variables to minimize the average power injected into a baffled plate. This leads to an indirect reduction of the radiated acoustic power and global vibration over the band of interest. The dynamic behavior of the system is simulated by using the WBM, while GAs are used as optimization tools. Results show the large computational saving with respect to classic quadrature-based optimization procedures, both for single- and multi-band minimization. Furthermore, the optimal design is proven to be robust against DVA parameter perturbation.

8.1.2 Lorentzian-weighted frequency averaging

The square magnitude of a Butterworth filter of order one corresponds to a Lorentzian function. Accordingly, computing the Lorentzian-weighted frequency average only requires the frequency of analysis to be shifted to a complex value, of which the imaginary part is equal to the shape parameter of the Lorentzian. Due to its bell-shape, the Lorentzian cannot properly represent the features of a rectangular window, and its application is not as straightforward as in the case of band-averaging. In ch. 7, three possible applications are investigated, as summarized in the following.

Prediction of the ensemble mean input power

Under the assumption of ergodicity, the mean response of an ensemble of systems can be estimated by averaging the nominal response over the frequency. Accordingly, the research described in sec. 7.2 investigates the possibility of using the Lorentzian-weighted frequency average to represent the mean input power for an ensemble of structures. To this end, the Lorentzian shape parameter is chosen according to the natural frequency statistics of the system under investigation. Such a procedure allows weighing the response of which eigenfrequency positions are perturbed.

The strategy is applied for the prediction of the ensemble power injected into plates perturbed with random masses, showing good agreement with MC simulation results. The case of a multi-component system is also analyzed, and the ensemble mean is predicted with good accuracy by selectively performing the Lorentzian averaging only on the perturbed components.

Computation of the direct field dynamic stiffness

When an ensemble of systems is considered, the computation of the direct field dynamic stiffness can be performed by evaluating the ensemble average dynamic stiffness, or equivalently assuming the presence of a high level of damping. As discussed in sec. 7.3, the dynamic stiffness can also be evaluated by computing its Lorentzian-weighted frequency average. The procedure only requires analyzing the system at a complex frequency instead of a real one. Such a change can be interpreted as the introduction of additional apparent damping to the system.

This procedure does not require the system properties to be altered and provides a very general way of computing the direct field dynamic stiffness by means of deterministic techniques, such as FEM. The result can be exploited in the context of hybrid approaches, or for CLF computation.

Mass-frequency density function in the Fuzzy Structure Theory

The FST allows handling a complex structure by reducing its DOFs to the ones of the master, primary structure. All secondary structures and attached equipment are modeled as “fuzzy” oscillators. In Pierce’s version of the FST [166], fuzzy structures are defined by a function which describes the distribution of mass with respect to the natural frequency of the oscillator. In sec. 7.4, the Lorentzian function is proposed as a mass-frequency density function for the fuzzy attachments. By using the Lorentzian-weighted frequency integration, the impedance of the fuzzy structure is computed by taking into account a complex resonance frequency instead of a real one. Similarly to Pierce’s formulation, this leads to an apparent mass and damping on the master structure. Nevertheless, the Lorentzian allows a direct control on the mass distribution through the choice of the shape parameter.

8.2 Future research topics

The use of the residue theorem to evaluate weighted frequency integrals, is novel in the field of structural dynamics. The presented research attempts to cover some fundamental issues regarding the applicability of such techniques. However, research can still be extended in several directions towards novel areas.

The following section collects some ideas to extend the present work.

Weighting functions and quadrature rules The application of quadrature rules over paths in the complex plane has led to the formulation of families of weighting functions, of which the ability to resemble an ideal rectangular window is dependent on the accuracy of the scheme and on the chosen contour. Investigating the properties of these weighting functions might be a first step towards an optimized use of quadrature schemes in the complex plane. Finally, as the square magnitude of a Butterworth filter has been proven to be connected to the use of the midpoint rule over a semi-circle in the complex frequency plane, it would be interesting to investigate whether a similar relation exists for other well-known filters, i.e. Chebyshev filters.

Solution of weighted integrals in other domains The use of the residue theorem is particularly advantageous to integrate the response of second-order linear systems, due to the fact that the integrand becomes much smoother in the complex plane. Future research could extend these concepts to other fields of engineering, where there is a need for fast computations of weighted integrals.

Solution of highly oscillatory integrals in other domains The use of the residue theorem is particularly advantageous to integrate the response of vibrating systems due to the fact that the integrand becomes much smoother in the complex frequency plane. However, the concepts presented in this manuscript can be easily extended for the solution of oscillatory integrals in other fields of computational analysis, i.e. optics, quantum chemistry, image processing, electromagnetism, etc. Additionally, the proposed methodologies can be compared in terms of accuracy and robustness to other well-established techniques to estimate highly oscillatory integrals (sec. 2.3).

Application to heavily damped and unbounded problems The main limitation to the use of the residue theorem for band integration is the impossibility to compute averaged quadratic quantities. As their poles are spread all over the complex plane, they might be located inside the contour of integration, highly reducing the efficiency of the approach. In general, this is the case for bounded, lightly damped problems, such as finite plates and acoustic enclosures. Nevertheless, for heavily damped or unbounded problems, system poles might be far away from the real axis. This condition would allow extending the use of the residue theorem to averaged quadratic quantities.

A case of particular interest is the exterior acoustic problem. In fact, the presence of the Sommerfeld condition would suggest that poles naturally move away from the real axis. However, the effects of the coupling with a vibrating

structure and the presence of local resonances in the fluid have to be carefully considered.

With regard to structure-fluid coupling, a distinction should be made. When the problem is uncoupled, the structural vibration can be approximated by using, for example, rational functions, leading to a form which may allow the efficient use of the residue theorem. For coupled vibro-acoustic problems, system poles are unknown, limiting the efficient exploitation of the proposed techniques. However, there is no literature investigating the position of system poles for exterior unbounded problems, and, as such, this could be a topic of future research.

It is important to consider possible drawbacks of the numerical technique used to model the problem. For example, the BEM has a non-unique solution for exterior problems (with closed geometries). Consequently, the exterior solution presents fictitious resonances, corresponding to system poles possibly located close to the real axis. Although some approaches exist to mitigate this problem, the impact they have on the position of the system poles is not clear. This might be another open question for future research.

Lorentzian-weighted frequency averaging to predict the ensemble behavior

Approximating the behavior of an ensemble of systems by using frequency averaging procedures is very attractive from a computational point of view. A further gain can be achieved by exploiting the features of the Lorentzian function, which allows computing the average by adding an imaginary part to the real frequency of analysis. Future research could focus on the validity of the ergodic assumption and on the tuning of the width of the Lorentzian for the cases not explored in this manuscript.

The computation of the direct field dynamic stiffness is another application area for the Lorentzian-weighted averaging. Current investigations are proving the potential of the approach to compute CLFs. Moreover, due to the apparent damping introduced in the system, the use of a coarser mesh does not seem to affect the accuracy of the result. A complete understanding of the limits of this procedure is still missing.

A final topic of high interest for future research might be the investigation of the use of the Lorentzian Orthogonal Ensemble (LOE). It is observed in the literature that the LOE shows convergence towards the GOE [19].

Use of the Lorentzian within the SBEM The Stochastic BEM [214] is a BE technique which allows taking into account the effects of given geometrical variabilities on the system response. Due to the introduction of perturbations on the element positions, integrals are solved in an average sense. However, since both the position of the source and the receiver element are described in

a probabilistic way, integrating the Green's function is computationally very expensive, as many Gauss points are required. A possible step forward to speed up the integration is to use the Lorentzian as a probability distribution function. The use of the residue theorem might lead to an integral which only requires the integration of Green's functions evaluated at a point in the complex space.

Appendix A

The Wave Based Method

The WBM is a deterministic technique belonging to the family of Trefftz methods [201]. Unlike element-based techniques, the domain is partitioned into a small number of convex subdomains. The field variable is not described by low-order polynomial shape functions, but is expanded in terms of wave functions which a priori satisfy the governing partial differential equation. This guarantees a higher convergence rate compared to classic element-based techniques.

The development of the WBM started about 15 years ago, when Desmet proposed it for the solution of bounded acoustic, structural and coupled vibro-acoustic problems [49]. Successively, the application area has been extended to unbounded acoustics [11], assemblies of flat shells [205], and poro-elastic modeling [47]. Moreover, coupled approaches allow increasing the flexibility of the method. The hybrid FE/WBM [167] allows handling geometrically complex domains. The Multi-level WBM allows to efficiently take into account the presence of scatterers and inclusions in the domain [202]. Recently, a coupled BE/WBM has been developed for the inclusion of geometrically complex scatterers [6]. Finally, the hybrid WBM/SEA has been developed to deal with statistical/deterministic systems [208].

The following appendix is dedicated to the description of the WBM. In sec. A.1, the basic WB formulation is provided. The differences between classic FE and WB modeling are described in sec. A.2. Finally, in sec. A.3 and A.4, the formulations for 3D bounded acoustic problems and bending vibration of simply supported plates are presented, respectively.

A.1 The WB modeling

Consider a generic steady-state problem governed by the differential equation,

$$\mathcal{L}[\mathbf{w}(\mathbf{x})] = \mathbf{b}(\mathbf{x}) \quad \text{in } \Omega, \quad (\text{A.1})$$

where \mathcal{L} is a linear differential operator defined over the domain Ω with boundary $\partial\Omega$. $w(\mathbf{x})$ is a scalar, or a vector, field variable, and \mathbf{b} is an external loading defined over the domain Ω . Suppose that the boundary $\partial\Omega$ is split into n_{bound} non-overlapping parts, $\partial\Omega = \bigcup_i \partial\Omega_i$. Over each partition, boundary conditions are applied,

$$\mathcal{B}_i[\mathbf{w}(\mathbf{x})] = \bar{\mathcal{B}}_i(\mathbf{x}) \quad \text{on } \partial\Omega_i, \quad (\text{A.2})$$

with $\mathcal{B}_i[\bullet]$ a boundary differential operator, and $\bar{\mathcal{B}}_i$ the prescribed boundary field. Over each boundary a generalized residual can also be defined as

$$R_i(\mathbf{x}) = \mathcal{B}_i[\mathbf{w}(\mathbf{x})] - \bar{\mathcal{B}}_i(\mathbf{x}). \quad (\text{A.3})$$

Provided that the governing differential equation (A.1) can be cast into a number of Helmholtz equations, the WB modeling procedure consists of four main steps:

- Partitioning into convex subdomains;
- Field variable expansion;
- Construction of the system of equations;
- Solution of the system of equations.

Each of these steps is detailed in the following sections.

A.1.1 Partitioning into subdomains

When dealing with bounded problems, a sufficient condition to assure the convergence of the solution, is the convexity of the domain [49]. If the problem geometry is non-convex, the domain Ω can be divided into non-overlapping convex subdomains, $\Omega^{(\alpha)}$. If the domain is unbounded, the problem is decomposed into a bounded region, which surrounds the model, and an unbounded one. The truncation surface is generally taken as a sphere or a circle [11].

Continuity conditions are imposed at the interface I of neighboring subdomains α and β ,

$$B_I^{(\alpha,\beta)} \left(\mathbf{w}^{(\alpha)}(\mathbf{x}), \mathbf{w}^{(\beta)}(\mathbf{x}) \right) = 0, \quad \text{on } \partial\Omega_I^{(\alpha,\beta)}, \quad (\text{A.4})$$

where $B_I^{(\alpha,\beta)}$ represents a generalized boundary differential operator.

A.1.2 Field variable expansion

Each component of the field variable \mathbf{w} over the subdomain $\Omega^{(\alpha)}$ is approximated by the following expansion,

$$w_j^{(\alpha)}(\mathbf{x}) \approx \hat{w}_j^{(\alpha)}(\mathbf{x}) = \Psi_j^{(\alpha)}(\mathbf{x}) \cdot \mathbf{c}_j^{(\alpha)} + \hat{w}_{b,j}^{(\alpha)}(\mathbf{x}), \quad (\text{A.5})$$

where $\Psi_j^{(\alpha)}$ is a vector containing the wave functions evaluated at point \mathbf{x} , and $\mathbf{c}_j^{(\alpha)}$ is a vector containing the wave contribution factors. Finally, $\hat{w}_{b,j}^{(\alpha)}$ is the particular solution to the differential equation. The vectors Ψ and \mathbf{c} have dimension $n_j^{(\alpha)}$. The wave functions satisfy the governing differential equation and are selected based on the dimensions of the prism (or rectangle) circumscribing the physical domain of analysis, also called bounding box and illustrated in fig. 5.12. A first set of functions is chosen such that an integer number of half wavelengths fits into the corresponding dimension of the bounding box. The wavenumbers of the other wave functions are chosen to satisfy the dispersion relation,

$$\sum_i k_i^2 = k^2, \quad (\text{A.6})$$

where the index i sums up to 2 for 2D problems and to 3 for 3D.

The choice of the wave functions represents the distinctive characteristics of the WBM with respect to other indirect Trefftz approaches. In case the domain is unbounded, a set of wave functions is chosen such that it satisfies the governing differential equation and the Sommerfeld condition at infinity.

The number of wave functions to include in the expansion (A.5) can be infinite, in principle. In practice a frequency dependent truncation rule is applied to take into account only a finite number of terms, such that the maximum wavenumber component is larger than T times the physical wavenumber, where T is a user-defined truncation parameter, usually ranging from 1 to 6 [208].

A.1.3 Construction of the system of equations

Boundary conditions and subdomain continuity are enforced through a Galerkin weighted residual formulation. For each subdomain, they are

orthogonalized with respect to a test function $\tilde{\mathbf{w}}$ expanded using the same wave functions as in the field variable expansion. The solution can be found by solving the following integral equation,

$$\begin{aligned} & \sum_{\alpha} \sum_i \int_{\partial\Omega_i^{(\alpha)}} \tilde{\mathbf{w}}_i^{(\alpha)}(\mathbf{x}) \left(\mathcal{B}_i \left[\mathbf{w}^{(\alpha)}(\mathbf{x}) \right] - \bar{\mathcal{B}}_i(\mathbf{x}) \right) d\partial\Omega \quad (\text{A.7}) \\ & + \sum_{\alpha} \sum_{\beta \neq \alpha} \sum_i \int_{\partial\Omega_I^{(\alpha, \beta)}} \tilde{\mathbf{w}}_i^{(\alpha)}(\mathbf{x}) \mathcal{B}_I^{(\alpha, \beta)} \left[\mathbf{w}^{(\alpha)}(\mathbf{x}), \mathbf{w}^{(\beta)}(\mathbf{x}) \right] d\partial\Omega = 0. \end{aligned}$$

Since the wave functions can be highly oscillating functions, accurate quadrature schemes are needed to compute the boundary integrals. In the current implementation, the Gaussian quadrature is implemented. Typically 12 integration points per wavelength are sufficient to provide accurate estimates [208].

Since the test function is expanded in terms of the wave functions, eq. (A.7) leads to a system of equations,

$$\mathbf{A}\mathbf{c} = \mathbf{f}, \quad (\text{A.8})$$

of which the system matrix \mathbf{A} is complex, fully populated and frequency dependent.

A.1.4 Solution and post-processing

The system of equations is solved for the wave function contribution factors. In the post-processing part, the wave field is reconstructed by means of a weighted sum of wave functions, evaluated at the target point. Derived quantities can be obtained by analytic derivation of wave function expressions, without loss of accuracy.

A.2 Characteristics of WB modeling

The WB modeling philosophy is different compared to classic FEM. This section is dedicated to briefly compare the two worlds.

Problem discretization According to FE modeling, the problem domain is decomposed into a number of non-overlapping small elements, over which the field variable is described by means of low-order polynomial shape functions. The accuracy of the solution increases with decreasing size of the elements,

which are able to capture the oscillating behavior of the wavefield. On the contrary, discretization is not required in WB modeling, for which the domain is divided into a small number of large (convex) subdomains.

Geometrical flexibility The ability of representing complex geometries is one of the main strengths of FE modeling. Decreasing the size of the elements allows capturing complex geometrical details. On the other hand, when the number of WB subdomains increases, to represent a complex domain, the number of interfaces increases as well, with a consequent impact on the computational cost of the integration. For this reason, classic WB modeling performs at best when applied to problems with moderate geometrical complexity. Nevertheless, hybrid and Multi-level approaches have been developed to extend the range of applicability to more complex geometries.

Degrees of freedom In FE modeling the DOFs are the field variable at the nodal points, and the field is represented in terms of shape functions. In fact, one of the main drawbacks in FEM is the loss of accuracy when computing derived quantities, which are evaluated based on the nodal values. On the other hand, when a wave formulation is adopted, the DOFs are the contribution factors for each corresponding wave function. Derived quantities can be analytically computed from the wave functions, without loss of accuracy.

System matrix properties A relevant advantage of the FEM is the structure of the matrices. In fact they are sparsely populated, symmetric and generally real and frequency independent. Depending on the application, the size of a FE matrix can be very large, especially when moving towards higher frequencies, or when 3D acoustic problems are analyzed. WB matrices are complex, fully populated and frequency dependent. Moreover, due to the oscillatory nature of the wave functions, the matrices may suffer from ill-conditioning. However, due to the high convergence rate, WB matrices are generally much smaller than FEM.

Computational performance Matrix building and solution are the most computationally expensive phases when processing a numerical problem. For FEM, the former phase is relatively fast, as it requires the integration of low-order polynomial shape functions. On the other hand, the highly oscillating wave functions require a relatively large number of integration points to compute the boundary integrals. Concerning the processing part, the form of FEM matrices highly facilitates the solution of the system of equations, which

is slowed down by the size of the problem. On the contrary, the solution of a complex system of equations is relatively more expensive, but due to the small size of the matrix, the WBM can highly outperform FE modeling [208].

A.3 3D bounded acoustic problem

Suppose Ω_a is a 3D acoustic domain, bounded by $\partial\Omega_a$. The boundary is divided in three non-overlapping regions $\partial\Omega_a = \partial\Omega_{a,p} \cup \partial\Omega_{a,v} \cup \partial\Omega_{a,z}$, on which prescribed pressure, velocity and impedance are imposed, respectively. A volume velocity source is located at \mathbf{x}_q . The steady-state acoustic problem is governed by the Helmholtz equation (2.11), as described in sec. 2.1.2 and shown in fig. 2.2.

Considering a single convex domain, the pressure p can be approximated by the field variable expansion (A.5), as follows

$$p(\mathbf{x}) \approx \hat{p}(\mathbf{x}) = \mathbf{\Psi}(\mathbf{x}) \cdot \mathbf{c} + \hat{p}_q(\mathbf{x}), \quad (\text{A.9})$$

with $\mathbf{\Psi}$ and \mathbf{c} vectors containing n_a wave functions Ψ_a , and the corresponding contribution factors c_a .

The function \hat{p}_q is the particular solution of the Helmholtz equation subject to the source of volume velocity q and is defined as

$$\hat{p}_q(\mathbf{x}) = i\rho_a\omega q \frac{e^{-ik_a r_q}}{4\pi r_q}, \quad (\text{A.10})$$

where r_q is the Euclidean distance between the excitation point \mathbf{x}_q and the generic point \mathbf{x} .

For 3D bounded problems, three types of acoustic wave functions are identified, called r -, s - and t -set, respectively

$$\begin{aligned} \Psi_{a,r} &= \cos(k_{r,x}x) \cos(k_{r,y}y) e^{-ik_{r,z}z} & r &= 0, 1, \dots, n_r \\ \Psi_{a,s} &= \cos(k_{s,x}x) e^{-ik_{s,y}y} \cos(k_{s,z}z) & s &= 0, 1, \dots, n_s \\ \Psi_{a,t} &= e^{-ik_{t,x}x} \cos(k_{t,y}y) \cos(k_{t,z}z) & t &= 0, 1, \dots, n_t \end{aligned} \quad (\text{A.11})$$

From an infinite set of wavenumbers, a subset is selected based on the dimensions of the smallest prism circumscribing the geometry, of which the dimensions are $l_x \times l_y \times l_z$. The first two wavenumber components are chosen such that an integer number of half wavelengths fits into the dimension of the bounding box in the corresponding direction. The third component is computed

by means of eq. (A.6). This leads to the following wavenumber set,

$$\left\{ \begin{array}{l} (k_{r,x}, k_{r,y}, k_{r,z}) = \left(\frac{a_1\pi}{l_x}, \frac{a_2\pi}{l_y}, \pm \sqrt{k_a^2 - \left(\frac{a_1\pi}{l_x}\right)^2 - \left(\frac{a_2\pi}{l_y}\right)^2} \right) \\ (k_{s,x}, k_{s,y}, k_{s,z}) = \left(\frac{a_3\pi}{l_x}, \pm \sqrt{k_a^2 - \left(\frac{a_3\pi}{l_x}\right)^2 - \left(\frac{a_4\pi}{l_z}\right)^2}, \frac{a_4\pi}{l_z} \right) \\ (k_{t,x}, k_{t,y}, k_{t,z}) = \left(\pm \sqrt{k_a^2 - \left(\frac{a_5\pi}{l_y}\right)^2 - \left(\frac{a_6\pi}{l_z}\right)^2}, \frac{a_5\pi}{l_y}, \frac{a_6\pi}{l_z} \right) \end{array} \right. \quad (\text{A.12})$$

In practice, the coefficients $a_1, a_2, a_3, a_4, a_5, a_6$ are truncated by using the following rule,

$$\frac{n_1}{l_x} \approx \frac{n_2}{l_y} \approx \frac{n_3}{l_x} \approx \frac{n_4}{l_z} \approx \frac{n_5}{l_y} \approx \frac{n_6}{l_z} \geq T \frac{k_a}{\pi}, \quad (\text{A.13})$$

where n_1, n_2, n_3, n_4, n_5 and n_6 are the integer truncation numbers and T is a user defined truncation parameter. The total number of wavefunctions is

$$n_a = 2[(n_1 + 1)(n_2 + 1) + (n_3 + 1)(n_4 + 1) + (n_5 + 1)(n_6 + 1)]. \quad (\text{A.14})$$

The Galerkin weighted residual approach is used to build the system of equations, through the integral form,

$$\begin{aligned} - \int_{\partial\Omega_{a,p}} \mathcal{L}_v [\tilde{p}(\mathbf{x})] R_p(\mathbf{x}) d\partial\Omega_{a,p} + \int_{\partial\Omega_{a,v}} \tilde{p}(\mathbf{x}) R_v(\mathbf{x}) d\partial\Omega_{a,v} \\ + \int_{\partial\Omega_{a,z}} \tilde{p}(\mathbf{x}) R_z(\mathbf{x}) d\partial\Omega_{a,z} = 0 \end{aligned} \quad (\text{A.15})$$

where \mathcal{L}_v is the normal velocity operator,

$$\mathcal{L}_v = \frac{i}{\rho_a \omega} \frac{\partial}{\partial n_a}. \quad (\text{A.16})$$

The test function \tilde{p} is expressed in terms of the same wave functions as \hat{p} . The residuals are defined on each boundary: for prescribed pressure boundary condition,

$$R_p(\mathbf{x}) = \hat{p}(\mathbf{x}) - \bar{p}(\mathbf{x}) \quad \text{on } \partial\Omega_{a,p}, \quad (\text{A.17})$$

normal velocity

$$R_v(\mathbf{x}) = \mathcal{L}_v [\hat{p}(\mathbf{x})] - \bar{v}_n(\mathbf{x}) \quad \text{on } \partial\Omega_{a,v}, \quad (\text{A.18})$$

and normal impedance,

$$R_z(\mathbf{x}) = \mathcal{L}_z [\hat{p}(\mathbf{x})] - \frac{\hat{p}(\mathbf{x})}{\bar{Z}_n(\mathbf{x})} \quad \text{on } \partial\Omega_{a,z}. \quad (\text{A.19})$$

Substituting the field variable expansion (A.9) into eq. (A.15) leads to a system of n_a equations in n_a unknowns.

If Ω_a is divided in multiple convex subdomains, an additional integral term takes into account the continuity conditions between subdomains in eq. (A.15). Detailed expressions are reported in the literature [167].

A.4 Plate bending problem

Suppose Ω_p is the 2D plate domain of boundary $\partial\Omega_p$ of simply supported plate. The out-of-plane bending of a thin plate is governed by the Kirchhoff equation, (6.1).

Considering a single convex domain, the displacement field w can be approximated by the field variable expansion (A.5), as follows

$$w(\mathbf{x}) \approx \hat{w}(\mathbf{x}) = \mathbf{\Psi}(\mathbf{x}) \cdot \mathbf{c} + \hat{w}_f(\mathbf{x}), \quad (\text{A.20})$$

with $\mathbf{\Psi}$ and \mathbf{c} vectors containing n_b wave functions Ψ_b , and the corresponding contribution factors c_b .

The function \hat{w}_f is the particular solution of the Kirchhoff equation subject to the force of amplitude F_0 and is defined as

$$\hat{w}_f(\mathbf{x}) = -\frac{iF_0}{8k_b^2 D} [H_0^{(2)}(k_b r_f) - H_0^{(2)}(-ik_b r_f)], \quad (\text{A.21})$$

where r_f is the Euclidean distance between the excitation point \mathbf{x}_f and the generic point \mathbf{x} . $H_0^{(2)}$ is the Hankel function of the second kind with order zero.

For plate bending problems, the wave functions Ψ_b have mathematical form

$$\Psi_{b_1}(\mathbf{x}) = \cos(k_{b_{1,x}} x) e^{-ik_{b_{1,y}} y} \quad b_1 = 0, 1, \dots, n_{b_1}, \quad (\text{A.22})$$

$$\Psi_{b_2}(\mathbf{x}) = e^{-ik_{b_{2,x}} x} \cos(k_{b_{2,y}} y) \quad b_2 = 0, 1, \dots, n_{b_2}.$$

From an infinite set of wavenumbers, a subset is selected based on the dimension of the smallest rectangular box circumscribing the plate geometry, of which the dimensions are $l_x \times l_y$. The first wavenumber components are chosen such that an integer number of half wavelengths equals the dimension of the rectangular bounding box in the corresponding direction,

$$k_{b_{1,x}} = \frac{b_1 \pi}{l_x}, \quad (\text{A.23})$$

$$k_{b_{2,y}} = \frac{b_2 \pi}{l_y}. \tag{A.24}$$

The other wavenumber components are calculated from the bending wave number k_b corresponding to the considered frequency,

$$k_{b_{1,y}} = \begin{cases} \pm \sqrt{k_b^2 - k_{b_{1,x}}^2} \\ \pm i \sqrt{k_b^2 + k_{b_{1,x}}^2} \end{cases}, \tag{A.25}$$

$$k_{b_{2,x}} = \begin{cases} \pm \sqrt{k_b^2 - k_{b_{2,y}}^2} \\ \pm i \sqrt{k_b^2 + k_{b_{2,y}}^2} \end{cases}. \tag{A.26}$$

The coefficients b_1 and b_2 are truncated by using the rule

$$\frac{n_{b_1}}{l_x} \approx \frac{n_{b_2}}{l_y} \geq T \frac{k_a}{\pi}, \tag{A.27}$$

where n_{b_1} and n_{b_2} are the integer truncation numbers and T is the truncation parameter. The total number of wavefunctions is

$$n_b = 4(n_{b_1} + 1) + 4(n_{b_2} + 1). \tag{A.28}$$

The Galerkin weighted residual approach is used to build the system of equations. In case of a simply supported plate, the residual formulation results in the following expression

$$\int_{\partial\Omega_p} \mathcal{L}_Q[\tilde{w}(\mathbf{x})]R_w(\mathbf{x}) \, d\partial\Omega_p - \int_{\partial\Omega_p} \mathcal{L}_\theta[\tilde{w}(\mathbf{x})]R_m(\mathbf{x}) \, d\partial\Omega_p = 0, \tag{A.29}$$

where \mathcal{L}_Q and \mathcal{L}_θ are respectively the generalized shear force and rotation operators defined as follows,

$$\mathcal{L}_Q = -D \frac{\partial}{\partial n_p} \left[\frac{\partial^2}{\partial n_p^2} + (2 - \nu) \frac{\partial^2}{\partial s_p^2} \right], \tag{A.30}$$

$$\mathcal{L}_\theta = -\frac{\partial}{\partial n_p}, \tag{A.31}$$

where n_p and s_p are the in-plane normal and tangential directions of the plate boundary, respectively. The test function \tilde{w} is expressed in terms of the same wave functions as \hat{w} . The residuals are defined on the boundary: for prescribed out-of-plane displacements,

$$R_w(\mathbf{x}) = \hat{w}(\mathbf{x}) - \bar{w}(\mathbf{x}) \quad \text{on } \partial\Omega_p, \tag{A.32}$$

and prescribed bending moment,

$$R_m(\mathbf{x}) = \mathcal{L}_m [\hat{w}(\mathbf{x})] - \bar{m}(\mathbf{x}) \quad \text{on } \partial\Omega_p, \quad (\text{A.33})$$

where the bending moment operator is expressed as,

$$\mathcal{L}_m = -D \left(\frac{\partial^2}{\partial n_p^2} + \nu \frac{\partial^2}{\partial s_p^2} \right) \quad (\text{A.34})$$

Substituting the field variable expansion (A.20) into eq. (A.29) leads to a system of n_b equations in n_b unknowns.

For the sake of brevity, the WBM formulation is here presented only for the case of simply supported boundary conditions. The reader is referred to ref. [208] for a more complete and general formulation in structural dynamics.

Bibliography

- [1] *Matlab R2010a User Manual*.
- [2] *MSC.Nastran 2010 User Manual*.
- [3] Burden of Disease from Environmental Noise: Quantification of Healthy Life Years Lost in Europe. *World Health Organization* (2011).
- [4] ADHIKARI, S. Doubly Spectral Stochastic Finite-Element Method for Linear Structural Dynamics. *Journal of Aerospace Engineering* 24, 3 (2011), 264–276.
- [5] ARNST, M., CLOUTEAU, D., CHEBLI, H., OTHMAN, R., AND DEGRANDE, G. A non-parametric probabilistic model for ground-borne vibrations in buildings. *Probabilistic Engineering Mechanics* 21, 1 (2006), 18–34.
- [6] ATAK, O., BERGEN, B., HUYBRECHS, D., PLUYMERS, B., AND DESMET, W. Coupling of boundary element and wave based methods for the efficient solution of complex multiple scattering problems. *Journal of Computational Physics* 258 (2014), 165–184.
- [7] BABUSKA, I., AND MELENK, J. The partition of unity method. *International Journal for Numerical Methods in Engineering* 40, 4 (1997), 727–758.
- [8] BABUSKA, I., AND SAUTER, S. Is the pollution effect of the FEM avoidable for the Helmholtz equation considering high wavenumbers? *SIAM Review* 42, 3 (2000), 451–484.
- [9] BATHE, K.-J. *Finite Element Procedures*. Prentice Hall, 2007.
- [10] BENNINGHOF, J., KAPLAN, M., MULLER, M., AND KIM, M. Meeting the NVH computational challenge: Automated multi-level substructuring.

- In *Proceedings of the International Modal Analysis Conference XVIII (IMAC18)* (San Antonio, USA, 2000).
- [11] BERGEN, B. *Wave based modelling technique for unbounded acoustic problems*. PhD thesis, KU Leuven, 2011.
- [12] BERGEN, B., PLUYMERS, B., VAN GENECHTEN, B., VANDEPITTE, D., AND DESMET, W. A Trefftz based method for solving Helmholtz problems in semi-infinite domains. *Engineering Analysis with Boundary Elements* 36, 1 (2012), 30–38.
- [13] BERIOT, H., AND TOURNOUR, M. A review of stabilized FEM for Helmholtz equation. In *Proceedings of Noise and Vibration: Emerging Methods 2009 - NOVEM 2009* (Oxford, United Kingdom, 2009).
- [14] BERIOT, H., TOURNOUR, M., AND MASS, G. On a few recent advances of finite element methods for the Helmholtz equation. In *Proceedings of the Sixteenth International Congress on Sound and Vibration, ICSV16* (Krakov, Poland, 2009).
- [15] BETTESS, P. *Infinite Elements*. Penshaw Press, 1992.
- [16] BOUILLARD, P., AND IHLENBURG, F. Error estimation and adaptivity for the finite element method in acoustics: 2D and 3D applications. *Computer Methods in Applied Mechanics and Engineering* 176, 1-4 (1999), 147–163.
- [17] BREBBIA, C. *Boundary Element Techniques in Computer-Aided Engineering*. Series E, Applied Sciences. Springer, 2007.
- [18] BREBBIA, C., AND BUTTERFIELD, R. Formal equivalence of direct and indirect boundary element methods. *Applied Mathematical Modelling* 2, 2 (1978), 132–134.
- [19] BROUWER, P. W. *On the Random-Matrix theory of quantum transport*. PhD thesis, Leiden University, 1997.
- [20] BRUNEAU, M. *Fundamental of Acoustics*. ISTE Ltd., 2006.
- [21] BURTON, A. J., AND MILLER, G. F. The Application of Integral Equation Methods to the Numerical Solution of Some Exterior Boundary-Value Problems. *Proceedings of the Royal Society A: Mathematical, Physical and Engineering Sciences* 323, 1553 (1971), 201–210.
- [22] CARCATERRA, A., AND SESTIERI, A. Energy density equation and power flow in structures. *Journal of Sound and Vibration* 188 (1995), 269–282.

- [23] CARCATERRA, A., AND SESTIERI, A. Complex envelope displacement analysis: a quasi-static approach to vibrations. *Journal of Sound and Vibration* 201, 2 (1997), 205–233.
- [24] CASTANIER, M. P., TAN, Y.-C., AND PIERRE, C. Characteristic Constraint Modes for Component Mode Synthesis. *AIAA Journal* 39, 6 (2001), 1182–1187.
- [25] CHABAS, F., AND DESANTI, A., S. C. Probabilistic structural modeling in linear dynamic analysis of complex mechanical systems. Part II - Numerical analysis and applications. *La Recherche Aérospatiale* 5 (1986), 49–67.
- [26] CHARPENTIER, A., SREEDHAR, P., AND FUKUI, K. Efficient model of structure-borne noise in a fully trimmed vehicle from 200Hz to 1kHz. In *Proceedings of the 15th International Congress on Sound and Vibration* (Deajong, Korea, 2008).
- [27] CHENG, Y., DEYU, L., AND CHENG, L. Dynamic vibration absorbers for vibration control within a frequency band. *Journal of Sound and Vibration* 330, 8 (2011), 1582–1598.
- [28] CHEUNG, Y. K., JIN, W. G., AND ZIENKIEWICZ, O. C. Solution of Helmholtz equation by Trefftz method. *International Journal for Numerical Methods in Engineering* 32, 1 (1991), 63–78.
- [29] CHOI, K. K., AND KIM, N.-H. *Structural Sensitivity Analysis and Optimization 1: Linear Systems (Mechanical Engineering Series)*. Springer, 2005.
- [30] CICIRELLO, A., AND LANGLEY, R. S. The vibro-acoustic analysis of built-up systems using a hybrid method with parametric and non-parametric uncertainties. *Journal of Sound and Vibration* 332, 9 (2013), 2165–2178.
- [31] CLAEYS, C. C., VERGOTE, K., SAS, P., AND DESMET, W. On the potential of tuned resonators to obtain low-frequency vibrational stop bands in periodic panels. *Journal of Sound and Vibration* 332, 6 (2013), 1418–1436.
- [32] CLAEYS, C. C., VIVOLO, M., SAS, P., AND DESMET, W. Study of honeycomb panels with local cell resonators to obtain low-frequency vibrational stop bands. In *Proceedings of DYNACOMP* (Arcachon, France, 2012).

- [33] COOLS, R., HUYBRECHS, D., AND NUYENS, D. Recent topics in numerical integration. *International Journal of Quantum Chemistry* 109, 8 (2009), 1748–1755.
- [34] COTONI, V., GARDNER, B., CORDIOLI, J. A., CARNEAL, J., AND FULLER, C. Advanced Modeling of Aircraft Interior Noise Using the Hybrid FE-SEA Method. *SAE Technical Paper 2008-36-0575*, 0 (2008).
- [35] COTONI, V., SHORTER, P., AND LANGLEY, R. Numerical and experimental validation of a hybrid finite element-statistical energy analysis method. *Journal of the Acoustical Society of America* 122, 1 (2007), 259–270.
- [36] CRAIG, R. *Structural Dynamics: An Introduction to Computer Methods*. John Wiley & Sons, 1981.
- [37] CRAIK, R. J. M. *Sound Transmission Through Buildings Using Statistical Energy Analysis*. Gower, 1996.
- [38] CRANDALL, S. The role of damping in vibration theory. *Journal of Sound and Vibration* 11, 1 (1970), 3–18.
- [39] CRANE, M., BYRNE, J., GLYNN, J., AND BOYLE, J. Causality and the Complex Modulus Model of Damping. *Journal of Applied Mathematics and Mechanics* 75, 10 (1995), 807–808.
- [40] CREMER, L., HECKL, M., AND PETERSSON, B. *Structure-borne sound: Structural vibrations and sound radiation at audio frequencies*, 3rd edition ed. Springer, 2005.
- [41] D’AMICO, R., PRATELLESI, A., AND PIERINI, M. Improving the Convergence of the Fast Multipole BEM for the Exterior Sound Radiation of a Truck Muffler. *SAE International Journal of Commercial Vehicles* 5 (2012), 2012–01–1556.
- [42] D’AMICO, R., PRATELLESI, A., PIERINI, M., AND TOURNOUR, M. Efficient method to avoid fictitious eigenvalues for indirect BEM. In *Proceedings of the International Conference on Noise and Vibration, ISMA2010* (Leuven, Belgium, 2010).
- [43] DAVIS, P., AND RABINOWITZ, P. *Methods for numerical integration*. Academic Press Inc., London, 1984.
- [44] DE GERSEM, H., MOENS, D., DESMET, W., AND VANDEPITTE, D. A fuzzy finite element procedure for the calculation of uncertain frequency response functions of damped structures. Part 2 - Numerical case studies. *Journal of Sound and Vibration* 288, 3 (2005), 463–486.

- [45] DE MUNCK, M., MOENS, D., DESMET, W., AND VANDEPITTE, D. A response surface based optimisation algorithm for the calculation of fuzzy envelope FRFs of models with uncertain properties. *Computers & Structures* 86, 10 (2008), 1080–1092.
- [46] DEBNATH, N., DEB, S., AND DUTTA, A. Frequency band-wise passive control of linear time invariant structural systems with h_∞ optimization. *Journal of Sound and Vibration* 332, 23 (2013), 6044–6062.
- [47] DECKERS, E. *A Wave Based Approach for Steady-state Biot Models of Poroelastic Materials*. PhD thesis, KU Leuven, 2012.
- [48] DEN HARTOG, J. P. *Mechanical Vibrations (Dover Civil and Mechanical Engineering)*. Dover Publications, 1985.
- [49] DESMET, W. *A wave based prediction technique for coupled vibro-acoustic analysis*. PhD thesis, KU Leuven, 1998.
- [50] DESMET, W. Mid-frequency vibro-acoustic modelling challenges and potential solutions. In *Proceedings of the International Conference on Noise and Vibration (ISMA2002)* (2002).
- [51] DESSOMBZ, O., THOUVEREZ, LAINÉ, J.-P., AND JÉZÉQUEL, L. Analysis of mechanical systems using interval computations applied to finite element methods. *Journal of Sound and Vibration* 239, 5 (2001), 949–968.
- [52] DEY, S., DATTA, D., SHIRRON, J., AND SHEPHARD, M. p -version FEM for structural acoustics with a posteriori error estimation. *Computer Methods in Applied Mechanics and Engineering* 195, 17-18 (2006), 1946–1957.
- [53] DOMINGUEZ, J. *Boundary Elements in Dynamics*. Computational Mechanics Publications, 1993.
- [54] DURAND, J.-F., SOIZE, C., AND GAGLIARDINI, L. Structural-acoustic modeling of automotive vehicles in presence of uncertainties and experimental identification and validation. *Journal of the Acoustical Society of America* 124, 3 (2008), 1513–1525.
- [55] ERLANGGA, Y. A. Advances in iterative methods and preconditioners for the Helmholtz equation. *Archives of Computational Methods in Engineering* 15, 1 (2008), 37–66.
- [56] EWINS, D. *Modal testing: theory and practice*, 2nd edition ed. Research Studies Press Ltd., 2001.

- [57] FAHY, F. Statistical energy analysis: a wolf in sheep's cloathing? In *Proceedings of the Internoise* (Leuven, 1993).
- [58] FAHY, F., AND WALKER, J. *Advanced Applications in Acoustics, Noise and Vibration*. Spon Press, 2004.
- [59] FAIRWEATHER, G., AND KARAGEORGHIS, A. The method of fundamental solutions for elliptic boundary value problems. *Advances in Computational Mathematics* 9, 1-2 (1998), 69–95.
- [60] FARHAT, C., HARARI, I., AND FRANCA, L. The discontinuous enrichment method. *Computer Methods in Applied Mechanics and Engineering* 190, 48 (2001), 6455–6479.
- [61] FARHAT, C., HARARI, I., AND HETMANIUK, U. A discontinuous Galerkin method with Lagrange multipliers for the solution of Helmholtz problems in the mid-frequency regime. *Computer Methods in Applied Mechanics and Engineering* 192, 11-12 (2003), 1389–1419.
- [62] FISHMAN, G. *Monte Carlo: Concepts, Algorithms, and Applications*. Springer, 2003.
- [63] FRANCA, L., AND DUTRA DO CARMO, E. The Galerkin gradient least-squares method. *Computer Methods in Applied Mechanics and Engineering* 74, 1 (1989), 41–54.
- [64] FREDÖ, C. A SEA-like approach for the derivation of energy flow coefficients with a finite element model. *Journal of Sound and Vibration* 199, 4 (1997), 645–666.
- [65] FRIIS, L., AND OHLRICH, M. Vibration modeling of structural fuzzy with continuous boundary. *The Journal of the Acoustical Society of America* 123, 2 (2008), 718.
- [66] GAGLIARDINI, L., HOUILLON, L., BORELLO, G., AND PETRINELLI, L. Virtual SEA-FEA-based modeling of mid-frequency structure-borne noise. *Sound and Vibration* 39, 1 (2005), 22–28.
- [67] GASSER, F. A., NADER, A., AND AHMED, H. G. *Finite Element Analysis for Satellite Structures: Applications to Their Design, Manufacture and Testing*. Springer, 2012.
- [68] GIANNINI, O., CARCATERRA, A., AND SESTIERI, A. High frequency vibration analysis by the complex envelope vectorization. *Journal of the Acoustical Society of America* 121, 6 (2007), 3472.

- [69] GIVOLI, D. *Numerical Methods for Problems in Infinite Domains*. Elsevier Publishing Company, 1992.
- [70] GIVOLI, D. High-order local non-reflecting boundary conditions: a review. *Wave Motion* 39, 4 (2004), 319–326.
- [71] GIVOLI, D., AND PATLASHENKO, I. Dirichlet-to-Neumann boundary condition for time-dependent dispersive wave in three-dimensional guides. *Journal of Computational Physics* 199 (2004), 339–354.
- [72] GOLDBERG, D. *Genetic Algorithms in Search, Optimization, and Machine Learning*. Addison-Wesley Professional, 1989.
- [73] GREENBERG, M. *Advanced engineering mathematics*, 2nd edition ed. Pearson, 1998.
- [74] GUDDATI, M., AND YUE, B. Modified integration rules for reducing dispersion error in finite element methods. *Computer Methods in Applied Mechanics and Engineering* 193, 3 (2004), 275–287.
- [75] GUMEROV, N., AND DURAISWAMI, R. *Fast Multipole Methods for the Helmholtz Equation in Three Dimensions*. Elsevier Ltd., Oxford, 2004.
- [76] GUYADER, J.-L. *Vibration in Continuous Media (ISTE)*. Wiley-ISTE, 2006.
- [77] HAGSTROM, T. Radiation boundary conditions for the numerical simulation of waves. *Acta Numerica* 8 (1999), 47.
- [78] HALLEZ, R., AND DELANGHE, K. Solving large industrial models with the fast mutlipole method. In *Proceedings of the Sixteen International Congress on Sound and Vibration* (Krakow, Poland, 2009).
- [79] HAMMING, R. *Numerical Methods for Scientists and Engineers*. Dover Publications, Inc., 1962.
- [80] HARARI, I., AND HUGES, T. J. R. A cost comparison of boundary element and finite element methods for problems of time-harmonic acoustics. *Computer Methods in Applied Mechanics and Engineering* 97 (1992), 77–102.
- [81] HARARI, I., AND HUGES, T. J. R. Galerkin/least-squares finite element methods for the reduced wave equation with non-reflecting boundary conditions in unbounded domains. *Computer Methods in Applied Mechanics and Engineering* 98, 3 (1992), 411–454.

- [82] HARARI, I., AND MAGOULÉS, F. Numerical investigations of stabilized finite element computations for acoustics. *Wave Motion* 39, 4 (2004), 339–349.
- [83] HARARI, I., SLAVUTIN, M., AND TURKEL, E. Analytical and numerical studies of a finite element PML for the Helmholtz equation. *Journal of Computational Acoustics* 08, 1 (2000), 121–137.
- [84] HARDY, P., ICHCHOU, M., JÉZÉQUEL, L., AND TRENTIN, D. A hybrid local energy formulation for plates mid-frequency flexural vibrations. *European Journal of Mechanics - A/Solids* 28, 1 (2009), 121–130.
- [85] HAW-LING, L., AND PINSKY, P. Matrix-padé via Lanczos solutions for vibrations of fluid structure interaction. *International Journal for Numerical Methods in Engineering* 84 (2010), 1183–1204.
- [86] HENDY, D. Numerical evaluation of the sound power radiated from baffled, rectangular panels. *Journal of Sound and Vibration* 127, 2 (1988), 283–289.
- [87] HOLLAND, J. *Adaptation in Natural and Artificial Systems: An Introductory Analysis with Applications to Biology, Control, and Artificial Intelligence*. A Bradford Book, 1992.
- [88] HONG, S., WANG, A., AND VLAHOPOULOS, N. A hybrid finite element formulation for a beam-plate system. *Journal of Sound and Vibration* 298 (2006), 233–256.
- [89] HOWARD, C. Q., HANSEN, C. H., AND ZANDER, A. Vibro-acoustic noise control treatments for payload bays of launch vehicles: Discrete to fuzzy solutions. *Applied Acoustics* 66, 11 (2005), 1235–1261.
- [90] HUNT, J. *Dynamic Vibration Absorbers*. Mechanical Engineering Publications, 1979.
- [91] HUYBRECHS, D., AND VANDEWALLE, S. On the evaluation of highly oscillatory integrals by analytic continuation. *SIAM Journal on Numerical Analysis* 44, 3 (2006), 1026–1048.
- [92] IANCULESCU, C., AND L., T. Parallel iterative solution for the Helmholtz equation with exact non-reflecting boundary conditions. *Computer Methods in Applied Mechanics and Engineering* 195 (2006), 3709–3741.
- [93] IHLENBURG, F., AND BABUSKA, I. Finite Element Solution of the Helmholtz Equation with High Wave Number. Part II: the h -version of the FEM. *Computers & Mathematics with Applications* 30, 9 (1995), 9–37.

- [94] IHLENBURG, F., AND BABUSKA, I. Finite Element Solution of the Helmholtz Equation with High Wave Number. Part II: the hp -version of the FEM. *SIAM Journal on Numerical Analysis* 34, 1 (1997), 315–358.
- [95] ISERLES, A., AND NØRSETT, S. P. Efficient quadrature of highly oscillatory integrals using derivatives. *Proceedings of the Royal Society A: Mathematical, Physical and Engineering Sciences* 461, 2057 (2005), 1383–1399.
- [96] JOG, C. Topology design of structures subjected to periodic loading. *Journal of Sound and Vibration* 253, 3 (2002), 687–709.
- [97] KEANE, A. Statistical energy analysis of offshore structures. *Engineering Structures* 16, 2 (1994), 145–157.
- [98] KESSISSOGLOU, N., AND LANGLEY, R. Natural statistics of engineering structures. In *Proceedings of the Eleventh International Congress on Sound and Vibration, ICSV2004* (St. Petersburg, Russia, 2004).
- [99] KESSISSOGLOU, N., AND LANGLEY, R. Application of the statistical overlap factor to predict GOE statistics. In *Proceedings of Noise and Vibration Emerging Methods, NOVEM2005* (Saint Raphael, France, 2005).
- [100] KESSISSOGLOU, N., AND LUCAS, G. Gaussian orthogonal ensemble spacing statistics and the statistical overlap factor applied to dynamic systems. *Journal of Sound and Vibration* 324, 3-5 (2009), 1039–1066.
- [101] KITA, E., AND KAMIYA, N. Trefftz method: an overview. *Advances in Engineering Software* 24, 1-3 (1995), 3–12.
- [102] KOMPELLA, M., AND BERNHARD, R. Measurements of the statistical variation of structural-acoustic characteristics of automotive vehicles. In *Proceedings of SAE Noise and Vibration Conference* (Warrendale, USA, 1993).
- [103] KOO, K., D’AMICO, R., PLUYMERS, B., AND DESMET, W. Design optimization of the frequency averaged input power using the residue theorem. In *Proceedings of the 20th International Congress on Sound and Vibration, ICSV20* (Bangkok, Thailand, 2013).
- [104] KOO, K., PLUYMERS, B., DESMET, W., AND WANG, S. Vibro-acoustic design sensitivity analysis using the wave-based method. *Journal of Sound and Vibration* 330, 17 (2011), 4340–4351.

- [105] KOOPMANN, G. H. A method for computing acoustic fields based on the principle of wave superposition. *Journal of the Acoustical Society of America* 86, 6 (1989), 2433–2438.
- [106] LANCASTER, P. *Lambda-matrices and vibrating systems*. Pergamon Press, London, 1966.
- [107] LANGLEY, R. A derivation of the coupling loss factor used in Statistical Energy Analysis. *Journal of Sound and Vibration* 141 (1990), 207–219.
- [108] LANGLEY, R. A wave intensity technique for the analysis of high frequency vibration. *Journal of Sound and Vibration* 159, 3 (1992), 483–502.
- [109] LANGLEY, R. On the power input to point loaded hysteretically damped structures. *Journal of Sound and Vibration* 181, 4 (1995), 657–672.
- [110] LANGLEY, R. On the vibrational conductivity approach to high frequency dynamics for two-dimensional structural components. *Journal of Sound and Vibration* 182, 4 (1995), 637–657.
- [111] LANGLEY, R., AND BERCIN, A. A wave intensity technique analysis of high frequency vibrations. *Philosophical Transactions of the Royal Society of London A* 346, 1681 (1994), 489–499.
- [112] LANGLEY, R., AND BROWN, A. The ensemble statistics of the band-averaged energy of a random system. *Journal of Sound and Vibration* 275, 3-5 (2004), 847–857.
- [113] LANGLEY, R., AND BROWN, A. The ensemble statistics of the energy of a random system subjected to harmonic excitation. *Journal of Sound and Vibration* 275 (2004), 823–846.
- [114] LANGLEY, R., AND CORDIOLI, J. Hybrid deterministic-statistical analysis of vibro-acoustic systems with domain couplings on statistical components. *Journal of Sound and Vibration* 321, 3-5 (2009), 893–912.
- [115] LANGLEY, R., AND KOVALEVSKY, L. Automatic recognition of the components of a hybrid FE-SEA model from a finite element model. In *Proceeding of Emerging Methods for Noise and Vibration (NOVEM2012)* (Sorrento, Italy, April 2012).
- [116] LANGLEY, R. S. On the diffuse field reciprocity relationship and vibrational energy variance in a random subsystem at high frequencies. *Journal of the Acoustical Society of America* 121, 2 (2007), 913–921.

- [117] LANGLEY, R. S. A Reciprocity Approach for Computing the Response of Wiring Systems to Diffuse Electromagnetic Fields. *IEEE Transactions on Electromagnetic Compatibility* 52, 4 (2010), 1041–1055.
- [118] LANGLEY, R. S., AND BREMNER, P. A hybrid method for the vibration analysis of complex structural-acoustic systems. *Journal of the Acoustical Society of America* 105, 3 (1999), 1657.
- [119] LANGLEY, R. S., AND COTONI, V. Response variance prediction in the statistical energy analysis of built-up systems. *Journal of the Acoustical Society of America* 115, 2 (2004), 706–718.
- [120] LANGLEY, R. S., AND COTONI, V. Response variance prediction for uncertain vibro-acoustic systems using a hybrid deterministic-statistical method. *Journal of the Acoustical Society of America* 122, 6 (2007), 3445–3463.
- [121] LANGLEY, R. S., AND SHORTER, P. J. The wave transmission coefficients and coupling loss factors of point connected structures. *The Journal of the Acoustical Society of America* 113, 4 (2003), 1947.
- [122] LASE, Y., ICHCHOU, M., AND JÉZÉQUEL, L. Energy flow analysis of bars and beams: theoretical formulations. *Journal of Sound and Vibration* 192, 1 (1996), 281–305.
- [123] LE BOT, A. A vibro-acoustic model for high frequency analysis. *Journal of Sound and Vibration* 211, 4 (1998), 537–554.
- [124] LE BOT, A. Energy transfer for high frequencies in built-up structures. *Journal of Sound and Vibration* 250, 2 (2002), 247–275.
- [125] LE BOT, A. Comparison of vibrational conductivity and radiative energy transfer methods. *Journal of Sound and Vibration* 283, 1-2 (2005), 135–151.
- [126] LEFTERIU, S., SOUZA LENZI, M., BERIOT, H., TOURNOUR, M., AND DESMET, W. Fast frequency sweep method for indirect boundary element models arising in acoustics. In *Proceedings of the International Conference on Noise and Vibration (ISMA2012)* (Leuven, Belgium, September 2012).
- [127] LEGAULT, J., LANGLEY, R., AND WOODHOUSE, J. Physical consequences of a nonparametric uncertainty model in structural dynamics. *Journal of Sound and Vibration* 331, 25 (2012), 5469–5487.
- [128] LEISSA, A. *Vibration of plates*. Acoustical Society of America, 1993.

- [129] LEVIN, D. Analysis of a collocation method for integrating rapidly oscillatory functions. *Journal of Computational and Applied Mathematics* 78, 1 (1997), 131–138.
- [130] LIU, Y., AND NISHIMYRA, N. The Fast Multipole Boundary Element Method for potential problems: a tutorial. *Engineering Analysis with Boundary Elements* 30 (2006), 371–381.
- [131] LUCAS, G. *Vibrational Characteristics of Structures with Uncertainty*. PhD thesis, University of New South Wales, 2008.
- [132] LYON, R., AND DEJONG, R. *Theory and application of statistical energy analysis*. Butterworth-Heinemann, 1995.
- [133] LYON, R., AND MAIDANIK, G. Power flow between linearly coupled oscillators. *Journal of the Acoustical Society of America* 34 (1962), 623–639.
- [134] MACE, B. Statistical energy analysis, energy distribution models and system modes. *Journal of Sound and Vibration* 264, 2 (2003), 391–409.
- [135] MACE, B., AND SHORTER, P. Energy flow models from finite element analysis. *Journal of Sound and Vibration* 233, 3 (2000), 369–389.
- [136] MAIDANIK, G., AND DICKEY, J. *On the External Input Power Into Coupled Structures*. Springer-Verlag, 1999.
- [137] MALHOTRA, M., AND PINSKY, P. Efficient computation of multi-frequency far-field solutions of the Helmholtz equation using Padé approximation. *Journal of Computational Acoustics* 08, 01 (2000), 223–240.
- [138] MANNING, J. SEA: a practical NVH design analysis method. In *Proceedings of the Styrian Noise, Vibration and Harshness Congress* (Graz, Austria, November 2006).
- [139] MANNING, J. E. Formulation of SEA Parameters using Mobility Functions. *Philosophical Transactions of the Royal Society A: Mathematical, Physical and Engineering Sciences* 346, 1681 (1994), 477–488.
- [140] MANNING, J. E. Hybrid SEA for Mid-Frequencies. *SAE Technical Paper 2007-01-2305* (2007).
- [141] MANOHAR, C., AND KEANE, A. Statistics of energy flow in spring-coupled one-dimensional subsystems. *Philosophical Transactions of the Royal Society of London A* 346 (1994), 525–542.

- [142] MARBURG, S. Six boundary elements per wavelength: is that enough? *Journal of Computational Acoustics* 10 (2002), 25–51.
- [143] MARBURG, S., AND NOLTE, B. *Computational Acoustics of Noise Propagation in Fluids-Finite and Boundary Element Methods*. Springer, 2008.
- [144] MASSON, P., REDON, E., PRIOU, J.-P., AND GERVAIS, Y. The application of the Trefftz method for acoustics. In *Proceedings of the third International Congress on Sound and Vibration (ICSV)* (Montreal, Canada, 1994).
- [145] METHA, M. *Random Matrices*. Academic Press, New York, 1991.
- [146] MOENS, D., AND HANSS, M. Non-probabilistic finite element analysis for parametric uncertainty treatment in applied mechanics: Recent advances. *Finite Elements in Analysis and Design* 47, 1 (2011), 4–16.
- [147] MOENS, D., AND VANDEPITTE, D. A fuzzy finite element procedure for the calculation of uncertain frequency-response functions of damped structures: Part 1 - Procedure. *Journal of Sound and Vibration* 288, 3 (2005), 431–462.
- [148] MOENS, D., AND VANDEPITTE, D. A survey of non-probabilistic uncertainty treatment in finite element analysis. *Computer Methods in Applied Mechanics and Engineering* 194, 12-16 (2005), 1527–1555.
- [149] MOENS, I. *On the use and the validity of the energy finite element method for high frequency vibrations*. PhD thesis, KU Leuven, 2001.
- [150] MOORE, G. Cramming More Components Onto Integrated Circuits. *Proceedings of the IEEE* 86, 1 (1998), 82–85.
- [151] NANDY, A. K., AND JOG, C. S. Optimization of vibrating structures to reduce radiated noise. *Structural and Multidisciplinary Optimization* 45, 5 (2012), 717–728.
- [152] NEFSKE, J., AND SUNG, S. Power flow finite element analysis of dynamic systems: basic theory and application to beams. *NCA Publications* 3 (1987), 47–54.
- [153] NGATCHOU, P., ZAREI, A., AND EL-SHARKAWI, A. *Pareto Multi Objective Optimization*. Institute of Electrical and Electronics Engineers, 2005, pp. 84–91.
- [154] NILSSON, C.-M., AND FINNVEDEN, S. Input power to waveguide calculated by a finite element method. *Journal of Sound and Vibration* 305 (2007), 641–658.

- [155] NOUY, A. Recent Developments in Spectral Stochastic Methods for the Numerical Solution of Stochastic Partial Differential Equations. *Archives of Computational Methods in Engineering* 16, 3 (2009), 251–285.
- [156] OBERKAMPF, W., DELAND, S., RUTHERFORD, B., DIEGERT, K., AND ALVIN, K. A new methodology for the estimation of total uncertainty in computational simulation. In *Proceedings of of the 40th AIAA/ASME/ASCE/AHS/ASC Structures, Structural Dynamics and Materials Conference, number AIAA-99-1612* (1999), pp. 3061–3083.
- [157] OBERKAMPF, W., DELAND, S., RUTHERFORD, B., DIEGERT, K., AND ALVIN, K. Error and uncertainty in modelling and simulation. *Reliability Engineering & System Safety* 75, 3 (2002), 333–357.
- [158] OCHMANN, M. The source simulation technique for acoustic radiation problems. *Acta Acustica united with Acustica* 81, 6 (1995), 512–527.
- [159] OHAYON, R., AND SOIZE, C. *Structural Acoustic and Vibration-Mechanical Models, Variational Formulations and Discretization*. Academic press, 1998.
- [160] OLVER, S. Moment-free numerical integration of highly oscillatory functions. *IMA Journal of Numerical Analysis* 26, 2 (2005), 213–227.
- [161] PEAKE, M., TREVELYAN, J., AND COATES, G. Novel basis functions for the partition of unity boundary element method for Helmholtz problems. *International Journal for Numerical Methods in Engineering* 93, 9 (2013), 905–918.
- [162] PEIFFER, A. Comparison of the computational expense of hybrid FEM/SEA and FEM calculation. In *Noise and Vibration: Emerging Methods (NOVEM2012)* (Sorrento, Italy, April 2012).
- [163] PELLISSETTI, M., CAPIEZ-LERNOUT, E., PRADLWATER, H., SOIZE, C., AND SCHÜ'ELLER. Reliability analysis of a satellite structure with a parametric and a non-parametric probabilistic model. *Computer Methods in Applied Mechanics and Engineering* 198, 2 (2008), 344–357.
- [164] PIERCE, A. Causality and mathematical models in vibration and acoustics, a realistic perspective. *Journal of the Acoustical Society of America* 105, 5 (1999), 2710–2716.
- [165] PIERCE, A. D. Resonant-frequency-distribution of internal mass inferred from mechanical impedance matrices, with application to fuzzy structure theory. *Journal of Vibration and Acoustics* 119, 3 (1997), 324.

- [166] PIERCE, A. D., SPARROW, V. W., AND RUSSELL, D. A. Fundamental Structural-Acoustic Idealizations for Structures with Fuzzy Internals. *Journal of Vibration and Acoustics* 117, 3A (1995), 339.
- [167] PLUYMERS, B. *Wave based modelling methods for steady-state vibro-acoustics*. PhD thesis, KU Leuven, 2006.
- [168] PLUYMERS, B., DESMET, W., VANDEPITTE, D., AND SAS, P. Application of an efficient wave-based prediction technique for the analysis of vibro-acoustic radiation problems. *Journal of Computational and Applied Mathematics* 168, 1-2 (2004), 353–364.
- [169] PLUYMERS, B., HAL, B., VANDEPITTE, D., AND DESMET, W. Trefftz-Based Methods for Time-Harmonic Acoustics. *Archives of Computational Methods in Engineering* 14, 4 (2007), 343–381.
- [170] PRATELLESI, A., PIERINI, M., BALDANZINI, N., AND D' AMICO, R. A stochastic BEM formulation for vibro-acoustic analysis of structures in the mid-to-high frequency range. WITPress, 2010, pp. 239–250.
- [171] PRATELLESI, A., VIKTOROVITCH, M., BALDANZINI, N., AND PIERINI, M. A hybrid formulation for mid-frequency analysis of assembled structures. *Journal of Sound and Vibration* 309, 3-5 (2008), 454–568.
- [172] RACHOWICZ, W., PARDO, D., AND DEMKOWICK, L. Fully automatic *hp*-adaptivity in three dimensions. *Computer Methods in Applied Mechanics and Engineering* 195, 37-40 (2006), 4816–4842.
- [173] RADE, D., AND STEFFEN, V. Optimization of dynamic vibration absorbers over a frequency band. *Mechanical Systems and Signal Processing* 14, 5 (2000), 679–690.
- [174] RAGNARSSON, P., PLUYMERS, B., DONDEERS, S., AND DESMET, W. Subcomponent modelling of input parameters for Statistical Energy Analysis by using a wave-based boundary condition. *Journal of Sound and Vibration* 329, 1 (2010), 96–108.
- [175] RUSSELL, D. A., AND SPARROW, V. W. Backscattering from a baffled finite plate strip with fuzzy attachments. *Journal of the Acoustical Society of America* 98, 3 (1995), 1527–1533.
- [176] SAAD, Y. *Iterative Methods for Sparse Linear Systems*, 2nd edition ed. 2003.
- [177] SCHENCK, H. Improved integral formulation for acoustic radiation problems. *Journal of the Acoustical Society of America* 1968 (44), 41–58.

- [178] SCHUËLLER, G., AND PRADLWARTER, H. Uncertain linear systems in dynamics: Retrospective and recent development by stochastic approaches. *Engineering Structures* 31, 11 (2009), 2507–2517.
- [179] SESTIERI, A., AND CARCATERRA, A. Vibroacoustic: The challenges of a mission impossible? *Mechanical Systems and Signal Processing* 34, 1-2 (2013), 1–18.
- [180] SHORTER, P., AND LANGLEY, R. Vibro-acoustic analysis of complex systems. *Journal of Sound and Vibration* 288, 3 (2005), 669–699.
- [181] SHORTER, P. J., AND LANGLEY, R. S. On the reciprocity relationship between direct field radiation and diffuse reverberant loading. *Journal of the Acoustical Society of America* 117, 1 (2005), 85–95.
- [182] SIMMONS, C. Structure-borne sound transmission through plate junctions and estimates of SEA coupling loss factors using the finite element method. *Journal of Sound and Vibration* 144, 2 (1991), 215–227.
- [183] SLADEK, J., SLADEK, V., AND VAN KEER, R. Global and local Trefftz boundary integral formulations for sound vibration. *Advances in Engineering Software* 33, 7-10 (2002), 469–476.
- [184] SMITH, M. A hybrid energy method for predicting high frequency vibrational response of point-loaded plates. *Journal of Sound and Vibration* 202, 3 (1997), 375–394.
- [185] SOIZE, C. Probabilistic structural modeling in linear dynamic analysis of complex mechanical systems. Part I - theoretical elements. *La Recherche Aérospatiale* 5 (1986), 23–48.
- [186] SOIZE, C. A nonparametric model of random uncertainties for reduced matrix models in structural dynamics. *Probabilistic Engineering Mechanics* 15, 3 (2000), 277–294.
- [187] SOIZE, C. Generalized probabilistic approach of uncertainties in computational dynamics using random matrices and polynomial chaos decompositions. *International Journal for Numerical Methods in Engineering* 81, 81 (2010), 939–970.
- [188] SOUZA LENZI, M., LEFTERIU, S., BERIOT, H., AND DESMET, W. A fast frequency sweep approach using Padé approximations for solving Helmholtz finite element models. *Journal of Sound and Vibration* 332, 8 (2013), 1897–1917.

- [189] STEFANOU, G. The stochastic finite element method: past, present and future. *Computer Methods in Applied Mechanics and Engineering* 198, 9-12 (2009), 1031–1051.
- [190] STRASBERG, M. Insuring causality of frequency-response functions with hysteretic damping. *Journal of the Acoustical Society of America* 109 (2001).
- [191] STRASBERG, M., AND FEIT, D. Vibration damping of large structures induced by attached small resonant structures. *Journal of the Acoustical Society of America* 99, 1 (1996), 335–344.
- [192] STROUBOULIS, T., COPPS, K., AND BABUSKA, I. The generalized finite element method. *Computer Methods in Applied Mechanics and Engineering* 190, 32-33 (2001), 4081–4193.
- [193] SUN, J. Q., JOLLY, M. R., AND NORRIS, M. A. Passive, Adaptive and Active Tuned Vibration Absorbers: A Survey. *Journal of Mechanical Design* 117, B (1995), 234.
- [194] SUN, Z., SUN, J., WANG, C., AND DAI, Y. Dynamic vibration absorbers used for increasing the noise transmission loss of aircraft panels. *Applied Acoustics* 48, 4 (1996), 311–321.
- [195] TEZAU, R., KALASHNIKOVA, I., AND FARHAT, C. The discontinuous enrichment method for medium-frequency Helmholtz problems with a spatially variable wavenumber. *Computer Methods in Applied Mechanics and Engineering* (2013).
- [196] THITE, A., AND MACE, B. Robust estimation of coupling loss factors from finite element analysis. *Journal of Sound and Vibration* 303, 3-5 (2007), 814–831.
- [197] THOMPSON, L., AND KUNTHONG, P. A residual based variational method for reducing dispersion error in Finite Element Methods. In *ASME 2005 International Mechanical Engineering Congress and Exposition* (Orlando, Florida, USA, November 2005), no. IMECE2005-80551, pp. 29–40.
- [198] THOMPSON, L. L., AND PINSKY, P. A Galerkin least-squares finite element method for the two-dimensional Helmholtz equation. *International Journal for Numerical Methods in Engineering* 38, 3 (1995), 371–397.
- [199] TOLL, J. Causality and the dispersion relation: logical foundations. *Physical review* 104, 6 (1956), 1760–1770.

- [200] TREFETHEN, L. Is Gauss quadrature better than Clenshaw-Curtis? *SIAM review* 50, 1 (2008), 67–87.
- [201] TREFFTZ, E. Ein Gegenstück zum Ritzschen Verfahren. In *Proceedings of the Second International Congress on Applied Mechanics* (Zurich, Switzerland, 1926).
- [202] VAN GENECHTEN, B. *Trefftz-based mid-frequency analysis of geometrically complex vibro-acoustic systems: hybrid methodologies and multi-level modelling*. PhD thesis, KU Leuven, 2010.
- [203] VAN GENECHTEN, B., ATAK, O., BERGEN, B., DECKERS, E., JONCKHEERE, S., LEE, J. S., MARESSA, A., VERGOTE, K., PLUYMERS, B., VANDEPITTE, D., AND ET AL. An efficient Wave Based Method for solving Helmholtz problems in three-dimensional bounded domains. *Engineering Analysis with Boundary Elements* 36, 1 (2012), 63–75.
- [204] VAN HAL, B. *Automation and performance optimization of the wave based method for interior structural-acoustic problems*. PhD thesis, KU Leuven, 2004.
- [205] VANMAELE, C. *Development of a wave based prediction technique for the efficient analysis of low- and mid- frequency structural vibrations*. PhD thesis, KU Leuven, 2007.
- [206] VANMAELE, C., VANDEPITTE, D., AND DESMET, W. An efficient wave based prediction technique for plate bending vibrations. *Computer Methods in Applied Mechanics and Engineering* 196, 33-34 (2007), 3178–3189.
- [207] VENTER, G. *Review of Optimization Techniques*. Wiley Blackwell (John Wiley & Sons), 2010.
- [208] VERGOTE, K. *Dynamic analysis of structural components in the mid frequency range using the wave based method: non-determinism and inhomogeneities*. PhD thesis, KU Leuven, 2012.
- [209] VERGOTE, K., VAN GENECHTEN, B., VANDEPITTE, D., AND DESMET, W. Development of a wave based prediction technique for the efficient analysis of low- and mid- frequency structural vibrations. *Computers & Structures* 89, 11-12 (2011), 868–877.
- [210] VERGOTE, K., VANMAELE, C., VANDEPITTE, D., AND DESMET, W. An efficient wave based approach for the time-harmonic vibration analysis of 3D plate assemblies. *Journal of Sound and Vibration* 332, 8 (2013), 1930–1946.

- [211] VIKTOROVITCH, M., MORON, P., THOUVEREZ, F., AND JÉZÉQUEL, L. A stochastic approach of the energy analysis for one-dimensional structures. *Journal of Sound and Vibration* 216, 3 (1998), 361–378.
- [212] VIKTOROVITCH, M., AND PRATELLESI, A. A hybrid mid-frequency formulation for vibro-acoustic predictions. *Noise Control Engineering Journal* 56, 1 (2008), 71–84.
- [213] VIKTOROVITCH, M., THOUVEREZ, F., AND JÉZÉQUEL, L. A new random boundary element formulation applied to high frequency phenomena. *Journal of Sound and Vibration* 223, 2 (1999), 273–296.
- [214] VIKTOROVITCH, M., THOUVEREZ, F., AND JÉZÉQUEL, L. An integral formulation with random parameters adapted to the study of the vibrational behaviour of structures in the middle- and high-frequency field. *Journal of Sound and Vibration* 247, 3 (2001), 431–452.
- [215] WEAVER, R. Mean and mean-square response of a prototypical master/fuzzy structure. *Journal of the Acoustical Society of America* 101, 3 (1997), 1441–1449.
- [216] WEIDEMAN, J. A. C., AND TREFETHEN, L. N. The kink phenomenon in Fejér and Clenshaw-Curtis quadrature. *Numerische Mathematik* 107, 4 (2007), 707–727.
- [217] WILLIAMS, A. *Electronic Filter Design Handbook*. McGraw Hill, 1988.
- [218] WOHLEVER, J., AND BERNHARD, R. Mechanical energy flow models of rods and beams. *Journal of Sound and Vibration* 153, 1 (1992), 1–19.
- [219] WONG, R. *Asymptotic Approximation of Integrals (Classics in Applied Mathematics)*. SIAM: Society for Industrial and Applied Mathematics, 2001.
- [220] XIE, G., D.J., T., AND JONES, C. Mode count and modal density of structural systems: relationships with boundary conditions. *Journal of Sound and Vibration* 274 (2004), 621–651.
- [221] ZHAO, X., AND VLAHOPOULOS, N. A basic hybrid finite element formulation for mid-frequency analysis of beams connected at an arbitrary angle. *Journal of Sound and Vibration* 269, 1-2 (2004), 135–164.
- [222] ZIELINSKI, A. P., AND HERRERA, I. Trefftz method: Fitting boundary conditions. *International Journal for Numerical Methods in Engineering* 24, 5 (1987), 871–891.

- [223] ZIENKIEWICZ, O. C. *The Finite Element Method*, 6th ed. Butterworth-Heinemann, 2005.
- [224] ZITZLER, E., LAUMANN, M., AND BLEULER, S. *A Tutorial on Evolutionary Multiobjective Optimization*. Springer-Verlag, 2004.

Curriculum vitae

Personal data

Roberto D'Amico
Born 5 September 1985, Prato, Italy
damico.rob@gmail.com

Professional experience

09/2011 - present: Ph.D. researcher at KU Leuven, Belgium

Topic: Efficient frequency averaging techniques; numerical techniques for noise and vibration; uncertainty and variability.
Funding: Marie Curie ITN Project “Mid-Frequency” and the Research Fund KU Leuven.

01/2010 - 09/2011: Ph.D. researcher at University of Florence, Italy

Topic: Stochastic BEM; numerical techniques for noise and vibration; uncertainty and variability; acoustic BEM and Fast Multipole BEM industrial applications.
Funding: Collaborative EU Project “MID-MOD”.

09/2009 - 12/2009: Internship at LMS International, Belgium

Topic: Improvement of solution accuracy for acoustic BEM and Fast Multipole BEM.

09/2008 - 06/2009: Internship at Pramac, Italy

Topic: Design of a novel lifting mechanism for hand pallet trucks.

Education

10/2007 - 12/2009: M.Sc. degree in Mechanical Engineering, University of Florence, Italy

Thesis: Fast multipole boundary element formulation for the vibro-acoustic analysis of automotive and railway structures.

Grade: 110/110 cum laude

Other: Received the “Ciullini award” from Ordine degli Ingegneri della Provincia di Firenze (Register of Engineers of Florence, 2011) and the “Pier Luigi Ferrara award” from Nuovo Pignone (General Electric, 2010).

10/2004 - 09/2007: B.Sc. degree in Industrial Engineering, University of Florence, Italy

Thesis: Design of a traversing gear for probe positioning in a wind tunnel.

Grade: 110/110 cum laude

Other: Received the “Bardazzi award” (2008) and the “Ducati award” in the mechanical design competition “La Fisica in Moto” (2006).

List of Publications

Articles in refereed journals

- [1] D'AMICO, R., KOO, K., CLAEYS, C. C., PLUYMERS, B. AND DESMET, W. Optimal dynamic vibration absorber design for minimizing the band-averaged input power using the residue theorem. *Accepted with revisions for publication in the Journal of Sound and Vibration* (2014).
- [2] D'AMICO, R., HUYBRECHS, D., AND DESMET, W. A refined use of the residue theorem for the evaluation of band-averaged input power into linear second-order dynamic systems. *Journal of Sound and Vibration* 333, 6 (2014), 1796–1817.
- [3] DECKERS, E., ATAK, O., COOX, L., D'AMICO, R., DEVRIENDT, H., JONCKHEERE, S., KOO, K., PLUYMERS, B., VANDEPITTE, D. AND DESMET, W. The wave based method: an overview of 15 years of research. *Wave Motion* 51, 4 (2013), 550–565.
- [4] D'AMICO, R., KOO, K., HUYBRECHS, D., AND DESMET, W. On the use of the residue theorem for the efficient evaluation of band-averaged input power into linear second-order dynamic systems. *Journal of Sound and Vibration* 332, 26 (2013), 7205–7225.
- [5] D'AMICO, R., PRATELLESI, A., BALDANZINI, N. AND PIERINI, M. Reformulation of the Stochastic BEM to improve the computational efficiency in the prediction of vibro-acoustic behaviour of structures with uncertainties. *Journal of Sound and Vibration* 332, 9 (2013), 2132–2148.
- [6] D'AMICO, R., PRATELLESI, A. AND PIERINI, M. Improving the convergence of the Fast Multipole BEM for the exterior sound radiation of a truck muffler. *SAE International Journal of Commercial Vehicles* 5, 1 (2012), 407–419.

- [7] D'AMICO, R., NEHER, J., WENDER, B. AND PIERINI, M. On the improvement of the solution accuracy for exterior acoustic problems with BEM and FMBEM. *Engineering Analysis with Boundary Elements* 36, 7 (2012), 1104–1115.

Chapters in academic books

- [8] DESMET, W., PLUYMERS, B., ATAK, O., BERGEN, B., D'AMICO, R., DECKERS, E., JONCKHEERE, S., KU, K., LEE, J. S., MARESSA, A., NAVARRETE ALZATE, N., VAN GENECHTEN, B., VANDEPITTE, D. AND VERGOTE, K. The Wave Based Method. In *“Mid-Frequency” CAE Methodologies for Mid-Frequency Analysis in Vibration and Acoustics, Chapter 1, KU Leuven* (2012).

Articles in conference proceedings

- [9] D'AMICO, R., KOO, K., CLAEYS, C., PLUYMERS, B. AND DESMET, W. Optimization of the frequency averaged input power into plates with dynamic vibration absorbers using the Wave Based Method. In *Proceedings of the International Conference on Vibration Problems (ICOVP2013)* (Lisbon, Portugal, 2013).
- [10] KOO, K., D'AMICO, R., PLUYMERS, B. AND DESMET, W. Design optimization of the frequency averaged input power using the residue theorem. In *Proceedings of the 20th International Congress on Sound and Vibration (ICSV20)* (Bangkok, Thailand, 2013).
- [11] DECKERS, E., ATAK, O., COOX, L., D'AMICO, R., DEVRIENDT, H., JONCKHEREE, S., KOO, K., PLUYMERS, B., VANDEPITTE, D. AND DESMET, W. The Wave Based Method: current state of the art. In *Proceedings of the 1st Euro-Mediterranean Conference on Structural Dynamics and Vibroacoustics (MEDYNA2013)* (Marrakesh, Morocco, 2013).
- [12] D'AMICO, R., VERGOTE, K., LANGLEY, R. AND DESMET, W. On the use of the Lorentzian function for the evaluation of the frequency averaged input power into plates. In *Proceedings of the International Conference on Noise and Vibration Engineering (ISMA2012)* (Leuven, Belgium, 2012).
- [13] D'AMICO, R., VERGOTE, K., AND DESMET, W. Lorentzian-weighted frequency averaging for the evaluation of the input power into one-

- dimensional structural dynamic systems. In *Proceedings of the Inter-Noise 2012 Conference* (New York, US, 2012).
- [14] D'AMICO, R., PRATELLESI, A. AND PIERINI, M. Improving the convergence of the Fast Multipole BEM for the exterior sound radiation of a truck muffler. In *Proceedings of the 7th International Styrian Noise Vibration & Harshness Congress: the European Automotive Noise Conference (ISNVH2012)* (Graz, Austria, 2012).
- [15] D'AMICO, R., PRATELLESI, A., BALDANZINI, N. AND PIERINI, M. Stochastic Boundary Element Method to predict the effects of geometrical uncertainties in the mid-frequency vibro-acoustic analysis. In *Proceedings of Noise and Vibration: emerging methods 2010 (NOVEM2012)* (Sorrento, Italy, 2012).
- [16] BARTOLOZZI, G., D'AMICO, R., PRATELLESI, A., AND PIERINI, M. An efficient method for selecting CHIEF points. In *Proceedings of the 7th International Conference on Structural Dynamics (EURODYN2011)* (Leuven, Belgium, 2011).
- [17] D'AMICO, R., PRATELLESI, A., PIERINI, M. AND TOURNOUR, M. Efficient Method to Avoid Fictitious Eigenvalues for Indirect BEM. In *Proceedings of International Conference on Noise and Vibration Engineering (ISMA2010)* (Leuven, Belgium, 2010).
- [18] PRATELLESI, A., PIERINI, M., BALDANZINI, N. AND D'AMICO, R. A Stochastic BEM Formulation for the Vibro-acoustic Analysis of Mid and High-frequency Structures. In *Proceedings of the 32nd International Conference on Boundary Elements and Other Mesh Reduction Methods* (New Forest, UK, 2010).
- [19] D'AMICO, R., PRATELLESI, A., PIERINI, M. AND TOURNOUR, M. Mitigation of the Non-uniqueness Problem for the Indirect Boundary Element Method. In *Proceedings of the 10th International Conference on Recent Advances in Structural Dynamics* (Southampton, UK, 2010).

Abstracts in conference proceedings

- [20] DESMET, W., ATAK, O., BERGEN, B., D'AMICO, R., DECKERS, E., JONCKHEERE, S., KU, K., VAN GENECHTEN, B., VERGOTE, K., PLUYMERS, B., AND VANDEPITTE, D. The Wave Based Method: an efficient alternative for vibro-acoustic predictions in the mid-frequency range. In *Proceedings of Innovations in Wave Modelling 2012* (Nottingham, UK, 2012).



SCHOOL OF ENGINEERING
DEPARTMENT OF INDUSTRIAL
ENGINEERING
Via di Santa Marta, 3
50139 Firenze, Italy

FACULTY OF ENGINEERING SCIENCE
DEPARTMENT OF MECHANICAL
ENGINEERING
PRODUCTION ENGINEERING,
MACHINE DESIGN AND AUTOMATION
Celestijnenlaan 300B
B-3001 Heverlee, Belgium

